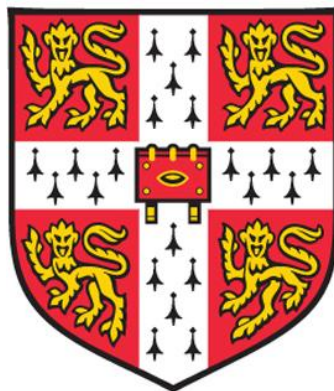


UNIVERSITY OF CAMBRIDGE

Department of Materials Science and Metallurgy



**Metal Oxides for Efficient Infrared
to Visible Upconversion**

Isabelle Etchart

Corpus Christi College

A dissertation submitted for the degree of Doctor of Philosophy

PREFACE

This dissertation is submitted for the degree of Doctor of Philosophy at the University of Cambridge, UK. The research described in this thesis was carried out by myself in the period October 2007 to August 2010, under the supervision of Prof. Anthony K. Cheetham, Goldsmith's Professor of Materials Science, Department of Materials Science and Metallurgy, University of Cambridge.

To the best of my knowledge, the work described in this dissertation is original, except where due reference has been made to the work of others. This dissertation is the result of my own work. Unless stated, the experiments were performed by myself using the facilities available in various institutions, including the University of Cambridge, Queen Mary University of London, the University of Surrey, and Saint-Gobain Recherche.

No part of this dissertation, or any similar to it, has been, or is currently being submitted for any degree at this, or any other university.

This dissertation is less than 60,000 words in length.

Isabelle Etchart

Cambridge

August, 2010

ABSTRACT**Metal Oxides for Efficient Infrared to Visible Upconversion**

Upconversion phosphor materials are attracting considerable attention for their possible applications in solar cells with improved efficiency, nanomaterials for bio-imaging, lasers and novel display technologies. Upconversion materials, usually consisting of crystals doped with lanthanide ions, can convert low-energy incident radiation into higher energy emitted radiation. Several mechanisms are involved, including multiple photon absorption and energy transfers between dopants. Up to now, reported upconversion efficiencies have been relatively low, excitation thresholds quite high, and the investigated phosphors (generally fluorides) often presented poor chemical stability (hygroscopy), limiting their industrial applicability.

In this dissertation, we investigate the upconversion luminescence characteristics of rare-earth-doped $\text{RE}_2\text{BaZnO}_5$ ($\text{RE} = \text{Y}, \text{Gd}$) phosphors, for near-infrared to visible upconversion. Being oxides, these materials have good chemical, thermal and mechanical properties. A variety of dopants, including Yb^{3+} , Er^{3+} , Ho^{3+} and Tm^{3+} , were embedded in the host lattice, resulting in bright red, green, blue and white light emissions under 980 nm excitation and at relatively low excitation powers. Upconversion efficiencies up to $\sim 5.2\%$, 2.6% , 1.7% and 0.3% were respectively achieved in samples doped with Yb^{3+} , Er^{3+} (green and red emission), Yb^{3+} , Ho^{3+} (green emission), Yb^{3+} , Tm^{3+} (blue and near-infrared emission) and Yb^{3+} , Er^{3+} , Tm^{3+} (white light emission). We believe that our green, red and white emitting systems are the most efficient upconverting samples reported to date for green, red and white light emission, which makes them serious candidates for many of the applications listed above. The upconversion mechanisms were determined for the first time by means of in-depth steady-state and time-resolved spectroscopic investigations, including concentration and power dependence studies associated with temperature-dependent lifetime measurements.

ACKNOWLEDGMENTS

It is my privilege to express my deepest gratitude to Professor Anthony K. Cheetham, for giving me the opportunity to do my PhD in his group, for his conscientious guidance, tremendous friendliness, continuous encouragements, his trust in me, and for the valuable freedom he gave. I have to admit it was a huge disappointment for me when Tony announced, while I was applying to work with him, that he was going to move from Santa Barbara, California, to Cambridge, thus putting an end to my California dream, but I guess Cambridge was not too bad in the end!

I am also sincerely grateful to my supervisors from Saint-Gobain Recherche, Dr Arnaud Huignard, Dr Mathieu Bérard, Dr Marine Laroche, Dr Francois-Julien Vermersch and Dr Paul-Henri Guéring, who provided me, at different stages of this PhD, with conscientious industrial guidance and deep scientific insights. Thank you for your continuous enthusiasm and encouragement, and great dedication to this PhD! I am very thankful too to Olivier Delrieu, research engineer at Saint-Gobain Recherche, for doing some of the upconversion efficiency measurements, in a very professional way! It was extremely helpful. Last but not least, I am very grateful to Saint-Gobain for funding this PhD.

I also express my deepest gratitude to Dr William Gillin for giving me access to his spectroscopic facilities in Queen Mary University of London, for the excellent training he provided, for continuous support and trust, and for valuable feedback in paper writing. I am also extremely thankful to Ignacio Hernández for sharing the optical facilities, for the deep scientific insights, for his tremendous dynamism and dedication in assisting me ("call me anytime if you have a problem, I will come over, I don't live far!"), for his extreme patience, excellent feedback during the paper writing process and for continuous encouragement! I really appreciated working with you!

I am also extremely thankful to Dr Richard J. Curry, for giving me access to his spectroscopic facilities at the University of Surrey, for providing excellent training, for assisting me in the experiments, for deep scientific insights, for introducing me to Dr William Gillin for time-resolved experiments, and finally for excellent feedback during the paper writing process. Thank you for being so patient and dedicated! I also thank Mohammad N. Nordin, a PhD student at the University of Surrey, for assistance with some experiments, and also for his extreme patience and dedication!

Many thanks to my present (Ryan, Wei Li, Prashant, Hamish, Thiru, Ali, Jin, Tom, Paul, Josh, Dominik, Erika) and past (Pi'Keng, Pi'Note, P'Bee, James, Crystal, Barbara) group members, for their friendship and continuous support! I really enjoyed your company in our regular tea times, parties, trips to the pub, occasional traveling, punting, etc. I am particularly grateful to Ryan for always being very helpful in the lab, for sharing his chemistry expertise with me, and for helping me improve my English. Thank you so much! I also thank Thiru, Wei Li, Ryan and Jin for valuable feedback in the thesis writing process. I am also grateful to Pat for

her tremendous friendliness, and for being a very efficient and professional intermediate between Tony and his students. Thank you also to all the people in the Materials Science and Metallurgy Department who gave me access to their equipment; Kevin Roberts (furnaces), Rumen Tomov and Amr Abdelkader (ball-mill), Rob Cornell (ICP-AES), Mary Vickers and Andrew Moss (XRD), Anna Moisala (Raman), Stuart Wimbush (Pulsed Laser Deposition), etc. Thank you also to David Duke, Nathan Cliff and Les Allen for being extremely helpful in the new Cheetham lab installation process back in 2007, and all through this PhD.

This endeavour would not have been a success without the enduring support and encouragement of my friends, in Paris (Fleur, Christine, Guillaume, Anastasia, Marc, Alex, Lea, Heng, Hannoh, Bouh, Erik, etc) and in Cambridge (Marijn, Sri, Milos, Albert, Trudy, Anastasia, Pete, Steve, Arnaud, Tom, Geoff, BJ, Rob, Rose, Amr, Aurélie, Laure, Mohammad, Luke, etc). Thanks to my French friends for always finding time to entertain me during my periods at Saint-Gobain. It was fantastic to meet so many international people, from the various places in Cambridge, and get to know more about them and their various research areas (Medicine, History of Science, Archaeology, Criminology, Divinity, Chemistry, etc).

I am also extremely grateful to Corpus Christi College, for accepting me as a member of the College, and for providing me with an excellent social life that contributed strongly to making my PhD so pleasant. I enjoyed the long hours spent in Leckhampton and in the main college, socialising and sharing meals with my friends, attending parties, playing various sports, enjoying barbecues and pool parties during the summer, etc. That's probably what I will miss most when I leave Cambridge.

Finally, the blessings of my family gave me the strength to take up this work and complete it to the best of my ability. I am very grateful to my parents and to my sisters for their continuous encouragements, love and guidance throughout my studies.

Last but not least, I would like to thank my sweetheart, Owen, for his unconditional support, encouragements, patience, interesting scientific insights, and for all the good times we spent together, in Cambridge and elsewhere. Thank you for sharing this Cambridge experience with me, and making it so enjoyable! Good luck with the end of your PhD, which will be, for sure, very successful!

TABLE OF CONTENTS

PREFACE	i
ABSTRACT	ii
ACKNOWLEDGMENTS	iii
TABLE OF CONTENTS	v

CHAPTER 1: General Introduction **1**

1.1. Introduction to upconversion	1
1.2. Aims of the research	2
1.3. Organisation of the PhD	2
1.3.1. Supervision	2
1.3.2. Research laboratories and collaborations	2
1.3.3. Organisation of the research	3
1.4. Previous work	4
1.5. Organisation of the PhD dissertation	4
1.6. Contributions to the PhD work.....	5
References	6

CHAPTER 2: Lanthanides and their Optical Properties..... **8**

2.1. Introduction	8
2.2. Energy levels of lanthanide elements	8
2.2.1. Electronic structure of lanthanide elements	8
2.2.2. $4f$ energy levels of lanthanide elements	9
2.2.2.1. $4f$ energy level splitting	9
2.2.2.2. The Dieke diagram	11

2.3. Lanthanide excitation processes	13
2.3.1. Three types of energy absorption transition	13
2.3.2. Processes involved upon lanthanide excitation	14
2.4. Lanthanide de-excitation processes	15
2.4.1. Radiative emission transitions	15
2.4.1.1. Radiative emission transitions in a simplified 2-level system	15
2.4.1.2. Selection rules for optical transitions	16
2.4.1.3. Judd-Ofelt theory	17
2.4.2. Non-radiative emission transitions	18
2.4.2.1. Multiphonon relaxation	18
2.4.2.2. Concentration quenching	20
2.5. Energy transfers	20
2.5.1. Introduction	20
2.5.2. Radiative and non-radiative energy transfers	20
2.5.3. Energy transfer probability	21
2.5.3.1. Non-radiative energy transfer	21
2.5.3.2. Radiative energy transfer	23
2.5.3.3. How to distinguish between radiative and non-radiative energy transfers	23
2.6. Summary	24
References	25
CHAPTER 3: Upconversion	27
3.1. Introduction	27
3.2. Conversion of low-energy incident radiation into higher-energy emitted radiation	28
3.3. Main upconversion mechanisms	29
3.3.1. Upconversion by excited state absorption (ESA)	29
3.3.2. Upconversion by sensitised energy transfer upconversion (ETU)	30
3.3.3. Upconversion by cooperative luminescence	31
3.3.4. Upconversion by cooperative sensitisation	32
3.3.5. Upconversion by photon avalanche	33
3.4. Rate equations relevant to upconversion processes	34
3.4.1. Rate equations in a simplified 3-level system	34
3.4.2. Pump power dependence of upconversion in the case where ETU is dominant over ESA	36
3.4.3. Pump power dependence of upconversion in the case where ESA is dominant over ETU	37

3.5. Time-evolution of upconversion luminescence emission	37
3.6. Upconversion materials and their potential applications	39
3.6.1. Upconversion materials investigated over the last five years	39
3.6.2. Main applications of upconversion materials	39
3.7. Summary	41
References	43
CHAPTER 4: Experimental	48
4.1. Introduction	48
4.2. Synthesis of materials	48
4.2.1. Background: solid-state and solution synthesis methods	48
4.2.2. Synthesis protocols used during this PhD	50
4.3. Structural characterisation: X-ray diffraction and Rietveld refinement	52
4.3.1. Background: X-ray diffraction and Rietveld refinement	52
4.3.2. Experimental setup for X-ray diffraction measurements	52
4.4. Elemental analysis: ICP-AES	53
4.4.1. Introduction to ICP-AES	53
4.4.2. Sample preparation for ICP-AES	53
4.5. Spectroscopic characterisation	54
4.5.1. Upconversion photoluminescence and efficiency quantification	54
4.5.1.1. Background	54
4.5.1.2. Experimental setup for steady-state upconversion emission measurement	55
4.5.2. Time-resolved spectroscopy	58
4.5.2.1. Background	58
4.5.2.2. Experimental setup for time-resolved spectroscopy experiments	59
4.5.3. Reflectance and absorbance spectroscopy	60
4.5.3.1. Background	60
4.5.3.2. Experimental setup for reflectance measurements	61
4.6. Summary	61
References	63

CHAPTER 5: Oxide phosphors for efficient light upconversion; Yb³⁺ and Er³⁺ co-doped RE₂BaZnO₅ (RE = Y, Gd) 64

5.1. Introduction	64
5.2. Results	65
5.2.1. Crystal structure	65
5.2.2. Determination of dopant concentration	67
5.2.3. Reflectance in the infrared, visible and ultraviolet	68
5.2.4. Upconversion luminescence emission	69
5.2.5. Concentration dependence of upconversion efficiencies	69
5.2.6. Pump power dependence of upconversion emission	73
5.2.7. Colour tunability with excitation pulse duration	74
5.2.8. Lifetime measurements	76
5.3. Discussion	78
5.4. Conclusions	81
References	82

CHAPTER 6: Efficient oxide phosphors for light upconversion; green emission from Yb³⁺ and Ho³⁺ co-doped RE₂BaZnO₅ (RE = Y, Gd) 83

6.1. Introduction	83
6.2. Results	83
6.2.1. Crystal structure	84
6.2.2. Reflectance in the infrared, visible and ultraviolet	85
6.2.3. Upconversion luminescence emission	86
6.2.4. Concentration dependence of upconversion efficiencies	86
6.2.5. Pump power dependence of upconversion emission	89
6.2.6. Lifetime measurements and temperature dependence	90
6.3. Discussion	95
6.3.1. Population and depopulation mechanisms of the excited levels	95
6.3.2. Temperature dependence of population and depopulation dynamics	99
6.4. Conclusions	101
References	102

CHAPTER 7: Oxide phosphors for light upconversion; Yb³⁺ and Tm³⁺ co-doped Y₂BaZnO₅	104
7.1. Introduction	104
7.2. Results	104
7.2.1. Crystal structure	105
7.2.2. Reflectance in the infrared, visible and ultraviolet	106
7.2.3. Upconversion luminescence emission	106
7.2.4. Concentration dependence of upconversion emission properties	107
7.2.5. Pump power dependence of upconversion emission	111
7.2.6. Lifetime measurements and dependence on dopant concentration	112
7.3. Discussion	115
7.3.1. Population mechanisms of the excited levels	115
7.3.2. Tm ³⁺ concentration dependence of lifetimes	117
7.3.3. Yb ³⁺ concentration dependence of lifetimes	119
7.4. Conclusions	120
References	121
CHAPTER 8: White light emission in Yb³⁺, Er³⁺ and Tm³⁺ doped Y₂BaZnO₅	122
8.1. Introduction	122
8.2. Two different strategies for white light production	122
8.3. Results	123
8.3.1. Crystal structure	123
8.3.2. Reflectance in the infrared	125
8.3.3. White light upconversion luminescence emission	126
8.3.3.1. Typical emission spectra under 977 nm excitation	126
8.3.3.2. Colour coordinates and upconversion efficiency	128
8.3.4. Lifetime measurements	132
8.3.5. Emission spectra under selective dopant excitation	135
8.4. Discussion	137
8.5. Conclusions	140
References	141

CHAPTER 9: Summary and conclusions	142
9.1. Summary	142
9.1.1. Upconversion properties of RE ₂ BaZnO ₅ : Yb ³⁺ , Er ³⁺ (RE = Y, Gd)	143
9.1.2. Upconversion properties of RE ₂ BaZnO ₅ : Yb ³⁺ , Ho ³⁺ (RE = Y, Gd)	144
9.1.3. Upconversion properties of Y ₂ BaZnO ₅ : Yb ³⁺ , Tm ³⁺	145
9.1.4. Y ₂ BaZnO ₅ doped with Yb ³⁺ , Er ³⁺ and Tm ³⁺ for white light upconversion emission	146
9.2. Conclusions	148
9.3. Future work	148
References	149
APPENDIX A: Rate equations in Yb³⁺, Er³⁺ co-doped materials	150
APPENDIX B: Supplementary data on RE₂BaZnO₅: Yb³⁺, Ho³⁺ (RE = Y, Gd) materials ...	154
APPENDIX C: Rate equations in Yb³⁺, Ho³⁺ co-doped materials	157
APPENDIX D: Supplementary data on Y₂BaZnO₅: Yb³⁺, Tm³⁺ materials	161
APPENDIX E: Rate equations in Yb³⁺, Tm³⁺ co-doped materials	165

CHAPTER 1: General Introduction

1.1. Introduction to Upconversion

Upconversion is a non-linear optical effect that can be used to convert low energy incident radiation (e.g. infrared light) into higher energy emitted radiation (e.g. visible light). It was first discovered in the 1960's by Auzel, Ovsyankin and Feofilov.¹⁻³ Since then, it has been the focus of much research, mainly for infrared to visible upconversion, taking advantage of the development, in the 1990's, of cheap and high-powered InGaAs laser diode excitation sources emitting at 980 nm. Upconverting materials could be used in many (future) applications, including bio-imaging,^{4,5} lasers,^{6,7} novel display technologies^{8,9} and solar cells.¹⁰⁻¹² Most of the lanthanide upconversion work is focused on the investigation of lanthanide-doped halide¹³⁻¹⁶ and oxide¹⁷⁻²⁰ host materials (sometimes in the form of glass²¹⁻²⁴).

Among these materials, β -NaYF₄: Yb³⁺ (18%), Er³⁺ (2%) has been often reported to be the most efficient infrared to visible upconverter.²⁵⁻²⁷ Despite being highly efficient, these fluoride materials have some important limitations that make them impractical for real world applications. First of all, as fluorides, they have poor chemical, thermal and mechanical properties. Moreover, because at ambient conditions β -NaYF₄ possesses a second polymorph (α -NaYF₄) with low upconversion efficiency, the synthesis of high purity β -NaYF₄ usually requires difficult synthesis conditions (long-annealing times, long reaction times and high temperatures) in order to overcome the free-energy barrier for the $\alpha \rightarrow \beta$ phase transition. Finally, the excitation power thresholds for upconversion emission in these fluorides are very high, making them unsuitable for many commercial applications. Despite these limitations, lanthanide-doped NaYF₄ materials are by far the most studied upconversion materials to date. In recent years much effort has been devoted to the synthesis of β -NaYF₄ nanocrystals with various sizes and morphologies, mainly for infrared to green, red, blue and white upconversion. Core-shell nanoparticles seem to be attracting much interest these days for their improved upconversion performances.^{28,29}

1.2. Aims of the research

The first goal of the PhD was to make novel upconverting materials which can be used in commercial applications (including solar-cells and 3D-displays), for infrared to visible upconversion. In order to be practical for the potential applications listed in section 1.1, upconversion materials must satisfy the following criteria:

- High chemical, thermal and mechanical stabilities
- High upconversion efficiency
- Low excitation threshold
- Good colour tunability
- Low cost
- Ease of synthesis and processing
- etc

In addition to synthesising materials with these characteristics, the second goal of the PhD was to gain an in-depth understanding of the upconversion mechanisms involved.

1.3. Organisation of the PhD

1.3.1. Supervision

The work presented in this thesis has been supervised by Prof. A. K. Cheetham, Goldsmith's Professor of Materials Science, in the Department of Materials Science and Metallurgy, University of Cambridge. Additional industrial supervision was given, at different stages of the PhD, by Dr A. Huignard, Dr M. Bérard, Dr M. Laroche, Dr F. J. Vermersch and Dr P. H. Guéring of Saint-Gobain Recherche.

1.3.2. Research laboratories and collaborations

The experiments presented in this thesis have been carried out in four different research laboratories:

- Department of Materials Science and Metallurgy, University of Cambridge, UK
(material synthesis, chemical and structural characterisation)
- Advanced Technology Institute, University of Surrey, UK
(luminescence spectra acquisition under pulsed excitation and at different excitation wavelengths)
- Saint-Gobain Recherche, France
(luminescence spectra acquisition under 980 nm excitation, upconversion efficiency measurements)
- Physics Department, Queen Mary University of London, UK
(time-resolved spectroscopy under pulsed excitation)

Collaborations were initiated with Dr R. J. Curry (University of Surrey), Dr. W. P. Gillin and Dr. I. Hernández (Queen Mary University of London) in February 2009 and September 2009, respectively, for spectroscopic measurements on the upconversion materials.

1.3.3. Organisation of the research

The first year of the PhD was devoted to learning about upconversion, and also to the assessment of the potential of lanthanide-doped inorganic-organic hybrid materials for light upconversion. No infrared to visible upconversion emission was achieved on these hybrid materials. However, the negative results obtained during that year helped us gain a better understanding of the dominant factors which can limit upconversion. We showed that the absence of upconversion in these hybrid materials was mainly due to the presence of high non-radiative emission rates, responsible for the quenching of upconversion luminescence, and arising from the presence of high vibration-energy organic functions at the proximity of the optically active ions. The results obtained on lanthanide-doped inorganic-organic hybrid materials will not be presented in this thesis. In 2008, we decided to change the focus of the PhD towards more conventional, purely inorganic materials. In particular, special attention was given to the investigation of lanthanide-doped metal oxide hosts due to their good chemical, thermal and mechanical stabilities.

1.4. Previous work

In this thesis, we present results obtained on Y_2BaZnO_5 and $\text{Gd}_2\text{BaZnO}_5$ hosts doped with lanthanide ions (Yb^{3+} , Er^{3+} , Ho^{3+} and Tm^{3+}) for green, red, blue and white upconversion emission under near-infrared (~ 980 nm) excitation. These ternary oxide hosts were first reported by Raveau et al. in 1982.^{30,31} Since then, they have attracted attention for their interesting magnetic^{31,32} and optical properties. The optical properties of RE_2BaMO_5 (RE = Y, Gd, Er, Yb, Eu and M = Cu, Zn) have been investigated mainly for down-conversion.^{33,34} High resolution absorption spectroscopy measurements at low temperature revealed the presence of two non-equivalent RE^{3+} sites in the structure.³¹ The upconversion properties of $\text{RE}_2\text{BaZnO}_5$ (RE = Gd, La) doped with Yb^{3+} and Er^{3+} were first reported by Birkel et al.³⁵ (Cheetham group, Materials Research Laboratory, University of Santa Barbara) for green, red and sometimes blue upconversion under 980 nm continuous excitation. In this PhD, we have focused mainly on Y_2BaZnO_5 and $\text{Gd}_2\text{BaZnO}_5$ hosts doped with lanthanide ions (Yb^{3+} , Er^{3+} , Ho^{3+} , Tm^{3+}) for green, red, blue and white upconversion emission properties. We have increased the upconversion performances of the previously reported Yb^{3+} , Er^{3+} co-doped materials³⁴ by changing the synthesis conditions and dopant concentrations. We have also focused on getting a good understanding of the upconversion mechanisms involved in our materials via in-depth spectroscopic studies.

1.5. Organisation of the PhD dissertation

This thesis is organised in 9 chapters. Chapters 1, 2 and 3 are introductory chapters. The PhD topic, aim, previous work and general organisation of the PhD work and dissertation are presented in chapter 1 (current chapter). Chapter 2 and 3 constitute literature reviews of lanthanide spectroscopy (lanthanide electronic structure and energy levels, processes involved in lanthanide excitation and de-excitation, energy transfers between lanthanide ions) and upconversion (dominant upconversion mechanisms, population densities of the energy levels populated by upconversion and their non-linear excitation power dependence, upconversion emission dynamics, materials that have been the focus of recent upconversion research and their potential applications), respectively. In chapter 4 we describe the experimental techniques used in sample preparation and characterisation. Subsequently, chapters 5, 6, 7 and 8 present our results on $\text{RE}_2\text{BaZnO}_5$ (RE = Y, Gd) oxide materials doped

with various lanthanide ions (Yb^{3+} , Er^{3+} , Ho^{3+} , Tm^{3+}), for infrared to green, red, blue and white upconversion. Steady-state and dynamic upconversion properties are investigated. Finally, the results are summed up in chapter 9 and the future work is mentioned.

1.6. Contributions to the PhD work

All the experimental work (experiment planning, syntheses, chemical, structural and spectroscopic characterisation) have been performed by myself, unless stated in this thesis. Some of the upconversion efficiency measurements presented in chapter 5 (section 5.2.5), chapter 6 (section 6.2.4) and chapter 7 (section 7.2.4) were performed by O. Delrieu, Research Technician at Saint-Gobain Recherche. Most of the spectroscopic characterisation work presented in this thesis has been carried out at Queen Mary University of London. After being trained to use the equipment by Dr W. P. Gillin and Dr I. Hernández, I made all the measurements presented in this thesis by myself, with the valuable technical assistance, when needed, of Dr. Hernández. A limited number of experiments (results presented in chapter 5, section 5.2.7, exclusively) were performed at the University of Surrey. I was trained by Dr R. J. Curry and M. N. Nordin, and did the measurements with their assistance.

References

- ¹ F. Auzel, *C.R. Acad. Sci. (Paris)*, 1966, **263B**, 819.
- ² F. Auzel, *C.R. Acad. Sci. (Paris)*, 1966, **262**, 1016.
- ³ V. V. Ovsyankin and P.P. Feofilov, *Sov. Phys. JETP Lett.*, 1966, **4**, 317.
- ⁴ R. S. Niedbala, H. Feindt, K. Kardos, T. Vail, J. Burton, B. Bielska, S. Li, D. Milunic, P. Bourdelle and R. Vallejo, *Anal. Biochem.*, 2001, **293**, 22.
- ⁵ M. Seydack, *Biosens. Bioelectron.*, 2005, **20**, 2454.
- ⁶ L. F. Johnson and H. J. Guggenheim, *Appl. Phys. Lett.*, 1971, **19**, 44.
- ⁷ E. Heumann, S. Bär, K. Rademaker, G. Huber, S. Butterworth, A. Dening and W. Seelert, *Appl. Phys. Lett.*, 2006, **88**, 061108.
- ⁸ E. Downing, L. Hesselink, J. Ralston and R. Macfarlane, *Science*, 1996, **273**, 1185.
- ⁹ A. Rapaport, J. Milliez, M. Bass, A. Cassanho and H. Jenssen, *J. Display Technol.*, 2006, **2**, 68.
- ¹⁰ C. Strümpel, M. McCann, G. Beaucarne, V. Arkhipov, A. Slaoui, V. Svrcek, C. del Cañizo and I. Tobias, *Sol. Energy Mater. Sol. Cells*, 2007, **91**, 238.
- ¹¹ T. Trupke, M.A. Green and P. Würfel, *J. Appl. Phys.*, 2002, **92**, 4117.
- ¹² A. Shalav, B. S. Richards and M. A. Green, *Sol. Energy Mater. Sol. Cells*, 2007, **91**, 829.
- ¹³ S. Heer, K. Kömpe, H. U. Güdel and M. Haase, *Adv. Mater.*, 2004, **16**, 2102.
- ¹⁴ A. Aebischer, S. Heer, D. Biner, K. Krämer, M. Haase and H. U. Güdel, *Chem. Phys. Lett.*, 2005, **407**, 124.
- ¹⁵ M. Pollnau, D. R. Gamelin, S. R. Lüthi, H. U. Güdel and M. P. Hehlen, *Phys. Rev. B*, 2000, **61**, 3337.
- ¹⁶ J. C. Boyer, F. Vetrone, L. A. Cuccia and J. A. Capobianco, *J. Am. Chem. Soc.*, 2006, **128**, 7444.
- ¹⁷ A. Patra, C. S. Friend, R. Kapoor and P. N. Prasad, *J. Phys. Chem. B*, 2002, **106**, 1909.
- ¹⁸ J. A. Capobianco, F. Vetrone, J. C. Boyer, A. Speghini and M. Bettinelli, *Opt. Mater.*, 2002, **19**, 259.
- ¹⁹ A. Patra, C. S. Friend, R. Kapoor and P. N. Prasad, *Chem. Mater.*, 2003, **15**, 3650.
- ²⁰ A. M. Pires, O. A. Serra, S. Heer and H. U. Güdel, *J. Appl. Phys.*, 2005, **98**, 063529.

- ²¹ Y. H. Wang and J. Ohwaki, *Appl. Phys. Lett.*, 1993, **63**, 3268.
- ²² X. Zou and T. Izumitani, *J. Non-Cryst. Solids*, 1993, **162**, 68.
- ²³ S. Tanabe, S. Yoshii, K. Hirao and N. Soga, *Phys. Rev. B*, 1992, **45**, 4620.
- ²⁴ M. P. Hehlen, N. J. Cockroft, T. R. Gosnell and A. J. Bruce, *Phys. Rev. B*, 1997, **56**, 9302.
- ²⁵ N. Menyuk, K. Dwight and J. W. Pierce, *Appl. Phys. Lett.*, 1972, **21**, 159.
- ²⁶ J. F. Suyver, A. Aebischer, S. García-Revilla, P. Gerner and H. U. Güdel, *Phys. Rev. B*, 2005, **71**, 125123.
- ²⁷ A. Aebischer, M. Hostettler, J. Hauser, K. Krämer, T. Weber, H. U. Güdel and H. B. Bürgi, *Angew. Chem. Int. Ed.*, 2006, **45**, 2802.
- ²⁸ G. S. Yi and G. M. Chow, *Chem. Mater.*, 2007, **19**, 341.
- ²⁹ H. S. Qian and Y. Zhang, *Langmuir*, 2008, **24**, 12123.
- ³⁰ C. Michel and B. Raveau, *J. Solid State Chem.*, 1982, **43**, 73.
- ³¹ C. Michel and B. Raveau, *J. Solid State Chem.*, 1983, **49**, 150.
- ³² G. F. Goya, R. C. Mercader, L. B. Steren, R. D. Sánchez, M. T. Causa and M. Tovar, *J. Phys.: Condens. Matter*, 1996, **8**, 4529.
- ³³ G. K. Cruz, H. C. Basso, M. C. Terrile and R. A. Carvalho, *J. Lumin.*, 2000, **86**, 155.
- ³⁴ S. Kunimi and S. Fujihara, *J. Electrochem. Soc.*, 2010, **157**, J175.
- ³⁵ A. Birkel, A. A. Mikhailovsky and A. K. Cheetham, *Chem. Phys. Lett.*, 2009, **477**, 325.

CHAPTER 2: Lanthanides and their Optical Properties

2.1. Introduction

All the upconversion mechanisms that will be presented in this thesis involve $4f-4f$ electronic transitions between the energy levels of trivalent lanthanide ions (e.g. Yb^{3+} , Er^{3+} , Ho^{3+} , Tm^{3+}) that are doped into a host lattice (e.g. Y_2BaZnO_5 , $\text{Gd}_2\text{BaZnO}_5$). These mechanisms involve lanthanide ion excitation processes via incident light absorption, energy transfers between the various dopants present in the host, radiative relaxation of the excited lanthanide ions via photon emission, and non-radiative relaxation processes via phonon emission or transfer of energy. Before we describe the upconversion mechanisms involved in our systems, we need to understand the basics of lanthanide spectroscopy. In this chapter, we present a literature review of the optical properties of lanthanide ions. The electronic structure and energy levels of lanthanides are presented, together with the mechanisms involved upon incident light absorption and lanthanide de-excitation. The last section is devoted to the presentation of energy transfer processes between dopants.

2.2. Energy levels of lanthanide elements

2.2.1. Electronic structure of lanthanide elements

Lanthanides¹ have unique luminescent properties and are considered to be non-toxic.² They emit in a wide range of wavelengths, covering the ultraviolet (UV), visible and near-infrared (NIR) regions, which makes them ideal candidates for many applications, including lasers, lighting and optical fibres.

The lanthanides (denoted Ln in this thesis) are the group of fifteen elements in the periodic table, from atomic numbers 57 to 71 (La, Ce, Pr, Nd, Pm, Sm, Eu, Gd, Tb, Dy, Ho, Er, Tm, Yb, Lu). It is worth noting that Yttrium ($Z = 39$) and Scandium ($Z = 21$) are often associated with the 15 lanthanides within the group of rare-earth elements (denoted RE in this thesis). The neutral lanthanide atoms have the ground state electronic configuration of a Xe core ($1s^2 2s^2 2p^6 3s^2 3p^6 4s^2 3d^{10} 4p^6 5s^2 4d^{10} 5p^6$), with two or three outer electrons ($6s^2$ or $6s^2 5d^1$), and a number of $4f$ electrons varying from 0 to 14. Movement along the lanthanide group

corresponds to the successive filling of the $4f$ electronic shell, from La ($4f^0$) to Lu ($4f^{14}$). Lanthanides are particularly common in their ionised trivalent state, having lost their $5d$ and $6s$ electrons. The electrons of the partially filled $4f$ shell are shielded from interactions with external forces by the overlying $5s^2$ and $5p^6$ shells. As a result, lanthanide energy levels are only slightly affected by the environment surrounding the ions, and remain practically invariant, for a given ion, in various hosts. The transitions involved in the upconversion processes presented in this thesis are $4f$ - $4f$ transitions. The absorption and emission cross-sections associated with these transitions are very small, as will be explained later. This results in relatively long lanthanide luminescence lifetimes (up to a few ms).

2.2.2. $4f$ energy levels of lanthanide elements

2.2.2.1. $4f$ energy level splitting

In this section, L and S are the quantum numbers associated with the total orbital angular momentum and the total spin of the lanthanide element under consideration, respectively. L and S are the sum of the quantum numbers l and s associated with the orbital angular momenta and the spin of each of the $4f$ electrons of the lanthanide ion considered, respectively. J is the quantum number associated with the total angular momentum, defined as $\vec{J} = \vec{L} + \vec{S}$ (the values of J are restricted to $|L - S| \leq J \leq |L + S|$). Table 2.1 lists the values of S , L and J for trivalent lanthanide ions in their ground state.³

When the lanthanide ions are doped into a solid, the degeneracy of the free-ion levels is removed by coulombic, spin-orbit and crystal-field interactions (Figure 2.1). Coulombic (or electrostatic) interactions arise from the existence of repulsions between the $4f$ electrons of the lanthanide ion considered. This results in a splitting of the free-ion levels into ^{2S+1}L energy levels, which are each $(2L + 1)(2S + 1)$ -fold degenerate. The electrostatic energy splitting of the ^{2S+1}L terms is typically around 10^4 cm^{-1} . Spin-orbit interactions (arising from the electromagnetic interaction between the electron spin and the magnetic field created by the electron's motion) split each ^{2S+1}L term into $(2J + 1)$ states denoted $^{2S+1}L_J$. The typical splitting of $^{(2S+1)}L_J$ terms is on the order of 10^3 cm^{-1} . Finally, the interaction of the $4f$ electrons with the crystal field of the surrounding environment results in a Stark splitting of the $^{(2S+1)}L_J$ terms into $(2J + 1)$ terms (if the number n of $4f$ electrons is even) or $(J + 1/2)$ terms (if n is

odd) denoted $^{(2S+1)}L_{J,\mu}$. In the case where n is odd, Kramer's doublets are observed. The Stark splitting is typically on the order of 10^2 cm^{-1} .

Ion	Z	Number of 4f electrons (n)	$S = \sum s$	$L = \sum l$	$J = L - S$ (if $n < 7$) $J = L + S$ (if $n \geq 7$)
La ³⁺	57		0	0	0
Ce ³⁺	58	↑	1/2	3	5/2
Pr ³⁺	59	↑ ↑	1	5	4
Nd ³⁺	60	↑ ↑ ↑	3/2	6	9/2
Pm ³⁺	61	↑ ↑ ↑ ↑	2	6	4
Sm ³⁺	62	↑ ↑ ↑ ↑ ↑	5/2	5	5/2
Eu ³⁺	63	↑ ↑ ↑ ↑ ↑ ↑	3	3	0
Gd ³⁺	64	↑ ↑ ↑ ↑ ↑ ↑ ↑	7/2	0	7/2
Tb ³⁺	65	↑↓ ↑ ↑ ↑ ↑ ↑ ↑	3	3	6
Dy ³⁺	66	↑↓ ↑↓ ↑ ↑ ↑ ↑ ↑	5/2	5	15/2
Ho ³⁺	67	↑↓ ↑↓ ↑↓ ↑ ↑ ↑ ↑	2	6	8
Er ³⁺	68	↑↓ ↑↓ ↑↓ ↑↓ ↑ ↑ ↑	3/2	6	15/2
Tm ³⁺	69	↑↓ ↑↓ ↑↓ ↑↓ ↑↓ ↑ ↑	1	5	6
Yb ³⁺	70	↑↓ ↑↓ ↑↓ ↑↓ ↑↓ ↑↓ ↑	1/2	3	7/2
Lu ³⁺	71	↑↓ ↑↓ ↑↓ ↑↓ ↑↓ ↑↓ ↑↓	0	0	0

Table 2.1: Electronic configurations of trivalent lanthanide ions in their ground state.³

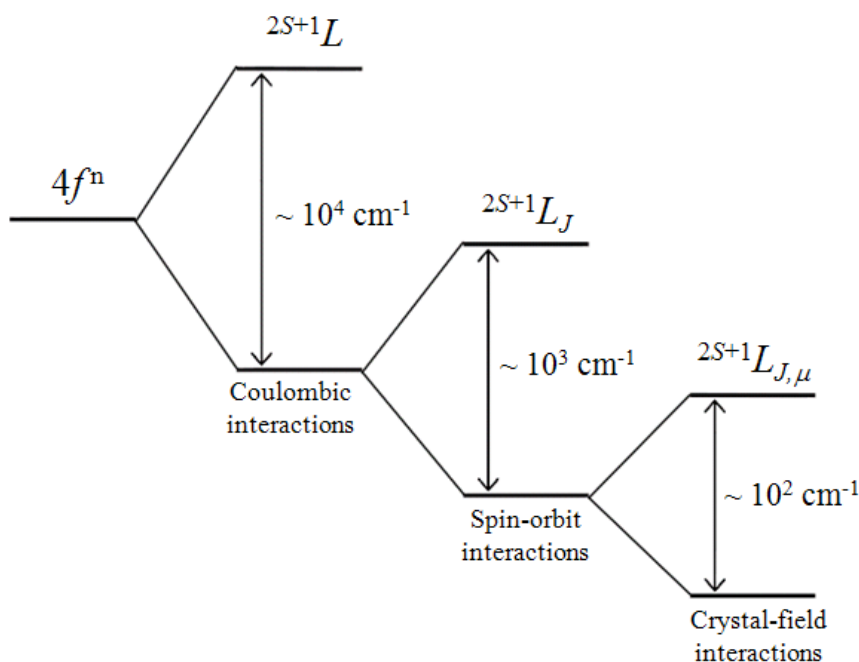


Figure 2.1: Interactions responsible for the loss of the lanthanide $4f$ free-ion degeneracy.

It is worth noting that for lanthanides, the crystal field interaction ($\sim 10^2 \text{ cm}^{-1}$) is smaller than the spin-orbit interaction ($\sim 10^3 \text{ cm}^{-1}$). This arises from the shielded character of the electrons in the $4f$ shell. This is not the case for transition-metal ions.

2.2.2.2. The Dieke diagram

The $4f$ energy levels of lanthanide ions are characteristic of each ion and are not affected much by the environment of the ion, as mentioned earlier. The $4f$ - $4f$ transition energies are therefore relatively invariant for a given ion in different host lattices. The characteristic $2S+1L_J$ energy levels of lanthanide ions doped into LaCl_3 ^{4,5} were measured by Dieke et al. in the 1960's. This work resulted in the elaboration of the so-called *Dieke diagram* (Figure 2.2), which has since then become a reference used to approximate the energy levels of the $2S+1L_J$ multiplet manifolds of trivalent lanthanide ions embedded in any host lattice. The Dieke diagram was extended to higher energies by Ogasawara et al.⁶ The width of each state in Figure 2.2 indicates the magnitude of the crystal-field splitting, and the centre of each multiplet approximates the location of the free ion $2S+1L_J$ energy level.

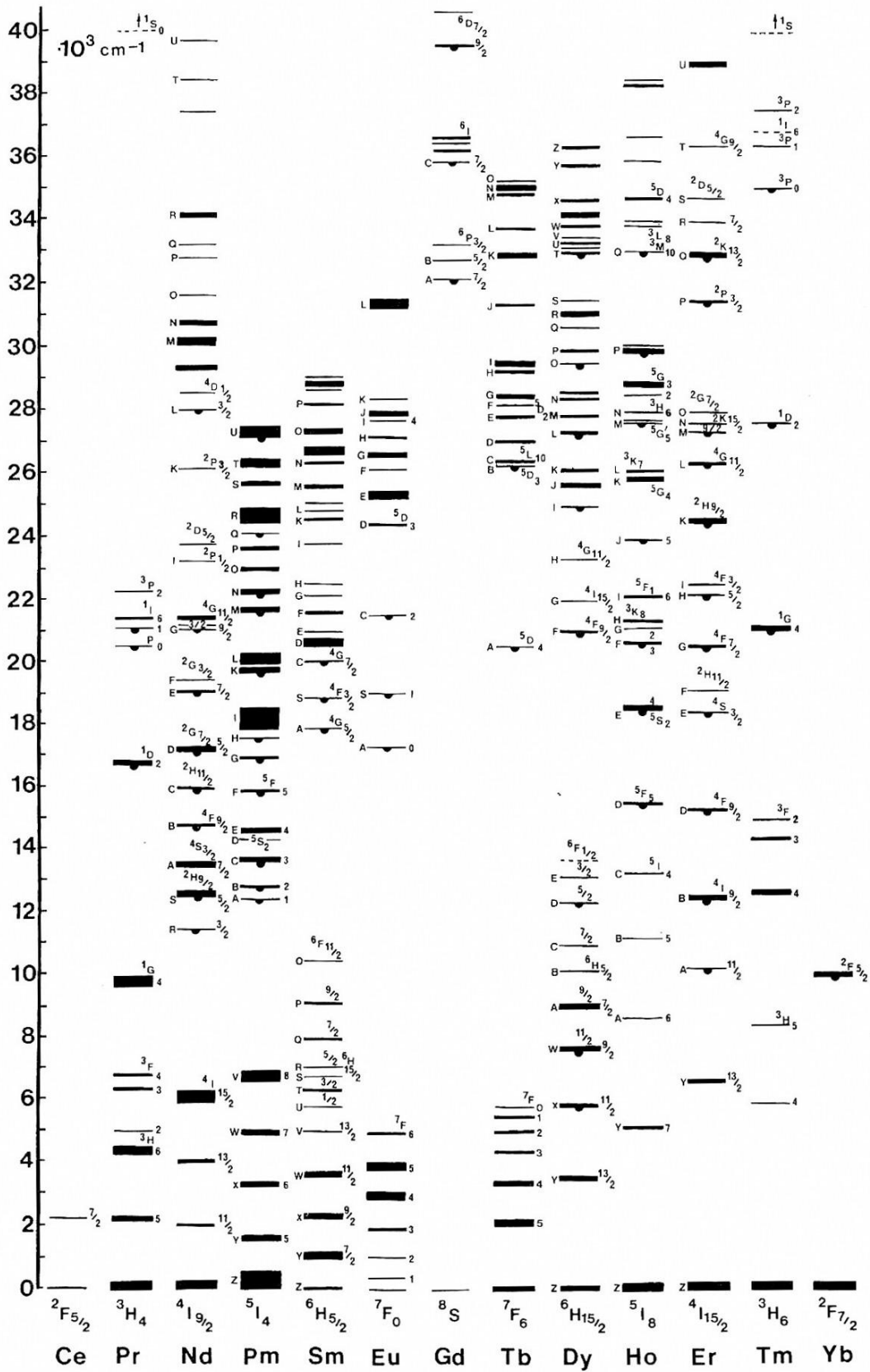


Figure 2.2: Dieke diagram: energy levels of the $^{2S+1}L_J$ multiplet manifolds of trivalent lanthanide ions.⁴

2.3. Lanthanide excitation processes

In this section, the processes involved upon excitation of a lanthanide ion by an electromagnetic radiation are described.

2.3.1. Three types of energy absorption transition

Lanthanide ions can exhibit three types of excitation transitions: $4f$ - $4f$ transitions, $4f$ - $5d$ transitions, and charge-transfer state transitions (Figure 2.3).³

$4f$ - $4f$ transitions

$4f$ - $4f$ transitions are very important in spectroscopy and will be the focus of this PhD thesis.³ They involve movements of electrons between the different energy levels of the $4f$ orbitals of the same lanthanide ion. $4f$ - $4f$ electric-dipole transitions are in theory forbidden by the parity rule (see explanation in section 2.4.1.2). However, they are in practice generally observed, but the corresponding emission bands are usually weak and narrow.

$4f$ - $5d$ transitions

In $4f$ - $5d$ transitions, one of the $4f$ electrons is excited to a $5d$ orbital of higher energy.³ This type of excitation absorption is usually denoted $4f^n \rightarrow 4f^{n-1}5d$ and is typically observed in Ce^{3+} ions ($4f^1$ configuration). Since empty, half filled or completely filled electron shell configurations are the most stable ones, the excess $4f$ electron of Ce^{3+} is easily transferred to the $5d$ orbital. Unlike $4f$ - $4f$ transitions, $4f$ - $5d$ transitions are allowed, which results in strong and broad absorption cross-sections.

Charge-transfer state (CTS) transitions

The last possible excitation mechanism is the charge-transfer state (CTS) transition, in which $2p$ electrons from the neighbouring anions (e.g. O^{2-} in oxides) are transferred to a $4f$ orbital.³ This is typically observed in Eu^{3+} ($4f^6$) which needs one additional electron to reach the half filled configuration. These transitions are allowed and result in broad and intense absorptions.

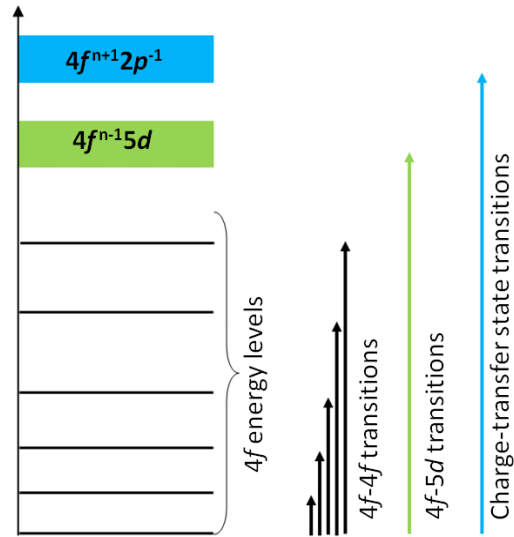


Figure 2.3: Schematic representation of the electronic absorption transitions of a lanthanide ion exhibiting 4f-4f, 4f-5d, and charge-transfer state transitions.

2.3.2. Processes involved upon lanthanide excitation

In this section, we describe the processes involved when exciting trivalent lanthanide ions with an electromagnetic radiation of frequency ν , in a simplified 2-level quantum system. Upon absorption of an incident photon, the electrons are excited from the lower state $|1\rangle$ of energy E_1 to the higher-lying excited state $|2\rangle$ of energy E_2 , where $E_2 - E_1 = h\nu$ (Figure 2.4). The time evolution of state $|2\rangle$'s population N_2 is given by:

$$\frac{dN_2}{dt} = \phi\sigma_{12}N_1(t) = -\frac{dN_1}{dt} \quad (\text{Eq. 1})$$

where ϕ is the incident pump rate and σ_{12} is the absorption cross-section per unit time between states $|1\rangle$ and $|2\rangle$.

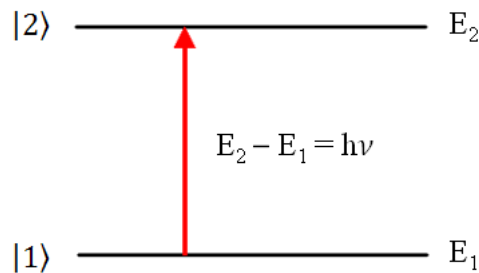


Figure 2.4: Trivalent lanthanide excitation process.

2.4. Lanthanide de-excitation processes

Upon absorption of an excitation photon, electrons are transferred from the lower-lying state $|1\rangle$ to the excited state $|2\rangle$, as mentioned in the previous section (Figure 2.4). The electrons then return to the lower state $|1\rangle$ via radiative and/or non-radiative transitions which are described in detail in this section.

2.4.1. Radiative emission transitions

In this section, we present radiative $4f-4f$ emission transitions and the selection rules associated with them. In the last part, Judd-Ofelt theory is introduced as an important tool for the prediction of lanthanide optical properties.

2.4.1.1. Radiative emission transitions in a simplified 2-level system

In the case of radiative emission transitions, the electrons are de-excited from state $|2\rangle$ to state $|1\rangle$ (Figure 2.4) by spontaneous emission of a photon of energy $h\nu = E_2 - E_1$. The time evolution of state $|2\rangle$'s population N_2 is given by:

$$\frac{dN_2}{dt} = -A_T N_2(t) = -(A_r + A_{nr})N_2(t) \quad (\text{Eq. 2})$$

where A_T is the total decay rate from state $|2\rangle$ to state $|1\rangle$, which can be decomposed into a radiative decay rate term A_r (called the Einstein coefficient of spontaneous emission) and a non-radiative decay rate term A_{nr} .

The experimental lifetime τ_{exp} associated with the light emitting state $|2\rangle$ is given by:

$$\tau_{exp} = \frac{1}{A_r + A_{nr}} \quad (\text{Eq. 3})$$

The radiative quantum efficiency η_r of the excited state $|2\rangle$ can be expressed as:

$$\eta_r = \frac{A_r}{A_T} = \frac{A_r}{A_r + A_{nr}} = \frac{\tau_{exp}}{\tau_r} \quad (\text{Eq. 4})$$

where $\tau_r = \frac{1}{A_r}$ is the radiative lifetime. As will be shown later in this chapter, A_r and τ_r can be predicted using the Judd-Ofelt theory.

2.4.1.2. Selection rules for optical transitions

The optical transition probability between two electronic states is given by the transition momentum $M = \langle \psi_i | \Gamma_D | \psi_f \rangle$, where Γ_D is the dipolar momentum operator, and ψ_i and ψ_f are the wavefunctions associated with the initial and final states. The intensity of a transition is proportional to M^2 and according to group theory, a transition is allowed if $M \neq 0$. Since light is an electromagnetic wave composed of an electric field \vec{E} and of an orthogonal magnetic field \vec{B} , electric dipolar transitions (ED) and magnetic dipolar transitions (MD) need to be considered. Magnetic dipole transitions are usually significantly weaker than electric dipole transitions (about two orders of magnitude smaller for lanthanide ions). The conditions for ED and MD transitions to be allowed are listed below.

Selection rules for Electric Dipole transitions

The electric dipole (ED) operator is odd. Therefore, ED transitions can only occur if $\langle \psi_i | \psi_f \rangle$ is odd. This means that ψ_i and ψ_f must have opposite parities. That is the so-called *parity rule* or *Laporte rule*. Electric dipole transitions are allowed if:

$$\Delta S = 0, \Delta L = \pm 1 \text{ and } \Delta J \leq \pm 6 \text{ (but } J = 0 \rightarrow J' = 0 \text{ transitions are forbidden)}$$

$$\text{If } J = 0, \Delta L = \pm 1 \text{ and } \Delta J = \pm 2, \pm 4, \pm 6$$

Selection rules for Magnetic Dipole transitions

The magnetic dipole (MD) operator, unlike the ED operator, is even. Therefore, MD transitions can only occur if ψ_i and ψ_f have same parities. Magnetic dipole transitions are allowed if:

$$\Delta S = 0, \Delta L = 0 \text{ and } \Delta J = 0, \pm 1 \text{ (but } J = 0 \rightarrow J' = 0 \text{ transitions are forbidden)}$$

$$\text{If } J = 0, \Delta L = 0 \text{ and } \Delta J = \pm 1$$

Forced Electric Dipole transitions

As mentioned earlier, $4f-4f$ electric dipole transitions between the $4f$ states of an isolated trivalent lanthanide ion are parity forbidden. However, when the lanthanides are introduced

into a crystal, the parity selection rule is usually relaxed due to the mixing of the $4f$ wavefunctions with a small amount of opposite-parity wavefunctions (e.g. $5d$ states, charge-transfer states, etc).⁷ In that case, *forced* electric dipole transitions are observed. These emissions are usually weak and very narrow.

2.4.1.3. Judd-Ofelt theory

In 1962, Judd⁸ and Ofelt,⁹ two independent researchers, published their work on the theory of $4f$ - $4f$ transition line intensities for trivalent lanthanide ions in crystals. It is a powerful tool to predict the optical properties of lanthanide ions in a crystal environment (e.g. spontaneous radiative emission rates, branching ratios, radiative lifetimes, etc). According to the Judd-Ofelt theory,^{8,9} the oscillator strength f for the absorption band corresponding to the electronic transition from an initial state $^{2S+1}L_J$ to a final state $^{2S'+1}L'_{J'}$ can be estimated as:¹⁰

$$f = f_{ED} + f_{MD} = \frac{8\pi^2 m c \nu}{3 h e^2 n^2 (2J+1)} (\chi_{ED} S_{ED} + \chi_{MD} S_{MD}) \quad (\text{Eq. 5})$$

where m is the mass of the electron, c the speed of light in vacuum, ν the wavenumber (cm^{-1}) associated with the transition, h the Planck constant, e the electronic charge, n the refractive index of the host lattice, χ the local field correction for the effective field induced by the host lattice, and S the line strength of the electronic transition involved.

Only the magnetic dipole transitions with selection rules $\Delta S = \Delta L = 0$ and $\Delta J = 0, \pm 1$ can contribute efficiently to the oscillator strength of lanthanide ions.

For electric dipole (ED) transitions,

$$\chi_{ED} = n \left(\frac{n^2 + 2}{3} \right)^2 \quad (\text{Eq. 6})$$

$$S_{ED} = e^2 \sum_{t=2,4,6} \Omega_t |\langle (S, L) J \| U^{(t)} \| (S', L') J' \rangle|^2 \quad (\text{Eq. 7})$$

For magnetic dipole (MD) transitions,

$$\chi_{MD} = n^3 \quad (\text{Eq. 8})$$

$$S_{MD} = \mu_B^2 |\langle (S, L) J \| L + 2S \| (S', L') J' \rangle|^2 \quad (\text{Eq. 9})$$

Where μ_B is the Bohr magneton.

In the expressions of S_{ED} and S_{MD} , Ω_2 , Ω_4 and Ω_6 are the Judd-Ofelt intensity parameters. Their values are largely independent of the crystal field, and only depend on the specific trivalent lanthanide ion. The values of $|\langle(S, L)J||U^{(t)}||S', L'J'\rangle|$, the reduced matrix elements of the irreducible tensor operator of rank t , are host-independent and have been reported by Carnall¹¹ and Kaminskii¹² for various lanthanide ions.

The spontaneous radiative decay rate A_r can be calculated using:¹⁰

$$A_r = A_{ED} + A_{MD} = \frac{64\pi^4\nu^3}{3h(2J+1)}(\chi_{ED}S_{ED} + \chi_{MD}S_{MD}) \quad (\text{Eq. 10})$$

The spontaneous radiative decay rate A_r is strongly related to the energy separation (or energy gap) between the 2 states of interest ($^{2S+1}L_J$ and $^{2S'+1}L'_{J'}$). In particular, there is a cubic dependence between the radiative rate A_r and the energy gap given by $h\nu$. The larger the energy gap, the larger the radiative emission rate.

The radiative lifetime τ_r of an emitting state $^{2S'+1}L'_{J'}$ is related to the spontaneous emission probabilities for all transitions from this state to the lower-lying $^{2S+1}L_J$ states:

$$\tau_r = \frac{1}{\sum_J A_r(J' \rightarrow J)} \quad (\text{Eq. 11})$$

2.4.2. Non-radiative emission transitions

Upon absorption of an excitation photon, electrons are transferred from a state $|1\rangle$ to a higher-lying excited state $|2\rangle$, as mentioned earlier (Figure 2.4). The electrons from state $|2\rangle$ can then relax to state $|1\rangle$ without photon emission. The emission transition is *non-radiative*. Some of the most relevant non-radiative transfer processes are listed in this section.

2.4.2.1. Multiphonon relaxation

In multiphonon relaxation, an ion in the excited state transfers, upon de-excitation, its energy to the lattice without photon emission. The energy dissipation occurs via the emission of phonons of energy $h\nu$.

Multiphonon relaxation rates A_{mp} increase exponentially with a decrease of the energy gap between the two states involved, and are temperature dependent:

$$A_{mp}(T) = A_{mp}(0)(n + 1)^p \quad (\text{Eq. 12})$$

where $p = \frac{\Delta E}{h\nu}$ is the number of phonons of energy $h\nu$ required to bridge the energy gap ΔE between the 2 states involved. $A_{mp}(0)$ is the multiphonon rate at $T = 0$ K, which follows a semi-empirical law: $A_{mp}(0) = Ce^{-\alpha\Delta E}$ where C and α are host-dependent positive constants. In (Eq. 12), $n = (e^{h\nu/kT} - 1)^{-1}$ is the Bose-Einstein occupation number. The so-called *energy gap law* is often used to estimate multiphonon relaxation rates:¹³

$$A_{mp}(T) = A_{mp}(0)e^{-\alpha\Delta E} \quad (\text{Eq. 13})$$

The phonons that participate mostly in multiphonon relaxation processes are those with the highest energies and the largest densities of states. There is a rule of thumb that states that the radiative emission from a $4f^n$ level can compete with multiphonon relaxation only if the energy gap to be bridged is larger than 5 times the maximum phonon energy of the host lattice. In order to minimise multiphonon relaxation rates (and therefore maximise radiative emission efficiencies), hosts with low maximum phonon energies are often chosen. The typical maximum phonon energies associated with a few inorganic host lattices are listed in Table 2.2. Halides are seen to exhibit lower maximum phonon energies than oxides.

Host	$h\nu_{max}$ (cm ⁻¹)
LaCl ₃	250 ¹⁴
LaF ₃	350 ¹⁵
NaYF ₄	370 ¹⁶
YAlO ₃	550 ¹⁷
Y ₂ O ₃	600 ¹⁸
YVO ₄	890 ¹⁹
Y ₂ BaZnO ₅	966 ²⁰

Table 2.2: Maximum phonon energies in different inorganic hosts.

2.4.2.2. Concentration quenching

Concentration quenching is observed in systems where dopant concentrations are high (i.e. the average distance between dopants is small, assuming their statistical distribution in the host lattice). High dopant concentrations favour high energy transfer rates between dopants. Cross-relaxation is a particular type of energy transfer where a fraction of the excitation energy absorbed by one luminescent ion is transferred to another identical ion. In some cases, the excitation energy can relocate far away from the dopant which had initially absorbed the incident photon, and eventually get trapped by a non-luminescent defect or impurity. In this case, the excitation energy is lost non-radiatively. This process leads to a reduction of luminescence efficiency. The mechanisms behind energy transfer processes will be described in detail in the next section.

2.5. Energy transfers

2.5.1. Introduction

In this section, we describe energy transfer processes between a donor and an acceptor. Studies of the transfer of electronic excitation between dopants in solids have been extensively carried out over the past 65 years. The theory behind non-radiative donor to acceptor energy transfers was developed by Förster²¹ and subsequently extended by Dexter²² and Inokuti.²³ In 1952, Botden²⁴ introduced the notion of relaxation by migration to account for luminescence concentration quenching. His theory was further developed by Dexter and Schulman.²⁵ The combined effects of donor-donor and donor-acceptor transfers have been studied extensively in a variety of systems including $\text{Eu}(\text{PO}_3)_3$: Cr^{3+} ,²⁶ YF_3 : Yb^{3+} , Ho^{3+} ,²⁷ LaCl_3 : Pr^{3+} , Nd^{3+} ,²⁸ and YVO_4 : Nd^{3+} .²⁹

2.5.2. Radiative and non-radiative energy transfers

In the case of a radiative energy transfer, a real photon is emitted by the sensitiser and then reabsorbed by the activator. The latter must be located within a photon travel distance. This is called the *emission-reabsorption* mechanism. In the case of a non-radiative energy transfer,

however, the excitation is transferred from the excited sensitiser to an activator without any photon emission.

In the next section, we will focus primarily on non-radiative energy transfers as the energy transfers involved in the upconversion mechanisms presented in chapters 5, 6, 7 and 8 are of that type.

2.5.3. Energy transfer probability

2.5.3.1. Non-radiative energy transfer

In this section, we consider the case of a non-radiative energy transfer between a donor (e.g. a sensitiser S) and an acceptor (e.g. an activator A). In the materials that will be presented in chapters 5, 6, 7 and 8, the sensitiser S is a trivalent ytterbium ion (Yb^{3+}), and the activator A is a trivalent erbium (Er^{3+}), holmium (Ho^{3+}) or thulium (Tm^{3+}) ion. Upon excitation with an electromagnetic radiation, the sensitiser S absorbs an incoming photon and is raised to an excited state S^* . It then returns to the ground state by transferring its energy to the activator A (without photon emission), which is then excited to its excited state A^* (the energy transfer can be denoted: $S^* + A \rightarrow S + A^*$, where the asterisk indicates an excited state). Note that before the energy transfer occurs, the activator can be in its ground state or in an excited state. According to Fermi's golden rule, the probability P_{SA} of energy transfer between an excited sensitiser S^* and a relaxed activator A is given by:

$$P_{SA} = \frac{2\pi}{\hbar} |\langle S^*, A | H_{SA} | S, A^* \rangle|^2 \int g_S(\nu) g_A(\nu) d\nu \quad (\text{Eq. 14})$$

where \hbar is the reduced Planck constant, H_{SA} the interaction Hamiltonian between sensitiser and activator, and $\int g_S(\nu) g_A(\nu) d\nu$ the spectral overlap between the emission spectrum of the sensitiser $g_S(\nu)$ and the absorption spectrum of the activator $g_A(\nu)$.

The energy transfer can be governed by electrostatic multipolar interactions or by exchange interactions. In the case of an energy transfer by electrostatic interaction, there is no physical contact between the interacting sensitiser S^* and activator A , and no electron is exchanged between them. It is sufficient that S^* induces a dipole oscillation on A . This type of interaction occurs when the interacting sensitiser and activator are far from each other (e.g. 20 Å). However, in the case where the energy transfer is governed by exchange interactions,

there is an exchange of electrons between the interacting sensitiser and activator; an excited electron of S^* travels to A whereas an electron of A goes to S^* . This requires an overlap of the sensitiser and activator electronic charge distributions. S and A must be very close to each other (maximum distance around 6 Å).

Energy transfer governed by electrostatic interactions

In the case where the energy transfer is governed by electrostatic interactions, the energy transfer probability P_{SA} is given by:

$$P_{SA} = \frac{2\pi}{\hbar} |\langle S^*, A | H_{SA}^{el} | S, A^* \rangle|^2 \int g_S(\nu) g_A(\nu) d\nu \quad (\text{Eq. 15})$$

where H_{SA}^{el} is the electrostatic interaction Hamiltonian. Assuming that the interaction mainly occurs by dipole-dipole interactions, P_{SA} is given by:²¹

$$P_{SA} = \left(\frac{1}{4\pi\epsilon_0} \right)^2 \frac{3\pi\hbar e^4}{n^4 m^2 \nu^2 R^6} f_S f_A \int g_S(\nu) g_A(\nu) d\nu \quad (\text{Eq. 16})$$

where ϵ_0 is the vacuum permittivity, e the electronic charge, n the refractive index, m the mass of the electron, ν the wavenumber associated with the transition, R the sensitiser to activator distance, f_S the oscillator strength associated with the sensitiser's emission and f_A the oscillator strength associated with the activator's absorption. As shown by Förster, the energy transfer probability can be expressed as:²¹

$$P_{SA}(R) = \frac{1}{\tau_S} \left(\frac{R_0}{R} \right)^6 \quad (\text{Eq. 17})$$

where τ_S is the sensitiser's excited state lifetime and R_0 is the Förster radius corresponding to the characteristic distance at which 50% of the sensitiser's energy is transferred to the activator. The non-radiative energy transfer probability in the case of a dipole-dipole interaction varies as $1/R^6$. As shown by Dexter, the energy transfer probability can be generalised to:²²

$$P_{SA}(R) = \frac{1}{\tau_S} \left(\frac{R_0}{R} \right)^a \quad (\text{Eq. 18})$$

where a is a positive integer taking the values $a = 6$ for dipole-dipole interactions, $a = 8$ for dipole-quadrupole interactions and $a = 10$ for quadrupole-quadrupole interactions.

Energy transfer governed by exchange interactions

If the sensitiser and the activator are located very close to each other so that the electronic orbitals overlap ($R \leq 6 \text{ \AA}$), a non-radiative energy transfer by exchange interaction can occur. This is called a Dexter transfer. The Dexter energy transfer probability by exchange interaction is given by:²²

$$P_{SA} = \frac{2\pi}{\hbar} |\langle S, A^* | H_{SA}^{exc} | S^*, A \rangle|^2 \int g_S(\nu) g_A(\nu) d\nu \quad (\text{Eq. 19})$$

where H_{SA}^{exc} is the exchange Hamiltonian. As shown by Hadah:³⁰

$$P_{SA} \propto e^{-\frac{2R}{a_0}} \int g_S(\nu) g_A(\nu) d\nu \quad (\text{Eq. 20})$$

where a_0 is the Bohr effective radius (around 0.3 \AA for lanthanides). The Dexter energy transfer probability decreases exponentially when the sensitiser to activator distance R increases. It is therefore a very short-range interaction. This type of interaction is only observed in materials with high dopant concentrations (i.e. very short distances between dopants).

2.5.3.2. Radiative energy transfer

In the case of a radiative energy transfer, the excited sensitiser S^* returns to the ground state by emission of a photon, that is then reabsorbed by the acceptor A (photon emission-reabsorption mechanism). In the case of a radiative energy transfer by dipole-dipole interaction, P_{SA} varies as $1/R^2$.³¹ Radiative energy transfers permit long-range energy diffusion (compared to non-radiative energy transfers by dipole-dipole interaction for which P_{SA} varies as $1/R^6$).

2.5.3.3. How to distinguish between radiative and non-radiative energy transfers

There are three main criteria to distinguish between radiative and non-radiative resonant energy transfers (besides the different power dependences of P_{SA} with R).³² When the energy transfer is radiative, real photons are emitted by the sensitiser and then absorbed by an activator located within a photon travel distance. As a result, radiative transfer rates depend on the shape and on the size of the sample. Moreover, for a radiative energy transfer, the sensitiser's emission spectrum changes with the activator's concentration, but its excited level

lifetime is independent on the activator's concentration and on the sensitiser to activator distance R .

In the upconverting materials that will be presented in chapters 5, 6, 7 and 8, the sensitiser's (Yb^{3+}) excited state lifetime is strongly dependent on the activator's (Er^{3+} , Ho^{3+} or Tm^{3+}) concentration, indicating the non-radiative character of the energy transfer. Given the low dopant concentrations in the materials, transfers by exchange interaction can be excluded. Energy transfers between sensitiser and activator occur therefore by non-radiative electrostatic interactions.

2.6. Summary

The spectroscopic properties of trivalent lanthanide elements were presented in this chapter. Various processes involved in trivalent lanthanide excitation and de-excitation were discussed. These same processes are involved in the upconversion mechanisms described in chapters 3, 5, 6, 7 and 8. The Judd-Ofelt theory and the energy-gap law were introduced as important tools to calculate radiative and non-radiative emission rates, respectively. The last section was devoted to the presentation of energy transfers between lanthanide ions.

References

- ¹ F. Szabadvary, in *Handbook on the Physics and Chemistry of Rare Earths*, ed. K. Gschneidner and L. Eyring, Elsevier, Amsterdam, 1988, vol. 11, ch. 73, pp. 33-80.
- ² T. Haley, in *Handbook on the Physics and Chemistry of Rare Earth*, ed. K. Gschneidner and L. Eyring, North Holland, Amsterdam, 1979, vol. 4, ch. 40, pp. 553-586.
- ³ G. I. Hatakoshi, in *Phosphor Handbook*, ed. W. M. Yen, S. Shionoya and H. Yamamoto, CRC Press, New York, 2nd edn., 2007, ch. 3, pp. 191-214.
- ⁴ G. H. Dieke, in *Spectra and Energy Levels of Rare Earth Ions in Crystals*, ed. H. M. Crosswhite and H. Crosswhite, Wiley Interscience, New York, 1968.
- ⁵ G. H. Dieke and H. M. Crosswhite, *Appl. Opt.*, 1963, **2**, 675.
- ⁶ K. Ogasawara, S. Watanabe, Y. Sakai, H. Toyoshima, T. Ishii, M. G. Brik and I. Tanaka, *Jpn. J. Appl. Phys.*, 2004, **43**, L611.
- ⁷ J. H. Van Vleck, *J. Phys. Chem.*, 1937, **41**, 67.
- ⁸ B. R. Judd, *Phys. Rev.*, 1962, **127**, 750.
- ⁹ G. S. Ofelt, *J. Chem. Phys.*, 1962, **37**, 511.
- ¹⁰ J. García Solé, L. E. Bausa and D. Jaque, in *An Introduction to the Optical Spectroscopy of Inorganic Solids*, John Wiley and Sons Ltd., England, 2005, ch. 7, pp. 224-233.
- ¹¹ W. T. Carnall, P. R. Fields and K. Rajnak, *J. Chem. Phys.*, 1968, **49**, 4412.
- ¹² A. A. Kaminskii, in *Laser Crystals, their Physics and Properties*, Springer-Verlag, New-York, Berlin, Heidelberg, 2nd edn., 1990.
- ¹³ J. M. F. Van Dijk and M. F. H. Schuurmans, *J. Chem. Phys.*, 1983, **78**, 5317.
- ¹⁴ I. Richman, R. A. Satten and E. Y. Wong, *J. Chem. Phys.*, 1963, **39**, 1833.
- ¹⁵ M. J. Weber, *Phys. Rev.*, 1967, **157**, 262.
- ¹⁶ J. F. Suyver, J. Grimm, M. K. van Veen, D. Biner, K. W. Krämer and H. U. Güdel, *J. Lumin.*, 2006, **117**, 1.
- ¹⁷ A. A. Kaminskii, in *Cristalline Lasers: Physical Processes and Operating Schemes*, CRC Press, New-York, Boca Raton, 1991.
- ¹⁸ H. Guo, W. Zhang, L. Lou, A. Brioude and J. Mugnier, *Thin Solid Films*, 2004, **458**, 274.
- ¹⁹ J. A. Capobianco, P. Kapro, F. S. Ermeneux, R. Moncorgé, M. Bettinelli and E. Cavalli, *Chem. Phys.*, 1997, **214**, 329.

- ²⁰ Maximum phonon energy as measured in our Y₂BaZnO₅ samples.
- ²¹ T. Förster, *Ann. Phys.*, 1948, **2**, 55.
- ²² D. L. Dexter, *J. Chem. Phys.*, 1953, **21**, 836.
- ²³ M. Inokuti and F. Hirayama, *J. Chem. Phys.*, 1965, **43**, 1978.
- ²⁴ T. P. J. Botden, *Philips Res. Rep.*, 1952, **7**, 197.
- ²⁵ D. L. Dexter and J. H. Schulman, *J. Chem. Phys.*, 1954, **22**, 1063.
- ²⁶ M. J. Weber, *Phys. Rev. B*, 1971, **4**, 2932.
- ²⁷ R. K. Watts and H. J. Richter, *Phys. Rev. B*, 1972, **6**, 1584.
- ²⁸ N. Krasutsky and H. W. Moos, *Phys. Rev. B*, 1973, **8**, 1010.
- ²⁹ D. Sardar and R. C. Powell, *J. Appl. Phys.*, 1980, **51**, 2829.
- ³⁰ C. Z. Hadad and S. O. Vasquez, *Phys. Rev. B*, 1999, **60**, 8586.
- ³¹ F. Auzel, in *Radiationless Processes*, ed. B. DiBartolo and V. Goldberg, Plenum Publishing Co., New York, 1980, p 213.
- ³² F. Auzel, *Chem. Rev.*, 2004, **104**, 139.

CHAPTER 3: Upconversion

3.1. Introduction

Since its discovery by Auzel^{1,2}, Ovsyankin³ and Feofilov³ in the 1960's, upconversion (UC) has been the focus of much research, especially for infrared to visible light conversion, taking advantage of the development, in the nineteen eighties, of cheap laser diodes emitting around 980 nm. In the past five years, the number of publications in the field has increased significantly. The recent research is oriented towards the assessment of the potential of upconverting materials for photovoltaic or bio-imaging applications. As mentioned in chapter 1, most of the upconversion work is focused on the investigation of lanthanide-doped halide⁴⁻⁹ and oxide¹⁰⁻¹³ host materials (sometimes in the form of glass¹⁴⁻¹⁷). Some limited literature can also be found on the upconversion properties of transition-metal doped systems.¹⁸⁻²⁰

In this chapter, we present a literature review of lanthanide-based upconversion. First of all, the various processes known to convert low energy incident radiation into higher energy emitted radiation are presented in section 3.2. Among them, upconversion, the main topic of this work, is the most efficient process for such energy conversion, hence its relevance for potential applications. In section 3.3, we present the dominant upconversion mechanisms and show that they can be described by simplified rate equations (section 3.4). By solving these rate equations in the steady-state regime, one can predict the variations of upconversion emission powers with the excitation power. In section 3.5, we present possible time-resolved luminescence dynamics. As will be shown in chapters 5, 6, 7 and 8, time-resolved spectroscopy is an important tool that can be used to understand what the dominant upconversion mechanisms in a specific material are. Finally, we describe the materials and applications that have been the focus of recent upconversion research (section 3.6).

3.2. Conversion of low-energy incident radiation into higher-energy emitted radiation

There are several processes that are well known to convert low-energy incident radiation into higher-energy emitted light. The most relevant processes for such light conversion are summarised in Figure 3.1.^{21,23} All the processes presented in Figure 3.1 are non-linear 2-photon optical processes, where two incident photons are converted into one emitted photon of significantly higher energy. The typical emitted power densities P_{em} vary quadratically with the incident power density P_{inc} with a proportionality coefficient μ such as $P_{em} = \mu P_{inc}^2$. There are several ways of defining an energy conversion efficiency, as will be seen in chapter 4. In order to compare the energy conversion efficiencies of the different processes presented in Figure 3.1, one can for example compare the typical values of μ associated with these processes.

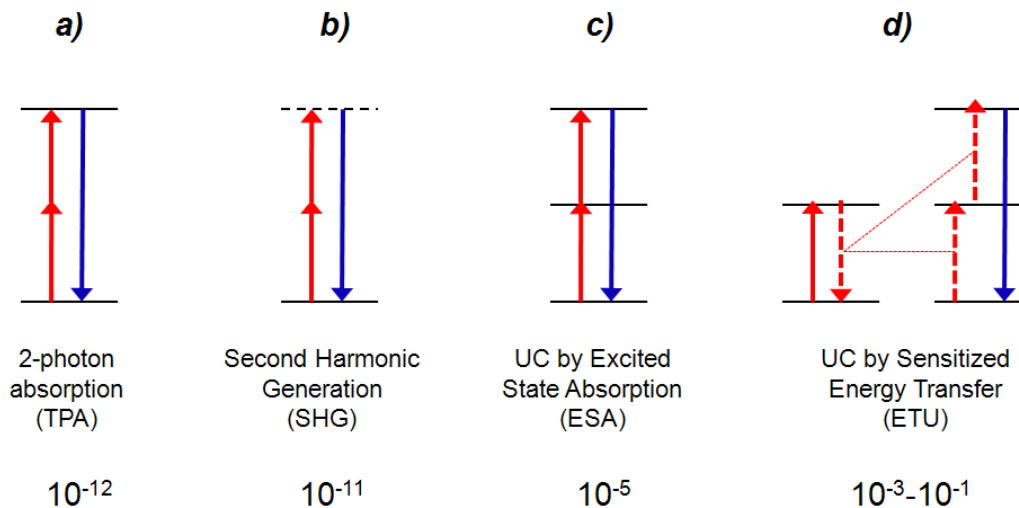


Figure 3.1: Most relevant processes to convert low-energy incident radiation into higher-energy emitted radiation, and the typical values of μ (in cm^2/W) associated with them.^{21,23}

These processes include, in order of increasing efficiency, two-photon absorption (TPA) (Figure 3.1a), second harmonic generation (SHG) (Figure 3.1b) and upconversion (UC) (Figure 3.1c and Figure 3.1d). In TPA and SHG, virtual intermediate levels are involved. This implies that the two excitation photons must coincide (and also be coherent for SHG, since the emitting level is also virtual), which makes these processes very unlikely and therefore very inefficient. As a result, very high excitation powers are usually required. The

most important difference between upconversion and the other processes shown in Figure 3.1 is that upconversion depends on a real intermediate state. This state must have a finite lifetime that is long enough for an excitation to be stored there, for such a time as to allow a second photon to further excite the phosphor into a higher-lying excited state. Since upconversion only involves real energy levels, very high excitation powers are no longer necessary. The excitation power thresholds for upconversion are typically about 6 to 11 orders of magnitude lower than those required for SHG or TPA. It is also worth mentioning that no coherent excitation source is required for upconversion. Given its high energy conversion efficiencies and low excitation power thresholds, upconversion is particularly relevant for (future) applications. In the next section, we focus on upconversion. The main upconversion mechanisms are presented, together with their typical energy conversion efficiencies.

3.3. Main upconversion mechanisms

The most relevant upconversion processes are described in this section.²¹ Very good reviews can be found in the literature.²²⁻²⁵ In some materials, several of the upconversion processes listed in this section contribute to the upconversion luminescence emission (see chapter 5, section 5.2.8).

3.3.1. Upconversion by excited state absorption (ESA)

Upconversion by ground state absorption/excited state absorption (GSA/ESA) (Figure 3.2) is the simplest upconversion mechanism. It only involves one dopant, typically a trivalent lanthanide ion such as erbium Er^{3+} . In GSA/ESA, the sequential absorption of two (or more) excitation photons by the dopant leads to the population of the excited level $|2\rangle$ from which the upconversion emission arises (Figure 3.2). The first excitation photon is absorbed by the ground state $|0\rangle$ and populates the intermediate state $|1\rangle$. Provided the lifetime of $|1\rangle$ is long enough, a second incident photon can be absorbed, exciting further the ion from its intermediate state $|1\rangle$ to a higher-lying excited state $|2\rangle$, from which upconversion luminescence originates.

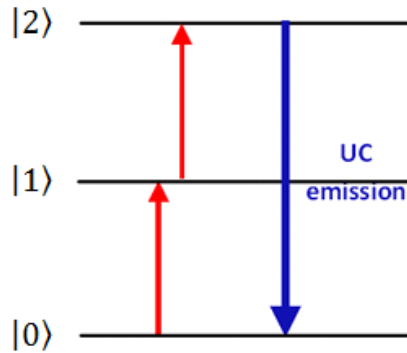


Figure 3.2: Schematic representation of the upconversion mechanism by ground state absorption/excited state absorption (GSA/ESA).

As mentioned in section 3.2, for a 2-photon upconversion process, the typical emission power density P_{em} varies quadratically with the incident power density P_{inc} with a proportionality coefficient μ (i.e. $P_{em} = \mu P_{inc}^2$). The typical value of μ for upconversion by GSA/ESA is on the order of $10^{-5} \text{ cm}^2/\text{W}$.²³ Upconversion by excited state absorption has been observed in a variety of systems including $\text{Y}_3\text{Al}_5\text{O}_{12}$,²⁶ BaTiO_3 ,²⁷ ZrO_2 ,²⁸ Y_2O_3 ,²⁹ and ZBLAN ³⁰ doped with Ln^{3+} (where $\text{Ln}^{3+} = \text{Er}^{3+}$, Tm^{3+} or Ho^{3+}).

3.3.2. Upconversion by sensitised energy transfer upconversion (ETU)

Upconversion by sensitised energy transfer upconversion (ETU) (Figure 3.3) is the most efficient upconversion mechanism. It is the focus of this PhD work. GSA/ETU was first introduced by Auzel who called it APTE (from the French ‘Addition de Photons par Transferts d’Energie’). It involves non-radiative energy transfers between two dopants; a sensitizer (e.g. Yb^{3+}) and an activator (e.g. Er^{3+} , Ho^{3+} , Tm^{3+}). The sensitizer usually has a strong absorption cross-section at the excitation wavelength. Once the sensitizer is excited (after absorption of an incident photon), it relaxes to a lower-energy state (the ground state in the case of Yb^{3+}) by transferring its energy to a neighbouring activator, raising the latter to a higher-energy state.

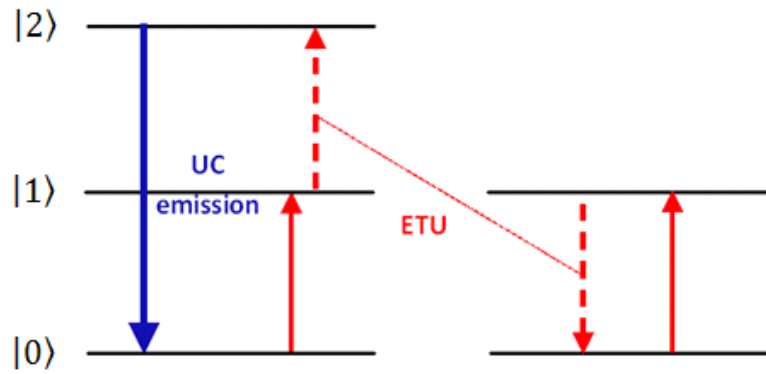


Figure 3.3: Schematic representation of the upconversion mechanism by sensitised energy transfer upconversion (ETU).

These energy transfer processes are generally based on electric dipole-dipole interactions. The typical value of μ for upconversion by sensitised ETU is generally on the order of 10^{-3} cm^2/W (two orders of magnitude higher than the value associated with GSA/ESA).²³ This type of upconversion has been reported in a variety of systems including NaYF_4 ,³¹⁻³⁴ BaY_2F_8 ,³⁵ Y_2O_3 ,^{13,37,38} $\text{Gd}_2\text{BaZnO}_5$,³⁹ $\text{La}_2\text{BaZnO}_5$,³⁹ glasses^{16,17,40,41} and vitroceraamics^{14,42} co-doped with Yb^{3+} and Ln^{3+} (where $\text{Ln}^{3+} = \text{Er}^{3+}, \text{Tm}^{3+}, \text{Ho}^{3+}, \text{Pr}^{3+}$). The infrared to visible upconversion properties (by sensitised ETU) of $\text{RE}_2\text{BaZnO}_5$ ($\text{RE} = \text{Y}, \text{Gd}$) oxides co-doped with $\text{Yb}^{3+}, \text{Ln}^{3+}$ ($\text{Ln}^{3+} = \text{Er}^{3+}, \text{Ho}^{3+}$ or Tm^{3+}) will be presented in chapters 5, 6, 7 and 8.

3.3.3. Upconversion by cooperative luminescence

In upconversion by cooperative luminescence (Figure 3.4), two excitation photons are sequentially absorbed by two different ions (e.g. two Yb^{3+} ions, but the two ions do not need to be the same species), bringing both of them into their excited state. Then, both ions decay simultaneously to their ground state, with the emission of one single photon that contains the combined energies of both ions. The cooperative emission occurs from a virtual level, which explains why the emission probability is rather low. The typical value of μ for upconversion by cooperative luminescence is on the order of 10^{-8} cm^2/W (to be compared with $\mu = 10^{-3}$ cm^2/W for upconversion by sensitised ETU).² Upconversion by cooperative luminescence has been reported in a variety of systems, including $\text{Y}_3\text{Al}_5\text{O}_{12}:\text{Yb}^{3+}$,⁴³ $\text{LaF}_3:\text{Pr}^{3+}$,⁴⁴ and in glasses doped with Yb^{3+} .⁴⁵

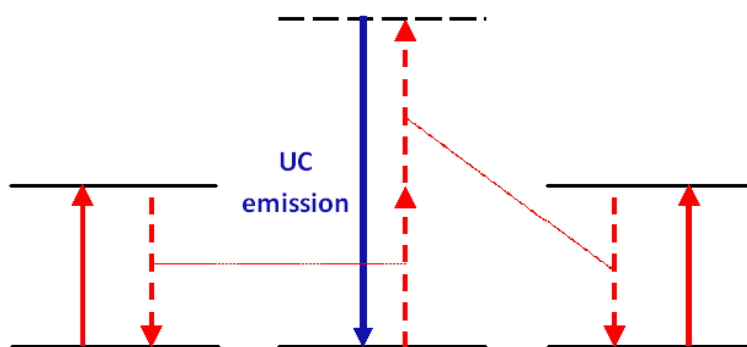


Figure 3.4: Schematic representation of the upconversion mechanism by cooperative luminescence.

3.3.4. Upconversion by cooperative sensitisation

The process involved in cooperative sensitisation⁴⁶ (Figure 3.5) is very similar to that of cooperative luminescence. Two excitation photons are sequentially absorbed by two different ions (e.g. two Yb^{3+} ions, but the two ions do not need to be the same species) bringing both of them into their excited state. However, unlike in cooperative luminescence, the energies of these two ions are now transferred to a third ion (e.g. Tb^{3+}) bringing the latter from its ground state to an excited state (of energy resonant with the sum of the individual energies of the two first ions).

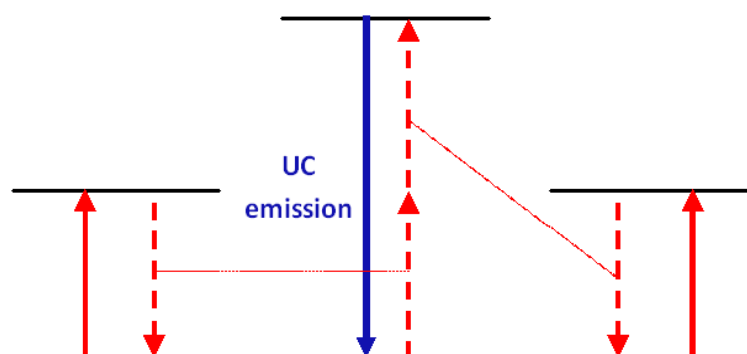


Figure 3.5: Schematic representation of the upconversion mechanism by cooperative sensitisation.

Because the upconversion emitting state is now real, upconversion by cooperative sensitisation is much more effective than upconversion by cooperative luminescence. The typical value of μ for cooperative sensitisation is on the order of $10^{-6} \text{ cm}^2/\text{W}$ (two orders of magnitude higher than the value of μ for cooperative luminescence and three orders of magnitude smaller than that for sensitised ETU).²³ Upconversion by cooperative sensitisation has been reported in a variety of $\text{Yb}^{3+}, \text{Tb}^{3+}$ co-doped systems, including SrCl_2 ,⁴⁷ $\text{Cs}_3\text{Tb}_2\text{Br}_9$,⁴⁸ and glasses.^{49,50}

3.3.5. Upconversion by photon avalanche

Upconversion by photon avalanche⁵¹ occurs through an interesting interplay between several competing absorption and energy transfer processes.⁵² Figure 3.6 shows a schematic of the photon avalanche mechanism in a three-level system:

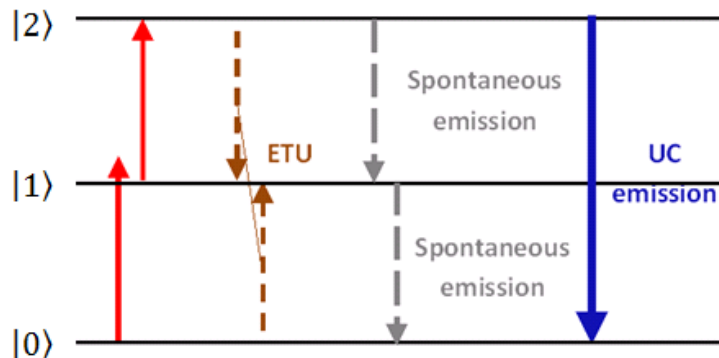


Figure 3.6: Schematic representation of the upconversion mechanism by photon avalanche.

Three conditions must be satisfied for photon avalanche to occur:

- The excitation photon energy must be non-resonant with the absorption transition from $|0\rangle$ to $|1\rangle$
- The excitation photon energy must be resonant with the absorption transition from $|1\rangle$ to $|2\rangle$
- There must be a strong $|0,2\rangle \rightarrow |1,1\rangle$ cross-relaxation process

Photon avalanche processes usually have very high incident power thresholds, making them impractical for most applications. Photon avalanche has been observed in a variety of systems including $\text{LaCl}_3: \text{Pr}^{3+}$,^{53,54} $\text{LiYF}_4: \text{Nd}^{3+}$,⁵⁵ $\text{YAlO}_3: \text{Tm}^{3+}$,⁵⁶ $\text{LiYF}_4: \text{Er}^{3+}$,⁵⁷ and $\text{Y}_3\text{Al}_5\text{O}_{12}: \text{Tm}^{3+}$.⁵⁸

Among the upconversion mechanisms presented in this section, sensitised energy transfer upconversion is by far the most efficient process for infrared to visible energy upconversion, hence its relevance for many applications. It is the focus of our PhD work (see results presented in chapters 5, 6, 7 and 8). In the next section, we introduce rate equations as an important tool to describe upconversion mechanisms and predict the dependence of upconversion emission powers on the incident power.

3.4. Rate equations relevant to upconversion processes

3.4.1. Rate equations in a simplified 3-level system

The rate equations for upconversion processes are usually non-trivial because they involve many different energy states associated with the dopants incorporated in the host lattice. These dopants can be different species, in which case they have different energy levels. When writing the rate equations governing upconversion, various processes need to be taken into account, including pump-induced transitions, radiative and non-radiation decays, energy transfers and cross-relaxations between dopants. However, simplifications can usually be made. For instance, when it comes to modelling near-infrared (980 nm excitation) to green upconversion processes in Er^{3+} singly-doped materials, a simplified 3-level system is assumed. The 3 levels considered are $\text{Er}^{3+} {}^4\text{I}_{15/2}$ (ground state), ${}^4\text{I}_{11/2}$ (intermediate state) and ${}^4\text{S}_{3/2}$ (green upconversion emitting state).⁵⁹ It is assumed that all the Er^{3+} excited states⁵⁹ located between $\text{Er}^{3+} {}^4\text{I}_{11/2}$ and $\text{Er}^{3+} {}^4\text{S}_{3/2}$ have very short lifetimes, implying that the electrons in these states decay quickly and non-radiatively to $\text{Er}^{3+} {}^4\text{I}_{11/2}$.

In this section, we present the equations governing upconversion in the case of a simplified 3 energy level system (Figure 3.7) where ground state absorption/excited state absorption (GSA/ESA) and ground state absorption/energy transfer upconversion (GSA/ETU) processes

are involved. N_0 , N_1 and N_2 are the population densities of the ground state $|0\rangle$, intermediate state $|1\rangle$ and upconversion emitting state $|2\rangle$, respectively. The following assumptions are made:⁶

- there is no pump depletion
- the ground state population density N_0 is constant
- the system is continuously pumped into the intermediate state $|1\rangle$ by GSA

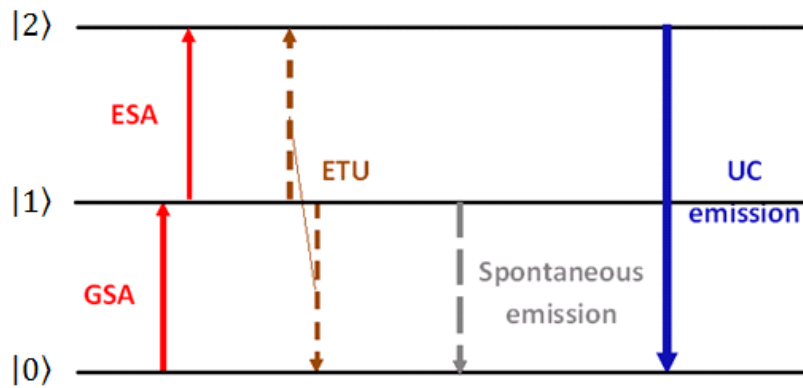


Figure 3.7: Schematic representation of the dominant upconversion processes in a 3 energy level system. The upconversion (UC) mechanism involves ground state absorption (GSA), excited state absorption (ESA) and energy transfer upconversion (ETU) steps.

In the equations presented below, σ_i is the absorption cross-section from state $|i\rangle$ (at the excitation wavelength), W_i the relaxation rate governing the energy transfer upconversion (ETU) from state $|i\rangle$, A_i the spontaneous emission rate from state $|i\rangle$ and ϕ the pump rate.

In view of Figure 3.7, the two equations governing upconversion in this 3-level system are:

$$\frac{dN_1}{dt} = \phi\sigma_0N_0 - \phi\sigma_1N_1 - 2W_1N_1^2 - A_1N_1 \quad (\text{Eq. 1})$$

$$\frac{dN_2}{dt} = \phi\sigma_1N_1 + W_1N_1^2 - A_2N_2 \quad (\text{Eq. 2})$$

In (Eq. 1), $\phi\sigma_0N_0$ is the increase of state |1>'s population by ground state absorption (GSA), and $-\phi\sigma_1N_1$, $-2W_1N_1^2$ and $-A_1N_1$ are the decrease of state |1>'s population by excited state absorption (ESA), energy transfer upconversion (ETU) and spontaneous emission, respectively. In (Eq. 2), $\phi\sigma_1N_1$ and $W_1N_1^2$ are the increase of state |2>'s population by excited state absorption (ESA) and energy transfer upconversion (ETU), respectively, while $-A_2N_2$ is the decrease of state |2>'s population by spontaneous emission.

The pump rate ϕ is proportional to the incident pump power P and is defined as:

$$\phi = \frac{\lambda P}{hc\pi w_p^2} \quad (\text{Eq. 3})$$

where λ is the pump wavelength, c the speed of light in vacuum and w_p the pump beam waist.

By solving (Eq. 1) and (Eq. 2), one can easily determine the dependence of the power emitted by upconversion on the excitation pump power P , in extreme cases such as those described below.

3.4.2. Pump power dependence of upconversion in the case where ETU is dominant over ESA

In the particular case where ETU is dominant over ESA, $\phi\sigma_1N_1$ can be neglected. The rate equations can therefore be simplified as follows:

$$\frac{dN_1}{dt} = \phi\sigma_0N_0 - 2W_1N_1^2 - A_1N_1 \quad (\text{Eq. 4})$$

$$\frac{dN_2}{dt} = W_1N_1^2 - A_2N_2 \quad (\text{Eq. 5})$$

In this case, if the upconversion rate (by energy transfer upconversion) is high compared to the spontaneous relaxation rate (i.e. $A_1N_1 \ll 2W_1N_1^2$), then, in the permanent regime, one gets: $N_2 \propto P$. The population density of the energy state from which the upconversion luminescence arises is linear with the excitation pump power. On the contrary, if the spontaneous relaxation dominates (i.e. $A_1N_1 \gg 2W_1N_1^2$), then $N_2 \propto P^2$, which means that the population density of the upconversion emitting energy state is quadratic with the excitation pump power.

3.4.3. Pump power dependence of upconversion in the case where ESA is dominant over ETU

In the particular case where ESA is dominant over ETU, $W_1 N_1^2$ can be neglected. The rate equations can therefore be simplified as follows:

$$\frac{dN_1}{dt} = \phi\sigma_0 N_0 - \phi\sigma_1 N_1 - A_1 N_1 \quad (\text{Eq. 6})$$

$$\frac{dN_2}{dt} = \phi\sigma_1 N_1 - A_2 N_2 \quad (\text{Eq. 7})$$

In this case, if the upconversion rate (by excited state absorption) is high compared to the spontaneous relaxation rate (i.e. $A_1 N_1 \ll \phi\sigma_1 N_1$), then, in the permanent regime, one gets: $N_2 \propto P$. On the contrary, if the spontaneous relaxation dominates (i.e. $A_1 N_1 \gg \phi\sigma_1 N_1$), then $N_2 \propto P^2$.

Since the power of the upconversion emission is proportional to the population density N_2 of the upconversion emitting state, these results show that, with increasing pump power (resulting in an increase of the importance of upconversion processes compared to that of spontaneous relaxation), the dependence of the upconversion emission power on the excitation power goes from quadratic to linear. These results can be generalised to a $(n+1)$ -energy level-system in which n photons are involved. In that case, the upconversion luminescence originates from state $|n\rangle$'s relaxation. The dependence of the upconversion emitted power on the pump power varies between $P_{UC} \propto P$ and $P_{UC} \propto P^n$.⁶

3.5. Time-evolution of upconversion luminescence emission

The time-evolution of the upconversion luminescence emission depends on the type(s) of upconversion process(es) involved (see section 3.5). In Figure 3.8, the typical time-evolutions (also called transients) of the upconversion luminescence emissions under pulsed (~ 10 ns pulses) upconversion excitation are presented in the cases where *a*) GSA/ESA and *b*) GSA/ETU processes dominate the upconversion mechanism. As previously explained in section 3.3, GSA/ESA consists of 2 sequential photon absorption steps by a single dopant (e.g. Er^{3+}), while GSA/ETU is a cooperative process which involves two dopants (e.g. Yb^{3+} and Er^{3+}) that interact together via energy transfers. For a GSA/ESA dominated mechanism (Figure 3.8a), the upconversion emitting state is populated during the excitation pulse, and

the upconversion emission intensity presents an exponential decrease once the excitation is turned off. In contrast, in the case where GSA/ETU dominates (Figure 3.8b), the upconversion luminescence transient exhibits a clear rise (after the end of the excitation pulse), followed by a decay. This is a clear fingerprint of an energy transfer process.

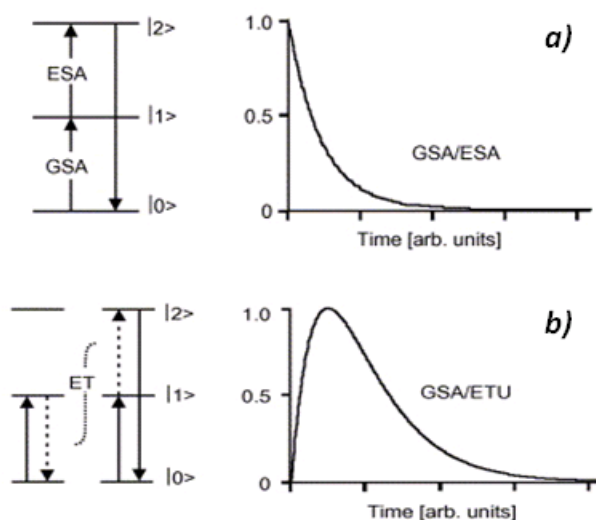


Figure 3.8: Typical transients³¹ representing the time-evolution of the upconversion luminescence emission after a short excitation pulse, for an upconversion mechanism dominated by a) GSA/ESA and b) GSA/ETU processes.

The results of time-resolved spectroscopy experiments on $\text{RE}_2\text{BaZnO}_5$ (RE = Y, Gd) materials co-doped with Yb^{3+} , Ln^{3+} ($\text{Ln}^{3+} = \text{Er}^{3+}$, Ho^{3+} , Tm^{3+}) will be presented in chapters 5, 6, 7 and 8. A good understanding of the various processes involved in the upconversion mechanism specific to these materials can be achieved by analysing the luminescence transients acquired under different excitation wavelengths, at different temperatures, and on samples containing various dopant concentrations.

3.6. Upconversion materials and their potential applications

3.6.1. Upconversion materials investigated over the last five year

In this section, we present the dominant upconversion materials that have attracted most interest within the upconversion community between the years 2005 to 2010. Lanthanide-doped β -NaYF₄ phosphors are by far the most frequently investigated materials, mainly for infrared to visible (green, red, blue and white) upconversion.^{4,31,32,34,60} As mentioned in chapter 2, the maximum phonon energy of β -NaYF₄ is low ($\sim 370 \text{ cm}^{-1}$) resulting in low non-radiative multiphonon relaxation rates, which is favourable to high upconversion efficiencies. A lot of work is done on the synthesis of NaYF₄ nanoparticles with controlled size, morphology, and luminescence chromaticity.^{7,31,32,61-63} Lanthanide-doped nanoparticles of other fluoride materials such as RE₃F₈ (RE = Y, Gd, La) are also often investigated for their upconversion properties.⁶⁴⁻⁶⁷ Upconverting nanoparticles are sometimes coated with a shell (*core-shell* nanoparticles are then produced), which results in improved upconversion efficiencies due to reduced surface quenching.^{64,68,69} The assessment of the potential of upconversion nanoparticles for applications in biology⁷⁰⁻⁷³ and photovoltaics^{74,75} has been the focus of recent research. NaREF₄ and RE₃F₈ (RE = Y, G, La) are fluorides, and as such, they have poor chemical stabilities. Lanthanide-doped oxide materials have started to attract interest within the upconversion community as they have better chemical, thermal and mechanical properties than fluorides, making them more suitable candidates for applications. The upconversion properties of lanthanide-doped RE₂O₃ (RE = Y, Gd, Lu),^{13,76} ZrO₂,^{77,78} RE₃Ga₅O₁₂ (RE = Y, Gd),^{79,80} YVO₄,^{81,82} and RE₂BaZnO₅ (RE = Gd, La) have been reported.³⁹

3.6.2. Main applications of upconversion materials

Potential applications of upconversion materials include lasers,^{83,84} novel display technologies,^{85,86} solar cells,⁸⁷⁻⁹⁰ and biophysics.^{34,91,92} In this section, we describe the use of upconversion materials in these applications.

Lasers

One of the first historical applications of upconversion materials was in the area of solid-state compact lasers⁸⁴ emitting in the visible. Early lanthanide based upconversion lasers only operated at low temperatures (below 100 K), making the systems impractical.⁹ For instance, $\text{BaY}_2\text{F}_8: \text{Yb}^{3+}, \text{Tm}^{3+}$ was reported to lase at 77 K,⁸³ but no emission was observed at room-temperature. Significant progress was made with the discovery of Er^{3+} doped LiLuF_4 crystals emitting bright green emission at room-temperature.⁹³ Most of the currently studied upconversion lasers are based on heavy-metal fluoride fibres (e.g. ZBLAN),⁹⁴ which tend to have poor chemical, thermal and mechanical properties. The development of highly efficient and stable materials (e.g. oxides) that can upconvert at room-temperature with low excitation density thresholds is required.

3D volumetric displays

Upconversion-based 3D displays were first introduced by Downing et al. in the 1990's.⁸⁶ Lanthanide-doped transparent heavy metal fluoride glasses were synthesised and shown to have good infrared to visible upconversion properties at room-temperature. A two-laser excitation system combined with a mechanical scanning system was used for the selective excitation of a voxel (i.e. volumetric pixel) of sample, at the crossing point of the two laser beams. Red, green and blue emissions could be obtained in glass layers doped with Pr^{3+} , Er^{3+} and Tm^{3+} . By rapid spatial scanning of the transparent upconverting material, the position of the excited voxel could be moved within the volume of the sample, thus allowing 3D images to be drawn. Since then, a new method based on a single laser beam pumping system (966 nm excitation) has been developed to enhance the display brightness.⁹⁵ Potential applications of 3D volumetric displays include computer assisted design, medical imaging, television and art.

Solar-cells

The use of upconverting materials is being considered in the photovoltaic industry for the development of high-efficiency solar cells. The largest losses in the traditional silicon solar-cells arise from the mismatch between the wavelengths in the solar spectrum and those that

can be efficiently used by the solar cells. In particular, the solar photons with energies below the bandgap of the silicon semiconductor (i.e. photons with a wavelength above 1100 nm) are not absorbed and do not contribute to energy conversion, while a portion of energy above the bandgap is also lost. Significant improvements in solar cell efficiencies can therefore be expected by combining luminescent upconversion and down-conversion layers that would shift the energies of these otherwise wasted photons to the spectral range that can be used by the solar cells. Trupke et al.⁹⁶ deposited an upconverting layer based on NaYF₄: Er³⁺ phosphors at the rear face of a silicon solar cell, and demonstrated that external quantum efficiencies close to 1% could be achieved under laser excitation at 1550 nm.

Bio-imaging

Upconversion nanomaterials could be used as probes for single molecule imaging in biological cells. For bioimaging, nanoparticles (having diameters below 50 nm after functionalisation) with high brightness and continuous emission are required. In addition, they need to be resistant to photobleaching and have a minimal spectral overlap with the cellular autofluorescence. Current imaging methods use organic dyes or fluorescent proteins. The use of such probes is problematic because of their sensitivity to photobleaching which limits the imaging times. Another major drawback is that these probes are usually excited by UV light, often resulting in tissue photo-toxicity and limited observation depth (due to poor light penetration). Fluorescence imaging using near-infrared excitation is expected to have a major impact in biomedical imaging. NaYF₄: Yb³⁺, Er³⁺ nanocrystals were shown to exhibit ideal properties for single molecule imaging experiments under ~ 980 nm excitation.⁹⁷ Unfortunately, being fluorides, these materials have poor chemical and thermal stabilities.

3.7. Summary

In this chapter, we have shown that upconversion is the most efficient process known to convert low-energy incident radiation into higher-energy emitted light, making it very relevant for many applications (e.g. lasers, displays, solar cells, bio-imaging, etc). The dominant upconversion processes were presented. Among them, upconversion by sensitised

energy transfer is the most efficient process for infrared to visible upconversion, and will therefore be the focus of the PhD work presented in chapters 5, 6, 7 and 8. We will show that by choosing properly the upconversion material (in particular the dopant concentrations incorporated within the host lattice), one can optimise the probabilities of the energy transfer processes leading to the population of upconversion emitting states, and minimise upconversion quenching processes, resulting in high upconversion efficiencies. Time-resolved spectroscopy experiments will be used in order to try and gain an understanding of the upconversion processes involved in our specific materials.

References

- ¹ F. Auzel, *C.R. Acad. Sci. (Paris)*, 1966, **263B**, 819.
- ² F. Auzel, *C.R. Acad. Sci. (Paris)*, 1966, **262**, 1016.
- ³ V. V. Ovsyankin and P. P. Feofilov, *Jetp Lett.*, 1966, **4**, 317.
- ⁴ S. Heer, K. Kömpe, H. U. Güdel and M. Haase, *Adv. Mater.*, 2004, **16**, 2102.
- ⁵ A. Aebischer, S. Heer, D. Biner, K. Krämer, M. Haase and H. U. Güdel, *Chem. Phys. Lett.*, 2005, **407**, 124.
- ⁶ M. Pollnau, D. R. Gamelin, S. R. Lüthi, H. U. Güdel and M. P. Hehlen, *Phys. Rev. B*, 2000, **61**, 3337.
- ⁷ J. C. Boyer, F. Vetrone, L. A. Cuccia and J. A. Capobianco, *J. Am. Chem. Soc.*, 2006, **128**, 7444.
- ⁸ J. J. Owen, A. K. Cheetham, N. A. Nighman, R. H. Jarman and R. J. Thrash, *J. Opt. Soc. Am. B*, 1994, **11**, 919.
- ⁹ J. J. Owen, A. K. Cheetham and R. A. McFarlane, *J. Opt. Soc. Am. B*, 1998, **15**, 684.
- ¹⁰ A. Patra, C. S. Friend, R. Kapoor and P. N. Prasad, *J. Phys. Chem. B*, 2002, **106**, 1909.
- ¹¹ J. A. Capobianco, F. Vetrone, J. C. Boyer, A. Speghini and M. Bettinelli, *Opt. Mater.*, 2002, **19**, 259.
- ¹² A. Patra, C. S. Friend, R. Kapoor and P. N. Prasad, *Chem. Mater.*, 2003, **15**, 3650.
- ¹³ A. M. Pires, O. A. Serra, S. Heer and H. U. Güdel, *J. Appl. Phys.*, 2005, **98**, 063529.
- ¹⁴ Y. H. Wang and J. Ohwaki, *Appl. Phys. Lett.*, 1993, **63**, 3268.
- ¹⁵ X. Zou and T. Izumitani, *J. Non-Cryst. Solids*, 1993, **162**, 68.
- ¹⁶ S. Tanabe, S. Yoshii, K. Hirao and N. Soga, *Phys. Rev. B*, 1992, **45**, 4620.
- ¹⁷ M. P. Hehlen, N. J. Cockroft, T. R. Gosnell and A. J. Bruce, *Phys. Rev. B*, 1997, **56**, 9302.
- ¹⁸ D. R. Gamelin and H. U. Güdel, *J. Am. Chem. Soc.*, 1998, **120**, 12143.
- ¹⁹ M. Wermuth and H. U. Güdel, *Chem. Phys. Lett.*, 1997, **281**, 81.
- ²⁰ O. S. Wenger and H. U. Güdel, *Inorg. Chem.*, 2001, **40**, 5747.
- ²¹ J. F. Suijver, in *Luminescence: from theory to applications*, ed. C. Ronda, Wiley-VCH Verlag GmbH and Co. KGaA, Weinheim, 2008, ch. 6, pp. 134.

- ²² F. Auzel, *Proc. IEEE*, 1973, **61**, 758.
- ²³ F. Auzel, *Chem. Rev.*, 2004, **104**, 139.
- ²⁴ Y. Mita and E. Nagasawa, *NEC Res. Dev.*, 1974, **33**, 61.
- ²⁵ G. F. J. Garlick, *Contemp. Phys.*, 1976, **17**, 127.
- ²⁶ T. Danger, J. Koetke, R. Brede, E. Heumann, G. Huber and B. H. T. Chai, *J. Appl. Phys.*, 1994, **76**, 1413.
- ²⁷ H. X. Zhang, C. H. Kam, Y. Zhou, X. Q. Han, S. Buddhudu, Q. Xiang, Y. L. Lam and Y. C. Chan, *Appl. Phys. Lett.*, 2000, **77**, 609.
- ²⁸ A. Patra, C. S. Friend, R. Kapoor and P. N. Prasad, *Appl. Phys. Lett.*, 2003, **83**, 284.
- ²⁹ J. A. Capobianco, J. C. Boyer, F. Vetrone, A. Speghini and M. Bettinelli, *Chem. Mater.*, 2002, **14**, 2915.
- ³⁰ H. Yang, Z. Dai and N. Zu, *J. Non-Cryst. Solids*, 2008, **354**, 1796.
- ³¹ J. F. Suyver, A. Aebischer, D. Biner, P. Gerner, J. Grimm, S. Heer, K. W. Krämer, C. Reinhard and H. U. Güdel, *Opt. Mater.*, 2005, **27**, 1111.
- ³² J. C. Boyer, L. A. Cuccia and J. A. Capobianco, *Nano Lett.*, 2007, **7**, 847.
- ³³ J. Shan, X. Qin, N. Yao and Y. Ju, *Nanotechnology*, 2007, **18**, 445607.
- ³⁴ S. Heer, O. Lehmann, M. Haase and H. U. Güdel, *Angew. Chem., Int. Ed. Engl.*, 2003, **42**, 3179.
- ³⁵ R. J. Thrash and L. F. Johnson, *J. Opt. Soc. Am. B*, 1994, **11**, 881.
- ³⁶ F. W. Ostermayer, J. J. P. Van der Ziel, H. M. Marcos, L. C. Van Uilert and J. E. Geusic, *Phys. Rev. B*, 1970, **3**, 2698.
- ³⁷ F. Vetrone, J. C. Boyer, J. A. Capobianco, A. Speghini and M. Bettinelli, *J. Appl. Phys.*, 2004, **96**, 661.
- ³⁸ D. Matsuura, *Appl. Phys. Lett.*, 2002, **81**, 4526.
- ³⁹ A. Birkel, A. A. Mikhailovsky and A. K. Cheetham, *Chem. Phys. Lett.*, 2009, **477**, 325.
- ⁴⁰ L. Wetenkamp, G. F. West and H. Többen, *J. Non-Cryst. Solids*, 1992, **140**, 35.
- ⁴¹ D. C. Yeh, W. A. Sibley and M. J. Suscavage, *J. Appl. Phys.*, 1988, **63**, 4644.
- ⁴² F. Auzel, D. Pecile and D. Morin, *J. Electrochem. Soc.*, 1975, **122**, 101.

- ⁴³ L. A. Díaz-Torres, E. De la Rosa, P. Salas and H. Desirena, *Opt. Mater.*, 2005, **27**, 1305.
- ⁴⁴ L. S. Lee, S. C. Rand and A. L. Schawlow, *Phys. Rev. B*, 2001, **29**, 6901.
- ⁴⁵ G. S. Maciel, A. Biswas, R. Kapoor and P. N. Prasad, *Appl. Phys. Lett.*, 2000, **76**, 1978.
- ⁴⁶ T. Miyakawa and D. L. Dexter, *Phys. Rev. B*, 1970, **1**, 70.
- ⁴⁷ G. M. Salley, R. Valiente and H. U. Güdel, *J. Lumin.*, 2001, **94**, 305.
- ⁴⁸ G. M. Salley, R. Valiente and H. U. Güdel, *Phys. Rev. B*, 2003, **67**, 134111.
- ⁴⁹ I. R. Martín, A. C. Yanes, J. Méndez-Ramos, M. E. Torres and V. D. Rodríguez, *J. Appl. Phys.*, 2001, **89**, 2520.
- ⁵⁰ E. Martins, C. B. de Araújo, J. R. Delben, A. S. L. Gomes, B. J. da Costa and Y. Messaddeq, *Opt. Commun.*, 1998, **158**, 61.
- ⁵¹ M. F. Joubert, *Opt. Mater.*, 1999, **11**, 181.
- ⁵² J. F. Suijver, in *Luminescence: from theory to applications*, ed. C. Ronda, Wiley-VCH Verlag GmbH and Co. KGaA, Weinheim, 2008, ch. 6, pp. 150.
- ⁵³ J. S. Chivian, W. E. Case and D. D. Eden, *Appl. Phys. Lett.*, 1979, **35**, 124.
- ⁵⁴ M. E. Koch, A. W. Kueny and W. E. Case, *Appl. Phys. Lett.*, 1990, **56**, 1083.
- ⁵⁵ M. F. Joubert, S. Guy and B. Jacquier, *Phys. Rev. B*, 1993, **48**, 10031.
- ⁵⁶ H. Ni and S. C. Rand, *Opt. Lett.*, 1991, **16**, 1424.
- ⁵⁷ F. Auzel and Y. Chen, *J. Lumin.*, 1995, **65**, 45.
- ⁵⁸ B. P. Scott, F. Zhao, R. S. F. Chang and N. Djeu, *Opt. Lett.*, 1993, **18**, 113.
- ⁵⁹ G. Dieke, in *Spectra and Energy Levels of Rare Earth Ions in Crystals*, Wiley Interscience Publishers, New York, 1968.
- ⁶⁰ N. Menyuk, K. Dwight and J. W. Pierce, *Appl. Phys. Lett.*, 1972, **21**, 159.
- ⁶¹ J. H. Zheng, J. Su, Z. H. Li, R. X. Yan and Y. D. Li, *Adv. Mater.*, 2005, **17**, 2119.
- ⁶² F. Wang, D. K. Chatterjee, Z. Q. Li, Y. Zhang, X. P. Fan and M. Q. Wang, *Nanotechnology*, 2006, **17**, 5786.
- ⁶³ L. Y. Wang and Y. D. Li, *Chem. Mater.*, 2007, **19**, 727.
- ⁶⁴ G. S. Yi and G. M. Chow, *J. Mater. Chem.*, 2005, **15**, 4460.
- ⁶⁵ S. Sivakumar, P. R. Diamente and F. C. van Veggel, *Chem.-Eur. J.*, 2006, **12**, 5878.

- ⁶⁶ D. Q. Chen, Y. S. Wang, K. L. Zheng, T. L. Guo, Y. L. Yu and P. Huang, *Appl. Phys. Lett.*, 2007, **91**, 251903.
- ⁶⁷ G. F. Wang, W. P. Qin, J. S. Zhang, J. S. Zhang, Wangyan, C. Y. Cao, L. L. Wang, G. D. Wei, P. F. Zhu and R. J. Kim, *J. Phys. Chem. C*, 2008, **112**, 12161.
- ⁶⁸ Z. Q. Li, Y. Zhang and S. Jiang, *Adv. Mater.*, 2008, **20**, 4765.
- ⁶⁹ Y. Wang, L. P. Tu, J. W. Zhao, Y. J. Sun, X. G. Kong and H. Zhang, *J. Phys. Chem. C*, 2009, **113**, 7164.
- ⁷⁰ K. Kuningas, T. Rantanen, T. Ukonaho, T. Lövgren and T. Soukka, *Anal. Chem.*, 2005, **77**, 7348.
- ⁷¹ D. K. Chatterjee, A. J. Rufalhah and Y. Zhang, *Biomaterials*, 2008, **29**, 937.
- ⁷² R. Kumar, M. Nyk, T. Y. Ohulchansky, C. A. Flask and P. N. Prasad, *Adv. Funct. Mater.*, 2009, **19**, 853.
- ⁷³ M. Wang, C. C. Mi, W. X. Wang, C. H. Liu, Y. F. Wu, Z. R. Xu, C. B. Mao and S. K. Xu, *ACS Nano*, 2009, **3**, 1580.
- ⁷⁴ S. Ivanova, F. Pelle, A. Tkachuk, M. F. Joubert, Y. Guyot and V. P. Gapontzev, *J. Lumin.*, 2008, **128**, 914.
- ⁷⁵ F. Lahoz, *Opt. Lett.*, 2008, **33**, 2982.
- ⁷⁶ G. Y. Chen, H. C. Liu, H. J. Liang, G. Somesfalean and Z. G. Zhang, *J. Phys. Chem. C*, 2008, **112**, 12030.
- ⁷⁷ A. Patra, P. Ghosh, P. S. Chowdhury, M. A. R. C. Alencar, B. W. Lozano, N. Rakov and G. S. Maciel, *J. Phys. Chem. B*, 2005, **109**, 10142.
- ⁷⁸ G. Y. Chen, G. Somesfalean, Y. Liu, Z. G. Zhang, Q. Sun and F. P. Wang, *Phys. Rev. B*, 2007, **75**, 195204.
- ⁷⁹ F. Pandozzi, F. Vetrone, J. C. Boyer, R. Naccache, J. A. Capobianco, A. Speghini and M. Bettinelli, *J. Phys. Chem. B*, 2005, **109**, 17400.
- ⁸⁰ M. Liu, S. W. Wang, J. Zhang, L. Q. An and L. D. Chen, *Opt. Mater.*, 2007, **29**, 1352.
- ⁸¹ Y. J. Sun, H. J. Liu, X. Wang, X. G. Kong and H. Zhang, *Chem. Mater.*, 2006, **18**, 2726.
- ⁸² K. S. Yang, F. Zheng, R. N. Wu, H. S. Li and X. Y. Zhang, *J. Rare-Earths*, 2006, **24**, 162.
- ⁸³ L. F. Johnson and H. J. Guggenheim, *Appl. Phys. Lett.*, 1971, **19**, 44.
- ⁸⁴ D. S. Funk, S. B. Stevens, S. S. Wu and J. G. Eden, *IEEE J. Quantum Electron.*, 1996, **32**, 638.

- ⁸⁵ E. Downing, L. Hesselink, J. Ralston and R. Macfarlane, *Science*, 1996, **273**, 1185.
- ⁸⁶ A. Rapaport, J. Milliez, M. Bass, A. Cassanho and H. Jenssen, *J. Display Technol.*, 2006, **2**, 68.
- ⁸⁷ C. Strümpel, M. McCann, G. Beaucarne, V. Arkhipov, A. Slaoui, V. Svrcek, C. del Cañizo and I. Tobias, *Sol. Energy Mater. Sol. Cells*, 2007, **91**, 238.
- ⁸⁸ T. Trupke, M.A. Green and P. Würfel, *J. Appl. Phys.*, 2002, **92**, 4117.
- ⁸⁹ B. S. Richards and A. Shalav, *IEEE Trans. Electron Devices*, 2007, **54**, 2679.
- ⁹⁰ A. Shalav, B. S. Richards and M. A. Green, *Sol. Energy Mater. Sol. Cells*, 2007, **91**, 829.
- ⁹¹ R. S. Niedbala, H. Feindt, K. Kardos, T. Vail, J. Burton, B. Bielska, S. Li, D. Milunic, P. Bourdelle and R. Vallejo, *Anal. Biochem.*, 2001, **293**, 22.
- ⁹² M. Seydack, *Biosens. Bioelectron.*, 2005, **20**, 2454.
- ⁹³ E. Heumann, S. Bär, K. Rademaker, G. Huber, S. Butterworth, A. Dening and W. Seelert, *Appl. Phys. Lett.*, 2006, **88**, 061108.
- ⁹⁴ D. S. Funk and J. G. Eden, *IEEE J. Sel. Top. Quantum Electron.*, 1995, **1**, 784.
- ⁹⁵ L. Hesselink, *Opt. Lett.*, 1998, **23**, 1107.
- ⁹⁶ T. Trupke, A. Shalav, B. S. Richards, P. Würfel and M. A. Green, *Sol. Energy Mater. Sol. Cells*, 2006, **90**, 3327.
- ⁹⁷ S. Wu, G. Han, D. J. Milliron, S. Aloni, V. Altoe, D. V. Talapin, B. E. Cohen and P. J. Schuck, *Proc. Natl. Acad. Sci. U.S.A.*, 2009, **106**, 10917.

CHAPTER 4: Experimental

4.1. Introduction

In this chapter, we present the experimental techniques used for material preparation and for their structural, chemical and optical characterisation. Upconversion phosphors were synthesised by solid-state chemistry (for most of them) or by the sol-gel Pechini route, as will be described in section 4.2. Structural analyses were performed using powder X-ray diffraction (section 4.3). The dopant concentrations incorporated within the materials were measured using inductively coupled plasma–atomic emission spectroscopy (section 4.4). In section 4.5, we present the spectroscopic techniques used for steady-state (under continuous wave cw, or μs -to- ms pulsed excitation), dynamic (under ns pulsed excitation) luminescence studies, upconversion efficiency quantification (under cw excitation) and reflectance measurements.

4.2. Synthesis of materials

4.2.1. Background: solid-state and solution synthesis methods

Solid-state synthesis route

In the literature, many phosphors are synthesised by solid-state reactions between starting materials, at high temperature, in air or in a reducing atmosphere.¹ High-purity solid reactants are usually ground thoroughly together, sometimes pelletised, and placed in a crucible. They then undergo several sintering stages, usually with intermediate grinding. Fluxes are sometimes added to the raw material mixture to help crystal growth, accelerate it, or lower the activation energy. Solid-state reactions present a number of advantages over liquid routes, including the ease to carry them out, the large availability of the starting materials, and the possibility of preparing compounds in large amounts. However, solid-state chemistry is not an ideal synthesis route due to the high sintering temperatures (up to 1500°C) and long reaction times required. The resulting products sometimes have poor homogeneity (presence

of secondary phases), and large and non-uniform particle sizes are often observed. To overcome some of these limitations, solution routes can be employed.

Sol-gel synthesis route

When control of phosphor morphology is required, solution synthesis routes at relatively low temperatures are preferred to solid-state reactions. Solution routes guarantee a mixing of the initial reactants at the atomic scale and a good solvation, which guarantees a fast diffusion. The temperatures involved are generally lower than those required for particle crystallisation in solid-state reactions, resulting in a reduction of thermally driven particle growth. Among the wet chemical routes, the sol-gel method^{2,3} has been used extensively for the synthesis of various types of materials, including powders, films, fibers and nanostructures of almost any shape, size, and chemical composition. It is a chemical synthesis technique that uses metal alkoxides in solution, through a series of chemical processes, including hydrolysis, gelation, drying, and thermal treatments. In a typical sol-gel reaction, the metal alkoxide solution is stirred, and a mixture of water, alcohol and acid is added to stimulate the hydrolysis. Gelation occurs and a porous solid, called xerogel, is obtained after drying. An additional heat treatment of the sol-gel produces pore-free materials. The removal of organics takes place by an endothermic carbonisation around 200°C and is followed by an exothermic oxidation at temperatures around 350°C. A final heat treatment at high temperatures (around 1000°C for oxides) is performed for crystallisation to occur. The Pechini method (Figure 4.1) is a type of sol-gel route, consisting of 2 main steps: metal complex formation and in-situ polymerisation of organics.⁴ In a typical experiment, citric acid is used to form stable metal complexes, and their polyesterification with polyethylene glycol (PEG) (or ethylene glycol EG) forms a polymeric resin.⁵ The metal complexes are immobilised in this rigid organic polymer networks, which leads to reduced segregation of the metal ions, and guarantees a good compositional homogeneity. Finally, the polymeric resin is calcined at around 1000°C and usually generates pure-phase metal oxides.

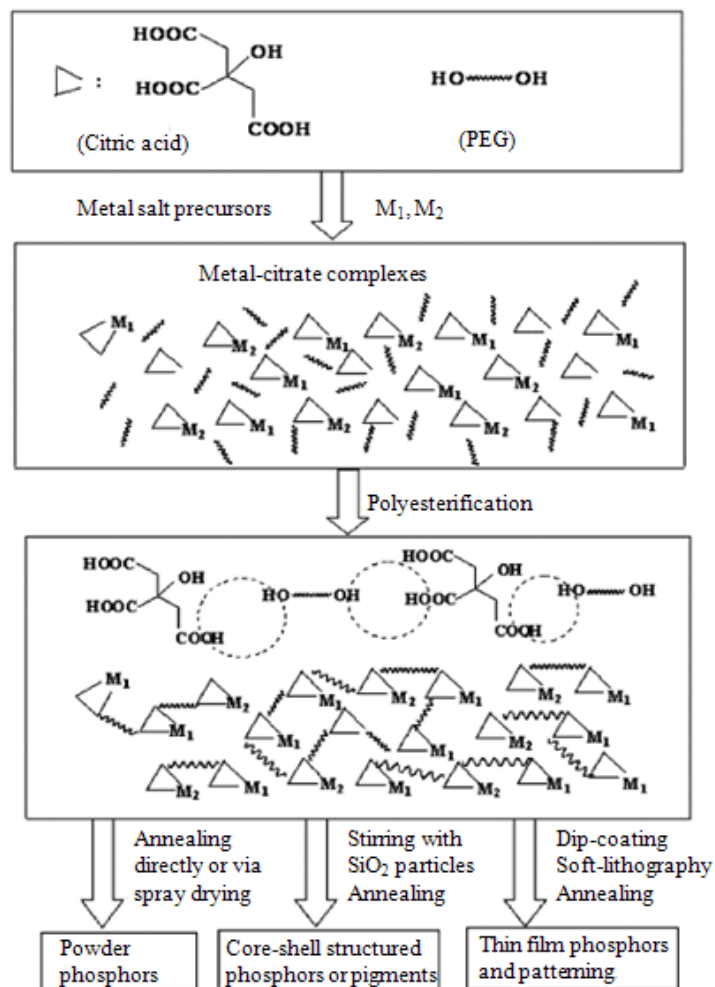


Figure 4.1: Schematic representation of the Pechini sol-gel route.⁴

4.2.2. Synthesis protocols used during this PhD

The typical synthesis protocols used for solid-state and Pechini sol-gel syntheses of RE₂BaZnO₅: Yb³⁺ (x%), Ln³⁺ (y%) (RE = Y, Gd and Ln³⁺ = Er³⁺, Ho³⁺, Tm³⁺) phosphors are described in this section.

Solid-state chemistry

For solid-state syntheses of RE₂BaZnO₅: Yb³⁺ (x%), Ln³⁺ (y%) (RE = Y, Gd and Ln = Er³⁺, Ho³⁺, Tm³⁺) phosphors, stoichiometric amounts of RE₂O₃ (*Alfa Aesar*, 99.99%), Yb₂O₃ (*Alfa Aesar*, 99.99%), Ln₂O₃ (*Alfa Aesar*, 99.99%), ZnO (*Fisher Scientific*, 99.5%) and BaCO₃

(Fisher Scientific, 99+%) were mixed, ground together, and sintered at 1200°C for 3 to 4 days (depending on the composition) with 3 to 4 intermediary grinding stages.

Pechini sol-gel route

For Pechini sol-gel syntheses of $\text{RE}_2\text{BaZnO}_5$: Yb^{3+} (x%), Ln^{3+} (y%) (RE = Y, Gd and Ln = Er, Ho, Tm) phosphors, stoichiometric amounts of $\text{RE}(\text{NO}_3)_3 \cdot 6\text{H}_2\text{O}$ (Sigma-Aldrich, 99.8%), $\text{Yb}(\text{NO}_3)_3 \cdot 5\text{H}_2\text{O}$ (Sigma-Aldrich, 99.9%), $\text{Ln}(\text{NO}_3)_3 \cdot 5\text{H}_2\text{O}$ (Sigma-Aldrich, 99.9%), $\text{Zn}(\text{NO}_3)_2 \cdot 6\text{H}_2\text{O}$ (Sigma-Aldrich, 98+%), and $\text{Ba}(\text{NO}_3)_2$ (Sigma-Aldrich, $\geq 99\%$) were dissolved in deionised water and heated (under stirring) at 70°C for 2 hours. Citric acid (Sigma-Aldrich, $\geq 99.5\%$) and ethylene glycol (Sigma-Aldrich, 99.8%) were then added (molar ratio of metal: citric acid : ethylene glycol of 1 : 1 : 2), and the temperature was gradually raised to 125°C and left at this temperature for 12 hours. The resulting polymeric foam was slowly heated to 400°C to decompose the organic material. The calcined powder was ground and finally sintered at 1150°C for 2 hours.

Comparison of the samples prepared via solid-state and Pechini sol-gel routes

Relatively pure and single-phase materials could be obtained via both methods, and the resulting products exhibited bright visible emission under infrared excitation. However, precise upconversion efficiency measurements showed that the materials synthesised by solid-state chemistry had significantly higher infrared to visible upconversion efficiencies (about 5 times higher) than those synthesised via liquid routes (with the upconversion efficiency defined as the ratio of the upconversion power emitted in the visible over the power absorbed in the infrared). This can be explained by the presence of residual organic functions present at the surface of the particles synthesised by solution routes (e.g. hydroxyl groups) and acting as quenching centres. It was therefore decided to focus on the characterisation of the materials obtained via solid-state routes. All the materials presented in chapters 5, 6, 7 and 8 have been synthesised by solid-state chemistry.

4.3. Structural characterisation: X-ray diffraction and Rietveld refinement

4.3.1. Background: X-ray diffraction and Rietveld refinement

X-ray diffraction (XRD) is used for structural characterisation. The XRD pattern of each crystalline material is unique. The positions of the diffraction peaks are determined by the spacing of the crystallographic planes and follow Bragg's law:

$$n\lambda = 2d\sin\theta \quad (\text{Eq. 1})$$

where n is an integer, λ the wavelength of the radiation used, d the spacing of the crystal planes, and θ the angle of the diffraction peak. The peak intensities are determined by the types and positions of the atoms in the crystal lattice according to the structure factor $F(hkl)$:

$$F(hkl) = \sum_{n=1}^N f_n \exp[2\pi i(hx_n + ky_n + lz_n)] \quad (\text{Eq. 2})$$

where hkl are the Miller indices of the reflecting planes, f_n the atomic scattering factors, and x_n , y_n , and z_n are the coordinates of the n^{th} atom in the unit cell containing N atoms.

Once the X-ray diffraction data has been collected, the crystal structure can usually be refined using the Rietveld refinement method.⁶ In the case of a single-phase material, if the phase structure is known (as is the case of Y_2BaZnO_5 and $\text{Gd}_2\text{BaZnO}_5$), the atomic coordinates are imported from a crystallographic information framework (CIF) file and the background, peak shape and lattice parameters are refined.

4.3.2. Experimental setup for X-ray diffraction measurements

The X-ray powder diffraction patterns presented in this thesis were measured using a theta-theta diffractometer (*Bruker D8*), equipped with a Cu $K\alpha$ source (generator: 40 kV and 40 mA), a scintillation detector with pulse-height analysis, and a variable knife-edge collimator for high resolution X-ray diffractometry. The best achievable instrumental resolution was 0.08° in 2θ .

4.4. Elemental analysis: ICP-AES

4.4.1. Introduction to ICP-AES

As will be demonstrated in chapters 5, 6, 7 and 8, upconversion properties vary strongly with dopant concentrations. It is therefore necessary to be able to measure these concentrations precisely. Inductively coupled plasma-atomic emission spectroscopy (ICP-AES)⁷ is a highly sensitive and specific method that can be used to quantify chemical traces of certain elements at the ppm (mg/L) level. In particular, several studies have shown that ICP-AES can be used for rare-earth trace detection.⁸⁻¹⁰ ICP-AES is based on the fact that each element emits energy at specific wavelengths peculiar to the nature of the element considered. Therefore, by determining which wavelengths are emitted by an excited sample, and by comparing the intensities of these emissions to those of calibration solutions, one can obtain the precise elemental composition of the sample of interest. In a typical experiment, the calibration standards and sample solutions are introduced into an argon plasma, through a sample introduction system consisting of a nebuliser, a spray chamber and a peristaltic pump. The sample introduction system transports the analytes in solution to a nebuliser that generates an aerosol which is then sprayed into the spray chamber (where larger drops are eliminated). Humidified argon gas is also injected into the nebuliser along with the sample. The fine aerosol mist containing the sample and argon gas is then injected into an argon plasma, which causes the sample to undergo desolvation and strong excitation. When the excited electrons return to their ground state, they emit light at specific wavelengths and intensities that are related to the sample's elemental composition. The light emitted by the sample (in the plasma) is focalised through a lens, sent to a spectrometer, and analysed with a photomultiplier tube.

4.4.2. Sample preparation for ICP-AES

Dopant concentrations in $\text{RE}_2\text{BaZnO}_5: \text{Yb}^{3+}, \text{Er}^{3+}$ (RE = Y, Gd) samples were quantified using ICP-AES. A Varian Liberty II Sequential ICP-AES instrument with axial viewing of the plasma was used for the measurements. The instrument was operated by applying an incident power of 1.4 kW and a plasma gas (argon) pressure of 200 kPa. Before ICP-AES analysis, the samples of interest were digested in high purity nitric acid (*Fisher Scientific*,

Nitric acid 69% Optima) inside an autoclave kept at 150°C for 3 days. For dopant concentration determination, calibration solutions with different concentrations of the elements to be quantified were prepared by dilution of 1000 ppm atomic absorption spectrometric standards (*Spex CertiPrep*) in high purity nitric acid (*Fisher Scientific*, Nitric acid 69% Optima). A blank solution (high purity deionised water), the calibration solutions and the digested samples were sequentially loaded into the ICP-AES instrument, nebulised, and dried (water evaporated). The remaining solids were then volatilised and atomised in the argon plasma. The light emitted upon de-excitation of the samples was analysed (in terms of emission wavelengths and intensities) using a monochromator connected to a photomultiplier. Quantitative dopant concentration measurements were based on the evaluation of emission peak height measurements. The following spectral lines were chosen: Er³⁺: 349.91 nm (background 349.95 nm) and Yb³⁺: 328.94 nm (background 328.99 nm). The detection limits were on the order of 2.5 ppm for Er³⁺ and 0.4 ppm for Yb³⁺.

4.5. Spectroscopic characterisation

After synthesis, structural and chemical characterisation, the steady-state and dynamic upconversion properties of the samples were analysed using various spectroscopic techniques described in this section. As set out in chapter 1, the spectroscopic measurements were performed using the facilities of various research laboratories, including Saint-Gobain Recherche (France) (experiments under cw excitation presented in section 4.5.1), the Advanced Technology Institute, University of Surrey (UK) (experiments under pulsed excitation, section 4.5.1) and Queen Mary University of London (UK) (section 4.5.2).

4.5.1. Upconversion photoluminescence and efficiency quantification

4.5.1.1. Background

In a typical photoluminescence experiment, the intensity of the light emitted by a sample (upon excitation by an electromagnetic radiation of given wavelength) is measured in a range of emission wavelengths. Relatively intense excitation sources and sensitive systems of detection are required when performing luminescence measurements on upconversion

samples. This is due to the relatively low efficiency of light upconversion compared to that of classical luminescence.

In order to be able to compare the upconversion performances of the various materials that are synthesised in this PhD (and also compare their performances with those of other materials reported in the literature), it is important to be able to quantify precisely their upconversion efficiencies. It is worth noting that most of the research papers on upconversion materials that are available in the literature do not quantify any upconversion efficiency. The upconversion emission is often qualified as ‘bright’ or ‘intense’ but no efficiency figure is usually given. Various definitions of upconversion efficiency are used in the seldom papers that do quantify the performances of their materials.¹¹⁻¹³ The most frequently chosen definition is the one which was used in this thesis (see chapters 5, 6, 7 and 8): the upconversion efficiency was defined as the ratio of the upconversion power emitted by the sample, over the incident power that it absorbs.^{11,14,15} An optical bench dedicated to the measurement of upconversion emission properties and to the quantification of upconversion efficiencies (under cw near-infrared excitation), was mounted and calibrated by Guillaume Goubert at Saint-Gobain Recherche (France). The upconversion measurements presented in this thesis have been performed by Olivier Delrieu (research technician at Saint-Gobain) and/or myself, using the optical setup described below.

4.5.1.2. Experimental setup for steady-state upconversion emission measurements

Upconversion photoluminescence measurement under cw ~ 980 nm sample excitation and efficiency quantification

The experimental setup used for upconversion emission spectra acquisition and efficiency measurements is shown in Figure 4.2. Prior to the measurements, the sample of interest was finely ground and sandwiched between two quartz plates (*Helma*, 106-QS), one of which was coated with a reflective film of silver. The sample holder was then placed at the rear-face of an integrating sphere (*Instrument System*, ISP-150-100). For the acquisition of upconversion luminescence spectra under near-infrared excitation, the sample of interest was excited using the 977 nm output of a temperature-controlled cw laser diode (*Thorlabs*, L980P100 and TCLDM9). The excitation signal was focused onto the centre of the sample holder using a

lens (*Newport*, KPX049AR.16). After initial alignment of the setup, efficiency measurements were performed in two steps. For the first measurement, the quartz sample holder at the rear-face of the integrating sphere was left empty (no sample inside, reflective rear-faced sample holder empty), and the laser excitation on the sample holder was collected using an optical fibre and analysed with a spectrometer (*Instrument System*, CAS 140B). From this measurement, the incident power in the near-infrared P_{inc}^{IR} (integrated over the 950-1000 nm range) was determined. For the second measurement, the sample under investigation was placed inside the quartz sample holder, and both the fraction of the excitation light that had not been absorbed by the sample (power $P_{not\ abs}^{IR}$ integrated over the 950-1000 nm range), and the emitted upconversion light (power P_{em} integrated over the 380-780 nm or 420-870 nm ranges, depending on the dopants used) were collected and quantified. The results of these two measurements were combined in order to calculate the fraction of the incident power *absorbed* by the sample (P_{abs}^{IR} in the 950-1000 nm range). The upconversion efficiency was calculated as the ratio of the power emitted by upconversion in the range of interest (e.g. 380-780 nm or 420-870 nm) over the power absorbed in the infrared (950-1000 nm range):

$$\eta_{UC} = \frac{P_{em}}{P_{abs}^{IR}} = \frac{P_{em}}{P_{inc}^{IR} - P_{not\ abs}^{IR}} \quad (\text{Eq. 3})$$

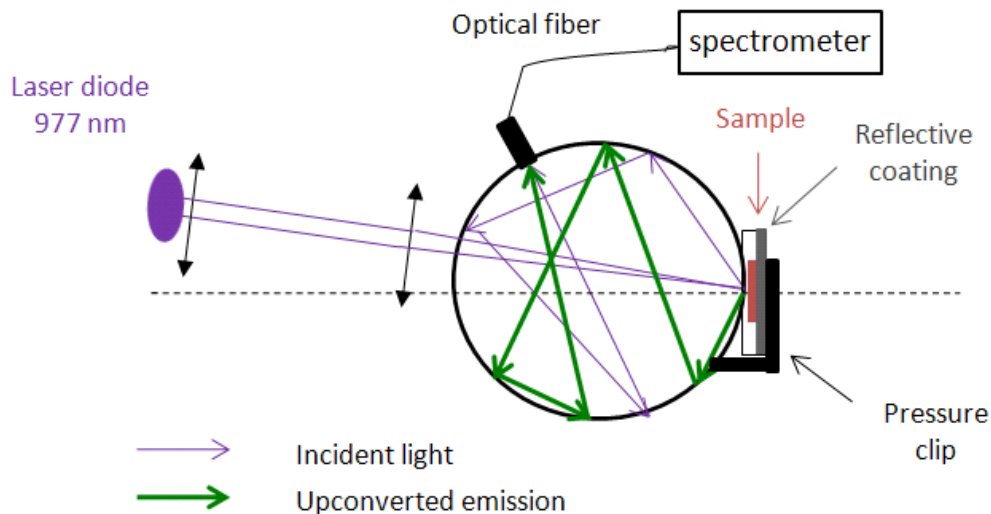


Figure 4.2: Schematic of the experimental setup used for upconversion efficiency measurements. The sample of interest was inserted in a partially reflective sample holder placed at the rear-face of an integrating sphere.

Prior to the measurements, the optical bench was calibrated and the measurement uncertainties were assessed taking into account backscattering phenomena and light losses (work performed by Guillaume Goubert). The retrodiffusion of the incident light on the sample was quantified using an undoped sample in order to mimic the sample scattering. No significant differences were found between the power measured on an empty sample holder (with a reflective rear-face), and the power scattered by the undoped sample. This can be explained by the fact that, in the undoped sample, almost all the incident light is backscattered. This result can be generalised to doped samples containing small dopant concentrations since scattering properties are not significantly affected when introducing dopants at low concentration. For simplicity, it was therefore decided to perform incident power (P_{inc}^{IR}) measurements on an empty sample holder with a reflective rear-face. Light losses were quantified as a function of the incident light wavelength and taken into account for emission spectra corrections. These losses occur mainly by reflexion on the sample holder (air/quartz and quartz/sample interfaces) and by transmission on the mirror located at the rear face of the sample holder.

Prior to efficiency quantifications, the collected emission spectra were corrected for the instrumental response. A preliminary study showed that the percentage error on efficiency measurements (from repeated measurements) is about 6%.

Sample excitation with a pulsed signal of constant frequency and variable pulse duration

This type of measurement has been performed on one set of Yb^{3+} , Er^{3+} co-doped samples (the results are presented in chapter 5, section 5.2.7) in order to understand how the excitation pulse duration affects the upconversion emission chromaticity. For the acquisition of near-infrared to visible upconversion emission spectra, the samples of interest were excited with the 977 nm output of a temperature-controlled cw laser diode (*Thorlabs*, L980P100 and TCLDM9) driven by a laser controller (*ILX-Lightwave* LDC-3742), and pulsed using a precision pulsed current source (*ILX Lightwave* LDP-3811). The upconversion emission spectra in the visible were recorded with a conventional set-up consisting of a monochromator (*Bentham* TMc 300-C, grating 1200 lines/mm blazed at 500 nm) and detected using a Si-photodiode (*Newport* Si 818-UV) via lock-in detection (*Signal recovery*, dual phase DSP 7265). Longpass and shortpass filters were used as appropriate (*Schott* RG

715, *Edmund Optics* NT47-819). All spectra have been corrected for the instrumental response.

4.5.2. Time-resolved spectroscopy

4.5.2.1. Background

Time-resolved spectroscopy is an important tool to study the dynamics of upconversion processes. Information such as radiative and non-radiative lifetimes of excited states can be obtained. In a typical time-resolved spectroscopy experiment, the sample of interest is excited with a pulsed or modulated excitation, and the evolution of the total luminescence is monitored as a function of the time following the pulse emission. A luminescence *transient* is recorded. The most important parameters describing the luminescence dynamics are the rise and decay times. By fitting the decay section of the transient associated with an emission line, the lifetime of the corresponding luminescence emitting level is obtained. The inverse of this lifetime is the probability of de-excitation per unit time of the state from which the emission arises.

The choice of the time-resolved measurement setup and methodology depend strongly on the typical timescale (e.g. ps, ns, μ s, ms, s, etc) of the process under study. As a general rule of thumb, the excitation pulse duration must be at least one or two orders of magnitude shorter than the typical timescale of the process under study. Time-resolved experiments are relatively easy to carry out when the typical durations of the processes under study are longer than hundreds of nanoseconds (as is the case for the samples described in this thesis). In this case, tunable optical parametric oscillators (OPO) can be used for sample excitation (or any other pulsed laser with short pulse emission and sufficient per pulse energy). Photomultiplier tubes (PMT) (combined with a monochromator) can also be used for luminescence transient detection as they have a sufficiently short response time (typically on the order of 3 ns). When performing time-resolved experiments under pulsed excitation, it is important to choose an excitation system with an adapted pulse repetition frequency to ensure the material under study relaxes completely between two excitation pulses.

4.5.2.2. Experimental setup for time-resolved spectroscopy experiments

Because of the Laporte-forbidden character of $4f-4f$ transitions, the excited states of lanthanide ions usually exhibit relatively long lifetimes (in the range 10 μs to 10 ms). Nanosecond pulsed lasers can therefore be used for sample excitation. The pulsed excitation source used must also have a low pulse repetition rate (e.g. 10 Hz) so that the electrons have enough time to relax from excited states to ground states between two excitation pulses. The setup used for luminescence lifetime measurements on upconversion samples is shown in Figure 4.3.

In a typical measurement, the pulsed emission (~ 7 ns, 10 Hz) of an optical parametric oscillator (OPO) (*Continuum Panther OPO*) pumped by the third harmonic ($\lambda = 355$ nm) of a Q-switched YAG:Nd laser (*Surelite I laser*) was used for excitation (excitation wavelength tunable from 410 nm to 1700 nm).

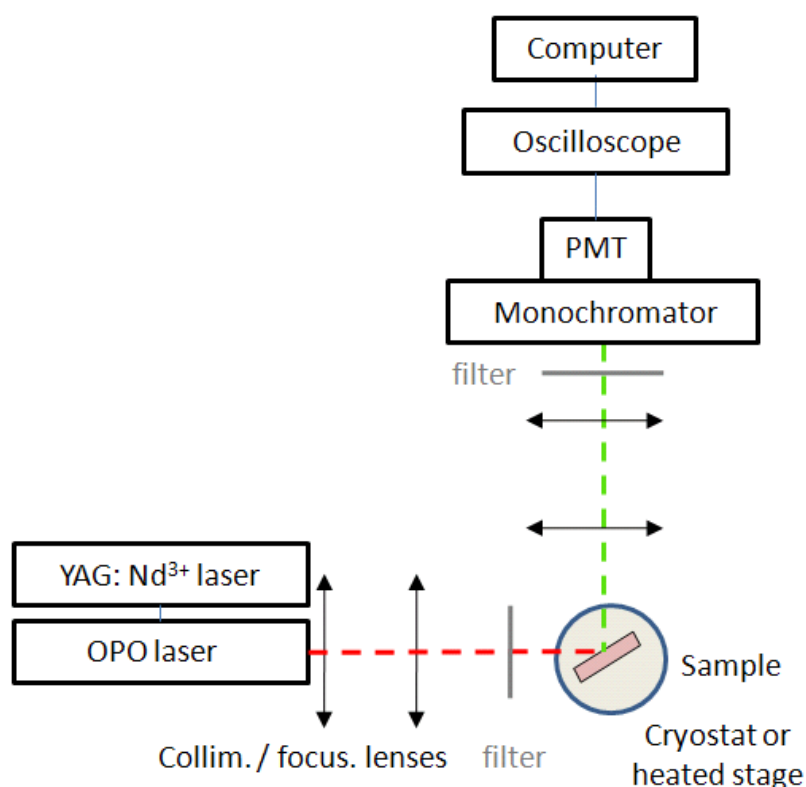


Figure 4.3: Schematic of the time-resolved spectroscopy setup used for lifetime measurements.

The luminescence emission (by upconversion or classical luminescence, depending on the measurements) from the sample was separated from the pump light using shortpass (*Edmund Optics*, Techspec series) or longpass (*Schott*, GG series) filters, and was then passed through a spectrometer (*Jobin Yvon*, *Triax 550*) and detected using a photomultiplier tube (PMT) detector (*Hamamatsu* R550) connected to a 500-MHz digital oscilloscope (*LeCroy*, 9350A). The transients were averaged 255 times to improve the signal to noise ratio. A continuous flow cryostat (*Oxford Instruments* Optistat and ITC) or a temperature-controlled heated stage (*Linkam* THMS600 and TMS94) were used for measurements at temperature below and above 293 K, respectively. The temperature could be varied from 80 K to 573 K.

4.5.3. Reflectance and absorbance spectroscopy

4.5.3.1. Background

Reflectance and absorbance spectroscopy are used to measure the intensity of light absorbed near the sample surface or in the bulk of the sample, as a function of wavelength. From these measurements, one can obtain the wavelengths and oscillator strengths associated with the transitions from the electronic ground states to the different excited states of the optically active dopants. While luminescence spectra only reveal the energy levels involved in light emission transitions, the absorbance and reflectance spectra reveal all the energy levels, whether they are involved in light emission or not. When the measurements are performed on powder samples, special care must be taken to collect the light, because powders scatter light. An integrating sphere is often used in such cases. For a powder sample, there are 2 main components contributing to the reflected light. The first fraction of light is deflected or scattered after being partially absorbed by the sample. It is diffuse due to scattering. The second fraction of light is totally reflected by the surface of the sample (i.e. specular reflection). The reflectance R of a powder material can be expressed as:

$$R = \frac{I}{I_0} \quad (\text{Eq. 4})$$

where I is the intensity of the reflected light and I_0 is the intensity of the incident light.

In the next section, we present the method used to measure absorbance and reflectance spectra on a sample that does not photoluminesce (under the excitation conditions used for

the absorbance or reflectance measurements). This is the case for the upconverting materials that will be described in chapters 5, 6, 7 and 8.

4.5.3.2. Experimental setup for reflectance measurements

A PerkinElmer Lambda 750 spectrometer equipped with an integrating sphere was used for the measurement of reflectance properties on the upconversion materials presented in this thesis (chapters 5, 6, 7 and 8). Two radiation sources were used: a deuterium lamp for excitation in the ultraviolet and a halogen lamp for excitation in the near-infrared and visible. A double-monochromator optical system guaranteed a high spectral purity of the incident light on the sample under study. Two detectors were used, a photomultiplier tube (PMT) for measurements in the ultraviolet and in the visible, and a lead sulphide (PbS) detector for the near-infrared. For measurements with powders, the sample of interest was positioned at the rear-face of an integrating sphere and illuminated with a beam of light. The light reflected from the sample surface was collected by the integrating sphere, and, by means of multiple diffuse reflections, a portion of this light was transferred to the detection system.

4.6. Summary

In this chapter, the experimental techniques used in this PhD work were presented. The syntheses of the materials were performed using high temperature solid-state chemistry or low temperature solution sol-gel routes (e.g. sol-gel Pechini). The materials obtained by solid-state reaction were shown to have significantly higher upconversion efficiencies than those resulting from liquid routes. As a result, it was decided to focus on the spectroscopic characterisation of the materials resulting from solid-state syntheses. The samples investigated in chapters 5, 6, 7 and 8 were all obtained via this synthesis route. X-ray diffraction analyses were performed in order to check the phase purity and good crystallinity of the materials. The dopant concentrations were measured using inductively coupled plasma-atomic emission spectroscopy. Most of the experimental work was devoted to the spectroscopic characterisation of the upconversion materials. Reflectance measurements were performed in order to access the dopant energy levels in our specific hosts (e.g. Y_2BaZnO_5 and $\text{Gd}_2\text{BaZnO}_5$). Steady-state upconversion emission spectra were acquired in order to access the upconversion emission wavelengths and intensities, and also to quantify precisely

upconversion efficiencies on samples containing various dopant concentrations. Finally, time-resolved spectroscopy techniques (luminescence transient acquisition for different dopant concentrations and at different temperatures) were essential in order to try and understand the specific upconversion mechanisms involved in our materials.

References

- ¹ E. Nakazawa, in *Phosphor Handbook*, ed. S. Shionoya and W. M. Yen, CRC Press, Boca Raton, 1999, ch. 2, p. 101.
- ² C. J. Brinker and G. W. Scherer, in *Sol-Gel Science: The Physics and Chemistry of Sol-Gel Processing*, Academic Press, London, 1990.
- ³ M. Yoshimura and J. Livage, *MRS Bull.*, 2000, **25**, 12.
- ⁴ J. Lin, M. Yu, C. Lin and X. Liu, *J. Phys. Chem. C*, 2007, **111**, 5835.
- ⁵ M. Kakihana and M. Yoshimura, *Bull. Chem. Soc. Jpn.*, 1999, **72**, 1427.
- ⁶ H. M. Rietveld, *J. Appl. Crystallogr.*, 1969, **2**, 65.
- ⁷ J. M. Mermet, *J. Anal. At. Spectrom.*, 2005, **20**, 11.
- ⁸ P. Liang, B. Hu, Z. C. Jiang, Y. C. Qin and T. Y. Peng, *J. Anal. At. Spectrom.*, 2001, **16**, 863.
- ⁹ M. I. Rucandio, *Fresenius J. Anal. Chem.*, 1997, **357**, 661.
- ¹⁰ R. Djingova and J. Ivanova, *Talanta*, 2001, **57**, 821.
- ¹¹ F. Vetrone, J. C. Boyer, J. A. Capobianco, A. Speghini and M. Bettinelli, *Appl. Phys. Lett.*, 2002, **80**, 1752.
- ¹² J. F. Suyver, J. Grimm, K. W. Krämer and H. U. Güdel, *J. Lumin.*, 2005, **114**, 53.
- ¹³ F. Auzel, *Chem. Rev.*, 2004, **104**, 139.
- ¹⁴ R. H. Page, K. I. Schaffers, P. A. Waide, J. B. Tassano, S. A. Payne, W. F. Krupke and W. K. Bischel, *J. Opt. Soc. Am. B*, 1998, **15**, 996.
- ¹⁵ R. S. Quimby, M. G. Drexhage and M. J. Suscavage, *Electron. Lett.*, 1987, **23**, 32.

CHAPTER 5: Oxide phosphors for efficient light upconversion; Yb^{3+} and Er^{3+} co-doped $\text{RE}_2\text{BaZnO}_5$ ($\text{RE} = \text{Y}, \text{Gd}$)

5.1. Introduction

As mentioned in chapter 1, the aim of this PhD work was to produce stable materials with high upconversion efficiencies, low excitation thresholds and good colour tunability properties under infrared excitation. The second aim was to gain an in-depth understanding of the dominant processes involved in the upconversion mechanisms of these materials. This PhD work has been mainly focused on the investigation of lanthanide-doped Y_2BaZnO_5 and $\text{Gd}_2\text{BaZnO}_5$ materials for green, red, blue and white upconversion under near-infrared excitation. Being oxides, these materials have good chemical, thermal and mechanical stabilities. $\text{RE}_2\text{BaZnO}_5$ ($\text{RE} = \text{Y}, \text{Gd}$) ternary oxide hosts were first reported by Raveau et al. in 1982.^{1,2} Since then, they have attracted attention for their interesting magnetic and optical properties. The optical properties of RE_2BaMO_5 ($\text{RE} = \text{Y}, \text{Gd}, \text{Er}$ and $\text{M} = \text{Cu}, \text{Zn}$) compounds have been investigated, mainly for their luminescence properties.³ Recently, Birkel et al.⁴ investigated for the first time the upconversion properties of $\text{Gd}_2\text{BaZnO}_5: \text{Yb}^{3+}, \text{Er}^{3+}$ and $\text{La}_2\text{BaZnO}_5: \text{Yb}^{3+}, \text{Er}^{3+}$ materials under continuous wave (cw) near-infrared excitation. They reported green and red emissions (with sometimes an additional weak emission in the blue) under cw ~ 980 nm excitation. They showed that the green and red emitting states were populated via a 2-photon process. The upconversion performances of their systems were not reported in their paper,⁴ but according to Birkel, the maximum upconversion efficiency they achieved was around 1.4% (the efficiency being defined as the ratio of the power emitted in the visible over the power absorbed in the infrared). No time-resolved luminescence investigation was performed, and therefore they could not elucidate the upconversion mechanisms specific to their systems.

In this chapter, the optical properties of Yb^{3+} and Er^{3+} co-doped $\text{RE}_2\text{BaZnO}_5$ ($\text{RE} = \text{Y}$ or Gd) materials, synthesised by solid-state reaction, are investigated in detail. Two main upconversion emission bands centred around 548 nm (green) and 673 nm (red) are observed under 977 nm laser excitation. Studies of the luminescence properties as a function of dopant concentration are described and relatively high infrared to visible upconversion efficiencies

of up to $\sim 5.2\%$ are obtained at room-temperature. Under cw excitation, the upconversion emission chromaticity can be varied by changing the concentrations of Yb^{3+} and Er^{3+} incorporated within the host lattice. Under pulsed 977 nm excitation (of constant pulse repetition rate) and for fixed dopant concentrations, we show that the upconversion emission chromaticity can also be varied by changing the excitation pulse duration. The results of power dependence studies and lifetime measurements are presented. This detailed study of the upconversion processes allows us to identify, for the first time, the dominant upconversion mechanisms in Yb^{3+} , Er^{3+} co-doped $\text{RE}_2\text{BaZnO}_5$ oxides ($\text{RE} = \text{Y}, \text{Gd}$).

5.2. Results

The outline of this result section is the following: in section 5.2.1, the crystal structure of $\text{RE}_2\text{BaZnO}_5: \text{Yb}^{3+}, \text{Er}^{3+}$ ($\text{RE} = \text{Y}, \text{Gd}$) materials is presented (for data acquisition, the methodology presented in chapter 4, section 4.3.2 was used). In section 5.2.2, the dopant concentrations are quantified precisely by inductively coupled plasma-atomic emission spectroscopy (see section 4.4.2 for methodology). All the dopant concentrations presented in this chapter are expressed in terms of molar percentages. Section 5.2.3 is devoted to the presentation of reflectance spectroscopy results, which provide information on the energy levels of the Er^{3+} and Yb^{3+} excited states (see section 4.5.3). Subsequently, the results of steady-state luminescence experiments are presented in sections 5.2.4 to 5.2.7 (see section 4.5.1 for methodology). The upconversion emission spectra were recorded on samples containing different dopant concentrations, and the upconversion efficiencies were calculated under cw near-infrared excitation. In sections 5.2.6 and 5.2.8, we present the results of incident power dependence studies (see section 4.5.1) and time-resolved luminescence studies (see section 4.5.2), respectively. The results of the spectroscopic measurements presented in section 5.2 will be combined in section 5.3 in order to propose a model for the upconversion mechanism.

5.2.1. Crystal structure

Figure 5.1 displays the typical powder X-ray diffraction patterns of *a*) $\text{Y}_2\text{BaZnO}_5: \text{Yb}^{3+}$ (7%), Er^{3+} (3%), and *b*) $\text{Gd}_2\text{BaZnO}_5: \text{Yb}^{3+}$ (7%), Er^{3+} (3%). Both crystal structures are

orthorhombic, space group Pnma . Relatively pure phases were obtained, as shown by the good quality of the Rietveld refinements (Figure 5.1).⁵

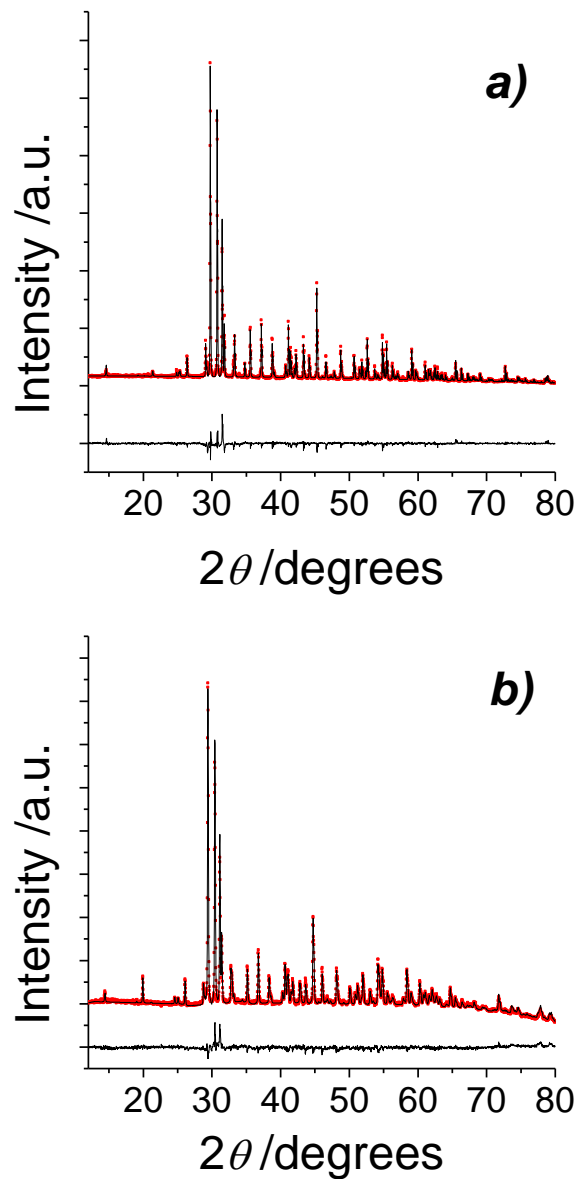


Figure 5.1: Rietveld refinements based upon powder X-ray diffraction patterns of a) $\text{Y}_2\text{BaZnO}_5: \text{Yb}^{3+}$ (7%), Er^{3+} (3%) and b) $\text{Gd}_2\text{BaZnO}_5: \text{Yb}^{3+}$ (7%), Er^{3+} (3%).

Cell parameters were obtained for both structures: a) $a = 12.3354(2)$ Å, $b = 5.70897(7)$ Å and $c = 7.06887(9)$ Å (ICDD 87082), and b) $a = 12.4861(4)$ Å, $b = 5.7713(2)$ Å and $c = 7.1720(2)$ Å (ICDD 88602). Note that the lattice parameters obtained in the doped samples are slightly smaller than those in the pure phases, which is attributed to the smaller ionic radii of Yb^{3+} (0.0925 nm) and Er^{3+} (0.0945 nm) compared to Y^{3+} (0.096 nm) and Gd^{3+} (0.100 nm).⁶

The basic structure of $\text{RE}_2\text{BaZnO}_5$ ($\text{RE} = \text{Y}, \text{Gd}$) compounds is presented in Figure 5.2. It consists of REO_7 , BaO_{11} and ZnO_5 polyhedra. RE^{3+} ions occupy two different 7-fold coordinated sites (with the same symmetry) inside a monocapped trigonal prism. Two such units share faces and form the basic structure of RE_2O_{11} dimers. Finally, these dimers are connected in 3 dimensions by sharing edges. In Y_2BaZnO_5 , the typical distance between two RE^{3+} neighbouring ions ranges from 3.3345(5) Å to 3.6522(5) Å (ICDD 87082). The Ba^{2+} ions reside in distorted 11-fold coordinated cages, and Zn^{2+} ions exhibit a distorted square-based pyramidal configuration. In $\text{RE}_2\text{BaZnO}_5$: Yb^{3+} , Er^{3+} doped compounds, Yb^{3+} and Er^{3+} ions substitute partially for RE^{3+} ions.

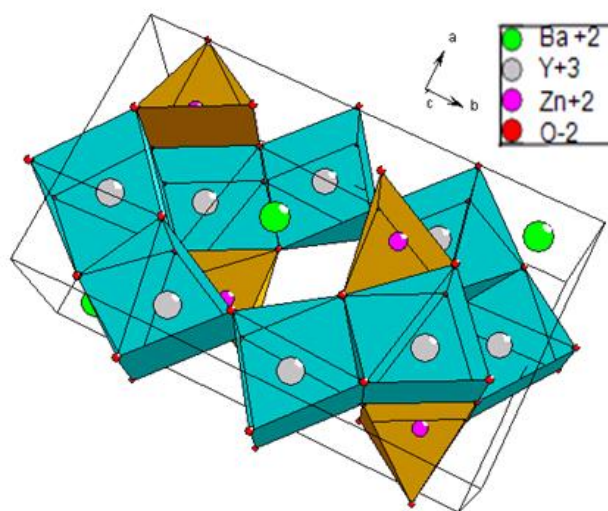


Figure 5.2: Crystal structure of $\text{RE}_2\text{BaZnO}_5$ ($\text{RE} = \text{Y}, \text{Gd}$).

5.2.2. Determination of dopant concentration

The Yb^{3+} and Er^{3+} concentrations in samples of nominal composition Y_2BaZnO_5 : Yb^{3+} (x%), Er^{3+} (y%) ($5 \leq x \leq 10$ and $1 \leq y \leq 5$) were measured by ICP-AES (Figure 5.3). The maximum percentage difference between the nominal dopant concentrations and the concentrations measured by ICP-AES was around 10%.

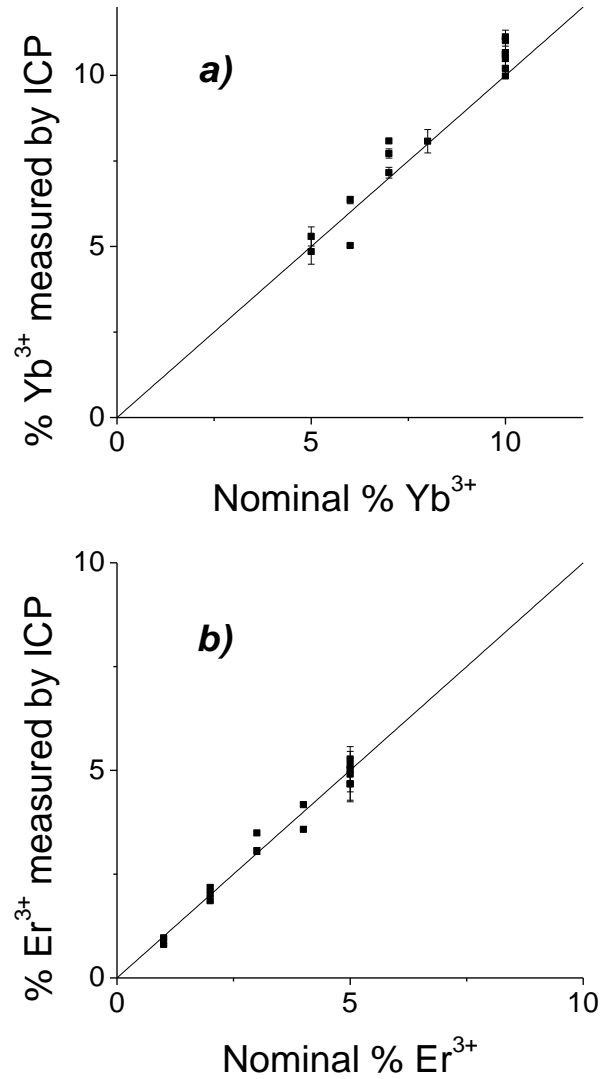


Figure 5.3: Dopant concentrations: comparison of the nominal values of the a) Yb^{3+} and b) Er^{3+} dopant concentrations with those measured by ICP-AES.

5.2.3. Reflectance in the infrared, visible and ultraviolet

A typical room-temperature reflectance spectrum of $\text{RE}_2\text{BaZnO}_5: \text{Yb}^{3+}, \text{Er}^{3+}$ ($\text{RE} = \text{Y}, \text{Gd}$) samples in the range 200-1700 nm is presented in Figure 5.4. A broad band due to the $\text{Yb}^{3+} {}^2\text{F}_{7/2} \rightarrow {}^2\text{F}_{5/2}$ absorption transition is observed in the 870-1040 nm region, and overlaps with the narrow $\text{Er}^{3+} {}^4\text{I}_{15/2} \rightarrow {}^4\text{I}_{11/2}$ absorption band around 977 nm. Under 977 nm excitation, both Yb^{3+} and Er^{3+} ions are therefore excited, but the absorption cross-section of Yb^{3+} is about one order of magnitude higher than that of Er^{3+} .⁷

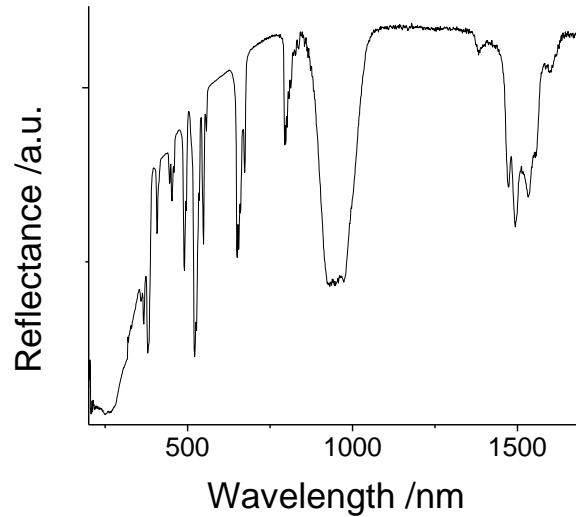


Figure 5.4: Room-temperature reflectance spectrum of $\text{Y}_2\text{BaZnO}_5: \text{Yb}^{3+}$ (7%), Er^{3+} (3%).

5.2.4. Upconversion luminescence emission

Under cw 977nm excitation at room-temperature, $\text{Y}_2\text{BaZnO}_5: \text{Yb}^{3+}, \text{Er}^{3+}$ powders yield greenish-orange emission, visible to the naked eye. Typical emission spectra (Figure 5.5a) show an intense emission corresponding to the $\text{Er}^{3+} {}^4\text{F}_{9/2} \rightarrow {}^4\text{I}_{15/2}$ electronic ($4f-4f$) transition at around 673 nm (red), and a weaker emission assigned to the $\text{Er}^{3+} ({}^4\text{S}_{3/2}, {}^2\text{H}_{11/2}) \rightarrow {}^4\text{I}_{15/2}$ transitions ($\text{Er}^{3+} {}^4\text{S}_{3/2}$ and $\text{Er}^{3+} {}^2\text{H}_{11/2}$ are thermalised levels) at around 514 and 548 nm (green) (see Figure 2.2, chapter 2 for the Er^{3+} energy diagram). Under 490 nm cw excitation, corresponding to the direct excitation of the above lying $\text{Er}^{3+} {}^4\text{F}_{7/2}$ level (see Figure 2.2, chapter 2), the red to green emission intensity ratio is closer to 1 (Figure 5.5b). In that case, the $\text{Er}^{3+} {}^4\text{F}_{9/2}$ level is populated by non-radiative relaxation from the ${}^4\text{S}_{3/2}$ and ${}^2\text{H}_{11/2}$ thermalised levels.

5.2.5. Concentration dependence of upconversion efficiencies

The upconversion emission intensity and spectral properties depend on dopant concentrations. In Figure 5.6, the emission spectra of four selected samples of the $\text{Y}_2\text{BaZnO}_5: \text{Yb}^{3+}$ (x%), Er^{3+} (10-x%) ($x = 2, 5, 6, 7$) family are presented under cw 977 nm excitation ($\sim 25.10^{-3} \text{ W/mm}^2$).

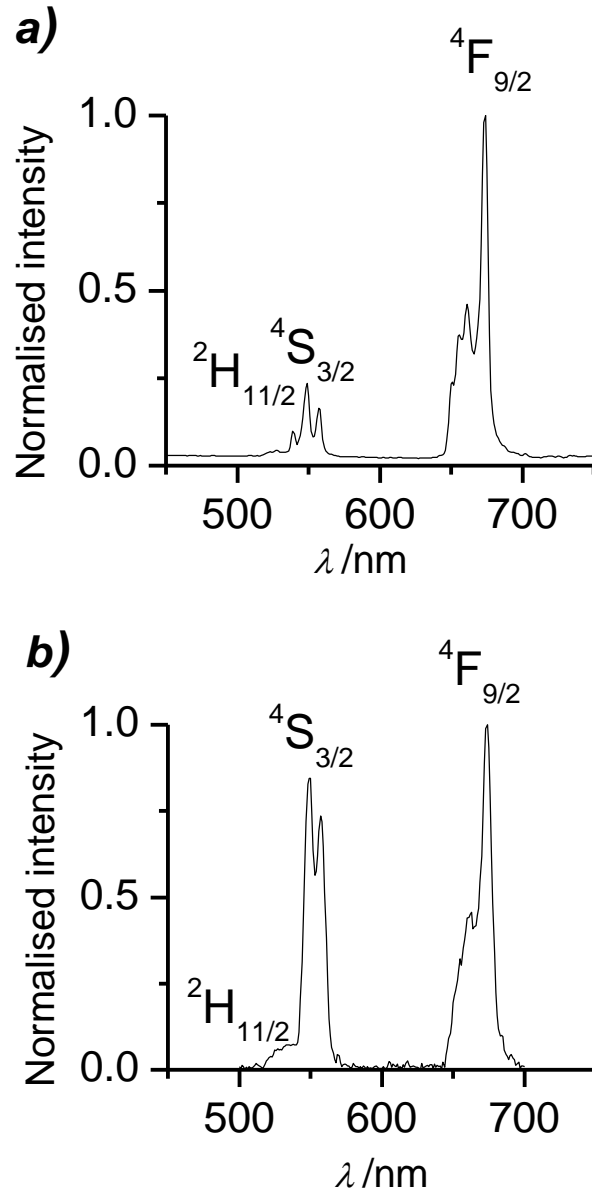


Figure 5.5: Typical luminescence spectra of $\text{Y}_2\text{BaZnO}_5:\text{Yb}^{3+}, \text{Er}^{3+}$ phosphors at room-temperature under a) 977 nm excitation, and b) 490 nm excitation. The emitting levels are assigned.

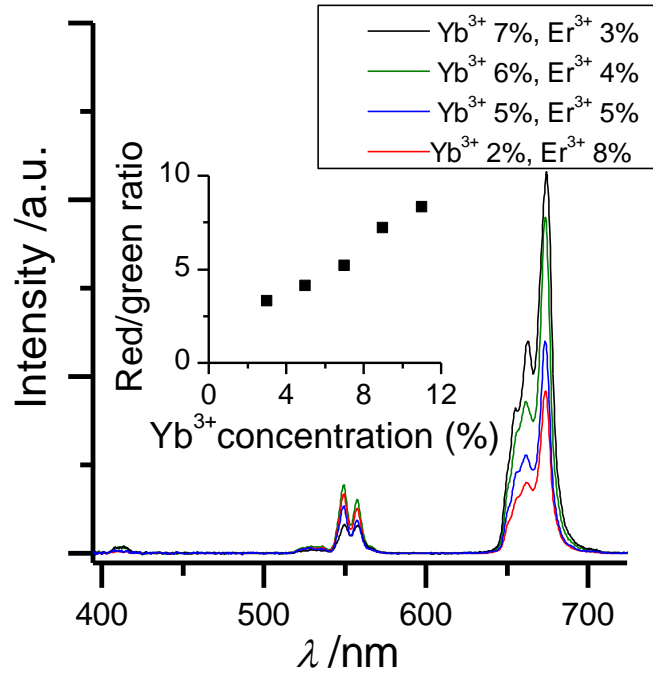


Figure 5.6: Upconversion luminescence spectra for selected samples of the $\text{Y}_2\text{BaZnO}_5: \text{Yb}^{3+} (x\%), \text{Er}^{3+} (10-x\%)$ ($x = 2, 5, 6, 7$) family at room-temperature under 977 nm excitation ($\sim 25 \cdot 10^{-3} \text{ W/mm}^2$). The inset presents the red to green emission intensity ratio for selected $\text{Y}_2\text{BaZnO}_5: \text{Yb}^{3+} (x\%), \text{Er}^{3+} (3\%)$ ($x = 3, 5, 7, 9, 11$) samples at room-temperature under 977 nm excitation ($\sim 25 \cdot 10^{-3} \text{ W/mm}^2$).

The red to green emission intensity ratio is seen to increase with the Yb^{3+} to Er^{3+} concentration ratio. The inset of Figure 5.6 shows the evolution of the red to green emission intensity ratio for five selected $\text{Y}_2\text{BaZnO}_5: \text{Yb}^{3+} (x\%), \text{Er}^{3+} (3\%)$ samples ($x = 3, 5, 7, 9, 11$), where the Er^{3+} concentration is fixed to 3% and the Yb^{3+} concentration varies from 3% to 11%, under 977 nm excitation ($\sim 25 \cdot 10^{-3} \text{ W/mm}^2$). The red to green intensity ratio is again seen to increase with the Yb^{3+} concentration. This concentration dependence of spectral emission properties indicates that the green and red level population mechanisms are different; in particular, the $\text{Er}^{3+} {}^4\text{F}_{9/2}$ red emitting level is not exclusively populated by non-radiative relaxation processes from the higher-lying ${}^4\text{S}_{3/2}$ and ${}^2\text{H}_{11/2}$ green emitting levels. Moreover, the increase of the red to green ratio with the Yb^{3+} concentration (at fixed concentration of Er^{3+}) suggests the existence of additional green level depopulation and/or red level population processes at higher Yb^{3+} concentrations. These results will be explained in a section 5.3.

The upconversion efficiencies of a variety of $Gd_2BaZnO_5: Yb^{3+}$ (x%), Er^{3+} (y%) samples ($0 \leq x, y \leq 10$) were measured at room-temperature under 977 nm excitation ($\sim 25 \cdot 10^{-3}$ W/mm² incident power density) (Figure 5.7). Three independent measurements were performed for each sample. The upconversion efficiency was calculated as the ratio of the upconverted emission in the 380-780 nm range over the power absorbed in the infrared (950-1000 nm range):

$$\eta_{UC} = \frac{P_{em}}{P_{abs}^{IR}} = \frac{P_{em}}{P_{inc}^{IR} - P_{not\ abs}^{IR}} \quad (\text{Eq. 1})$$

where P_{em} is the power of the upconversion light emitted in the 380-780 nm range, P_{abs}^{IR} is the power of the fraction of incident light that has been absorbed by the sample, P_{inc}^{IR} is the incident power in the near-infrared (integrated over the 950-1000 nm range) and $P_{not\ abs}^{IR}$ is the power of the fraction of incident light that has not been absorbed by the sample.

Samples containing between 3-4% of Er^{3+} , and total dopant concentrations (Yb^{3+} plus Er^{3+}) in the 10-13% range were shown to present the highest efficiencies for infrared to visible upconversion. A maximum upconversion efficiency of $5.2 \pm 0.2\%$ was obtained with $Gd_2BaZnO_5: Yb^{3+}$ (7%), Er^{3+} (3%) at room-temperature under 977 nm excitation ($\sim 25 \cdot 10^{-3}$ W/mm²). It is worth noting that very similar upconversion efficiency values and concentration dependence trends were measured on $Y_2BaZnO_5: Yb^{3+}$ (x%), Er^{3+} (y%) samples.

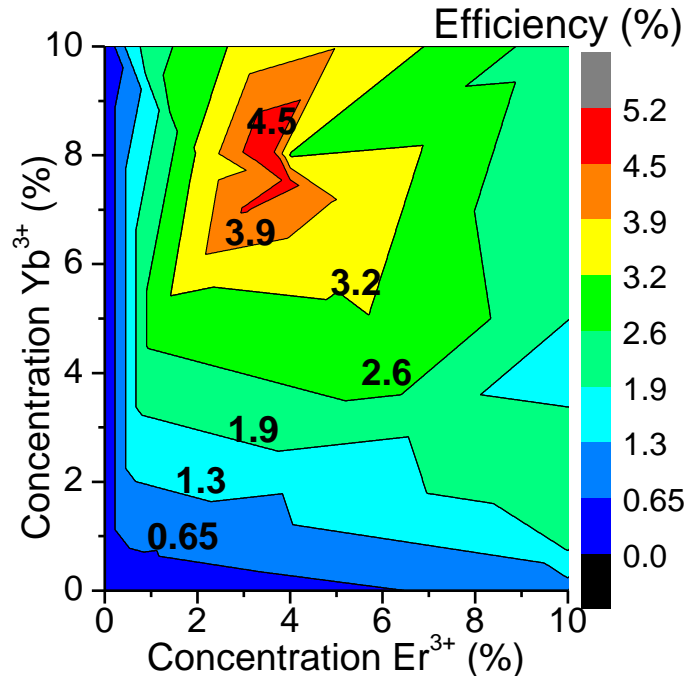


Figure 5.7: Room-temperature upconversion efficiencies as a function of dopant concentrations for a variety of $\text{Gd}_2\text{BaZnO}_5:\text{Yb}^{3+}, \text{Er}^{3+}$ samples under 977 nm excitation ($\sim 25 \cdot 10^{-3} \text{ W/mm}^2$ incident power density). The upconversion efficiency is expressed as the ratio of the upconverted emission in the range 380-780 nm over the power absorbed in the range 950-1000 nm. The colour bar on the right is used to display the UC efficiency values for each dopant composition. Contour lines (lines with the same upconversion efficiency value) and contour labels displaying the UC efficiencies associated to those contour lines are also included. The typical percentage error in efficiency measurements is around 6%.

5.2.6. Pump power dependence of upconversion emission

Pump power density dependences of the green $\text{Er}^{3+} ({}^4\text{S}_{3/2}, {}^2\text{H}_{11/2}) \rightarrow {}^4\text{I}_{15/2}$ and red $\text{Er}^{3+} {}^4\text{F}_{9/2} \rightarrow {}^4\text{I}_{15/2}$ emission powers were investigated at room-temperature under 977 nm excitation. Both green and red emission powers show a quadratic dependence on the excitation power in the low power regime, which confirms that two-photon steps are involved in the upconversion process (Figure 5.8). It is worth mentioning that for $\sim 25 \cdot 10^{-3} \text{ W/mm}^2$ excitation power densities, about half of the incident light is absorbed by the sample, i.e. $P_{abs}^{IR} \sim \frac{1}{2} P_{inc}^{IR}$.

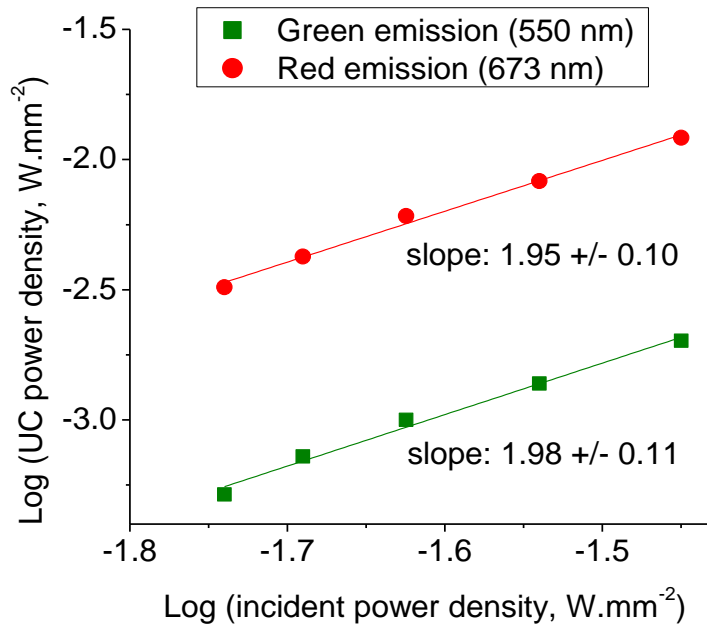


Figure 5.8: Pump power density dependence of the green Er^{3+} (${}^4\text{S}_{3/2}$, ${}^2\text{H}_{11/2}$) \rightarrow ${}^4\text{I}_{15/2}$ and red Er^{3+} ${}^4\text{F}_{9/2} \rightarrow$ ${}^4\text{I}_{15/2}$ emission powers at room-temperature under 977 nm excitation. The results are presented in a decadic double-logarithmic scale.

The rate equations describing the upconversion mechanism in $\text{RE}_2\text{BaZnO}_5:\text{Yb}^{3+}, \text{Er}^{3+}$ ($\text{RE} = \text{Y}, \text{Gd}$) were written, simplified and solved in the steady-state regime and at low incident power (Appendix A). A quadratic dependence was found between the green Er^{3+} (${}^4\text{S}_{3/2}$, ${}^2\text{H}_{11/2}$) and red Er^{3+} ${}^4\text{F}_{9/2}$ emitting level populations and the incident pump power. Since upconversion emission powers are proportional to the population densities of the emitting levels, the experimental power dependence results are in good agreement with the theoretical predictions.

5.2.7. Colour tunability with excitation pulse duration

In this experiment, a $\text{Gd}_2\text{BaZnO}_5:\text{Yb}^{3+}$ (7%), Er^{3+} (3%) sample was excited at 977 nm with a 154 Hz pulsed radiation (corresponding to a fixed pulse repetition period of 6.5 ms), where the pulse duration P_d was varied from 50 μs to 4000 μs using a precision pulsed current source. The pulse repetition frequency was set to a relatively low frequency (154 Hz) for the system under study to have enough time to relax completely from excited states to ground

states between two excitation pulses. Figure 5.9 displays the red to green emission intensity ratio as a function of P_d . The inset of Figure 5.9 presents the evolution of the green and red emission intensities as a function of P_d . As can be seen in the inset, the red and green emission intensities increase continuously by lengthening the pulse duration. A variation of the emission colour (called *chromaticity*) from green to reddish-orange is observed with increasing P_d .

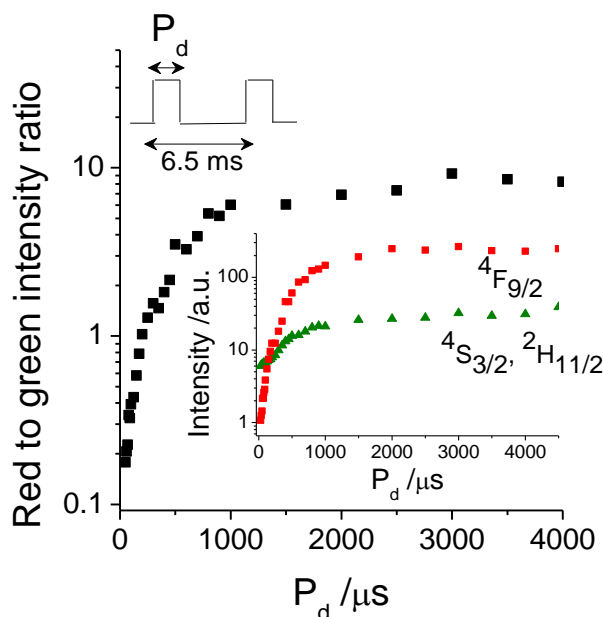


Figure 5.9: Variation of the red to green emission intensity ratio with the excitation pulse duration, P_d . The values of P_d range from $50 \mu\text{s}$ to $4000 \mu\text{s}$. The pulse amplitude and repetition rate are constant (154 Hz repetition rate, i.e. 6.5 ms between two successive pulses). The individual variations of the red and green emission intensities with P_d are presented in the inset. The emission intensities and intensity ratio are presented on a decadic log scale.

In a separate experiment, the rise times of the Er^{3+} ($^4\text{S}_{3/2}$, $^2\text{H}_{11/2}$) and Er^{3+} $^4\text{F}_{9/2}$ green and red emitting levels were measured under 7-ns pulsed 977 nm excitation (using an optical parametric oscillator OPO for sample excitation). The green level was shown to build up faster than the red one ($38 \mu\text{s}$ and $60 \mu\text{s}$ rise times, respectively). These results confirm that the green and red emitting levels are populated via two different routes. Note that the quadratic dependence of both the green and red emission powers with the incident power (Figure 5.8) guarantees the invariance of chromaticity, irrespective of the excitation power.

5.2.8. Lifetime measurements

The temporal evolution of the Er^{3+} ($^4\text{S}_{3/2}$, $^2\text{H}_{11/2}$) \rightarrow $^4\text{I}_{15/2}$ (green), Er^{3+} $^4\text{F}_{9/2} \rightarrow$ $^4\text{I}_{15/2}$ (red), Er^{3+} $^4\text{I}_{11/2} \rightarrow$ $^4\text{I}_{15/2}$, Er^{3+} $^4\text{I}_{13/2} \rightarrow$ $^4\text{I}_{15/2}$ and Yb^{3+} $^2\text{F}_{5/2} \rightarrow$ $^2\text{F}_{7/2}$ transitions in Y_2BaZnO_5 : Yb^{3+} (7%), Er^{3+} (3%) were recorded under pulsed 490 nm (direct excitation of Er^{3+} $^4\text{F}_{7/2}$), 808 nm (direct excitation of Er^{3+} $^4\text{I}_{9/2}$), 977 nm (direct excitation of Yb^{3+} $^2\text{F}_{5/2}$ and Er^{3+} $^4\text{I}_{11/2}$), and 890 nm (direct excitation of Yb^{3+} $^2\text{F}_{5/2}$) excitations, respectively. It is worth noting that unlike ytterbium, Er^{3+} does not absorb at 890 nm, which guarantees a selective excitation of Yb^{3+} under 890 nm excitation.

Intrinsic lifetimes under direct excitation

The intrinsic lifetimes of the Er^{3+} ($^4\text{S}_{3/2}$, $^2\text{H}_{11/2}$), $^4\text{F}_{9/2}$, $^4\text{I}_{11/2}$ and $^4\text{I}_{13/2}$ states under direct excitation were measured to be 80 ± 4 μs , 92 ± 5 μs , 314 ± 16 μs and 2.72 ± 0.14 ms, respectively, while the Yb^{3+} $^2\text{F}_{5/2}$ level had a lifetime of 735 ± 37 μs .

Lifetimes under upconversion excitation (977 nm)

The temporal evolution of the Er^{3+} ($^4\text{S}_{3/2}$, $^2\text{H}_{11/2}$) \rightarrow $^4\text{I}_{15/2}$ (green) and Er^{3+} $^4\text{F}_{9/2} \rightarrow$ $^4\text{I}_{15/2}$ (red) transitions were also recorded under 7-ns pulsed upconversion excitation at 977 nm, and are presented in Figure 5.10. At the end of the excitation pulse ($t \sim 7$ ns), no luminescence emission by Er^{3+} $^4\text{F}_{9/2}$ is observed; instead, the transient exhibits a typical (delayed) rise and a decay part. This is a clear fingerprint of an energy transfer process (see chapter 3, section 3.5). The Er^{3+} ($^4\text{S}_{3/2}$, $^2\text{H}_{11/2}$) \rightarrow $^4\text{I}_{15/2}$ transient, in contrast, has an instantaneous rise during the excitation pulse in addition to a delayed rise after the end of the excitation pulse, showing that both excited state absorption (ESA) and energy-transfer upconversion (ETU) processes are involved in the Er^{3+} ($^4\text{S}_{3/2}$, $^2\text{H}_{11/2}$) green level population. The experimental intensity data obtained under 977 nm excitation were fitted to:⁸

$$I(t) = A \left(1 - e^{-\frac{t}{\tau_r}} \right) \left(e^{-\frac{t}{\tau_d}} \right) \quad (\text{Eq. 2})$$

Where A is the intensity factor, and τ_r and τ_d represent the rise and decay times of the transient, respectively and are related to the transfer rate constants between Yb^{3+} and Er^{3+} and to the intrinsic lifetimes of the levels involved.⁸

The best fit for the $\text{Er}^{3+} \ ^4\text{F}_{9/2} \rightarrow \ ^4\text{I}_{15/2}$ transient under 977 nm excitation corresponds to $\tau_r = 60 \pm 3 \ \mu\text{s}$ and $\tau_d = 190 \pm 10 \ \mu\text{s}$. The rise and decay times of the $\text{Er}^{3+} (\ ^4\text{S}_{3/2}, \ ^2\text{H}_{11/2}) \rightarrow \ ^4\text{I}_{15/2}$ emission under 977 nm excitation are of $38 \pm 2 \ \mu\text{s}$ and $169 \pm 8 \ \mu\text{s}$, respectively.

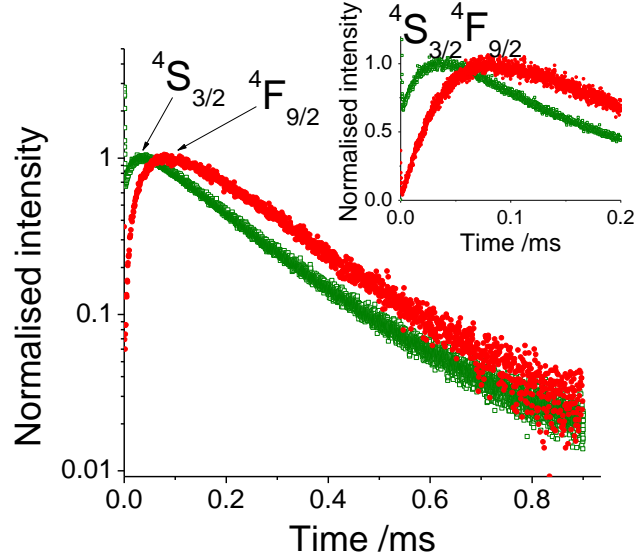


Figure 5.10: Temporal evolution of the green $\text{Er}^{3+} (\ ^4\text{S}_{3/2}, \ ^2\text{H}_{11/2})$ and red $\text{Er}^{3+} \ ^4\text{F}_{9/2}$ level emission intensities under pulsed 977 nm excitation. The normalised intensity is presented on a decadic log scale. The inset plots the intensity data on a linear scale. An optical parametric oscillator (OPO) was used for sample excitation, providing 7-ns pulses with a 10 Hz repetition rate.

Lifetime measurements were also performed on a Yb^{3+} -free $\text{Y}_2\text{BaZnO}_5: \text{Er}^{3+}$ (10%) sample where upconversion can only happen by ground state absorption/excited state absorption (GSA/ESA) (no energy transfer upconversion). Under 977 nm excitation, the lifetimes of the $\text{Er}^{3+} (\ ^4\text{S}_{3/2}, \ ^2\text{H}_{11/2})$ and $\text{Er}^{3+} \ ^4\text{F}_{9/2}$ green and red emitting levels were measured to be $539 \pm 27 \ \mu\text{s}$ and $1.23 \pm 0.06 \ \text{ms}$, respectively.

In $\text{Y}_2\text{BaZnO}_5: \text{Yb}^{3+}$ (7%), Er^{3+} (3%), the lifetimes associated with the green and red light emitting levels (under 977 nm excitation) are much shorter than those measured in the Yb^{3+} -free sample. This confirms the predominance of energy transfer in the depopulation mechanism of the upconversion emitting levels.

Finally, in the Yb^{3+} , Er^{3+} co-doped samples, the lifetimes measured under 977 nm excitation are longer than those obtained under direct 490 nm excitation. Given the relatively long Yb^{3+}

excited state lifetimes and the short Er^{3+} emitting level intrinsic lifetimes in the investigated samples, these results suggest that the upconversion emitting level lifetimes are dominated by energy transfer dynamics between Yb^{3+} and Er^{3+} (and not by the intrinsic lifetimes of Er^{3+}).⁹

5.3. Discussion

Before we propose a model for the dominant mechanisms governing upconversion emission in $\text{RE}_2\text{BaZnO}_5: \text{Yb}^{3+}, \text{Er}^{3+}$ ($\text{RE} = \text{Y}, \text{Gd}$), we summarise the key findings presented in section 5.2:

- i) The green and red emissions are assigned to the Er^{3+} ($^4\text{S}_{3/2}, ^2\text{H}_{11/2}$) \rightarrow $^4\text{I}_{15/2}$ and Er^{3+} $^4\text{F}_{9/2} \rightarrow ^4\text{I}_{15/2}$ transitions, respectively
- ii) The green and red emissions are 2-photon processes (Figure 5.8)
- iii) There are two different routes involved in the population mechanisms of the green Er^{3+} ($^4\text{S}_{3/2}, ^2\text{H}_{11/2}$) and red Er^{3+} $^4\text{F}_{9/2}$ upconversion emitting levels (Figure 5.6, Figure 5.9, Figure 5.10)
- iv) There is a small contribution of the non-radiative Er^{3+} ($^4\text{S}_{3/2}, ^2\text{H}_{11/2}$) \rightarrow $^4\text{F}_{9/2}$ relaxation to the population of the Er^{3+} $^4\text{F}_{9/2}$ red emitting level (Figure 5.5b)
- v) The red to green emission intensity ratio increases with increasing Yb^{3+} concentration at fixed Er^{3+} concentration (Figure 5.6)

Observation iii) suggests that two different intermediate levels of Er^{3+} are involved in the upconversion mechanisms populating the green Er^{3+} ($^4\text{S}_{3/2}, ^2\text{H}_{11/2}$) and red Er^{3+} $^4\text{F}_{9/2}$ emitting levels. For energy matching conditions, the second Yb^{3+} to Er^{3+} energy transfer populating the Er^{3+} ($^4\text{S}_{3/2}, ^2\text{H}_{11/2}$) thermalised green emitting levels, necessarily involves the $^4\text{I}_{11/2}$ intermediate level: $\text{Yb}^{3+} \ ^2\text{F}_{5/2} + \text{Er}^{3+} \ ^4\text{I}_{11/2} \rightarrow \text{Yb}^{3+} \ ^2\text{F}_{7/2} + \text{Er}^{3+} \ ^4\text{F}_{7/2}$ (Er^{3+}) (Figure 5.11). According to our experimental results, the intermediate level involved in the red level population mechanism is different from $^4\text{I}_{11/2}$. For favourable energy matching, the red level population route must therefore involve the $^4\text{I}_{13/2}$ intermediary level, via the following Yb^{3+} to Er^{3+} energy transfer: $\text{Yb}^{3+} \ ^2\text{F}_{5/2} + \text{Er}^{3+} \ ^4\text{I}_{13/2} \rightarrow \text{Yb}^{3+} \ ^2\text{F}_{7/2} + \text{Er}^{3+} \ ^4\text{F}_{9/2}$. Note that the $^4\text{I}_{13/2}$ level

is populated by non-radiative relaxation from the upper lying $^4\text{I}_{11/2}$ level (Figure 5.11). As seen in the previous section, the intrinsic lifetime of the $^4\text{I}_{13/2}$ level is much longer than that of $^4\text{I}_{11/2}$ (2.72 ms versus 314 μs), which makes the $\text{Yb}^{3+} \ ^2\text{F}_{5/2} + \text{Er}^{3+} \ ^4\text{I}_{13/2} \rightarrow \text{Yb}^{3+} \ ^2\text{F}_{7/2} + \text{Er}^{3+} \ ^4\text{F}_{9/2}$ energy transfer (populating directly the red emitting level $\text{Er}^{3+} \ ^4\text{F}_{9/2}$) more favourable than the $\text{Yb}^{3+} \ ^2\text{F}_{5/2} + \text{Er}^{3+} \ ^4\text{I}_{11/2} \rightarrow \text{Yb}^{3+} \ ^2\text{F}_{7/2} + \text{Er}^{3+} \ ^4\text{F}_{7/2}$ energy transfer (populating the green emitting level after $\text{Er}^{3+} \ ^4\text{F}_{7/2} \rightarrow (^4\text{S}_{3/2}, ^2\text{H}_{11/2})$ multiphonon relaxation). This explains the high red to green emission intensity ratios observed in these materials when excited at 977 nm (Figure 5.5a, Figure 5.6).

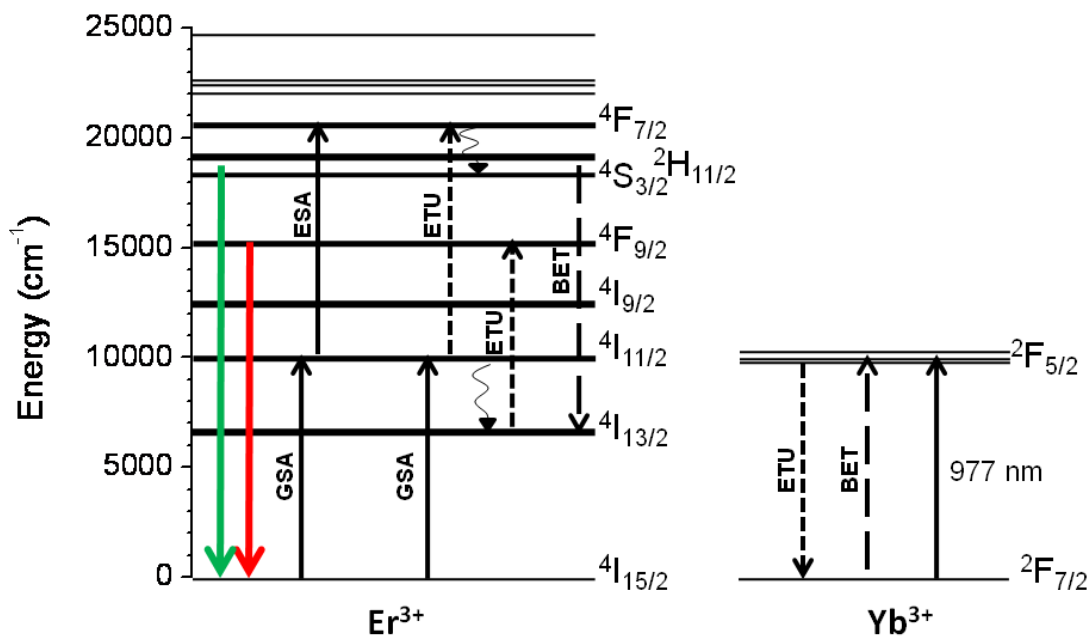


Figure 5.11: Simplified energy level diagram of Er^{3+} and Yb^{3+} ions and the dominant upconversion mechanisms in $\text{RE}_2\text{BaZnO}_5:\text{Yb}^{3+}, \text{Er}^{3+}$ ($\text{RE} = \text{Y}, \text{Gd}$). Radiative processes of ground state absorption (GSA), excited state absorption (ESA) and green and red luminescence, as well as non-radiative energy transfer upconversion (ETU), back energy transfer (BET) and multiphonon relaxation processes are represented.

The variation in chromaticity observed as the excitation pulse duration P_d is increased (Figure 5.9) is related to the temporal nature of the various energy level populations involved in the excitation and emission process. These are dominated by the $\text{Er}^{3+} \ ^4\text{I}_{11/2}$ energy level which has a lifetime of $\sim 314 \mu\text{s}$ and controls the intensity of red emission observed via the

competing rate for non-radiative relaxation to the ${}^4\text{I}_{13/2}$ level, radiative emission, further excitation via ETU or ESA to the $\text{Er}^{3+} {}^4\text{F}_{7/2}$ level and energy transfer to Yb^{3+} . Under steady-state conditions, corresponding to the population density of the ${}^4\text{I}_{11/2}$ energy level remaining unchanged, no variation in chromaticity should be observed. This is indeed the case for excitation pulses longer than ~ 1 ms (Figure 5.9). For very short excitation pulses, the green emission dominates (inset of Figure 5.9) indicating that the ETU and/or ESA rates (populating $\text{Er}^{3+} {}^4\text{F}_{7/2}$) are larger than non-radiative $\text{Er}^{3+} {}^4\text{I}_{11/2} \rightarrow {}^4\text{I}_{13/2}$ relaxation rates (populating $\text{Er}^{3+} {}^4\text{I}_{13/2}$). Close inspection of the inset of Figure 5.9 reveals that this remains the case until pulse widths of greater than ~ 150 μs are used. It is also of note that the increase of the green emission intensity with the excitation pulse duration is rather limited (the emission intensity measured at $P_d = 4000$ μs is only ~ 4 times higher than that measured at $P_d = 50$ μs), whereas the red emission intensity increases by more than 2 orders of magnitude. Interestingly the emission lifetimes of the red and green fluorescence are similar (92 and 80 μs respectively). The difference in emission intensities is therefore not related to a significant variation in their emission rates. A possible explanation of this relates to the fast population of the long-lived ${}^4\text{I}_{13/2}$ level by multiphonon relaxation from ${}^4\text{I}_{11/2}$. This is related to the relatively high phonon energy of the host (around 966 cm^{-1} according to our Raman studies). Once the $\text{Er}^{3+} {}^4\text{I}_{13/2}$ energy level is populated by multiphonon relaxation from $\text{Er}^{3+} {}^4\text{I}_{11/2}$, it undergoes ETU with the consequence of populating the $\text{Er}^{3+} {}^4\text{F}_{9/2}$ red-emitting level and further reducing the population density of excited Yb^{3+} ions; this will then impact on the probability of ETU from the ${}^4\text{I}_{11/2}$ state. To confirm our hypothesis, a full study of the excited state dynamics is required along with temporal modeling.

The dominant mechanisms likely to govern the upconversion emission in Y_2BaZnO_5 : Yb^{3+} (7%), Er^{3+} (3%) are summarised in Figure 5.11. Under 977 nm excitation, both Yb^{3+} and Er^{3+} absorb the incident radiation, so that the ${}^4\text{I}_{11/2}$ level of Er^{3+} can be populated via two different routes. Owing to the high absorption cross-section of Yb^{3+} under 977 nm excitation and the high Yb^{3+} to Er^{3+} transfer probability, the main population route of the $\text{Er}^{3+} {}^4\text{I}_{11/2}$ level involves an energy transfer between Yb^{3+} and Er^{3+} , as follows: $\text{Yb}^{3+} {}^2\text{F}_{5/2} + \text{Er}^{3+} {}^4\text{I}_{15/2} \rightarrow \text{Yb}^{3+} {}^2\text{F}_{7/2} + \text{Er}^{3+} {}^4\text{I}_{11/2}$. The second route, less likely due to the lower absorption cross-section of Er^{3+} , involves a ground-state absorption (GSA) of Er^{3+} (without any Yb^{3+} assistance): $\text{Er}^{3+} {}^4\text{I}_{15/2} + h\nu \rightarrow \text{Er}^{3+} {}^4\text{I}_{11/2}$. From the ${}^4\text{I}_{11/2}$ level of Er^{3+} , the ${}^4\text{F}_{7/2}$ level is populated by a second ET: $\text{Yb}^{3+} {}^2\text{F}_{5/2} + \text{Er}^{3+} {}^4\text{I}_{11/2} \rightarrow \text{Yb}^{3+} {}^2\text{F}_{7/2} + \text{Er}^{3+} {}^4\text{F}_{7/2}$, and in a lower measure, by an excited state absorption (ESA) of $\text{Er}^{3+} {}^4\text{I}_{11/2}$: $\text{Er}^{3+} {}^4\text{I}_{11/2} (\text{Er}^{3+}) + h\nu \rightarrow {}^4\text{F}_{7/2} (\text{Er}^{3+})$. The

electrons in the $\text{Er}^{3+} {}^4\text{F}_{7/2}$ level then relax rapidly and non-radiatively to the ${}^2\text{H}_{11/2}$ and ${}^4\text{S}_{3/2}$ thermalised levels due to the small energy gap to these lower-lying levels. The above processes then produce the two ${}^2\text{H}_{11/2} \rightarrow {}^4\text{I}_{15/2}$ and ${}^4\text{S}_{3/2} \rightarrow {}^4\text{I}_{15/2}$ green emission bands centered at 514 and 548 nm, respectively. The red emitting level is populated mostly by energy transfer from Yb^{3+} to Er^{3+} : $\text{Yb}^{3+} {}^2\text{F}_{5/2} + \text{Er}^{3+} {}^4\text{I}_{13/2} \rightarrow \text{Yb}^{3+} {}^2\text{F}_{7/2} + \text{Er}^{3+} {}^4\text{F}_{9/2}$ but also by multiphonon relaxation from ${}^4\text{S}_{3/2}$ and ${}^2\text{H}_{11/2}$.

The room-temperature intrinsic lifetimes of the three intermediary levels involved in the upconversion mechanisms are rather long: 314 μs (for $\text{Er}^{3+} {}^4\text{I}_{11/2}$), 735 μs (for $\text{Yb}^{3+} {}^2\text{F}_{5/2}$) and 2.72 ms (for $\text{Er}^{3+} {}^4\text{I}_{13/2}$), which increases the chances of a second $\text{Yb}^{3+} {}^2\text{F}_{5/2}$ to $\text{Er}^{3+} {}^4\text{I}_{13/2}$ or $\text{Yb}^{3+} {}^2\text{F}_{5/2}$ to $\text{Er}^{3+} {}^4\text{I}_{11/2}$ energy transfer. These second energy transfers are necessary for upconversion light generation. The lifetimes of the green and red emitting levels under 977 nm excitation are close to 170 μs and 190 μs , respectively. These values are comparable with those measured in $\text{NaYF}_4: \text{Yb}^{3+}, \text{Er}^{3+}$.¹⁰

5.4. Conclusions

The upconversion properties of $\text{RE}_2\text{BaZnO}_5: \text{Yb}^{3+}, \text{Er}^{3+}$ ($\text{RE} = \text{Y}, \text{Gd}$) oxide materials were investigated. We believe that the high upconversion efficiencies obtained at room-temperature ($> 5\%$) are the highest reported ones to date for an oxide phosphor. Page et al.¹¹ performed quantitative upconversion efficiency measurements on a variety of $\text{Yb}^{3+}, \text{Er}^{3+}$ co-doped hosts, including NaYF_4 , $\text{Y}_2\text{O}_2\text{S}$ and Y_2O_3 . The most efficient upconversion material they investigated was a $\text{NaYF}_4: \text{Yb}^{3+}$ (18%), Er^{3+} (2%) powder sample for which they reported an efficiency of 4%. The most efficient oxide was $\text{Y}_2\text{O}_3: \text{Yb}^{3+}$ (8%), Er^{3+} (6%) with an efficiency of 1%. In this chapter, we showed that $\text{Y}_2\text{BaZnO}_5: \text{Yb}^{3+}, \text{Er}^{3+}$ phosphors exhibit interesting colour tunability properties when varying the excitation pulse duration. Power dependence studies and lifetime measurements provided an accurate model for the upconversion mechanisms involved in these materials.

The majority of results reported in this chapter formed the basis of a publication:

Oxide phosphors for efficient light upconversion: Yb^{3+} and Er^{3+} co-doped $\text{RE}_2\text{BaZnO}_5$ ($\text{RE} = \text{Y}, \text{Gd}$), I. Etchart, A. Huignard, M. Bérard, M. N. Nordin, I. Hernández, R. J. Curry, W. P. Gillin and A. K. Cheetham, *J. Mater. Chem.*, 2010, **20**, 3989.

References

- ¹ C. Michel and B. Raveau, *J. Solid State Chem.*, 1982, **43**, 73.
- ² C. Michel and B. Raveau, *J. Solid State Chem.*, 1983, **49**, 150.
- ³ G. K. Cruz, H. C. Basso, M. C. Terrile and R. A. Carvalho, *J. Lumin.*, 2000, **86**, 155.
- ⁴ A. Birkel, A. A. Mikhailovsky and A. K. Cheetham, *Chem. Phys. Lett.*, 2009, **477**, 325.
- ⁵ H. M. Rietveld, *J. Appl. Crystallogr.*, 1969, **2**, 65.
- ⁶ R. D. Shannon and C. T. Prewitt, *Acta Crystallogr.*, 1969, **B25**, 925.
- ⁷ T. Xu, X. Shen, Q. Nie and Y. Gao, *Opt. Mater.*, 2006, **28**, 241.
- ⁸ R. Buisson and J. C. Vial, *J. Phys. Lett.*, 1981, **42**, L115.
- ⁹ F. Vetrone, J. C. Boyer, J. A. Capobianco, A. Speghini and M. Bettinelli, *Appl. Phys. Lett.*, 2002, **80**, 1752.
- ¹⁰ J. F. Suyver, J. Grimm, M. K. van Veen, D. Biner, K. W. Krämer and H. U. Güdel, *J. Lumin.*, 2006, **117**, 1.
- ¹¹ R. H. Page, K. I. Schaffers, P. A. Waide, J. B. Tassano, S. A. Payne, W. F. Krupke and W. K. Bischel, *J. Opt. Soc. Am. B*, 1998, **15**, 996.

CHAPTER 6: Efficient oxide phosphors for light upconversion; green emission from Yb^{3+} and Ho^{3+} co-doped $\text{RE}_2\text{BaZnO}_5$ ($\text{RE} = \text{Y}, \text{Gd}$)

6.1. Introduction

We will now focus on the investigation of $\text{RE}_2\text{BaZnO}_5: \text{Yb}^{3+}, \text{Ho}^{3+}$ ($\text{RE} = \text{Y}, \text{Gd}$) phosphors synthesised by solid-state reaction. The goal of this work was to produce an efficient green emitting phosphor under near-infrared excitation, and to gain an in-depth understanding of the upconversion mechanisms involved. Ho^{3+} is an excellent dopant for infrared to green upconversion because of its favourable intra-atomic $4f$ energy level structure (see Figure 2.2, chapter 2). Upconversion properties of singly-doped Ho^{3+} have been widely reported under 650 nm,¹⁻³ 750 nm⁴⁻⁷ and 875 nm^{8,9} excitations, usually with poor upconversion performances. Higher upconversion efficiencies have been achieved in materials co-doped with Yb^{3+} and Ho^{3+} , where Yb^{3+} acts as a sensitizer for Ho^{3+} owing to its strong absorption around 980 nm.^{10,11} The literature on $\text{Yb}^{3+}, \text{Ho}^{3+}$ co-doped materials is quite limited (compared to that on $\text{Yb}^{3+}, \text{Er}^{3+}$ systems). Oxide materials have been reported to be suitable hosts for Ho^{3+} upconversion.^{12,13}

In this chapter, we report, for the first time, the upconversion properties of $\text{RE}_2\text{BaZnO}_5: \text{Yb}^{3+}, \text{Ho}^{3+}$ ($\text{RE} = \text{Y}, \text{Gd}$) green emitting upconversion phosphors. We show that, by optimising dopant concentrations, bright green upconversion luminescence can be achieved, with a relatively high efficiency of up to 2.6%. The luminescence mechanisms are elucidated through power dependence studies and temperature-dependant lifetime measurements on samples with different dopant concentrations.

6.2. Results

The outline of this result section is the following: in section 6.2.1, the crystal structure of Yb^{3+} and Ho^{3+} co-doped Y_2BaZnO_5 materials is presented (for data acquisition, the methodology presented in chapter 4, section 4.3.2 was used). Section 6.2.2 is devoted to the

presentation of reflectance spectroscopy results which provide information on the energies of the Ho^{3+} and Yb^{3+} excited states in Y_2BaZnO_5 (see section 4.5.3). Subsequently, the results of steady-state luminescence experiments are presented in sections 6.2.3 to 6.2.5 (see section 4.5.1). The upconversion emission spectra were recorded on samples containing different dopant concentrations, and the upconversion efficiencies were quantified under near-infrared excitation. Note that all the dopant concentrations presented in this chapter are expressed in terms of molar percentages. In sections 6.2.5 and 6.2.6, we present the results of incident power dependence studies (see section 4.5.1) and time-resolved luminescence measurements (see section 4.5.2), respectively. Because Yb^{3+} to Ho^{3+} energy transfers are non-resonant (unlike Yb^{3+} to Er^{3+} energy transfers) (see Figure 2.2, chapter 2), the rates of the energy transfers between Yb^{3+} and Ho^{3+} are expected to be very temperature-dependent. The dependence of Yb^{3+} and Ho^{3+} excited states lifetimes on temperature was investigated. The results presented in section 6.2 will be discussed in section 6.3 and combined in order to propose an upconversion mechanism.

6.2.1. Crystal structure

Figure 6.1 shows the typical powder X-ray diffraction pattern of Y_2BaZnO_5 : Yb^{3+} , Ho^{3+} materials. The crystal structure is orthorhombic, space group Pnma. Relatively pure phases were obtained, as shown by the good quality of the Rietveld refinement.¹⁴

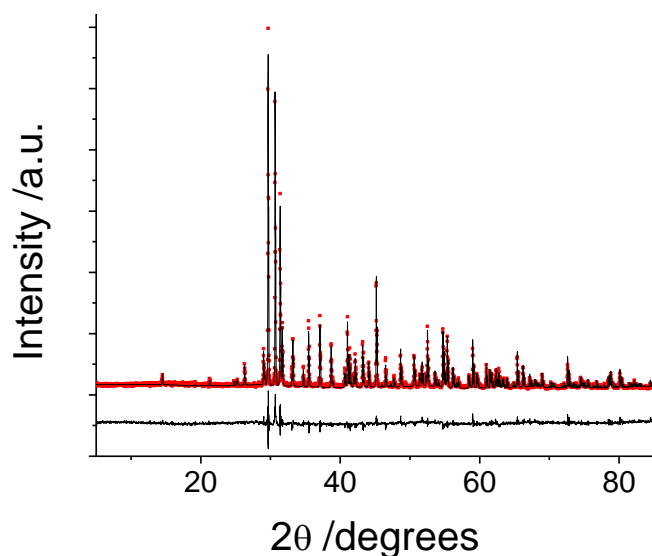


Figure 6.1: Rietveld refinement based upon the powder X-ray diffraction pattern of Y_2BaZnO_5 : Yb^{3+} (7%), Ho^{3+} (0.5%).

The cell parameters of $\text{Y}_2\text{BaZnO}_5: \text{Yb}^{3+}$ (7%), Ho^{3+} (0.5%) are the following: $a = 12.3387(1)$ Å, $b = 5.70975(5)$ Å and $c = 7.07037(7)$ Å (ICDD 87082). Note that the lattice parameters obtained in the doped samples are slightly smaller than those in the pure phase, which is attributed to the smaller ionic radii of Yb^{3+} (0.0925 nm) and Ho^{3+} (0.0958 nm) compared to Y^{3+} (0.096 nm).¹⁵ The basic structure of $\text{RE}_2\text{BaZnO}_5$ ($\text{RE} = \text{Y}, \text{Gd}$) compounds was presented in chapter 5, section 5.2.1. In $\text{RE}_2\text{BaZnO}_5: \text{Yb}^{3+}$, Ho^{3+} doped compounds, Yb^{3+} and Ho^{3+} ions substitute partially for RE^{3+} ions.

6.2.2. Reflectance in the infrared, visible and ultraviolet

A typical room-temperature reflectance spectrum of $\text{Y}_2\text{BaZnO}_5: \text{Yb}^{3+}$, Ho^{3+} samples in the range 200-1700 nm, is presented in Figure 6.2.

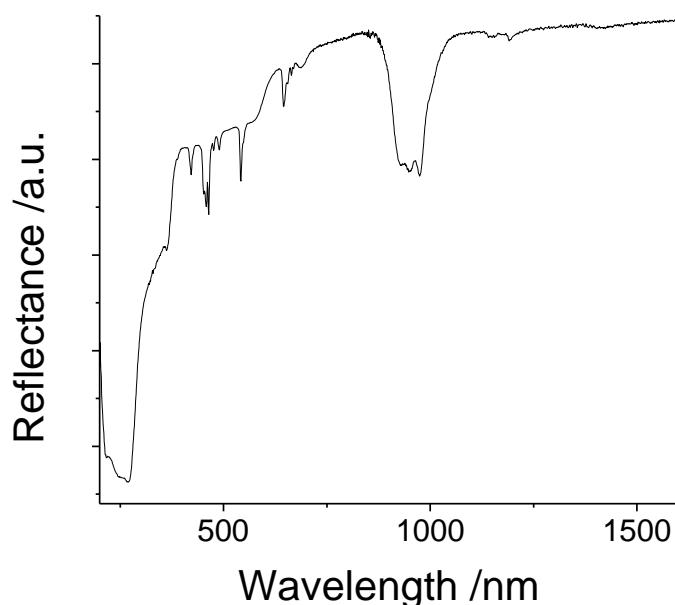


Figure 6.2: Room-temperature reflectance spectrum of $\text{Y}_2\text{BaZnO}_5: \text{Yb}^{3+}$ (7%), Ho^{3+} (0.5%).

A broad absorption band assigned to the $\text{Yb}^{3+} \ ^2\text{F}_{7/2} \rightarrow \ ^2\text{F}_{5/2}$ absorption is observed in the 870-1040 nm region, and overlaps poorly with the narrow $\text{Ho}^{3+} \ ^5\text{I}_8 \rightarrow \ ^5\text{I}_5$ (870 nm) absorption band. There is no overlap between the $\text{Yb}^{3+} \ ^2\text{F}_{7/2} \rightarrow \ ^2\text{F}_{5/2}$ and $\text{Ho}^{3+} \ ^5\text{I}_8 \rightarrow \ ^5\text{I}_6$ (1150 nm) absorption bands. Under ~ 977 nm excitation, therefore, only Yb^{3+} is directly excited.

6.2.3. Upconversion luminescence emission

Under near-infrared excitation at room-temperature, $\text{Y}_2\text{BaZnO}_5: \text{Yb}^{3+}, \text{Ho}^{3+}$ powders yield bright green emission, visible to the naked eye. Under 977 nm excitation (corresponding to the selective excitation of $\text{Yb}^{3+} {}^2\text{F}_{5/2}$) and 455 nm excitation (selective excitation of $\text{Ho}^{3+} {}^3\text{K}_8$) (see Figure 2.2, chapter 2), typical emission spectra reveal the presence of emission bands centred around 545 nm, 760 nm, 660 nm, 1040 nm (broad emission) and 1200 nm (Figure 6.3). A comparison of the emission spectra obtained under 977 nm and 455 nm excitation shows that the green (545 nm) to near-infrared (760 nm) emission intensity ratio does not vary with the excitation wavelength.

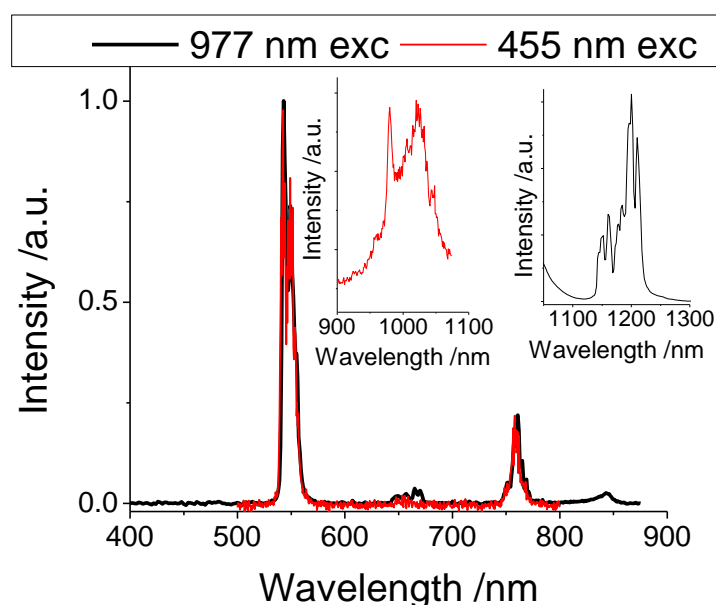


Figure 6.3: Typical room-temperature spectra of $\text{Y}_2\text{BaZnO}_5: \text{Yb}^{3+}, \text{Ho}^{3+}$ phosphors, under 977 nm and 455 nm excitations.

6.2.4. Concentration dependence of upconversion efficiencies

The upconverted emission intensity and spectral properties depend on the dopant concentrations. In Figure 6.4, the emission spectra of seven selected samples of the $\text{Y}_2\text{BaZnO}_5: \text{Yb}^{3+} (x\%), \text{Ho}^{3+} (0.5\%)$ ($x = 1, 3, 5, 7, 9, 11, 13$) family under cw 977 nm excitation ($\sim 36 \cdot 10^{-3} \text{ W/mm}^2$ incident power) are presented.

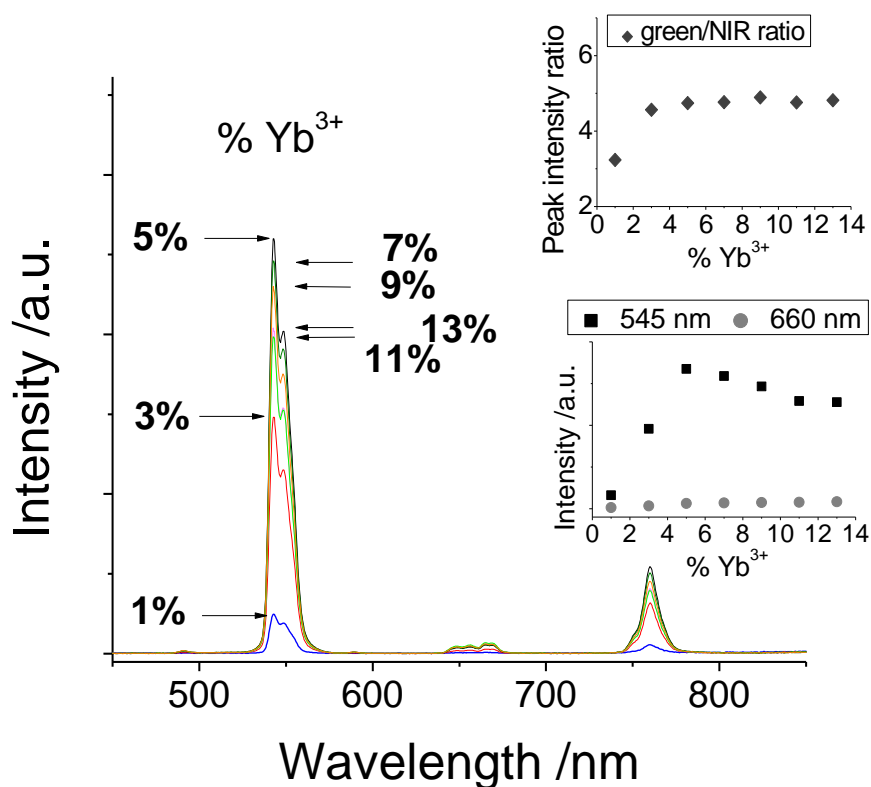


Figure 6.4: Room-temperature upconversion luminescence spectra for seven samples of the $\text{Y}_2\text{BaZnO}_5:\text{Yb}^{3+}(x\%),\text{Ho}^{3+}(0.5\%)$ ($x = 1, 3, 5, 7, 9, 11, 13$) family under cw 977 nm excitation ($\sim 36 \cdot 10^{-3} \text{ W/mm}^2$ incident power). The insets present the evolution of the green (545 nm) to near-infrared (760 nm) intensity ratio (top inset) and of the green (545 nm) and red (660 nm) emission intensities (bottom inset) as a function of Yb^{3+} concentration, under cw 977 nm excitation ($\sim 36 \cdot 10^{-3} \text{ W/mm}^2$ incident power).

In $\text{Y}_2\text{BaZnO}_5:\text{Yb}^{3+}(x\%),\text{Ho}^{3+}(0.5\%)$ samples, the upconversion emission intensity increases with the Yb^{3+} concentration, with an optimum performance around 5% Yb^{3+} (Figure 6.4). When the Yb^{3+} concentration is increased above 5%, the upconversion emission becomes less intense. This can be explained by the appearance of concentration quenching, as has been observed in previous studies. The top inset of Figure 6.4 shows the evolution of the green (545 nm) to near-infrared (760 nm) emission intensity ratio for the same seven samples. For Yb^{3+} concentrations above $\sim 3\%$, the green to near-infrared ratio is constant with the Yb^{3+} concentration. A lower green to near-infrared ratio is measured on the sample doped with 1% Yb^{3+} . In the bottom inset of Figure 6.4, the Yb^{3+} concentration dependence of the green (545 nm) and red (660 nm) emission intensities is represented. The green emission

intensity increases strongly with increasing Yb^{3+} concentration before reaching a maximum around 5% Yb^{3+} . For higher Yb^{3+} concentrations, the green emission intensity decreases with increasing Yb^{3+} concentration. For Yb^{3+} concentrations above 3%, the near-infrared (760 nm) emission intensity presents the same dependence on Yb^{3+} concentration as the green emission intensity. The red emission intensity is shown to increase very slightly with Yb^{3+} concentration.

The upconversion efficiencies of a variety of $\text{Y}_2\text{BaZnO}_5: \text{Yb}^{3+} (x\%), \text{Ho}^{3+} (y\%)$ samples ($0 \leq x \leq 15$ and $0 \leq y \leq 3$) were measured at room-temperature under 977 nm excitation ($\sim 25 \cdot 10^{-3} \text{ W/mm}^2$ incident power) (Figure 6.5 and Figure B.1, Appendix B). The upconversion efficiency was calculated as the ratio of the upconversion emission in the 380-780 nm range over the power absorbed in the near-infrared (950-1000 nm range):

$$\eta_{UC} = \frac{P_{em}}{P_{abs}^{IR}} = \frac{P_{em}}{P_{inc}^{IR} - P_{not\ abs}^{IR}} \quad (\text{Eq. 1})$$

where P_{em} is the power of the upconversion light emitted in the 380-780 nm range, P_{abs}^{IR} is the power of the fraction of incident light that has been absorbed by the sample, P_{inc}^{IR} is the incident power in the near-infrared (integrated over the 950-1000 nm range) and $P_{not\ abs}^{IR}$ is the power of the fraction of incident light that has not been absorbed by the sample.

Samples containing between 0.25-0.75% of Ho^{3+} , and total dopant concentrations (Yb^{3+} plus Ho^{3+}) in the 5-9% range were shown to exhibit the highest efficiencies for infrared to visible upconversion. A maximum upconversion efficiency of $2.6 \pm 0.2\%$ was obtained in $\text{Y}_2\text{BaZnO}_5: \text{Yb}^{3+} (7\%), \text{Ho}^{3+} (0.5\%)$, at room-temperature under 977 nm excitation ($\sim 25 \cdot 10^{-3} \text{ W/mm}^2$). It is worth noting that very similar upconversion efficiency values (and behaviours) were obtained from $\text{Gd}_2\text{BaZnO}_5: \text{Yb}^{3+}, \text{Ho}^{3+}$ samples.

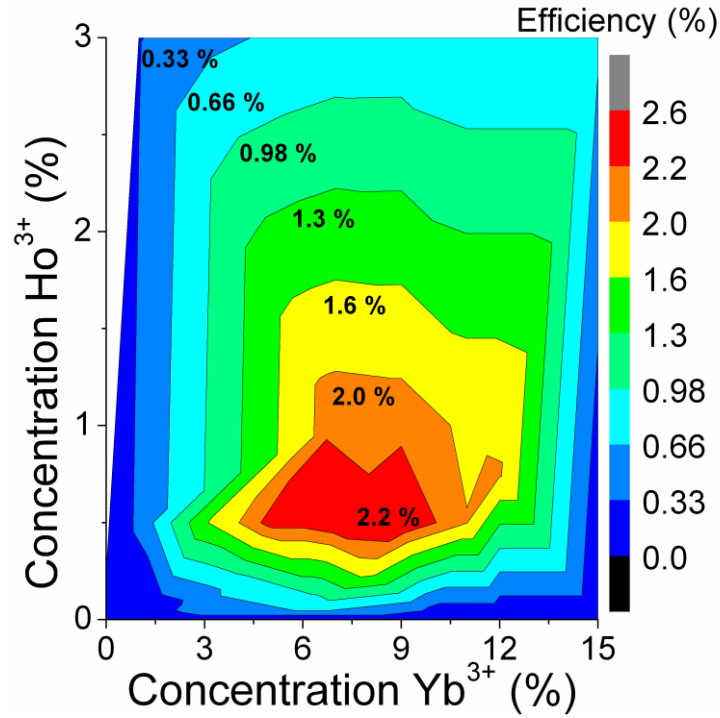


Figure 6.5: Room-temperature upconversion efficiencies as a function of Yb^{3+} and Ho^{3+} concentrations for a variety of $\text{Y}_2\text{BaZnO}_5:\text{Yb}^{3+}, \text{Ho}^{3+}$ samples, under 977 nm excitation ($\sim 25 \cdot 10^{-3} \text{ W/mm}^2$). The colour bar on the right is used to display the upconversion efficiency values for each dopant composition. Contour lines (lines with the same upconversion efficiency value) and contour labels displaying the UC efficiencies associated to those contour lines are also included.

6.2.5. Pump power dependence of upconversion emission

Pump power dependences of the green (545 nm), near-infrared (760 nm) and red (660 nm) emission powers were investigated at room-temperature under 977 nm excitation. The three emissions were shown to present an approximate quadratic dependence on the excitation power density in the low power regime (Figure 6.6). It is worth mentioning that for $\sim 25 \cdot 10^{-3} \text{ W/mm}^2$ excitation power densities, about half of the incident light is absorbed by the sample,

$$\text{i.e. } P_{\text{abs}}^{\text{IR}} \sim \frac{1}{2} P_{\text{inc}}^{\text{IR}}.$$

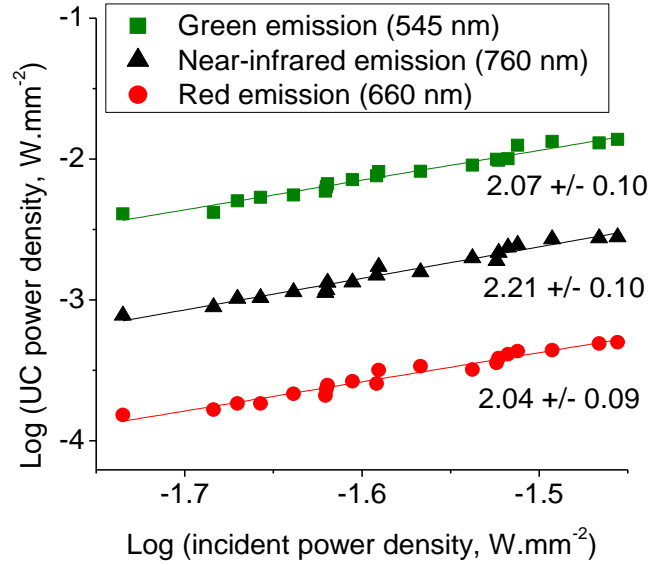


Figure 6.6: Pump power dependence of the green (545 nm), red (660 nm) and near-infrared (760 nm) upconversion emission at room-temperature under 977 nm excitation in $\text{Y}_2\text{BaZnO}_5: \text{Yb}^{3+}$ (7%), Ho^{3+} (0.5%). The results are presented in a decadic double-logarithmic scale.

The rate equations describing the upconversion mechanism in $\text{RE}_2\text{BaZnO}_5: \text{Yb}^{3+}, \text{Ho}^{3+}$ ($\text{RE} = \text{Y}, \text{Gd}$) were written, simplified and solved in the steady-state regime and at low incident power (Appendix C). A quadratic dependence was found for the green, red and near-infrared emitting level population densities with the incident pump power. Since upconversion emission intensities are proportional to the population densities of the associated emitting levels, the experimental power dependence results are in good agreement with the theoretical predictions.

6.2.6. Lifetime measurements and temperature dependence

The transients associated with the emission bands centred at around 545 nm, 760 nm, 1040 nm, and 1200 nm in $\text{Y}_2\text{BaZnO}_5: \text{Yb}^{3+}$ (7%), Ho^{3+} (0.5%) were recorded under pulsed 455 nm (direct excitation of $\text{Ho}^{3+} \text{ } ^3\text{K}_8$) and 977 nm (excitation of $\text{Yb}^{3+} \text{ } ^2\text{F}_{5/2}$) excitations at various temperatures between 80K and 573 K (see Figure 2.2, chapter 2). It is worth noting that Ho^{3+} does not absorb at 977 nm (see section 6.2.2), which guarantees a selective excitation of Yb^{3+}

under 977 nm excitation. A typical transient corresponding to the room-temperature temporal evolution of the green emission (545 nm) under pulsed 977 nm excitation of Y_2BaZnO_5 : Yb^{3+} (7%), Ho^{3+} (0.5%), is presented in Figure 6.7.

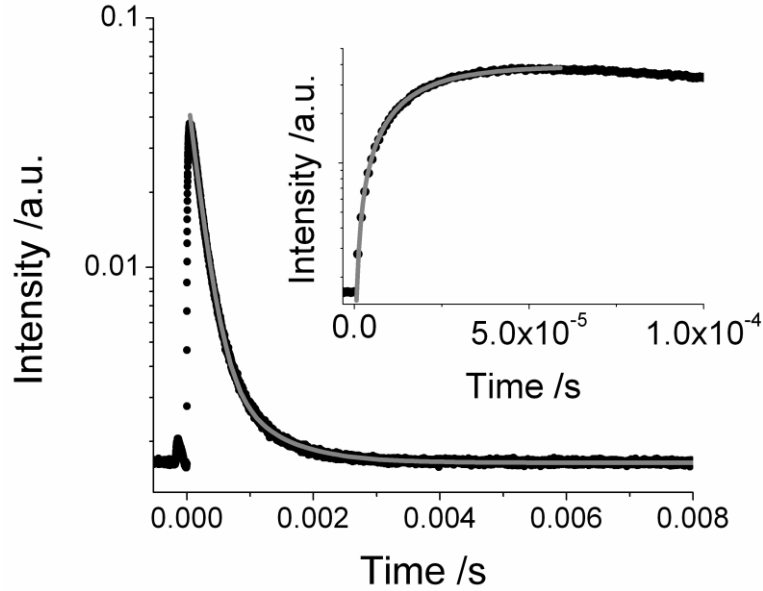


Figure 6.7: Typical room-temperature temporal evolution of the green (545 nm) emission under pulsed 977 nm excitation of Y_2BaZnO_5 : Yb^{3+} (7%), Ho^{3+} (0.5%), and data fitting in order to get average rise and decay times. Note that the small peak observed around $t \sim -140 \mu\text{s}$ is due to a triggering artefact. The inset presents an expansion of the initial rise.

At the end of the excitation pulse ($t \sim 7 \text{ ns}$), no luminescence intensity is observed; instead, the transient exhibits a typical delayed rise and a decay. This is a clear fingerprint of an energy transfer process (see chapter 3, section 3.5). The experimental intensity data were fitted to the expression:¹⁶

$$I(t) = A \left(1 - e^{-\frac{t}{\tau_r}} \right) \left(e^{-\frac{t}{\tau_d}} \right) \quad (\text{Eq. 2})$$

where A is an emission intensity factor, and τ_r and τ_d represent the rise and decay times of the transient. Note that τ_r and τ_d are related to the energy transfer rate constants between Yb^{3+} and Ho^{3+} and to the intrinsic lifetimes of the levels involved.¹⁶

The decay curves showed, in some cases a bi- or triexponential behaviour, corresponding to decay mechanisms via different depopulation channels. As such, when the transient decay

section could not be fitted by a single exponential, the effective fluorescent decay time τ_d was determined using the following equation (discretisation of the formula used in reference ¹⁷):

$$\tau_d = \frac{\sum_{i=1}^n A_i \tau_i^2}{\sum_{i=1}^n A_i \tau_i} \quad (\text{Eq. 3})$$

where A_i and τ_i are the amplitude and lifetime corresponding to the level depopulation channel i , respectively, and $n = 1, 2$ or 3 .

The fit of the typical room-temperature transient corresponding to the green emission (545 nm) under pulsed 977 nm excitation of $\text{Y}_2\text{BaZnO}_5: \text{Yb}^{3+}$ (7%), Ho^{3+} (0.5%) is presented in Figure 6.7. The transient decay function presents two distinct lifetimes. The best fit for the 545 nm emission transient corresponds to average rise and decay times of $\tau_r = 14.4 \pm 0.72$ μs and $\tau_d = 280 \pm 14$ μs , respectively.

In Figure 6.8, we present the temperature dependence of the lifetimes corresponding to *a*) the broad 1040 nm emission from Yb^{3+} under 977 nm excitation, *b*) the 545 nm (green) and 760 nm (near-infrared) emissions from Ho^{3+} under 977 nm and 455 nm excitations, and *c*) the 1200 nm emission from Ho^{3+} , under 977 nm and 455 nm excitations of $\text{Y}_2\text{BaZnO}_5: \text{Yb}^{3+}$ (7%), Ho^{3+} (0.5%). For clarity, the error bars are not shown in Figure 6.8, but they are typically on the order of 5% (statistical error from repeated measurements). The values of the lifetimes measured at different temperatures are presented in Appendix B, Table B.1.

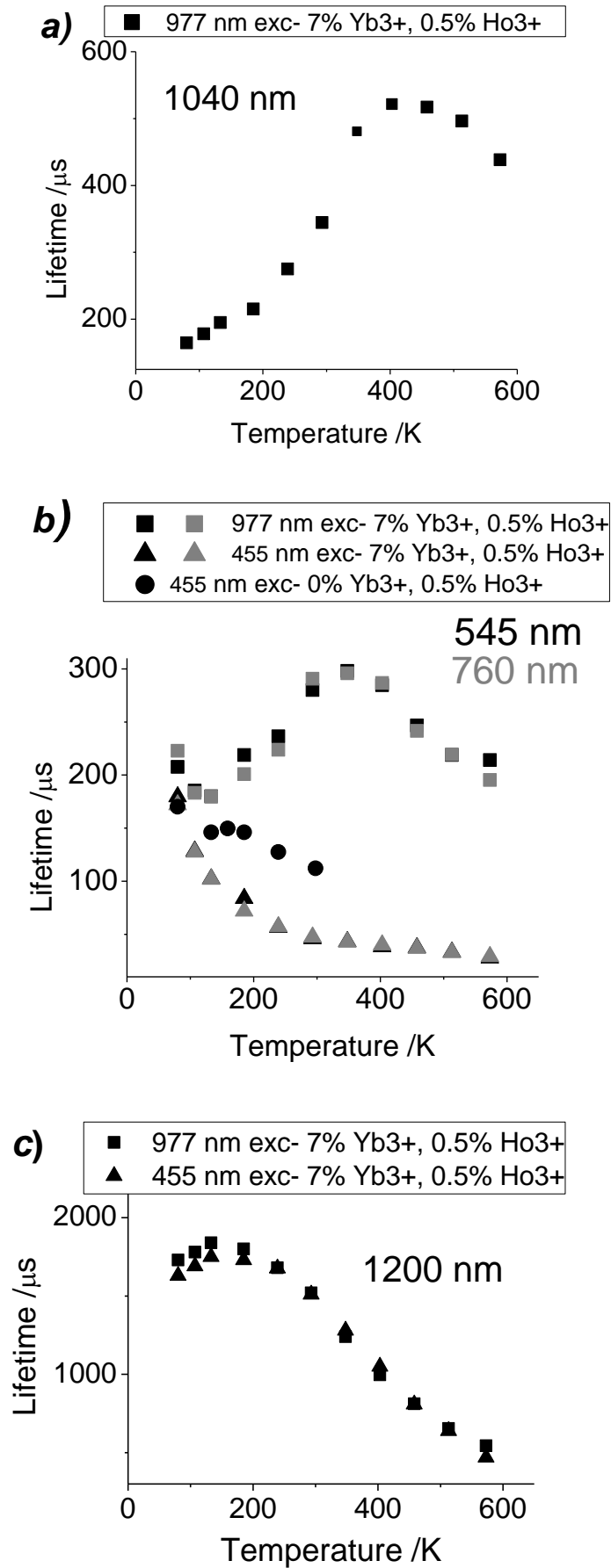


Figure 6.8: Temperature dependence of the lifetimes corresponding to a) the 1040 nm emission under pulsed 977 nm excitation, b) the 545 nm green and 760 nm near-infrared emissions under pulsed 977 nm and 455 nm excitations, c) the 1200 nm emission, under pulsed 977 nm and 455 nm excitation of $\text{Y}_2\text{BaZnO}_5: \text{Yb}^{3+}$ (7%), Ho^{3+} (0.5%). Note that in graph b), the temperature dependence (up to room-temperature) of the 545 nm green emission lifetime in a $\text{Y}_2\text{BaZnO}_5: \text{Yb}^{3+}$ (0%), Ho^{3+} (0.5%) sample (no Yb^{3+}) under pulsed 455 nm excitation is also represented for comparison. No data was recorded on that sample above room-temperature.

Under 977 nm excitation (Figure 6.8a), the lifetime corresponding to the broad emission around 1040 nm increases with increasing temperature, from $T = 80 \text{ K}$ ($\tau_d \sim 165 \pm 8 \text{ } \mu\text{s}$) to $T = 403 \text{ K}$ ($\tau_d \sim 522 \pm 26 \text{ } \mu\text{s}$), when it saturates. At temperatures above 405 K, the lifetime decreases again (Table B.1, Appendix B).

For Yb^{3+} concentrations above $\sim 3\%$, the transients corresponding to the green (545 nm) and near-infrared (760 nm) emissions present the same rise and decay times (within experimental errors) in the whole range of temperatures studied, and under both 977 nm and 455 nm excitations (Figure 6.8b). In $\text{Y}_2\text{BaZnO}_5: \text{Yb}^{3+}$ (7%), Ho^{3+} (0.5%), the 545 nm (and 760 nm) emission lifetimes present very different temperature dependences depending on whether they are excited at 977 nm or 455 nm (Figure 6.8b and Table B.1, Appendix B). Under 977 nm excitation, corresponding to the selective excitation of $\text{Yb}^{3+} \text{ } ^2\text{F}_{5/2}$, the 545 nm and 760 nm emission lifetimes decrease with decreasing temperature for $T < 350 \text{ K}$ and reach a minimum for $T = 133 \text{ K}$ ($\tau_d \sim 180 \pm 9 \text{ } \mu\text{s}$) before slightly increasing at lower temperatures. For $T > 350 \text{ K}$, the green (545 nm) and near-infrared (760 nm) emission lifetimes decrease with increasing temperature. On the other hand, under 455 nm direct excitation of $\text{Ho}^{3+} \text{ } ^3\text{K}_8$, the green and near-infrared (760 nm) emission lifetimes decrease monotonically with increasing temperature (this is the case in the whole range of temperatures studied). It is worth noting that in $\text{Y}_2\text{BaZnO}_5: \text{Yb}^{3+}$ (7%), Ho^{3+} (0.5%), the lifetimes associated with the green emission (545 nm) under 977 nm and 455 nm excitation conditions are similar at temperatures around 80 K (Table B.1, Appendix B). For increasing temperatures in the 80-400 K range, the two graphs plotting the temperature dependence of the lifetimes associated with the 545 nm emission under 977 nm and 455 nm excitation conditions diverge. Note that the lifetimes measured under 977 nm excitation are always longer than those measured under 455 nm

excitation.¹⁹ Figure 6.8b also shows the temperature dependence of the green emission lifetime under 455 nm excitation in a Ho^{3+} singly-doped Y_2BaZnO_5 : Yb^{3+} (0%), Ho^{3+} (0.5%) sample. Lifetimes measured in this Yb^{3+} -free sample under 455 nm excitation are seen to decrease with temperature, similarly to what is observed in Y_2BaZnO_5 : Yb^{3+} (7%), Ho^{3+} (0.5%). However, for a given temperature, the lifetimes measured in the Yb^{3+} -free sample are always longer than those measured in the Yb^{3+} , Ho^{3+} co-doped sample. Note that all the graphs plotted in Figure 6.8b tend to almost converge for $T = 80$ K.

The temperature dependence of the 1200 nm emission under 977 nm and 455 nm excitation conditions is presented in Figure 6.8c. The lifetimes measured under 977 nm and 455 nm excitation conditions are almost identical for temperatures above 220 K, but show a slight deviation at lower temperatures. In the whole temperature range (and especially at low temperatures), the lifetimes of the 1200 nm emission are very long. For $T > 185$ K, the 1200 nm emission lifetimes measured under both 977 and 455 nm excitations decay strongly with increasing temperature (Table B.1, Appendix B). For $T < 185$ K, the measured lifetimes decrease slightly with decreasing temperature.

6.3. Discussion

6.3.1. Population and depopulation mechanisms of the excited levels

A detailed investigation of the steady-state and dynamic emission properties of a variety of Y_2BaZnO_5 : Yb^{3+} (x%), Ho^{3+} (y%) ($0 < x \leq 3$ and $0 < y \leq 15$) samples was performed and the results were presented in the previous section.

Under 977 nm excitation of Yb^{3+} , the samples present a strong green upconversion emission, easily visible to the naked eye. Maximum upconversion efficiencies of $\sim 2.6\%$ are obtained at room-temperature on samples doped with Yb^{3+} and Ho^{3+} concentrations around 7% and 0.5%, respectively (Figure 6.5). The emission spectra measurements reveal the presence of emission bands centred around 545 nm, 660 nm, 760 nm, 1040 nm (strong and broad emission) and 1200 nm. Under 977 nm excitation, the transients corresponding to the emissions centred at 545 nm, 760 nm (Figure 6.7) and 1200 nm present a clear rise time after the excitation is turned off, indicating that the population mechanisms of the energy levels from which these emissions arise involve at least one Yb^{3+} to Ho^{3+} energy transfer step. Power dependence

was investigated. In view of these results, the emission centred at 760 nm can be exclusively assigned to the $(^5\text{S}_2, ^5\text{F}_4) \rightarrow ^5\text{I}_7$ transition. Note that a surprisingly low green to near-infrared ratio was observed on the sample doped with 1% Yb^{3+} (Figure 6.4). A possible explanation to this low value could be the existence of an additional channel for the 760 nm emission in addition to the $(^5\text{S}_2, ^5\text{F}_4) \rightarrow ^5\text{I}_7$ emission, possibly via a $\text{Ho}^{3+} ^5\text{I}_4 \rightarrow ^5\text{I}_8$ depopulation.¹² This fact, together with a significantly decreased green to red upconversion emission ratio for Yb^{3+} concentrations smaller than 3%, suggests that processes involving an excited state absorption (ESA) from the long-lived $^5\text{I}_7$ Ho^{3+} state could be relevant at low Yb^{3+} concentrations, due to a reduced energy transfer upconversion (ETU) probability.

According to the energy diagram (Figure 6.9), one can see two different ways of populating the thermalised $(^5\text{S}_2, ^5\text{F}_4)$ energy levels. The first mechanism involves two successive Yb^{3+} to Ho^{3+} energy transfer steps; $\text{Yb}^{3+} ^2\text{F}_{5/2} + \text{Ho}^{3+} ^5\text{I}_8 \rightarrow \text{Yb}^{3+} ^2\text{F}_{7/2} + \text{Ho}^{3+} ^5\text{I}_6$ and $\text{Yb}^{3+} ^2\text{F}_{5/2} + \text{Ho}^{3+} ^5\text{I}_6 \rightarrow \text{Yb}^{3+} ^2\text{F}_{7/2} + \text{Ho}^{3+} (^5\text{S}_2, ^5\text{F}_4)$. Alternatively, the $(^5\text{S}_2, ^5\text{F}_4)$ levels could be populated by a first Yb^{3+} to Ho^{3+} energy transfer step: $\text{Yb}^{3+} ^2\text{F}_{5/2} + \text{Ho}^{3+} ^5\text{I}_8 \rightarrow \text{Yb}^{3+} ^2\text{F}_{7/2} + \text{Ho}^{3+} ^5\text{I}_6$ followed by an excited state absorption (ESA) by $\text{Ho}^{3+} ^5\text{I}_6$ (with no Yb^{3+} assistance). However, given the high absorption cross-section of Yb^{3+} at 977 nm²¹ compared to that of Ho^{3+} ,²²⁻²⁴ and the relatively high Yb^{3+} to Ho^{3+} concentration ratios in the samples, the first mechanism involving two successive Yb^{3+} to Ho^{3+} energy transfers is expected to be dominant in the population process of $\text{Ho}^{3+} (^5\text{S}_2, ^5\text{F}_4)$, at moderate and high Yb^{3+} concentrations.

Inspection of the energy diagram reveals three possible ways of populating the $\text{Ho}^{3+} ^5\text{F}_5$ red emitting level. First, it could be populated by multiphonon relaxation from the above lying green emitting levels; $(^5\text{S}_2, ^5\text{F}_4) \rightarrow ^5\text{F}_5$. The second mechanism involves a phonon-assisted Yb^{3+} to Ho^{3+} energy transfer: $\text{Yb}^{3+} ^2\text{F}_{5/2} + \text{Ho}^{3+} ^5\text{I}_8 \rightarrow \text{Yb}^{3+} ^2\text{F}_{7/2} + \text{Ho}^{3+} ^5\text{I}_6$, followed by a multiphonon relaxation step to the long-lived $\text{Ho}^{3+} ^5\text{I}_7$ level: $^5\text{I}_6 \rightarrow ^5\text{I}_7$ and a second Yb^{3+} to Ho^{3+} energy transfer step populating directly the $\text{Ho}^{3+} ^5\text{F}_5$ red emitting level: $\text{Yb}^{3+} ^2\text{F}_{5/2} + \text{Ho}^{3+} ^5\text{I}_7 \rightarrow \text{Yb}^{3+} ^2\text{F}_{7/2} + \text{Ho}^{3+} ^5\text{F}_5$. Alternatively, the second $\text{Yb}^{3+} ^2\text{F}_{5/2}$ to $\text{Ho}^{3+} ^5\text{I}_7$ energy transfer step could be replaced by an excited state absorption (ESA) by $\text{Ho}^{3+} ^5\text{I}_7$. Again, given the high absorption cross-section of Yb^{3+} at 977 nm compared to that of Ho^{3+} , the mechanism involving two successive Yb^{3+} to Ho^{3+} energy transfers is expected to be dominant in the population process of $\text{Ho}^{3+} ^5\text{F}_5$, for samples with moderate or high Yb^{3+} concentrations.

Ytterbium concentration dependence studies of the emission properties of Y_2BaZnO_5 : Yb^{3+} (x%), Ho^{3+} (0.5%) (x = 1, 3, 5, 7, 9, 11) samples (inset Figure 6.4) show that for Yb^{3+}

concentrations below 5%, green (545 nm) and near infrared (760 nm) emission intensities increase with increasing Yb^{3+} concentration. This can be attributed to an increase in Ho^{3+} ($^5\text{S}_2$, $^5\text{F}_4$) population due to an increased Yb^{3+} sensitisation. Lifetime measurements show that under 977 nm excitation, the ($^5\text{S}_2$, $^5\text{F}_4$) level lifetime decreases with increasing Yb^{3+} concentration (for Yb^{3+} concentrations above 3%). This indicates that there is an additional process that depopulates the ($^5\text{S}_2$, $^5\text{F}_4$) level in the presence of Yb^{3+} ions and that this process is more favourable at high Yb^{3+} concentrations. It is worth mentioning that multiphonon relaxation rates are not expected to be dependent on dopant concentrations (and in particular Yb^{3+} concentrations) since the maximum phonon energy is invariant with dopant concentrations at these low doping levels (Figure B.2, Appendix B). The Yb^{3+} concentration-dependent depopulation of Ho^{3+} ($^5\text{S}_2$, $^5\text{F}_4$) could be attributed to a back-energy transfer mechanism between Ho^{3+} and Yb^{3+} : $\text{Ho}^{3+} (^5\text{S}_2, ^5\text{F}_4) + \text{Yb}^{3+} ^2\text{F}_{7/2} \rightarrow \text{Ho}^{3+} ^5\text{I}_6 + \text{Yb}^{3+} ^2\text{F}_{5/2}$.^{25,26} Energy transfers from Ho^{3+} to Yb^{3+} do exist, as evidenced by the broad emission attributed to $\text{Yb}^{3+} ^2\text{F}_{5/2} \rightarrow ^2\text{F}_{7/2}$ under selective excitation of Ho^{3+} at 455 nm (Figure 6.3).

The increase in the green and infrared (760 nm) emission intensities for Yb^{3+} concentrations below 5% indicates that, in this concentration range, the ($^5\text{S}_2$, $^5\text{F}_4$) levels become more populated by Yb^{3+} to Ho^{3+} energy transfer than they are depopulated by Ho^{3+} to Yb^{3+} back-energy transfer. For Yb^{3+} concentrations below 5%, the red emission intensity also increases slightly. This indicates that the higher the Yb^{3+} concentration, the higher the ratio between $\text{Ho}^{3+} ^5\text{F}_5$ population and $\text{Ho}^{3+} ^5\text{F}_5$ depopulation. When the Yb^{3+} concentration exceeds 5%, the green emission intensity starts decreasing with increasing Yb^{3+} concentration. This means that the higher the Yb^{3+} concentration, the higher the influence of Ho^{3+} to Yb^{3+} back-energy transfer (depopulating Ho^{3+} ($^5\text{S}_2$, $^5\text{F}_4$)) compared to that of the Yb^{3+} to Ho^{3+} energy transfer route populating Ho^{3+} ($^5\text{S}_2$, $^5\text{F}_4$). In this same Yb^{3+} concentration range, the red emission intensity keeps increasing slightly despite the decrease in green level population (Figure 6.4). Moreover, a comparison of the emission spectra measured under 977 nm and 455 nm excitations shows that the $\text{Ho}^{3+} ^5\text{F}_5$ level emission is enhanced in the upconversion spectrum (as evidenced by the lower green to red emission intensity ratio) (Figure 6.3). This indicates that the Ho^{3+} ($^5\text{S}_2$, $^5\text{F}_4$) \rightarrow $^5\text{F}_5$ multiphonon relaxation is not the only process populating $\text{Ho}^{3+} ^5\text{F}_5$ under 980 nm excitation. Yb^{3+} to $\text{Ho}^{3+} ^5\text{I}_7$ energy transfer cannot be neglected when considering the population mechanisms of $\text{Ho}^{3+} ^5\text{F}_5$; the increase in red emission can be attributed to the increase of the $\text{Yb}^{3+} ^2\text{F}_{5/2} + \text{Ho}^{3+} ^5\text{I}_7 \rightarrow \text{Yb}^{3+} ^2\text{F}_{7/2} + \text{Ho}^{3+} ^5\text{F}_5$ energy transfer rates with increasing Yb^{3+} concentration. The importance of this red level population channel

involving the long-lived $\text{Ho}^{3+} \ ^5\text{I}_7$ is confirmed by the observation of the transients corresponding to the emissions at 545 nm, 760 nm and 660 nm (Figure B.3, Appendix B). Both the green and near-infrared (760 nm) emissions are seen to have the same rise time; the red (660 nm) emission, however, presents a different rise time that is shorter. This suggests that the main population mechanism of the red emitting level upconversion is not multiphonon relaxation from $\text{Ho}^{3+} (\ ^5\text{S}_2, \ ^5\text{F}_4)$ since this would lead to longer rise times of the red level compared to that associated with the 545 nm and 760 nm emissions. These results confirm that the contribution of Yb^{3+} to Ho^{3+} energy transfer: $\text{Yb}^{3+} \ ^2\text{F}_{5/2} + \text{Ho}^{3+} \ ^5\text{I}_7 \rightarrow \text{Yb}^{3+} \ ^2\text{F}_{7/2} + \text{Ho}^{3+} \ ^5\text{F}_5$ to the population of $\text{Ho}^{3+} \ ^5\text{F}_5$ cannot be neglected.

6.3.2. Temperature dependence of population and depopulation dynamics

Temperature dependence studies of the $\text{Yb}^{3+} \ ^2\text{F}_{5/2}$ lifetimes under direct 977 nm excitation (observation of the transients corresponding to the broad emission around 1040 nm emission) in $\text{Y}_2\text{BaZnO}_5: \text{Yb}^{3+} (7\%), \text{Ho}^{3+} (0.5\%)$ show that the maximum lifetimes are at around 420 K. Lifetimes decrease strongly with decreasing temperature down to 80 K, which is the limit of our measurements (Figure 6.8a). One can see two major ways of depopulating the $\text{Yb}^{3+} \ ^2\text{F}_{5/2}$ level; the first process involves Yb^{3+} to Ho^{3+} energy transfers (three different transfer processes must be considered: $\text{Yb}^{3+} \ ^2\text{F}_{5/2} + \text{Ho}^{3+} \ ^5\text{I}_8 \rightarrow \text{Yb}^{3+} \ ^2\text{F}_{7/2} + \text{Ho}^{3+} \ ^5\text{I}_6$; $\text{Yb}^{3+} \ ^2\text{F}_{5/2} + \text{Ho}^{3+} \ ^5\text{I}_6 \rightarrow \text{Yb}^{3+} \ ^2\text{F}_{7/2} + \text{Ho}^{3+} (\ ^5\text{S}_2, \ ^5\text{F}_4)$, and $\text{Yb}^{3+} \ ^2\text{F}_{5/2} + \text{Ho}^{3+} \ ^5\text{I}_7 \rightarrow \text{Yb}^{3+} \ ^2\text{F}_{7/2} + \text{Ho}^{3+} \ ^5\text{F}_5$). The second process would involve $\text{Yb}^{3+} \ ^2\text{F}_{5/2} \rightarrow \ ^2\text{F}_{7/2}$ multiphonon relaxation, but in view of the large energy gap between the Yb^{3+} ground and excited states ($\sim 10400 \text{ cm}^{-1}$), the rates of multiphonon relaxation are expected to be low. Besides, the temperature dependence of $\text{Yb}^{3+} \ ^2\text{F}_{5/2}$ lifetimes (presented in Figure 6.8a) is very different from what is expected for a process governed by multiphonon relaxation.²⁷ We have observed that excitation hopping between Yb^{3+} ions does not contribute significantly to the $\text{Yb}^{3+} \ ^2\text{F}_{5/2}$ lifetime, as no significant concentration dependence has been found with the Yb^{3+} concentration in singly doped samples. We therefore conclude that, for $T < 420 \text{ K}$, the decrease of lifetimes with decreasing temperature reflects the increase in the global Yb^{3+} to Ho^{3+} transfer rate (which includes three contributions corresponding to the transfers to $\text{Ho}^{3+} \ ^5\text{I}_8$, $\text{Ho}^{3+} \ ^5\text{I}_6$ and $\text{Ho}^{3+} \ ^5\text{I}_7$). This increase can be assigned to an improved overlap between the emission from Yb^{3+} emission and any of the absorptions by $\text{Ho}^{3+} \ ^5\text{I}_8$, $\text{Ho}^{3+} \ ^5\text{I}_6$ and/or $\text{Ho}^{3+} \ ^5\text{I}_7$. The remarkable increase of the green

upconversion intensity at low temperatures supports this idea and suggests that the energy transfer to $\text{Ho}^{3+} {}^5\text{I}_6$ is the main beneficiary of this transfer probability increase.

Temperature dependence studies in $\text{Y}_2\text{BaZnO}_5: \text{Yb}^{3+}$ (7%), Ho^{3+} (0.5%) of the $\text{Ho}^{3+} {}^5\text{I}_6$ lifetimes (observation of the transients associated with the 1200 nm emission) show that for $T > 200$ K, the $\text{Ho}^{3+} {}^5\text{I}_6$ lifetimes measured under 977 nm and 455 nm excitation are very similar and decrease with increasing temperature (Figure 6.8c). The $\text{Ho}^{3+} {}^5\text{I}_6$ level can be depopulated by multiphonon relaxation to $\text{Ho}^{3+} {}^5\text{I}_7$, by Yb^{3+} to Ho^{3+} ET: $\text{Yb}^{3+} {}^2\text{F}_{5/2} + \text{Ho}^{3+} {}^5\text{I}_6 \rightarrow \text{Yb}^{3+} {}^2\text{F}_{7/2} + \text{Ho}^{3+} ({}^5\text{S}_2, {}^5\text{F}_4)$, or by phonon-assisted Ho^{3+} to Yb^{3+} back-energy transfer $\text{Ho}^{3+} {}^5\text{I}_6 + \text{Yb}^{3+} {}^2\text{F}_{7/2} \rightarrow \text{Ho}^{3+} {}^5\text{I}_8 + \text{Yb}^{3+} {}^2\text{F}_{5/2}$. The decrease of $\text{Ho}^{3+} {}^5\text{I}_6$ lifetimes with increasing temperature suggests that the $\text{Ho}^{3+} {}^5\text{I}_6$ dynamics might be governed mainly by the Ho^{3+} , and in particular by the $\text{Ho}^{3+} {}^5\text{I}_6 \rightarrow {}^5\text{I}_7$ multiphonon relaxation rate which is expected to increase with temperature. The slight lifetime decrease in the 185 K-80 K range suggests that, despite the low Ho^{3+} concentrations in the samples, cross-relaxation mechanisms involving the lowest excited states of Ho^{3+} occur at low temperatures. These mechanisms are weak and only possible due to the long lifetimes of the levels involved.²⁸

The temperature dependence study of the temporal evolution of the Ho^{3+} green emission at 545 nm in $\text{Y}_2\text{BaZnO}_5: \text{Yb}^{3+}$ (7%), Ho^{3+} (0.5%) shows that the thermal behaviour is completely different under 455 nm excitation (selective excitation of $\text{Ho}^{3+} {}^3\text{K}_8$) compared with that under 977 nm excitation (upconversion through selective excitation of $\text{Yb}^{3+} {}^2\text{F}_{5/2}$) (Figure 6.8c). Interestingly, the lifetimes measured under 977 nm excitation are longer than those measured under 455 nm excitation, for $T > 80$ K. This is a clear indication that, under 977 nm excitation, the upconversion dynamics are governed by the Yb^{3+} - Ho^{3+} interaction dynamics and not by the intrinsic $\text{Ho}^{3+} ({}^5\text{S}_2, {}^5\text{F}_4)$ lifetimes.²⁹ Under 455 nm excitation, the strong decrease of $\text{Ho}^{3+} ({}^5\text{S}_2, {}^5\text{F}_4)$ lifetimes with increasing temperature (Figure 6.8c) suggests that $\text{Ho}^{3+} ({}^5\text{S}_2, {}^5\text{F}_4) \rightarrow {}^5\text{F}_5$ multiphonon relaxation governs the green and near-infrared (760 nm) emitting level depopulation dynamics. A comparison of the lifetimes in $\text{Y}_2\text{BaZnO}_5: \text{Yb}^{3+}$ (7%), Ho^{3+} (0.5%) and $\text{Y}_2\text{BaZnO}_5: \text{Yb}^{3+}$ (0%), Ho^{3+} (0.5%) under 455 nm excitation shows that, for each temperature, the sample containing Yb^{3+} (7%) presents lower intrinsic lifetimes than the Yb^{3+} free sample. This indicates that Ho^{3+} to Yb^{3+} back-energy transfer does exist, even under 455 nm excitation. At high temperatures, its contribution, however, is low compared to that of $({}^5\text{S}_2, {}^5\text{F}_4) \rightarrow {}^5\text{F}_5$ multiphonon relaxation.

Under 977 nm excitation, a distinct behaviour for the Ho^{3+} ($^5\text{S}_2$, $^5\text{F}_4$) lifetimes is observed; lifetimes decrease with decreasing temperature. The lifetimes measured under 977 nm and 455 nm excitation tend to (almost) converge at $\sim 80\text{K}$. This observation is noteworthy, and suggests that there is a change in the dynamics regime at low temperatures; the system is no longer governed by Yb^{3+} - Ho^{3+} transfer times but by Ho^{3+} ($^5\text{S}_2$, $^5\text{F}_4$) \rightarrow $^5\text{F}_5$ intrinsic de-excitation times. We believe that this chapter constitutes the first report of a dynamics regime change by means of temperature variation in a Yb^{3+} , Ho^{3+} co-doped system.

The relevant upconversion mechanisms in $\text{RE}_2\text{BaZnO}_5$: Yb^{3+} , Ho^{3+} ($\text{RE} = \text{Y}, \text{Gd}$) materials are summarised in Figure 6.9.

6.4. Conclusions

A very efficient near-infrared to green upconversion phosphor has been described in this chapter. The upconversion properties of Y_2BaZnO_5 : Yb^{3+} , Ho^{3+} oxide materials were investigated for the first time. Upconversion efficiencies were quantified as a function of dopant concentrations. We believe that the high upconversion efficiencies obtained at room-temperature ($\sim 2.6\%$) are the highest reported ones to date for a phosphor co-doped with Yb^{3+} and Ho^{3+} .

Power dependence studies and temperature-dependent lifetime measurements provided a model for the upconversion mechanisms involved in these materials. The strong green (545 nm) and near-infrared (760 nm) emissions arise from the thermalised Ho^{3+} ($^5\text{S}_2$, $^5\text{F}_4$) levels populated mainly by two successive Yb^{3+} to Ho^{3+} energy transfer steps under 977 nm excitation. Temperature-dependent lifetime studies in Y_2BaZnO_5 : Yb^{3+} (7%), Ho^{3+} (0.5%) suggest that there is an interesting change in upconversion dynamics occurring at low temperatures.

Most of the results presented in this chapter have been accepted for publication:

Efficient oxide phosphors for light upconversion; green emission from Yb^{3+} and Ho^{3+} co-doped $\text{RE}_2\text{BaZnO}_5$ ($\text{RE} = \text{Y}, \text{Gd}$), I. Etchart, I. Hernández, A. Huignard, M. Bérard, W. P. Gillin, R. J. Curry and A. K. Cheetham, *J. Mater. Chem.*, 2010, DOI:10.1039/c0jm01652g

References

- ¹ S. R. Bullock, B. R. Reddy, P. Vankateswarlu and S. K. Nash-Stevenson, *J. Opt. Soc. Am.*, 1997, **14**, 553.
- ² B. R. Reddy, S. K. Nash-Stevenson and P. Vankateswarlu, *J. Opt. Soc. Am. B*, 1994, **11**, 923.
- ³ X. Zou and H. Toratani, *J. Non-Cryst. Solids*, 1996, **201**, 37.
- ⁴ D. N. Patel, B. R. Reddy and S. K. Nash-Stevenson, *Opt. Mater.*, 1998, **10**, 225.
- ⁵ P. Muller, M. Wermuth and H. U. Güdel, *Chem. Phys. Lett.*, 1998, **290**, 105.
- ⁶ R. M. Moses, J. P. R. Wells, H. G. Gallagher, T. P. J. Han, M. Yamada, N. Kodama and T. Yosida, *Chem. Phys. Lett.*, 1998, **286**, 291.
- ⁷ S. Kuck and I. Sokólska, *Chem. Phys. Lett.*, 2000, **325**, 257.
- ⁸ L. B. Shaw, R. S. F. Chang and N. Djeu, *Phys. Rev. B*, 1994, **50**, 6609.
- ⁹ M. Malinowski, Z. Frukacz, M. Szuflińska, A. Wnuk and M. Kaczkan, *J. Alloys Compd.*, 2000, **300**, 389.
- ¹⁰ E. De la Rosa, P. Salas, H. Desirena, C. Angeles and R. A. Rodriguez, *Appl. Phys. Lett.*, 2005, **87**, 241912.
- ¹¹ W. Ryba-Romanowski, S. Golab, G. Dominiak-Dzik, P. Solarz and T. Lukasiewicz, *Appl. Phys. Lett.*, 2001, **79**, 3026.
- ¹² J. C. Boyer, F. Vetrone, J. A. Capobianco, A. Speghini, M. Zambelli and M. Bettinelli, *J. Lumin.*, 2004, **106**, 263.
- ¹³ J. A. Capobianco, J. C. Boyer, F. Vetrone, A. Speghini and M. Bettinelli, *Chem. Mater.*, 2002, **14**, 2915.
- ¹⁴ H. M. Rietveld, *J. Appl. Crystallogr.*, 1969, **2**, 65.
- ¹⁵ R. D. Shannon and C. T. Prewitt, *Acta Crystallogr.*, 1969, **B25**, 925.
- ¹⁶ R. Buisson and J. C. Vial, *J. Phys. Lett.*, 1981, **42**, L115.
- ¹⁷ E. Nakazawa, in *Phosphor Handbook*, ed. S. Shionoya and W. M. Yen, CRC Press, Boca Raton, 1999, ch. 2, p. 101.
- ¹⁸ R. S. Quimby and B. G. Aitken, *J. Non Cryst. Solids*, 2003, **320**, 100.
- ¹⁹ I. R. Martín, V. D. Rodríguez, V. Lavín and U. R. Rodríguez-Mendoza, *J. Alloys Compd.*, 1998, **275&277**, 345.

- ²⁰ J. C. Boyer, F. Vetrone, J. A. Capobianco, A. Speghini and M. Bettinelli, *Chem. Phys. Lett.*, 2004, **390**, 403.
- ²¹ R. Lisiecki, W. Ryba-Romanowski, T. Lukasiewicz, M. Mond and K. Petermann, *Laser Phys.*, 2005, **15**, 306.
- ²² Z. Wang, Y. Yin and D. Yuan, *J. Alloys Compd.*, 2007, **436**, 364.
- ²³ I. R. Martin, V. D. Rodríguez, M. Morales, U. R. Rodríguez-Mendoza and V. Lavín, *J. Appl. Spectrosc.*, 1995, **62**, 865.
- ²⁴ P. J. Derén and J. C. Krupa, *J. Alloys Compd.*, 2004, **380**, 362.
- ²⁵ L. Esterowitz, J. Noonan and J. Bahler, *Appl. Phys. Lett.*, 1967, **10**, 126.
- ²⁶ R. K. Watts, *J. Chem. Phys.*, 1970, **53**, 3552.
- ²⁷ C. B. Layne, W. H. Lowdermilk and M. J. Weber, *Phys. Rev. B*, 1997, **16**, 10.
- ²⁸ D. A. Zubenko, M. A. Noginov, V. A. Smirnov and I. A. Shcherbakov, *Phys. Rev. B*, 1997, **55**, 8881.
- ²⁹ I. Hernandez, R. H. C. Tan, J. M. Pearson, P. B. Wyatt and W. P. Gillin, *J. Phys. Chem. B*, 2009, **113**, 7474.

CHAPTER 7: Oxide phosphors for light upconversion; Yb^{3+} and Tm^{3+} co-doped Y_2BaZnO_5

7.1. Introduction

In this chapter, the optical properties of Yb^{3+} and Tm^{3+} co-doped Y_2BaZnO_5 samples synthesised by solid-state reaction, are investigated in detail for infrared to blue upconversion. The goal of this work was to produce efficient infrared to blue upconversion phosphors, and to gain an in-depth understanding of the upconversion mechanisms involved. Tm^{3+} is an excellent dopant candidate for blue light emission because of its favourable intra-atomic $4f$ energy level structure. The emission properties of Tm^{3+} have been reported under ~ 650 nm,^{1,2} 800 nm,^{3,4} 980 nm⁵⁻⁷ and 1064 nm^{2,8} excitations. In this chapter, we report, for the first time, the upconversion properties of $\text{Y}_2\text{BaZnO}_5:\text{Yb}^{3+}, \text{Tm}^{3+}$ materials. The upconversion mechanisms are elucidated through power dependence studies and lifetime measurements on samples with different dopant concentrations. Efficiencies are also reported.

7.2. Results

The outline of this result section is the following. In section 7.2.1, the crystal structure of Yb^{3+} and Tm^{3+} co-doped Y_2BaZnO_5 materials is presented (for data acquisition, the methodology presented in chapter 4, section 4.3.2 was used). Section 7.2.2 is devoted to the presentation of reflectance spectroscopy results which provide information on the energies of the Tm^{3+} and Yb^{3+} excited states in Y_2BaZnO_5 (see section 4.5.3). Subsequently, the results of steady-state luminescence experiments are presented in sections 7.2.3 to 7.2.5 (methodology in section 4.5.1). The upconversion emission spectra were recorded on samples containing different dopant concentrations, and the upconversion efficiencies were quantified under near-infrared excitation. Note that all the dopant concentrations presented in this chapter are expressed in terms of molar percentages. In sections 7.2.5 and 7.2.6, we present the results of incident power dependence studies (see section 4.5.1) and time-resolved luminescence experiments (see section 4.5.2), respectively. The concentration dependence of Yb^{3+} and Tm^{3+} excited state lifetimes is investigated in order to understand how dopant

concentrations affect upconversion mechanisms and efficiencies. It is worth noting that the upconversion luminescence measurements presented in section 7.2 were performed under either 974 nm or 977 nm excitation (depending on the equipment used). The emission properties are the same whichever excitation wavelength is used. The results presented in section 7.2 will be discussed in section 7.3 and combined in order to propose an upconversion mechanism.

7.2.1. Crystal structure

Figure 7.1 displays a typical powder X-ray diffraction pattern of $\text{Y}_2\text{BaZnO}_5: \text{Yb}^{3+}, \text{Tm}^{3+}$ materials. The crystal structure is orthorhombic, space group Pnma. Relatively pure phases were obtained, as shown by the good quality of the Rietveld refinement. Cell parameters in $\text{Y}_2\text{BaZnO}_5: \text{Yb}^{3+}$ (6%), Tm^{3+} (0.25%) are the following: $a = 12.3358(2) \text{ \AA}$, $b = 5.7087(1) \text{ \AA}$ and $c = 7.0686(1) \text{ \AA}$ (ICDD 87082). Note that the lattice parameters are slightly smaller in the doped samples than those in the pure phases, which is attributed to the smaller ionic radii of Yb^{3+} (0.093 nm) and Tm^{3+} (0.094 nm) compared to that of Y^{3+} (0.096 nm).⁹ The basic structure of Y_2BaZnO_5 compounds was presented in chapter 5, section 5.2.1.

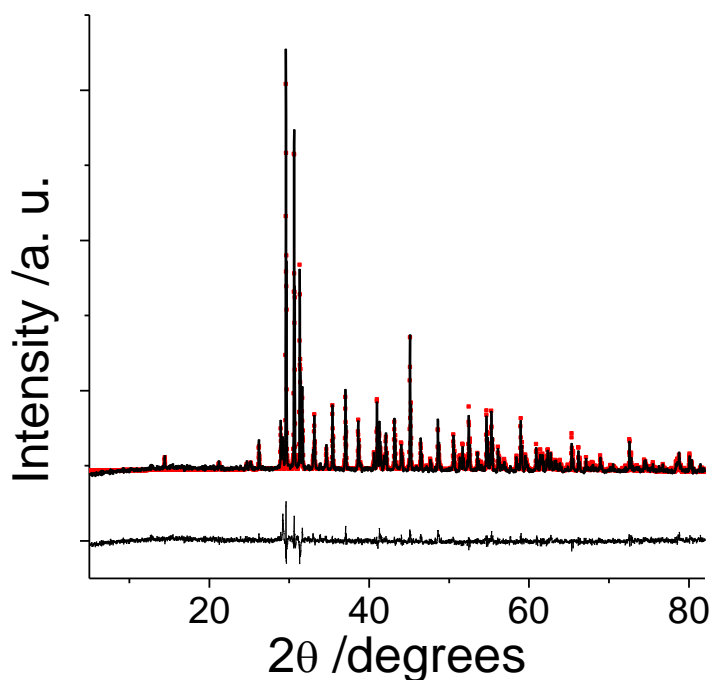


Figure 7.1: Rietveld refinement based upon the powder X-ray diffraction pattern of $\text{Y}_2\text{BaZnO}_5: \text{Yb}^{3+}$ (6%), Tm^{3+} (0.25%).

7.2.2. Reflectance in the infrared, visible and ultraviolet

A typical room-temperature reflectance spectrum of $\text{Y}_2\text{BaZnO}_5:\text{Yb}^{3+},\text{Tm}^{3+}$ samples in the range 200-1700 nm is presented in Figure 7.2. A broad absorption band assigned to the $\text{Yb}^{3+} {}^2\text{F}_{7/2} \rightarrow {}^2\text{F}_{5/2}$ absorption is observed in the 870-1040 nm region, and does not overlap with the narrow $\text{Tm}^{3+} {}^3\text{H}_6 \rightarrow {}^3\text{H}_5$ (1214 nm) or $\text{Tm}^{3+} {}^3\text{H}_6 \rightarrow {}^3\text{H}_4$ (794 nm) absorption bands. Therefore, under 974 nm and 977 nm excitation, only Yb^{3+} is directly excited .

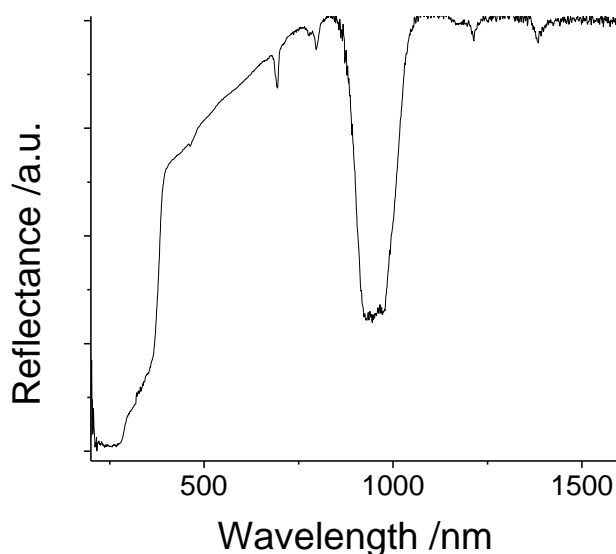


Figure 7.2: Room-temperature reflectance spectrum of $\text{Y}_2\text{BaZnO}_5:\text{Yb}^{3+}$ (6%), Tm^{3+} (0.25%).

7.2.3. Upconversion luminescence emission

Following ~ 974 nm excitation at room-temperature, $\text{Y}_2\text{BaZnO}_5:\text{Yb}^{3+},\text{Tm}^{3+}$ powders yield blue and red emission easily visible to the naked eye. Typical emission spectra show an intense near-infrared emission at around 796 nm, and considerably weaker visible emissions at around 479 nm (blue) and 654 nm (red) (Figure 7.3). The emission spectrum measured under 463 nm excitation (corresponding to the direct excitation of the $\text{Tm}^{3+} {}^1\text{G}_4$ state) is also presented in Figure 7.3 (see chapter 2, Figure 2.2). Similar red to blue emission intensity ratios are measured under 974 nm and 463 nm excitation conditions. The near-infrared to blue emission intensity ratio, however, is strongly dependent on the excitation wavelength and is considerably lower under 463 nm excitation.

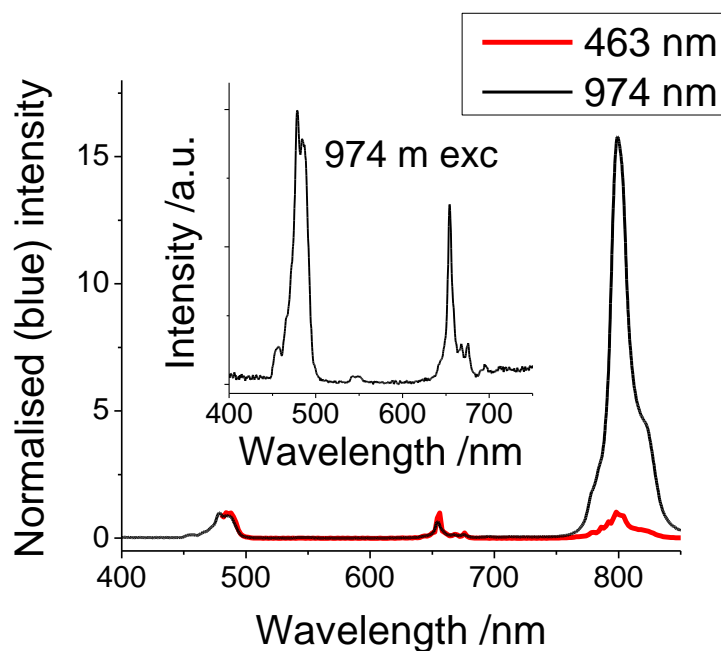


Figure 7.3: Typical room-temperature luminescence spectra of Y_2BaZnO_5 : Yb^{3+} (6%), Tm^{3+} (0.25%) phosphors under 974 nm and 463 nm excitation conditions. The inset presents an expansion of the emission spectrum in the visible range under 974 nm excitation.

The room-temperature emission spectra in the infrared of Y_2BaZnO_5 : Yb^{3+} (6%), Tm^{3+} (0.25%), under 974 nm and 463 nm excitation, present broad bands centred at around 1022 nm and 1218 nm (Figure D.1, Appendix D). Note that the 1022 nm emission is also observed under 790 nm excitation of the sample (Figure D.2, Appendix D).

7.2.4. Concentration dependence of upconversion emission properties

The upconversion emission intensity and spectral properties depend on dopant concentrations. The emission spectra of selected samples of the Y_2BaZnO_5 : Yb^{3+} (10%), Tm^{3+} (y%) ($y = 0.25, 0.5, 0.75, 1.0$) and Y_2BaZnO_5 : Yb^{3+} (x%), Tm^{3+} (0.25%) ($x = 2, 4, 6, 8, 10, 12, 14$) families are presented in Figure 7.4. For constant ytterbium concentration and in the range of Tm^{3+} concentrations studied, 0.25% Tm^{3+} results in the strongest blue emission (Figure 7.4a). For fixed Tm^{3+} concentration of 0.25%, maximum blue emission is observed for Yb^{3+} concentrations around 6% (Figure 7.4b).

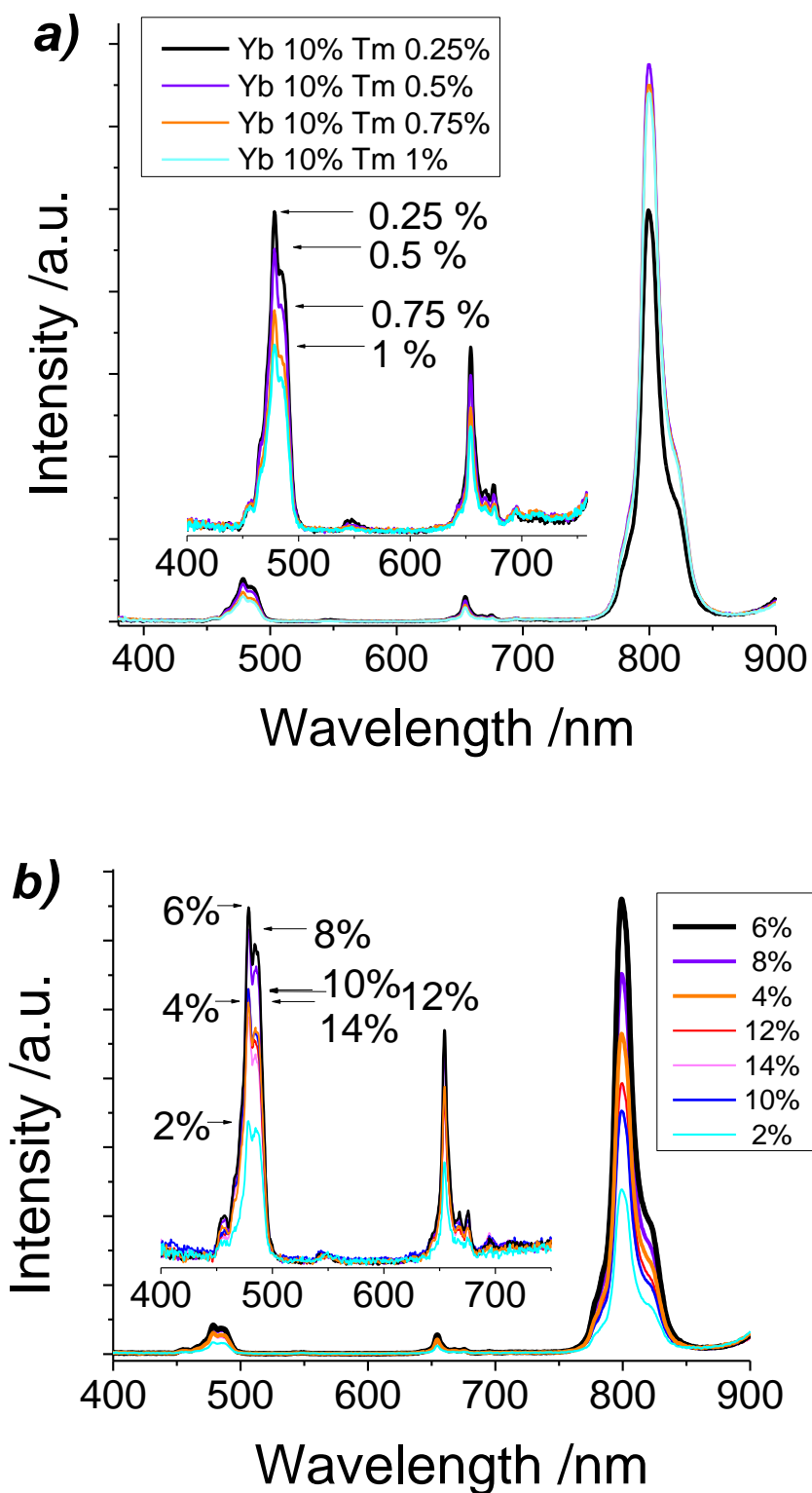


Figure 7.4: Room-temperature upconversion luminescence spectra for selected samples of the a) $\text{Y}_2\text{BaZnO}_5:\text{Yb}^{3+}$ (10%), Tm^{3+} ($y\%$) ($y = 0.25, 0.5, 0.75, 1$) and b) $\text{Y}_2\text{BaZnO}_5:\text{Yb}^{3+}$ ($x\%$), Tm^{3+} (0.25%) ($x = 2, 4, 6, 8, 10, 12, 14$) families under 977 nm excitation.

The upconversion efficiencies of a variety of $Y_2BaZnO_5: Yb^{3+}$ (x%), Tm^{3+} (y%) samples ($2 \leq x \leq 14$ and $0 \leq y \leq 2$) were measured at room-temperature under 977 nm excitation ($\sim 25 \cdot 10^{-3}$ W/mm² incident power) (Figure 7.5 and Figure D.3, Appendix D). The upconversion efficiency was calculated as the ratio of the upconversion emission in the 420-870 nm (for the total upconversion efficiency) or 420-530 nm (for the blue upconversion efficiency) range, over the power absorbed in the infrared (950-1000 nm range):

$$\eta_{UC} = \frac{P_{em}}{P_{abs}^{IR}} = \frac{P_{em}}{P_{inc}^{IR} - P_{not\ abs}^{IR}} \quad (\text{Eq. 1})$$

where P_{em} is the power of the upconversion light emitted in the 420-870 nm or 420-530 nm range, P_{abs}^{IR} is the power of the fraction of incident light that has been absorbed by the sample, P_{inc}^{IR} is the incident power in the near-infrared (integrated over the 950-1000 nm range) and $P_{not\ abs}^{IR}$ is the power of the fraction of incident light that has not been absorbed by the sample.

Among the compositions studied, samples containing around 0.25% of Tm^{3+} and 6% of Yb^{3+} were shown to exhibit the highest efficiencies for infrared to visible upconversion. Maximum upconversion efficiencies of $1.7 \pm 0.07\%$ (total upconversion efficiency integrated over the 420-870 nm emission range) and $0.086 \pm 0.003\%$ (blue upconversion efficiency integrated over the 420-530 nm range) were obtained with $Y_2BaZnO_5: Yb^{3+}$ (6%), Tm^{3+} (0.25%), at room-temperature and under $\sim 25 \cdot 10^{-3}$ W/mm² near-infrared excitation.

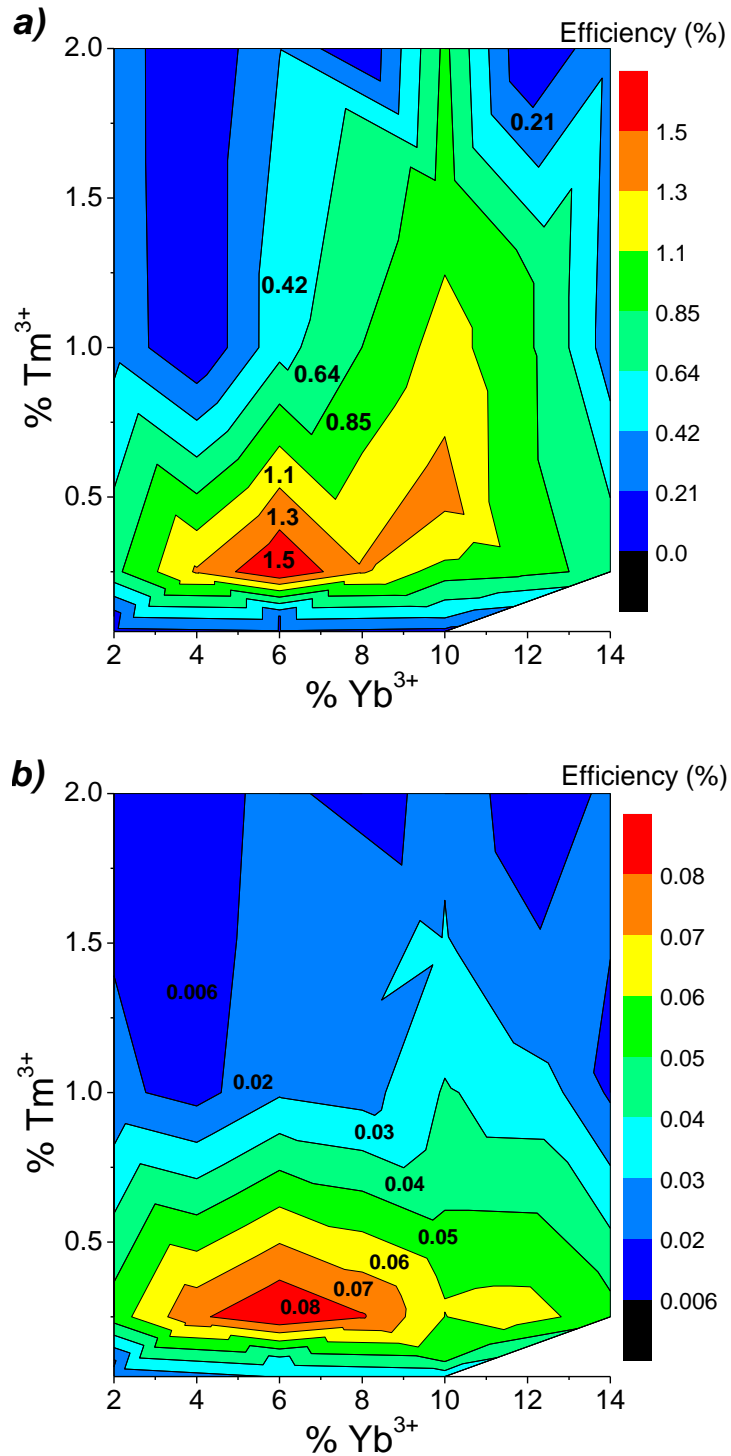


Figure 7.5: Room-temperature a) total upconversion efficiency in the 420-870 nm emission range, and b) blue upconversion efficiency in the 420-530 nm emission range, as a function of dopant concentrations for a variety of $\text{Y}_2\text{BaZnO}_5: \text{Yb}^{3+}, \text{Tm}^{3+}$ samples. The colour bar on the right is used to display the upconversion efficiency values for each dopant composition. Contour lines (lines with the same upconversion efficiency value) and contour labels displaying the UC efficiencies associated to those contour lines are also included.

7.2.5. Pump power dependence of upconversion emission

Room-temperature pump power density dependences of the blue (479 nm), red (654 nm) and near-infrared (796 nm) emissions under 977 nm excitation of $\text{Y}_2\text{BaZnO}_5: \text{Yb}^{3+}$ (6%), Tm^{3+} (0.25%) were examined, and the results are presented in a double-decadic logarithmic plot in Figure 7.6. In the low incident power regime, the near-infrared emission power presents an approximately quadratic dependence on the excitation power density, while the blue and red emission powers present a cubic behaviour (Figure 7.6).

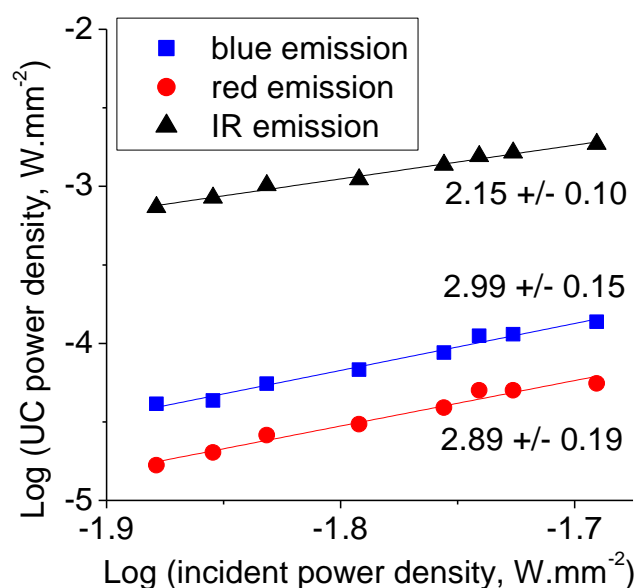


Figure 7.6: Pump power density dependence of the blue (479 nm), red (654 nm) and near-infrared (796 nm) emission powers under 977 nm excitation of $\text{Y}_2\text{BaZnO}_5: \text{Yb}^{3+}$ (6%), Tm^{3+} (0.25%) at room-temperature. The results are presented in a double-decadic logarithmic scale.

The rate equations describing the upconversion mechanism in $\text{Y}_2\text{BaZnO}_5: \text{Yb}^{3+}$, Tm^{3+} were written, simplified and solved in the steady-state regime and at low incident power (Appendix E). The population densities of the blue (479 nm) and red (654) emitting levels were predicted to exhibit a cubic dependence on the incident pump power, while a quadratic dependence was predicted for the near-infrared (796 nm) emitting level population density. Since upconversion emission intensities are proportional to the population densities of the

associated emitting levels, the experimental power dependence results are in good agreement with the theoretical predictions.

7.2.6. Lifetime measurements and dependence on dopant concentration

The transients associated with the emission lines of $\text{Y}_2\text{BaZnO}_5:\text{Yb}^{3+}$ (6%), Tm^{3+} (0.25%) centred at around 479 nm, 654 nm, 796 nm, 1040 nm and 1218 nm were recorded under pulsed 463 nm (direct excitation of $\text{Tm}^{3+} \ ^1\text{G}_4$) and 974 nm (excitation of $\text{Yb}^{3+} \ ^2\text{F}_{5/2}$) at room-temperature (see chapter 2, Figure 2.2). It is worth noting that Tm^{3+} does not absorb at 974 nm (see section 7.2.2), which guarantees a selective excitation of Yb^{3+} under 974 nm excitation. Typical transients corresponding to the room-temperature temporal evolution of the blue (479 nm), red (654 nm) and near-infrared (796 nm) emission lines under pulsed 974 nm excitation of $\text{Y}_2\text{BaZnO}_5:\text{Yb}^{3+}$ (6%), Tm^{3+} (0.25%) are presented in Figure 7.7. At the end of the 7 ns excitation pulse, no luminescence intensity is observed; instead, the transients exhibit a typical delayed rise and a decay. This is a clear fingerprint of an energy transfer process (see chapter 3, section 3.5). The experimental intensity data were fitted to the expression:¹⁰

$$I(t) = A \left(1 - e^{-\frac{t}{\tau_r}} \right) \left(e^{-\frac{t}{\tau_d}} \right) \quad (\text{Eq. 2})$$

where A is an emission intensity factor, and τ_r and τ_d represent the rise and decay times of the transient. Note that τ_r and τ_d are related to the transfer rate constants between Yb^{3+} and Tm^{3+} and to the intrinsic lifetimes of the states involved.¹⁰ The decay curves showed, in some cases, a biexponential behaviour, corresponding to decay mechanisms via two different depopulation channels. As such, when the transient decay section could not be fitted by a single exponential, the effective fluorescent decay time τ_d was determined using the following equation (discretisation of the formula used in reference ¹¹):

$$\tau_d = \frac{\sum_{i=1}^n A_i \tau_i^2}{\sum_{i=1}^n A_i \tau_i} \quad (\text{Eq. 3})$$

where A_i and τ_i are the amplitude and lifetime corresponding to the depopulation channel i and $n = 1, 2$.

The room-temperature transient decay functions associated with the blue, red and near-infrared emission lines under 974 nm excitation present 2, 2 and 1 distinct τ_i , corresponding to 2, 2 and 1 distinct depopulation channels, respectively. The values of the effective fluorescent decay times τ_d of the blue, red and near-infrared emissions in these samples are listed in Table D.1 (Appendix D). In $\text{Y}_2\text{BaZnO}_5: \text{Yb}^{3+}$ (6%), Tm^{3+} (0.25%) (composition presenting the maximum upconversion efficiency), the best fits associated with the blue, red and near-infrared transients correspond to average decay times of $\tau_d = 176 \pm 9 \mu\text{s}$, $\tau_d = 181 \pm 9 \mu\text{s}$ and $\tau_d = 435 \pm 22 \mu\text{s}$, respectively (Figure D.4 and Table D.1, Appendix D). It is worth noting that the transients associated with the blue (479 nm) and red (654 nm) emission present the same rise and decay times (within experimental errors) (Figure 7.7).

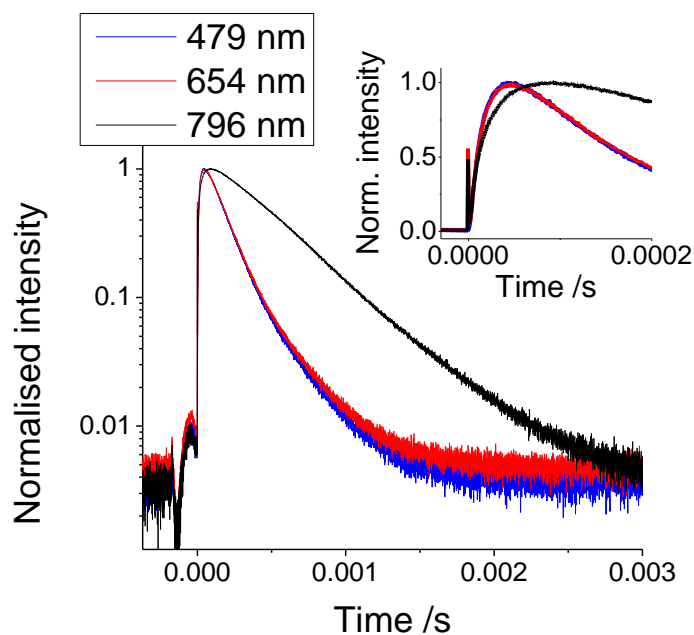


Figure 7.7: Typical room-temperature transients associated with the blue (479 nm), red (654 nm) and near-infrared (796 nm) emissions under 974 nm pulsed excitation of $\text{Y}_2\text{BaZnO}_5: \text{Yb}^{3+}$ (6%), Tm^{3+} (0.25%). The inset presents an expansion of the initial rise. Note that the small peak observed around $t \sim -45 \mu\text{s}$ is due to a triggering artefact.

The lifetimes associated with the room-temperature emissions around 479 nm, 654 nm, 796 nm, 1022 nm and 1218 nm were measured for a variety of samples of the a) $\text{Y}_2\text{BaZnO}_5: \text{Yb}^{3+}$ (10%), Tm^{3+} (y%) (y = 0.25, 0.5, 1, 2) and b) $\text{Y}_2\text{BaZnO}_5: \text{Yb}^{3+}$ (x%), Tm^{3+} (0.25%) (x = 0, 2,

6, 10) families under 974 nm and 463 nm pulsed excitations (Figure 7.8, Table D.1, Appendix D). The typical percentage error on lifetime measurements was estimated to be on the order of 5%. For clarity, the error bars are not shown in Figure 7.8a and Figure 7.8b.

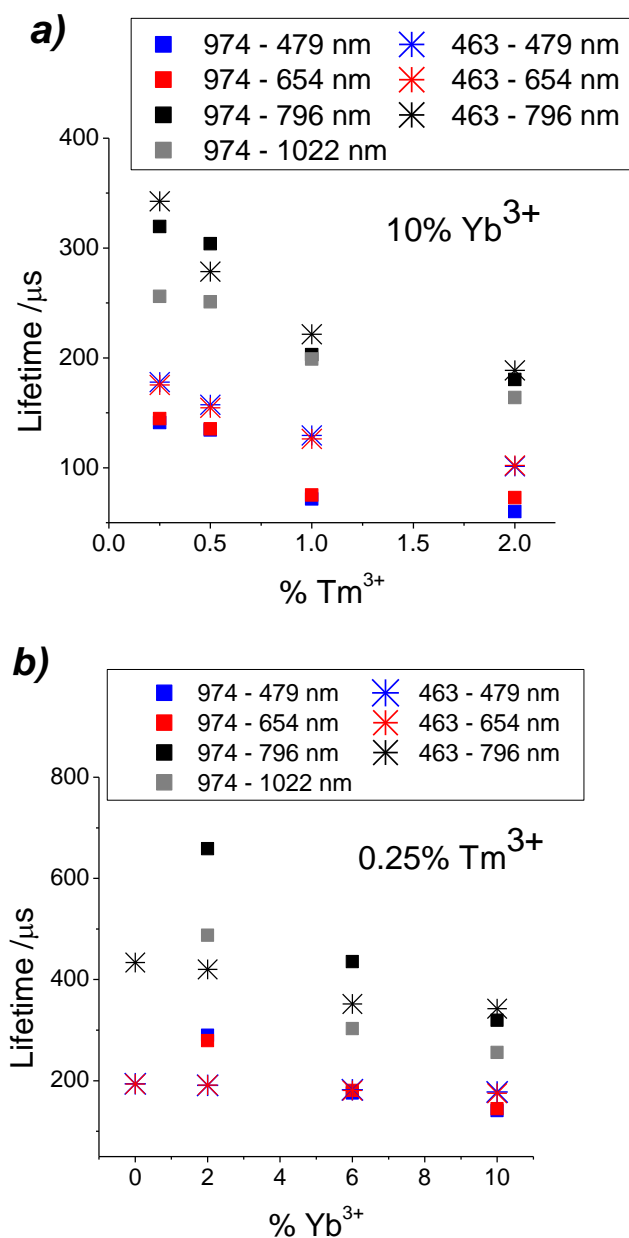


Figure 7.8: Concentration dependence of the lifetimes corresponding to the room-temperature emissions around 479 nm, 654 nm, 796 nm and 1022 nm in a variety of samples of the a) $\text{Y}_2\text{BaZnO}_5:\text{Yb}^{3+}$ (10%), Tm^{3+} (y%) ($y = 0.25, 0.5, 1, 2$) and b) $\text{Y}_2\text{BaZnO}_5:\text{Yb}^{3+}$ (x%), Tm^{3+} (0.25%) ($x = 0, 2, 6, 10$) families under 974 nm and 463 nm pulsed excitations. The legend of the figure is of the form ‘X – Y nm’ where X and Y are the excitation and emission wavelengths, respectively.

The lifetimes associated with the blue (479 nm), red (654 nm), near-infrared (760 nm) and infrared (1022 nm) emissions under direct excitation (~ 463 nm) and upconversion excitation (~ 974 nm) decrease with increasing Tm^{3+} concentration (Figure 7.8a and Table D.1, Appendix D). The lifetimes associated with the 479 nm and 654 nm emissions are similar (within experimental errors) in the whole range of Tm^{3+} concentrations studied, It is worth noting that, in the Tm^{3+} concentration range that we investigated, the decrease in lifetimes occurs mainly when increasing the Tm^{3+} concentration from 0.5% to 1%.

The Yb^{3+} concentration dependence of the room-temperature lifetimes associated with the 479 nm, 654 nm, 796 nm and 1022 nm emissions in $\text{Y}_2\text{BaZnO}_5: \text{Yb}^{3+}(\text{x}\%), \text{Tm}^{3+}(0.25\%)$ ($x = 0, 2, 6, 10$) samples is presented in Figure 7.8b (the lifetime values are reported on Table D.1, Appendix D). The lifetimes decrease with increasing Yb^{3+} concentration. Again, the lifetimes associated with the 479 nm and 654 nm emissions are similar (within experimental errors) in the whole range of Yb^{3+} concentrations studied (this is true under 974 nm and 463 nm excitation conditions). As shown in Table D.1 (Appendix D), the lifetimes for all the emission centres decrease upon 974 nm excitation. The lifetimes measured under direct 463 nm excitation present a different dependence on Yb^{3+} concentration. Under 463 nm excitation, the lifetimes associated with the blue (479 nm) and red (654 nm) emissions are quasi invariant in the Yb^{3+} concentration range that was investigated; for instance, the lifetimes associated with the emission at 479 nm take the values $\tau_d^{direct} \sim 191 \pm 10 \mu\text{s}$ for 2% Yb^{3+} and $\tau_d^{direct} \sim 176.5 \pm 9 \mu\text{s}$ for 10% Yb^{3+} (Figure 7.8b and Table D.1, Appendix D).

A careful inspection of the emission spectra in Figure 7.3 and Figure 7.4a reveals the presence of a small emission band around 454 nm. The lifetime associated with that emission is significantly shorter than that of the 479 nm emission (Figure D.5, Appendix D).

7.3. Discussion

7.3.1. Population mechanisms of the excited levels

A detailed investigation of the steady-state and dynamic emission properties of a variety of $\text{Y}_2\text{BaZnO}_5: \text{Yb}^{3+}(\text{x}\%), \text{Tm}^{3+}(\text{y}\%)$ ($0 \leq x \leq 14$ and $0 \leq y \leq 2$) samples was performed and the results were presented in the previous section. Under 974 nm excitation, the samples present blue and red upconversion emissions visible to the naked eye. The emission spectra reveal the

presence of emission bands centred around 479 nm (blue emission), 654 nm (red emission) and 796 nm (near-infrared emission). Under 974 nm excitation, the transients corresponding to the emissions centred at 479 nm, 654 nm and 796 nm display a clear rise time after the excitation is turned off, indicating that the population mechanisms of the states from which these emissions arise involve at least one Yb^{3+} to Tm^{3+} energy transfer step (Figure 7.7). Power dependence studies show that, under 974 nm excitation, the emission centred around 796 nm exhibits a quadratic dependence on the excitation power, indicating a two-photon population process of its emitting state(s) (Figure 7.6). The emissions centred around 479 nm and 654 nm show a cubic dependence, indicating a three-photon population process (Figure 7.6). According to the energy diagram of Tm^{3+} represented in Figure 7.9,¹² the blue emission centred at 479 nm can be exclusively assigned to the $\text{Tm}^{3+} \ ^1\text{G}_4 \rightarrow \ ^3\text{H}_6$ transition. The red emission (654 nm) could be attributed to $\text{Tm}^{3+} \ ^1\text{G}_4 \rightarrow \ ^3\text{F}_4$,^{6,7,13} and/or $\text{Tm}^{3+} \ ^3\text{F}_{2,3} \rightarrow \ ^3\text{H}_6$ transitions,^{5,7,13} and the near-infrared emission (796 nm) to $\text{Tm}^{3+} \ ^3\text{H}_4 \rightarrow \ ^3\text{H}_6$,^{7,13,14} and/or $\text{Tm}^{3+} \ ^1\text{G}_4 \rightarrow \ ^3\text{H}_5$ ^{6,7,13} transitions. The similarity in the lifetimes and rise times associated with the 479 nm and 654 nm emissions over the whole range of concentrations studied (Figure 7.7, Figure 7.8) suggests that these two emissions essentially arise from the same multiplet of Tm^{3+} , in particular $\ ^1\text{G}_4$. The transient corresponding to the 796 nm emission presents a mono-exponential behaviour (Figure 7.7) with a characteristic lifetime that is significantly longer than that of the blue (479 nm) and red (654 nm) emissions (Figure 7.8). In view of these results, the emissions centred at 654 nm and 796 nm can be exclusively assigned to the $\text{Tm}^{3+} \ ^1\text{G}_4 \rightarrow \ ^3\text{F}_4$ and $\text{Tm}^{3+} \ ^3\text{H}_4 \rightarrow \ ^3\text{H}_6$ transitions, respectively. The infrared emissions centred around 1022 nm (broad emission) and 1218 nm can be attributed to the $\text{Yb}^{3+} \ ^2\text{F}_{5/2} \rightarrow \ ^2\text{F}_{7/2}$ and $\text{Tm}^{3+} \ ^3\text{H}_5 \rightarrow \ ^3\text{H}_6$ transitions, respectively.

According to our findings, the population of the $\text{Tm}^{3+} \ ^3\text{H}_4$ state, from which the strong near-infrared emission at 796 nm arises, involves two successive Yb^{3+} to Tm^{3+} energy transfers (ET) with intermediate multiphonon relaxation steps; $\text{Yb}^{3+} \ ^2\text{F}_{5/2} + \text{Tm}^{3+} \ ^3\text{H}_6 \rightarrow \text{Yb}^{3+} \ ^2\text{F}_{7/2} + \text{Tm}^{3+} \ ^3\text{H}_5$ (first ET), $\text{Tm}^{3+} \ ^3\text{H}_5 \rightarrow \ ^3\text{F}_4$ (multiphonon relaxation), $\text{Yb}^{3+} \ ^2\text{F}_{5/2} + \text{Tm}^{3+} \ ^3\text{F}_4 \rightarrow \text{Yb}^{3+} \ ^2\text{F}_{7/2} + \text{Tm}^{3+} \ ^3\text{F}_{2,3}$ (second ET), $\text{Tm}^{3+} \ ^3\text{F}_{2,3} \rightarrow \ ^3\text{H}_4$ (multiphonon relaxation), as shown in Figure 7.9. The blue (479 nm) and red (654 nm) emissions arising from the $\text{Tm}^{3+} \ ^1\text{G}_4$ state require an additional energy transfer step: $\text{Yb}^{3+} \ ^2\text{F}_{5/2} + \text{Tm}^{3+} \ ^3\text{H}_4 \rightarrow \text{Yb}^{3+} \ ^2\text{F}_{7/2} + \text{Tm}^{3+} \ ^1\text{G}_4$ (third ET).

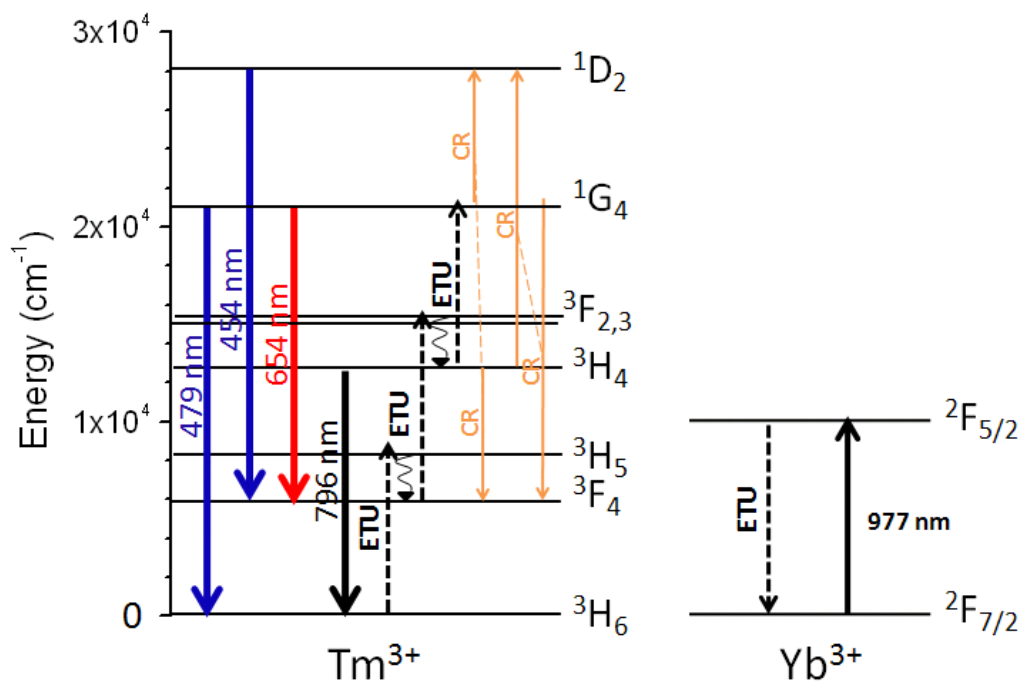


Figure 7.9: Simplified energy diagram of Tm^{3+} and Yb^{3+} ions and the dominant upconversion mechanisms in $\text{Y}_2\text{BaZnO}_5: \text{Yb}^{3+}, \text{Tm}^{3+}$. Blue, red and near-infrared luminescence, as well as (non-resonant) non-radiative energy transfer upconversion (ETU), multiphonon relaxation, and cross-relaxation (CR) processes, are represented.

The near-infrared (796 nm) to blue (479 nm) emission intensity ratio is much smaller under 463 nm excitation than it is under 974 nm excitation (Figure 7.3). This can be assigned to the fact that, compared to the $\text{Tm}^{3+} 1\text{G}_4$ state, the $\text{Tm}^{3+} 3\text{H}_4$ state is relatively much more populated under upconverting conditions (by two successive Yb^{3+} to Tm^{3+} energy transfer steps) than it is by multiphonon relaxation under direct excitation of $\text{Tm}^{3+} 1\text{G}_4$. Again, the $\text{Tm}^{3+} 1\text{G}_4$ state population under upconverting conditions requires three successive Yb^{3+} to Tm^{3+} energy transfers, while the $\text{Tm}^{3+} 3\text{H}_4$ state population only requires two.

7.3.2. Tm^{3+} concentration dependence of lifetimes

The decrease in $\text{Tm}^{3+} 1\text{G}_4$ lifetimes with increasing Tm^{3+} concentration under direct 463 nm excitation (Figure 7.8a) suggests the existence of cross-relaxation mechanisms between Tm^{3+}

ions that depopulate the $\text{Tm}^{3+} \ ^1\text{G}_4$ state. According to the energy diagram of Tm^{3+} (Figure 7.9), this could be attributed to the following cross-relaxations:

- 1) $\text{Tm}^{3+} \ ^1\text{G}_4 + \text{Tm}^{3+} \ ^3\text{H}_4 \rightarrow \text{Tm}^{3+} \ ^3\text{F}_4 + \text{Tm}^{3+} \ ^1\text{D}_2$ ^{13,15}
- 2) $\text{Tm}^{3+} \ ^3\text{H}_4 + \text{Tm}^{3+} \ ^1\text{G}_4 \rightarrow \text{Tm}^{3+} \ ^3\text{F}_4 + \text{Tm}^{3+} \ ^1\text{D}_2$ ^{13,15} and/or
- 3) $\text{Tm}^{3+} \ ^1\text{G}_4 + \text{Tm}^{3+} \ ^3\text{H}_6 \rightarrow \text{Tm}^{3+} \ ^3\text{H}_5 + \text{Tm}^{3+} \ ^3\text{H}_4$ ¹⁶
- 4) $\text{Tm}^{3+} \ ^3\text{H}_6 + \text{Tm}^{3+} \ ^1\text{G}_4 \rightarrow \text{Tm}^{3+} \ ^3\text{H}_5 + \text{Tm}^{3+} \ ^3\text{H}_4$ ¹⁶

All these processes are expected to depopulate the $\text{Tm}^{3+} \ ^1\text{G}_4$ level at high Tm^{3+} concentrations, which is in agreement with the results presented on Figure 7.4a. Processes 1) and 2) are also expected to depopulate the 796 nm emitting level $\text{Tm}^{3+} \ ^3\text{H}_4$ level while processes 3) and 4) populate it. According to Figure 7.4a, for Tm^{3+} concentrations higher than 0.5%, the 796 nm emission intensity decreases with increasing Tm^{3+} concentration; processes 3) and 4) can therefore be ruled out. A careful observation of the emission spectra in Figure 7.3 and Figure 7.4a reveals the presence of a small emission band around 454 nm. According to the energy diagram (Figure 7.9), the emission at 454 nm can be assigned to the $\text{Tm}^{3+} \ ^1\text{D}_2 \rightarrow \ ^3\text{F}_4$ transition. Note that the population of $\text{Tm}^{3+} \ ^1\text{D}_2$ via a fourth Yb^{3+} to Tm^{3+} energy transfer is very unlikely, due to the large energy mismatch (about 3500 cm^{-1}) between the $\text{Yb}^{3+} \ ^2\text{F}_{5/2} - \ ^2\text{F}_{7/2}$ and $\text{Tm}^{3+} \ ^1\text{D}_2 - \ ^1\text{G}_4$ energy gaps. ^{13,15} The existence of the 454 nm emission band confirms that cross-relaxation processes 1) and 2) are relevant at high Tm^{3+} concentrations. At least two emission bands centred at around 365 nm and 454 nm arise from the $\text{Tm}^{3+} \ ^1\text{D}_2$ state. The decrease in $\text{Tm}^{3+} \ ^3\text{H}_4$ lifetimes with increasing Tm^{3+} concentration under 463 nm excitation (Figure 7.8a and Table D.1, Appendix D) is in good agreement with the existence of cross-relaxation mechanisms between Tm^{3+} ions via processes 1) and 2). The lifetimes associated with the $\text{Yb}^{3+} \ ^2\text{F}_{5/2} \rightarrow \ ^2\text{F}_{7/2}$ emission (1022 nm) decrease with increasing Tm^{3+} concentration (Figure 7.8a). This can be attributed to an increase in Yb^{3+} to Tm^{3+} energy transfer probabilities due to a decrease in the average $\text{Yb}^{3+} - \text{Tm}^{3+}$ distance. Under 974 nm excitation, the lifetimes associated with the 479 nm, 654 nm and 796 nm emissions in $\text{Y}_2\text{BaZnO}_5: \text{Yb}^{3+} (10\%), \text{Tm}^{3+} (y\%)$ ($y = 0.25, 0.5, 1, 2$) materials also decrease with increasing dopant concentration, following the same trend as that of the $\text{Yb}^{3+} \ ^2\text{F}_{5/2}$ lifetimes (Figure 7.8a, Table D.1 Appendix D). This suggests that $\text{Yb}^{3+} - \text{Tm}^{3+}$ interaction dynamics govern the upconversion temporal behaviour under 974 nm excitation (and not the intrinsic de-excitation of Tm^{3+} multiplets).

7.3.3. Yb^{3+} concentration dependence of lifetimes

Under 463 nm excitation, the lifetimes associated with the 479 nm and 654 nm emissions (arising from $\text{Tm}^{3+} \ ^1\text{G}_4$) are almost invariant in the range of Yb^{3+} concentrations that we studied (Figure 7.8b and Table D.1, Appendix D). This suggests that the intrinsic lifetime of $\text{Tm}^{3+} \ ^1\text{G}_4$ is almost unaffected by the Yb^{3+} concentration present in the samples. The very slight decrease in lifetimes with increasing Yb^{3+} concentration could be attributed to energy transfer between Tm^{3+} and Yb^{3+} , depopulating $\text{Tm}^{3+} \ ^1\text{G}_4$ at high Yb^{3+} concentrations. The existence of energy transfer mechanisms is further supported by the observation of a small emission from Yb^{3+} centred around 1022 nm under selective Tm^{3+} excitation at 463 nm (Figure D.1, Appendix D). Under 463 nm excitation, the lifetimes associated with the 796 nm emission (from $\text{Tm}^{3+} \ ^3\text{H}_4$) decrease with increasing Yb^{3+} concentration (Figure 7.8b and Table D.1, Appendix D) due to the energy transfer between Tm^{3+} and Yb^{3+} , depopulating $\text{Tm}^{3+} \ ^3\text{H}_4$ at high Yb^{3+} concentrations.¹⁷ The Yb^{3+} emission around 1022 nm is also observed under selective Tm^{3+} excitation at 790 nm (Figure D.2, Appendix D), corroborating the presence of such energy transfers.

The lifetimes associated with the $\text{Yb}^{3+} \ ^2\text{F}_{5/2} \rightarrow \ ^2\text{F}_{7/2}$ emission (1022 nm) decrease significantly with increasing Yb^{3+} concentration (Figure 7.8b). We have observed that excitation hopping between Yb^{3+} ions does not contribute significantly to the $\text{Yb}^{3+} \ ^2\text{F}_{5/2}$ lifetime, as no significant concentration dependence has been found with the Yb^{3+} concentration, in singly doped samples. Besides, the lifetimes measured on Yb^{3+} singly-doped samples were significantly higher than those of Yb^{3+} , Tm^{3+} co-doped samples. The decrease in $\text{Yb}^{3+} \ ^2\text{F}_{5/2}$ lifetimes can therefore be attributed to an increase in Yb^{3+} to Tm^{3+} energy transfer rates. Under 974 nm excitation, the Yb^{3+} concentration dependence of the lifetimes associated with the 479 nm, 654 nm and 796 nm emissions in Y_2BaZnO_5 : Yb^{3+} (x%), Tm^{3+} (0.25%) (x = 0, 2, 6, 10) samples is significantly different from that observed under 463 nm excitation. In particular, the $\text{Tm}^{3+} \ ^1\text{G}_4$ and $\text{Tm}^{3+} \ ^3\text{H}_4$ level lifetimes decrease markedly with increasing Yb^{3+} concentration, following the same trend as that of the $\text{Yb}^{3+} \ ^2\text{F}_{5/2}$ lifetimes. This supports the view that Yb^{3+} - Tm^{3+} interaction dynamics play a dominant role in the observed upconversion emitting level lifetimes.

7.4. Conclusions

The upconversion properties of $\text{Y}_2\text{BaZnO}_5: \text{Yb}^{3+}, \text{Tm}^{3+}$ oxide materials were investigated as a function of dopant concentration. Power dependence studies and lifetime measurements provided a model for the upconversion mechanisms involved in these materials. The strong near-infrared (796 nm) emission arises from the $\text{Tm}^{3+} {}^3\text{H}_4$ level populated via two successive Yb^{3+} to Tm^{3+} energy transfer steps. The weaker blue (479 nm) and red (654 nm) emissions originate from $\text{Tm}^{3+} {}^1\text{G}_4$ and involve three energy transfer steps. Maximum upconversion efficiencies of $1.70 \pm 0.07\%$ (420-870 nm emission range) and $0.086 \pm 0.003\%$ (420-530 nm emission range) were obtained in $\text{Y}_2\text{BaZnO}_5: \text{Yb}^{3+}$ (6%), Tm^{3+} (0.25%) at room-temperature under $\sim 25 \cdot 10^{-3} \text{ W/mm}^2$ excitation. As expected, the efficiency of the blue emission is lower than that of the green and red emissions in Yb^{3+} , Er^{3+} and Yb^{3+} , Ho^{3+} co-doped samples because it is a three-photon process (and not a two-photon process as the green and red emissions by Er^{3+} and Ho^{3+}). Cross-relaxation mechanisms have been found for higher Tm^{3+} concentrations, and are responsible for the depopulation of the states from which the 479 nm, 654 nm and 796 nm emissions originate. The present work has shown that we can upconvert ~ 977 nm infrared radiation to produce blue light with reasonable efficiency. This opens up the possibility of creating white light by combining the present Yb^{3+} , Tm^{3+} co-doped material with our Yb^{3+} , Er^{3+} (red plus green) phosphors (presented in chapter 5), in order to produce white light. We will explore this possibility in the next chapter.

Most of the results presented in this chapter have been submitted for publication:

Oxide phosphors for light upconversion; Yb^{3+} and Tm^{3+} co-doped Y_2BaZnO_5 , I. Etchart, I. Hernández, A. Huignard, M. Bérard, M. Laroche, W. P. Gillin, R. J. Curry and A. K. Cheetham, submitted for publication.

References

- ¹ S. Tanabe, K. Suzuki, N. Soga and T. Hanada, *J. Opt. Soc. Am. B*, 1994, **11**, 933.
- ² D. C. Hanna, R. M. Percival, I. R. Perry, R. G. Smart, J. E. Townsend and A. C. Tropper, *Opt. Commun.*, 1990, **78**, 187.
- ³ N. Rakov, G. S. Maciel, M. L. Sundheimer, S. L. D. Menezes, A. S. L. Gomes, Y. Messaddeq, F. C. Cassanjes, G. Poirier and S. J. L. Ribeiro, *J. Appl. Phys.*, 2002, **92**, 6337.
- ⁴ I. R. Martín, J. Méndez-Ramos, V. D. Rodríguez, J. J. Romero and J. García-Solé, *Opt. Mater.*, 2003, **22**, 327.
- ⁵ J. F. Suyver, J. Grimm, M. K. van Veen, D. Biner, K. W. Krämer and H. U. Güdel, *J. Lumin.*, 2006, **117**, 1.
- ⁶ R. J. Thrash and L. J. Johnson, *J. Opt. Soc. Am. B*, 1994, **11**, 881.
- ⁷ Q. Y. Zhang, T. Li, Z. H. Jiang, X. H. Ji and S. Buddhudu, *Appl. Phys. Lett.*, 2005, **87**, 171911.
- ⁸ T. Komukai, T. Yamamoto, T. Sugawa and Y. Miyajima, *IEEE J. Quantum. Electron.*, 1995, **31**, 1880.
- ⁹ R. D. Shannon and C. T. Prewitt, *Acta Crystallogr.*, 1969, **B25**, 925.
- ¹⁰ R. Buisson and J. C. Vial, *J. Phys. Lett.*, 1981, **42**, L115.
- ¹¹ E. Nakazawa, in *Phosphor Handbook*, ed. S. Shionoya and W. M. Yen, CRC Press, Boca Raton, 1999, ch. 2, p. 101.
- ¹² G. H. Dieke, *Spectra and energy levels of rare earth ions in crystals*, Interscience Publishers, New York, 1968.
- ¹³ N. K. Giri, S. K. Singh, D. K. Rai and S. B. Rai, *Appl. Phys. B*, 2010, **99**, 271.
- ¹⁴ R. Lisiecki, G. Dominiak-Dzik, T. Lukasiewicz and W. Ryba-Romanowski, *J. Mol. Struct.*, 2004, **704**, 323.
- ¹⁵ X. B. Chen and Z. F. Song, *J. Opt. Soc. Am. B*, 2007, **24**, 965.
- ¹⁶ W. Guo, Y. Chen, Y. Lin, X. Gong, Z. Luo and Y. Huang, *J. Phys. D: Appl. Phys.*, 2008, **41**, 115409.
- ¹⁷ F. Pandozzi, F. Vetrone, J. C. Boyer, R. Naccache, J. A. Capobianco, A. Speghini and M. Bettinelli, *J. Phys. Chem. B*, 2005, **109**, 17400.

CHAPTER 8: White light emission in Yb^{3+} , Er^{3+} and Tm^{3+} doped Y_2BaZnO_5

8.1. Introduction

In the previous chapters, we have seen that green, red and blue light can be produced by upconversion in $\text{Y}_2\text{BaZnO}_5: \text{Yb}^{3+}, \text{Er}^{3+}$ (emission in the green and in the red) (chapter 5), $\text{Y}_2\text{BaZnO}_5: \text{Yb}^{3+}, \text{Ho}^{3+}$ (emission in the green) (chapter 6) and $\text{Y}_2\text{BaZnO}_5: \text{Yb}^{3+}, \text{Tm}^{3+}$ (emission in the blue) (chapter 7) compounds, under near-infrared excitation at room-temperature. A broad range of emission colours can therefore be obtained by combining the blue, green and red emissions via an incorporation of multiple dopants in various molar ratios. In the literature, a few reports can be found on white light production, usually in materials tri-doped with $\text{Yb}^{3+}, \text{Er}^{3+}, \text{Tm}^{3+}$,¹⁻³ $\text{Yb}^{3+}, \text{Ho}^{3+}, \text{Tm}^{3+}$,^{4,5} or $\text{Yb}^{3+}, \text{Er}^{3+}, \text{Pr}^{3+}$,⁶ and excited in the near-infrared (~ 980 nm).

In this chapter, we report on the first design of white upconversion luminescence in $\text{Yb}^{3+}, \text{Er}^{3+}, \text{Tm}^{3+}$ -doped Y_2BaZnO_5 phosphors under near-infrared excitation (~ 980 nm). White light is produced via two strategies; host tri-doping and powder mixing. The steady-state and dynamic upconversion properties are investigated. The upconversion efficiencies of the white emitting compositions are quantified precisely and the CIE (Commission Internationale de l'éclairage) x, y colour coordinates are measured.

8.2. Two different strategies for white light production

The white light emitting compounds presented in this chapter have been produced via two different methods.

The first method consisted of doping Y_2BaZnO_5 with three dopants: Er^{3+} (for red and green emission), Tm^{3+} (for blue emission) and Yb^{3+} (sensitiser for Er^{3+} and Tm^{3+}) in one single phase. The samples produced by host tri-doping are denoted $\text{Y}_2\text{BaZnO}_5: \text{Yb}^{3+}, \text{Er}^{3+}, \text{Tm}^{3+}$ in this chapter. Upon optimisation of the ratios between the concentrations of $\text{Yb}^{3+}, \text{Er}^{3+}$ and Tm^{3+} , white light could be produced.

In the second method, two powders, namely $\text{Y}_2\text{BaZnO}_5: \text{Yb}^{3+}, \text{Er}^{3+}$ (red and green emission) and $\text{Y}_2\text{BaZnO}_5: \text{Yb}^{3+}, \text{Tm}^{3+}$ (blue emission) were thoroughly mixed together (via a 20-minute grinding with a small amount of acetone). The samples produced via powder mixing are denoted $\text{Y}_2\text{BaZnO}_5: \text{Yb}^{3+}, \text{Er}^{3+} + \text{Y}_2\text{BaZnO}_5: \text{Yb}^{3+}, \text{Tm}^{3+}$ in this chapter. For given individual $\text{Y}_2\text{BaZnO}_5: \text{Yb}^{3+}, \text{Er}^{3+}$ and $\text{Y}_2\text{BaZnO}_5: \text{Yb}^{3+}, \text{Tm}^{3+}$ compositions (i.e. fixed concentrations of Yb^{3+} , Er^{3+} and Tm^{3+} in the 2 individual powders to be mixed), the mass ratio of the 2 powders was adjusted in order to obtain white emission.

8.3. Results

The outline of this result section is the following: in section 8.3.1, the crystal structure of Y_2BaZnO_5 materials doped with Yb^{3+} , Er^{3+} and Tm^{3+} is presented for samples prepared by host-tridoping and powder mixing (see section 4.3.2). Section 8.3.2 is devoted to the presentation of reflectance spectroscopy results, which provide information on the energy levels of the Er^{3+} , Tm^{3+} and Yb^{3+} excited states (see section 4.5.3). Subsequently, the results of steady-state emission spectra acquisition and efficiency quantification are presented in sections 8.3.3 (see section 4.5.1 for methodology). Note that all the dopant concentrations presented in this chapter are expressed in terms of molar percentages. In sections 8.3.4, we present the results of time-resolved luminescence studies (see section 4.5.2). The emission spectra of the white emitting compounds under selective dopant excitation are presented in section 8.3.5. All the results are combined in section 8.4 in order to propose a model for the upconversion mechanism in white light emitting upconversion materials.

8.3.1. Crystal structure

Figure 8.1 displays the typical powder X-ray diffraction patterns of *a*) a tri-doped $\text{Y}_2\text{BaZnO}_5: \text{Yb}^{3+}, \text{Er}^{3+}, \text{Tm}^{3+}$ compound, and of *b*) a $\text{Y}_2\text{BaZnO}_5: \text{Yb}^{3+}, \text{Er}^{3+} + \text{Y}_2\text{BaZnO}_5: \text{Yb}^{3+}, \text{Tm}^{3+}$ powder mixture.

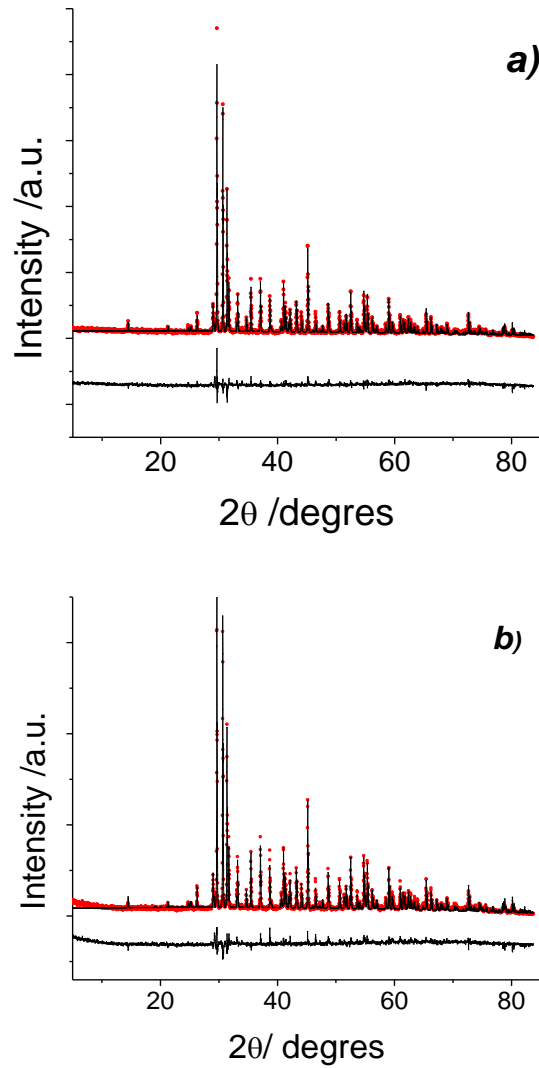


Figure 8.1: Rietveld refinements based upon the X-ray powder diffraction pattern of a) $\text{Y}_2\text{BaZnO}_5:\text{Yb}^{3+}$ (10%), Er^{3+} (0.3%), Tm^{3+} (1%), and b) a $\text{Y}_2\text{BaZnO}_5:\text{Yb}^{3+}$ (10%), Er^{3+} (0.4%) (4.8% w/w) + $\text{Y}_2\text{BaZnO}_5:\text{Yb}^{3+}$ (10%), Tm^{3+} (0.25%) (95.2% w/w) powder mixture.

The crystal structure of a) is orthorhombic, space group Pnma. Relatively pure phases were obtained, as shown by the good quality of the Rietveld refinement (Figure 8.1a). The cell parameters of $\text{Y}_2\text{BaZnO}_5:\text{Yb}^{3+}$ (10%), Er^{3+} (0.3%), Tm^{3+} (1%) were obtained: $a = 12.3283(2)$ Å, $b = 5.7056(1)$ Å and $c = 7.0646(1)$ Å (ICDD 87082). Note that the lattice parameters are slightly smaller in the doped samples than those in the pure phases, which is attributed to the smaller ionic radii of Yb^{3+} (0.093 nm), Er^{3+} (0.0945 nm) and Tm^{3+} (0.094 nm) compared to Y^{3+} (0.096 nm).⁷

In Figure 8.1b, the peaks associated with the XRD diffraction patterns of $\text{Y}_2\text{BaZnO}_5: \text{Yb}^{3+}, \text{Er}^{3+}$ and $\text{Y}_2\text{BaZnO}_5: \text{Yb}^{3+}, \text{Tm}^{3+}$ cannot be resolved. This is due to the good ionic radii match of Er^{3+} (0.0945 nm) and Tm^{3+} (0.094 nm) and to the similar Y : Yb : Er and Y : Yb : Tm molar ratios in both samples. The following cell parameters were obtained for the $\text{Y}_2\text{BaZnO}_5: \text{Yb}^{3+}$ (10%), Er^{3+} (0.4%) (4.8% w/w) + $\text{Y}_2\text{BaZnO}_5: \text{Yb}^{3+}$ (10%), Tm^{3+} (0.25%) (95.2% w/w) powder mixture, based on a single-phase Rietveld refinement: $a = 12.3286(2) \text{ \AA}$, $b = 5.7060(1) \text{ \AA}$ and $c = 7.0647(1) \text{ \AA}$ (ICDD 87082). The basic structure of Y_2BaZnO_5 was presented in chapter 5, section 5.2.1.

8.3.2. Reflectance in the infrared

The typical room-temperature reflectance spectra of *a*) a $\text{Y}_2\text{BaZnO}_5: \text{Yb}^{3+}, \text{Er}^{3+}, \text{Tm}^{3+}$ tri-doped sample, and *b*) a $\text{Y}_2\text{BaZnO}_5: \text{Yb}^{3+}, \text{Er}^{3+}$ + $\text{Y}_2\text{BaZnO}_5: \text{Yb}^{3+}, \text{Tm}^{3+}$ powder mixture, in the range 600-1300 nm, are presented in Figure 8.2. A broad absorption band due to the $\text{Yb}^{3+} {}^2\text{F}_{7/2} \rightarrow {}^2\text{F}_{5/2}$ transition is observed in the 870-1040 nm region, and overlaps with the $\text{Er}^{3+} {}^4\text{I}_{15/2} \rightarrow {}^4\text{I}_{11/2}$ absorption band around 977 nm, but not with the $\text{Tm}^{3+} {}^3\text{H}_6 \rightarrow {}^3\text{H}_5$ (1214 nm) or $\text{Tm}^{3+} {}^3\text{H}_6 \rightarrow {}^3\text{H}_4$ (794 nm) absorption bands. Therefore, upon 977 nm excitation, only Yb^{3+} and Er^{3+} are directly excited.

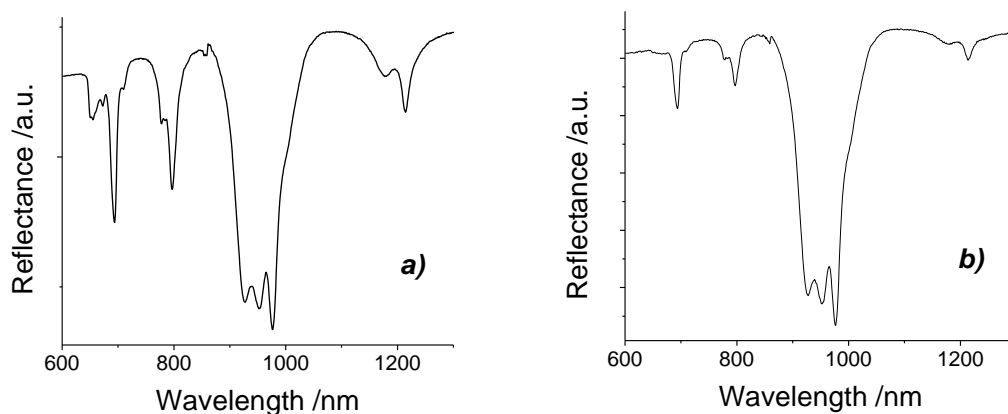


Figure 8.2: Room-temperature diffuse reflectance spectra of *a*) $\text{Y}_2\text{BaZnO}_5: \text{Yb}^{3+}$ (10%), Er^{3+} (0.3%), Tm^{3+} (1%), and *b*) $\text{Y}_2\text{BaZnO}_5: \text{Yb}^{3+}$ (10%), Er^{3+} (0.4%) (4.8% w/w) + $\text{Y}_2\text{BaZnO}_5: \text{Yb}^{3+}$ (10%), Tm^{3+} (0.25%) (95.2% w/w), in the 600-1300 nm range.

8.3.3. White light upconversion luminescence emission

8.3.3.1. Typical emission spectra under 977 nm excitation

The concentration dependence of upconversion emission properties was investigated in a variety of *a*) $\text{Y}_2\text{BaZnO}_5:\text{Yb}^{3+}, \text{Er}^{3+}, \text{Tm}^{3+}$ tri-doped samples and *b*) $\text{Y}_2\text{BaZnO}_5:\text{Yb}^{3+}, \text{Er}^{3+} + \text{Y}_2\text{BaZnO}_5:\text{Yb}^{3+}, \text{Tm}^{3+}$ powder mixtures, under 977 nm excitation at room-temperature. The dopant concentrations were adjusted in order to obtain white light. In particular, in $\text{Y}_2\text{BaZnO}_5:\text{Yb}^{3+}, \text{Er}^{3+}, \text{Tm}^{3+}$ tri-doped samples, white light was obtained by adjusting the ratios between the Yb^{3+} , Er^{3+} and Tm^{3+} concentrations doped into Y_2BaZnO_5 . For the $\text{Y}_2\text{BaZnO}_5:\text{Yb}^{3+}, \text{Er}^{3+} + \text{Y}_2\text{BaZnO}_5:\text{Yb}^{3+}, \text{Tm}^{3+}$ powder mixtures, the mass ratio between the two $\text{Y}_2\text{BaZnO}_5:\text{Yb}^{3+}, \text{Er}^{3+}$ and $\text{Y}_2\text{BaZnO}_5:\text{Yb}^{3+}, \text{Tm}^{3+}$ individual powders was adjusted before powder mixture. For each composition, the *x*, *y* CIE colour coordinates were measured.^{8,9} Typical percentage errors on *x* and *y* measurements are on the order of $\pm 0.5\%$.

In Figure 8.3, we present the typical room-temperature emission spectra (in the 380-750 nm range) of white emitting *a*) $\text{Y}_2\text{BaZnO}_5:\text{Yb}^{3+}$ (10%), Er^{3+} (0.3), Tm^{3+} (1%), and *b*) $\text{Y}_2\text{BaZnO}_5:\text{Yb}^{3+}$ (10%), Er^{3+} (0.4%) (4.8% w/w) + $\text{Y}_2\text{BaZnO}_5:\text{Yb}^{3+}$ (10%), Tm^{3+} (0.25%) (95.2% w/w), under 977 nm excitation ($\sim 90.10^{-3} \text{ W/mm}^2$). The colour coordinates corresponding to these white emitting samples are: *a*) $x = 0.2988$, $y = 0.2983$ and *b*) $x = 0.3059$, $y = 0.3130$. Under 977 nm excitation, three main emission bands centred around 479 nm, 550 nm and 673 nm are observed in the visible range (Figure 8.3). In some compounds, an additional weak emission around 454 nm is obtained. In the near-infrared region (750-1200 nm range), intense emissions centred around 796 nm and 1022 nm are observed for all the samples (Figure 8.4).

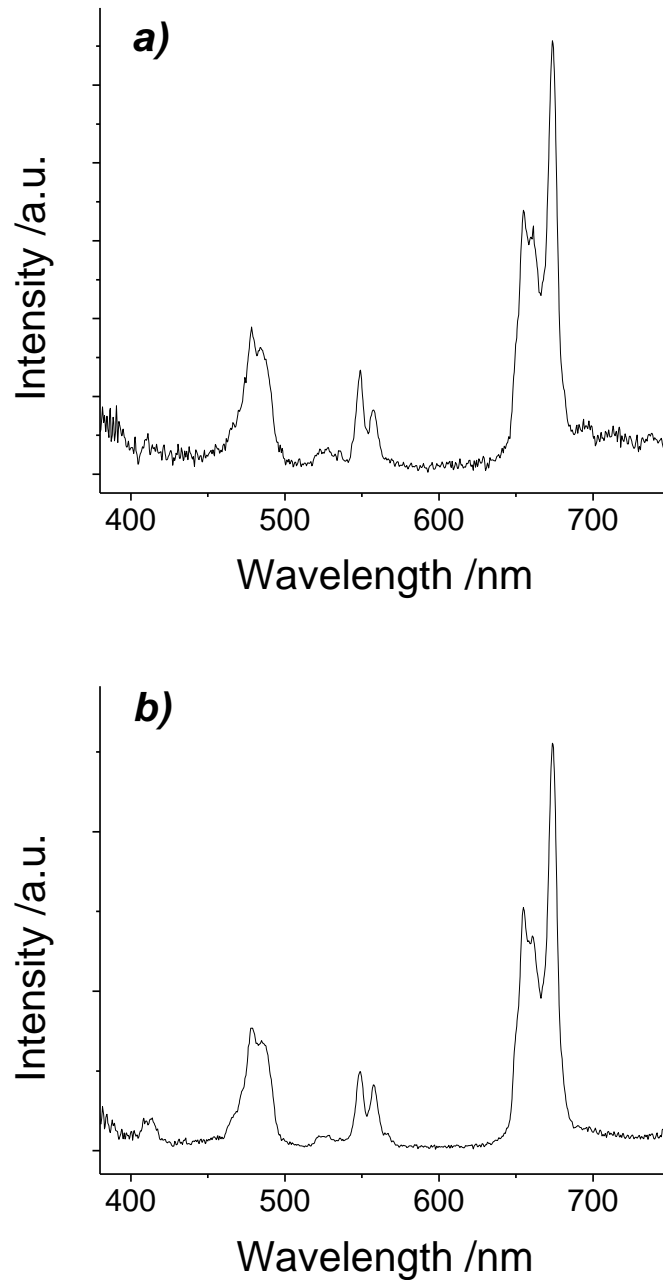


Figure 8.3: Typical room-temperature emission spectra of white emitting a) $\text{Y}_2\text{BaZnO}_5: \text{Yb}^{3+}$ (10%), Er^{3+} (0.3%), Tm^{3+} (1%) and b) $\text{Y}_2\text{BaZnO}_5: \text{Yb}^{3+}$ (10%), Er^{3+} (0.4%) (4.8% w/w) + $\text{Y}_2\text{BaZnO}_5: \text{Yb}^{3+}$ (10%), Tm^{3+} (0.25%) (95.2% w/w), under 977 nm excitation ($\sim 90 \cdot 10^{-3} \text{ W/mm}^2$).

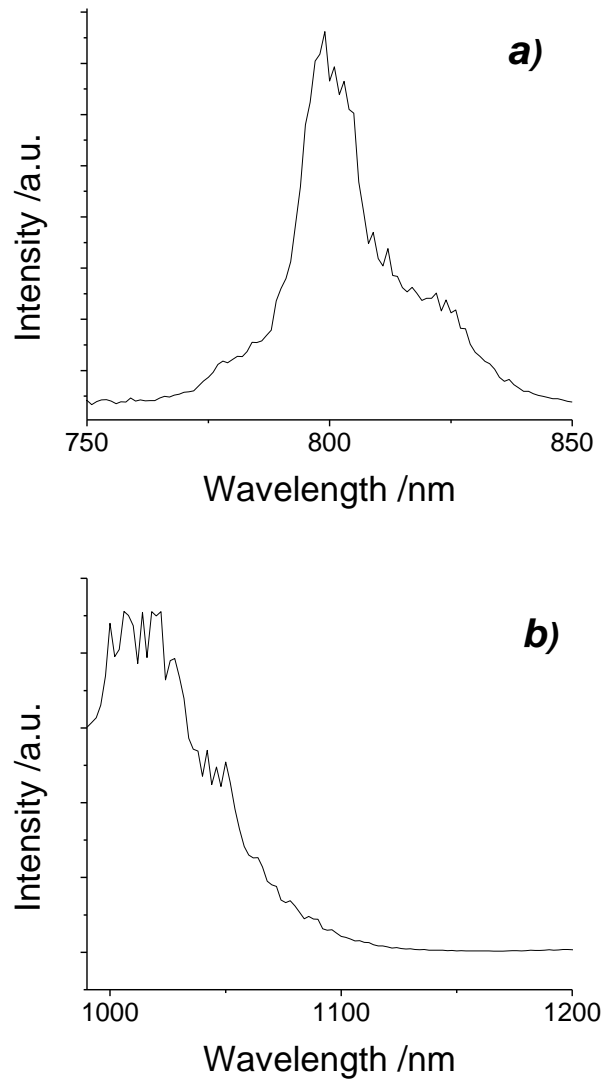


Figure 8.4: Typical emission spectra of $\text{Y}_2\text{BaZnO}_5: \text{Yb}^{3+}$ (10%), Er^{3+} (0.3%), Tm^{3+} (1%) in the 750-850 nm and 990-1200 nm ranges, under 977 nm excitation at room-temperature.

8.3.3.2. Colour coordinates and upconversion efficiency

The x and y colour coordinates and the upconversion efficiencies of white emitting a) $\text{Y}_2\text{BaZnO}_5: \text{Yb}^{3+}, \text{Er}^{3+}, \text{Tm}^{3+}$ tri-doped samples and b) $\text{Y}_2\text{BaZnO}_5: \text{Yb}^{3+}, \text{Er}^{3+}$ + $\text{Y}_2\text{BaZnO}_5: \text{Yb}^{3+}, \text{Tm}^{3+}$ powder mixtures were measured at room-temperature under 977 nm excitation and for different excitation powers. The upconversion efficiency was calculated as the ratio of the upconversion emission in the 380-780 nm range over the power absorbed in the infrared (950-1000 nm range):

$$\eta_{UC} = \frac{P_{em}}{P_{abs}^{IR}} = \frac{P_{em}}{P_{inc}^{IR} - P_{not\ abs}^{IR}} \quad (\text{Eq. 1})$$

where P_{em} is the power of the upconversion light emitted in the 380-780 nm range, P_{abs}^{IR} is the power of the fraction of incident light that has been absorbed by the sample, P_{inc}^{IR} is the incident power in the near-infrared (integrated over the 950-1000 nm range) and $P_{not\ abs}^{IR}$ is the power of the fraction of incident light that has not been absorbed by the sample.

Host tri-doping

In Table 8.1, we list the composition, x and y colour coordinates, excitation power density (on the sample), and room-temperature upconversion efficiencies of a few white emitting Y_2BaZnO_5 : Yb^{3+} , Er^{3+} , Tm^{3+} tri-doped compounds, under 977 nm excitation.

Dopant concentrations (tri-doped Y_2BaZnO_5)	P_{inc} (W/mm^2)	x	y	Efficiency (%) (380-780 nm)
Yb^{3+} (10%), Er^{3+} (0.2%), Tm^{3+} (1%)	90.10^{-3}	0.2935	0.3031	0.17
Yb^{3+} (10%), Er^{3+} (0.2%), Tm^{3+} (1%)	58.10^{-3}	0.3021	0.3097	0.16
Yb^{3+} (10%), Er^{3+} (0.2%), Tm^{3+} (1%)	25.10^{-3}	0.3103	0.3049	0.16
Yb^{3+} (10%), Er^{3+} (0.3%), Tm^{3+} (1%)	90.10^{-3}	0.2988	0.2983	0.30
Yb^{3+} (10%), Er^{3+} (0.3%), Tm^{3+} (1%)	58.10^{-3}	0.3050	0.3034	0.29
Yb^{3+} (10%), Er^{3+} (0.3%), Tm^{3+} (1%)	25.10^{-3}	0.3118	0.3055	0.29
Yb^{3+} (10%), Er^{3+} (0.4%), Tm^{3+} (1%)	90.10^{-3}	0.3259	0.3448	0.20
Yb^{3+} (10%), Er^{3+} (0.4%), Tm^{3+} (1%)	58.10^{-3}	0.3315	0.3412	0.19
Yb^{3+} (10%), Er^{3+} (0.4%), Tm^{3+} (1%)	25.10^{-3}	0.3348	0.3222	0.20

Table 8.1: Composition, excitation power density (on the sample), x y colour coordinates and upconversion efficiencies, of some white light emitting samples obtained by host tri-doping. The typical percentage errors on colour coordinates and upconversion efficiencies are on the order of $\pm 0.5\%$, and $\pm 6\%$, respectively.

The colour coordinates are positioned on a CIE x, y chromaticity diagram in Figure 8.5, together with the coordinates of the standard equal energy white light illuminant ($x = 0.33$, $y = 0.33$).

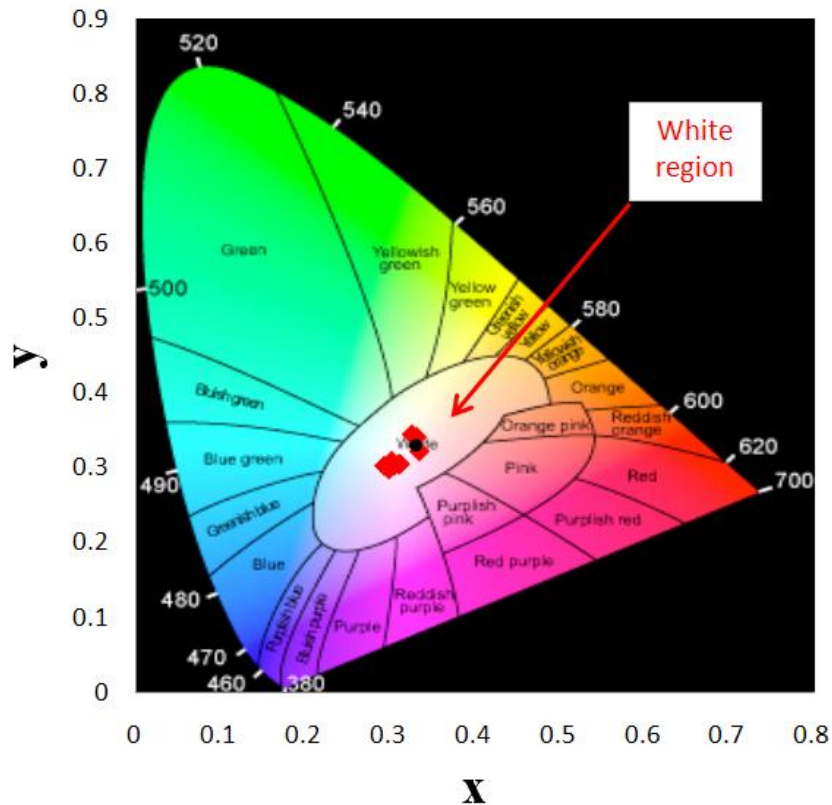


Figure 8.5: CIE chromaticity diagram and x, y colour coordinates of a few white light emitting compositions obtained by host tri-doping (in red) (see Table 8.1). The coordinates of the standard equal energy white light illuminant ($x = 0.33$, $y = 0.33$) are also positioned (black dot).

Powder mixing

In Table 8.2, we list the composition, x and y colour coordinates, excitation power density (on the sample) and upconversion efficiencies of a few white light emitting compounds obtained by powder mixing. The percentage error in the upconversion efficiency measurements was around $\sim 10\%$ (value obtained from repeated measurements). Note that the discrepancies are higher than those obtained with tri-doped white emitting compounds, which is probably due to a less homogeneous distribution of Yb^{3+} , Er^{3+} and Yb^{3+} , Tm^{3+} doped grains in the mixtures.

Powder 1 (mass m_1) Host: Y_2BaZnO_5	Powder 2 (mass m_2) Host: Y_2BaZnO_5	Mass Ratio m_2/m_1	P_{inc} (W/mm^2)	x	y	Efficiency (%) (380-780 nm)
Yb^{3+} (7%), Er^{3+} (3%)	Yb^{3+} (10%), Tm^{3+} (1%)	25	$90 \cdot 10^{-3}$	0.3319	0.3398	0.20
Yb^{3+} (7%), Er^{3+} (3%)	Yb^{3+} (10%), Tm^{3+} (1%)	25	$58 \cdot 10^{-3}$	0.3412	0.3475	0.20
Yb^{3+} (7%), Er^{3+} (3%)	Yb^{3+} (10%), Tm^{3+} (1%)	25	$25 \cdot 10^{-3}$	0.3468	0.3387	0.23
Yb^{3+} (7%), Er^{3+} (3%)	Yb^{3+} (10%), Tm^{3+} (1%)	30	$90 \cdot 10^{-3}$	0.3136	0.3260	0.19
Yb^{3+} (7%), Er^{3+} (3%)	Yb^{3+} (10%), Tm^{3+} (1%)	30	$58 \cdot 10^{-3}$	0.3281	0.3476	0.17
Yb^{3+} (7%), Er^{3+} (3%)	Yb^{3+} (10%), Tm^{3+} (1%)	30	$25 \cdot 10^{-3}$	0.3381	0.3440	0.23
Yb^{3+} (7%), Er^{3+} (3%)	Yb^{3+} (10%), Tm^{3+} (1%)	35	$90 \cdot 10^{-3}$	0.2886	0.3031	0.19
Yb^{3+} (7%), Er^{3+} (3%)	Yb^{3+} (10%), Tm^{3+} (1%)	35	$58 \cdot 10^{-3}$	0.3004	0.3180	0.19
Yb^{3+} (7%), Er^{3+} (3%)	Yb^{3+} (10%), Tm^{3+} (1%)	35	$25 \cdot 10^{-3}$	0.3201	0.3250	0.22
Yb^{3+} (10%), Er^{3+} (0.2%)	Yb^{3+} (10%), Tm^{3+} (0.25%)	5	$90 \cdot 10^{-3}$	0.3219	0.3428	0.30
Yb^{3+} (10%), Er^{3+} (0.4%)	Yb^{3+} (10%), Tm^{3+} (0.25%)	20	$90 \cdot 10^{-3}$	0.3059	0.3130	0.30

Table 8.2: Composition and mass ratio of the two individual powders mixed to produce white light, excitation power density on the resulting sample, colour coordinates and upconversion efficiencies of white light emitting powder mixtures. The typical percentage errors on colour coordinates and upconversion efficiencies are on the order of $\pm 0.5\%$, and $\pm 10\%$, respectively.

The colour coordinates are positioned on a CIE x,y chromaticity diagram in Figure 8.6, together with the coordinates of the standard equal energy white light illuminate ($x = 0.33$, $y = 0.33$).

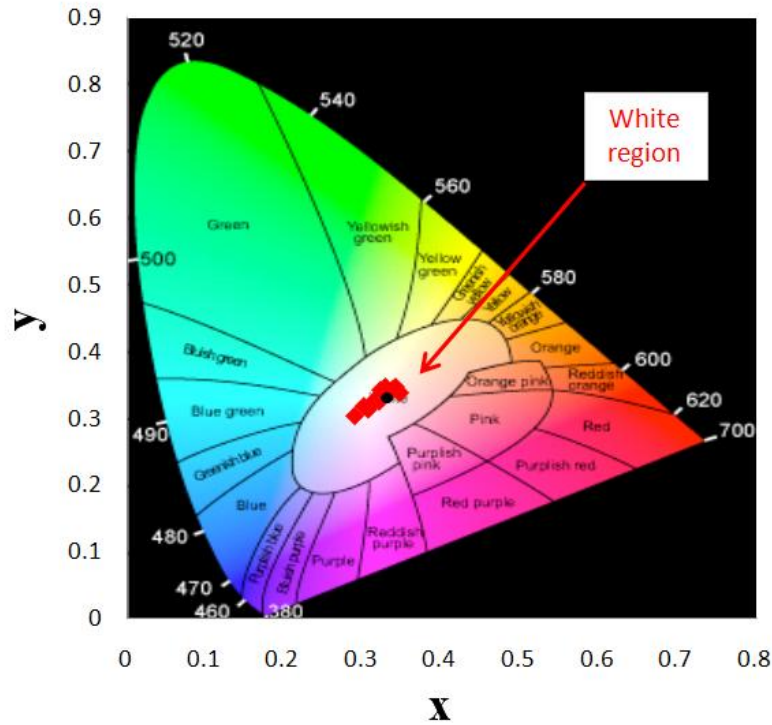


Figure 8.6: CIE chromaticity diagram and colour coordinates of a few white light emitting compositions obtained by powder mixing (in red) (see Table 8.2). The coordinates of the standard equal energy white light illuminate ($x = 0.33$, $y = 0.33$) are also positioned (black dot).

8.3.4. Lifetime measurements

In this section, we investigate the dynamic luminescent properties of white light emitting samples synthesised by host tri-doping, as they give better Yb^{3+} , Er^{3+} and Tm^{3+} dispersion than the samples obtained by powder mixing, resulting in lower discrepancies in lifetime measurements.

The transients associated with the emissions centred at around 479 nm (blue emission), 550 nm (green emission), 673 nm (red emission), 796 nm (near-infrared emission) and 1022 nm (infrared emission) in white emitting $\text{Y}_2\text{BaZnO}_5: \text{Yb}^{3+}$ (10%), Er^{3+} (0.3%), Tm^{3+} (1%) were recorded under pulsed 977 nm excitation (corresponding to the excitation of $\text{Yb}^{3+} \ ^2\text{F}_{5/2}$ and $\text{Er}^{3+} \ ^4\text{I}_{11/2}$), at room-temperature. Typical transients at 479 nm, 550 nm, 673 nm and 796 nm are presented in Figure 8.7.

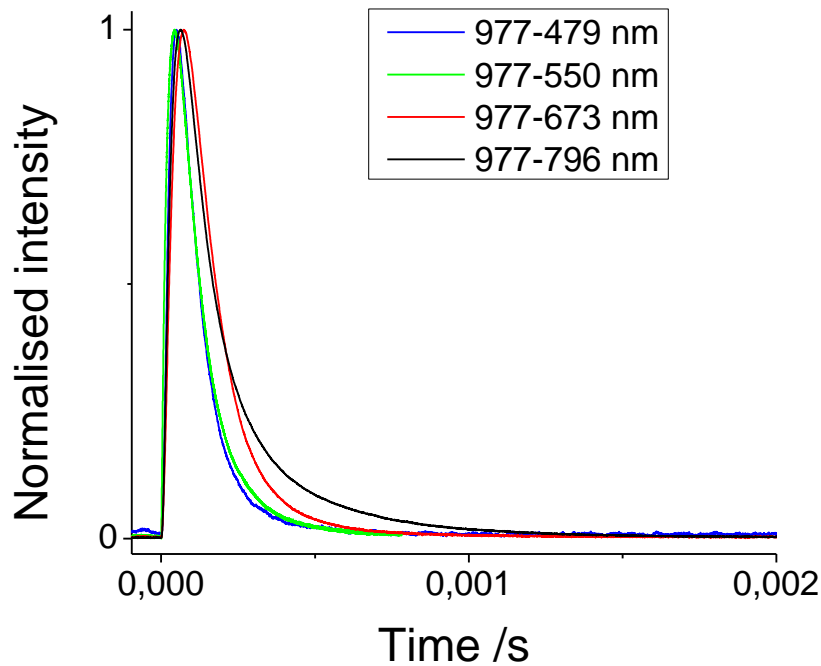


Figure 8.7: Typical room-temperature transients associated with the blue (479 nm), green (550 nm), red (673 nm) and near-infrared (796 nm) emission lines under pulsed 977 nm excitation of $\text{Y}_2\text{BaZnO}_5:\text{Yb}^{3+}$ (10%), Er^{3+} (0.3%), Tm^{3+} (1%).

As shown in Figure 8.7, at the end of the ~ 7 ns excitation pulse, no luminescence intensity is observed; instead, the transient exhibits a typical (delayed) rise followed by a decay part. This is a clear fingerprint of an energy transfer process (see chapter 3, section 3.5).

The experimental intensity data were fitted to the expression:¹⁰

$$I(t) = A \left(1 - e^{-\frac{t}{\tau_r}} \right) \left(e^{-\frac{t}{\tau_d}} \right) \quad (\text{Eq. 2})$$

where A is an emission intensity factor, and τ_r and τ_d represent the rise and decay times of the transient. Note that τ_r and τ_d are related to the transfer rate constants between Yb^{3+} and Er^{3+} or Yb^{3+} and Tm^{3+} , and to the intrinsic lifetimes of the states involved. The decay curves showed, in some cases, a bi-exponential behaviour, corresponding to decay mechanisms via two different depopulation channels. As such, when the transient decay section could not be fitted by a single exponential, the effective fluorescent decay time τ_d was determined using the following equation (discretisation of the formula used in reference ¹¹):

$$\tau_d = \frac{\sum_{i=1}^n A_i \tau_i^2}{\sum_{i=1}^n A_i \tau_i} \quad (\text{Eq. 3})$$

where A_i and τ_i are the amplitude and lifetime corresponding to the depopulation channel i and $n = 1$ or 2 .

The room-temperature lifetimes associated with the 479 nm, 550 nm, 673 nm, 796 nm and 1022 nm emissions under 977 nm excitation were measured in 3 samples, namely Y_2BaZnO_5 : Yb^{3+} (10%), Er^{3+} (0.3%), Tm^{3+} (1%) (tri-doped compound), Y_2BaZnO_5 : Yb^{3+} (10%), Er^{3+} (0.3%) (bi-doped compound) and Y_2BaZnO_5 : Yb^{3+} (10%), Tm^{3+} (1%) (bi-doped compound), and are listed in Table 8.3. The typical error in lifetime measurements is on the order of 5%. It is worth noting that the lifetimes associated with the emissions at 479 nm, 796 nm and 1022 nm are similar (within experimental errors) in Y_2BaZnO_5 : Yb^{3+} (10%), Er^{3+} (0.3%), Tm^{3+} (1%) and in Y_2BaZnO_5 : Yb^{3+} (10%), Tm^{3+} (1%). There is a significant difference however, between the lifetimes associated with the 550 nm, 673 nm and 1022 nm emissions measured in Y_2BaZnO_5 : Yb^{3+} (10%), Er^{3+} (0.3%), Tm^{3+} (1%) and Y_2BaZnO_5 : Yb^{3+} (10%), Er^{3+} (0.3%). In particular, the lifetimes associated with the 1022 nm emission in tri-doped Y_2BaZnO_5 : Yb^{3+} (10%), Er^{3+} (0.3%), Tm^{3+} (1%) are significantly shorter than those measured in bi-doped Y_2BaZnO_5 : Yb^{3+} (10%), Er^{3+} (0.3%).

Dopant concentration (host : Y_2BaZnO_5)	479 nm emission	550 nm emission	673 nm emission	796 nm emission	1022 nm emission
Yb^{3+} (10%), Er^{3+} (0.3%), Tm^{3+} (1%)	82 μs	92 μs	115 μs	195 μs	197 μs
Yb^{3+} (10%), Er^{3+} (0.3%)		255 μs	350 μs		699 μs
Yb^{3+} (10%), Tm^{3+} (1%)	71 μs			200 μs	199 μs

Table 8.3: Dopant concentration-dependence of the lifetimes associated with the 479 nm, 550 nm, 673 nm, 796 nm and 1022 nm emissions in Y_2BaZnO_5 : Yb^{3+} (10%), Er^{3+} (0.3%), Tm^{3+} (1%), Y_2BaZnO_5 : Yb^{3+} (10%), Er^{3+} (0.3%) and Y_2BaZnO_5 : Yb^{3+} (10%), Tm^{3+} (1%), under pulsed 977 nm excitation at room-temperature.

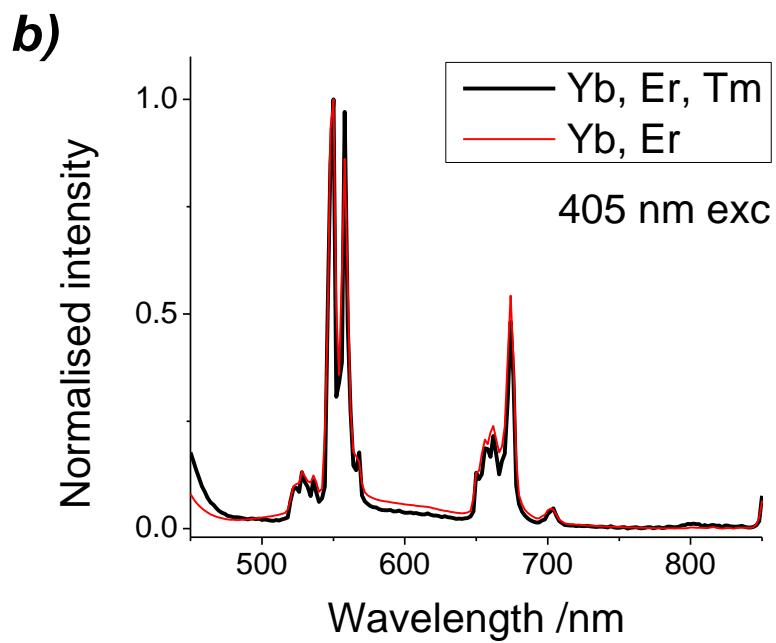
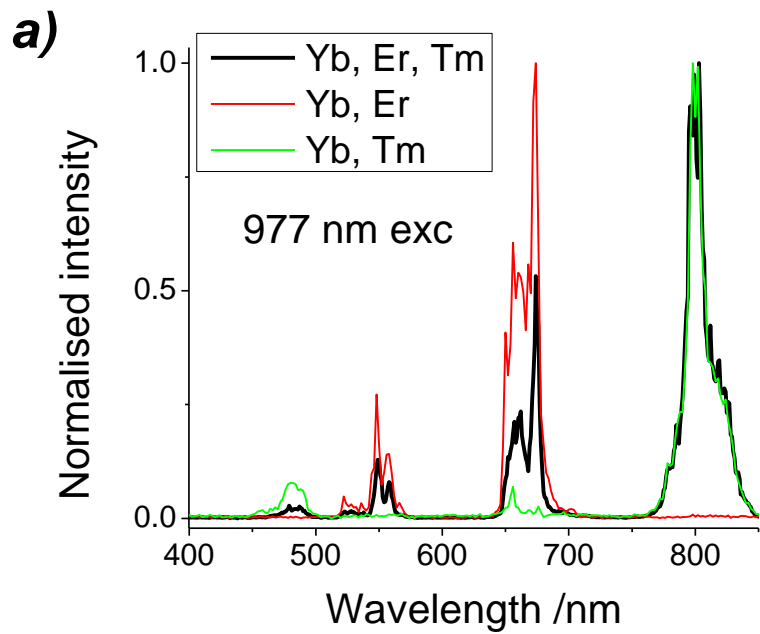
8.3.5. Emission spectra under selective dopant excitation

In this section, we focus once again on white light emitting samples synthesised by host tri-doping. In Figure 8.8, we present the emission spectra of $\text{Y}_2\text{BaZnO}_5: \text{Yb}^{3+}$ (10%), Er^{3+} (0.3%), Tm^{3+} (1%), $\text{Y}_2\text{BaZnO}_5: \text{Yb}^{3+}$ (10%), Er^{3+} (0.3%) and $\text{Y}_2\text{BaZnO}_5: \text{Yb}^{3+}$ (10%), Tm^{3+} (1%) samples, under pulsed 977 nm, 405 nm and/or 463 nm excitation. Under pulsed 977 nm excitation, 4 main emission bands centred at around 479 nm, 550 nm, 673 nm and 796 nm are observed (Figure 8.8a).

According to the Dieke diagram¹² and reflectance measurements, Er^{3+} can be selectively excited under 405 nm excitation, since neither Tm^{3+} nor Yb^{3+} absorb at that wavelength. The emission spectra of $\text{Y}_2\text{BaZnO}_5: \text{Yb}^{3+}$ (10%), Er^{3+} (0.3%), Tm^{3+} (1%) and $\text{Y}_2\text{BaZnO}_5: \text{Yb}^{3+}$ (10%), Er^{3+} (0.3%) under 405 nm excitation are presented in Figure 8.8b. No significant emission was observed under 405 nm excitation of $\text{Y}_2\text{BaZnO}_5: \text{Yb}^{3+}$ (10%), Tm^{3+} (1%).

Tm^{3+} ions can be (quasi) selectively excited at 463 nm; Yb^{3+} does not absorb at that wavelength, and luminescence measurements on $\text{Y}_2\text{BaZnO}_5: \text{Yb}^{3+}$ (10%), Er^{3+} (0.3%) under 463 nm excitation showed that the absorption of Er^{3+} is extremely weak at that wavelength (but not completely null). In Figure 8.8c, we present the emission spectra of $\text{Y}_2\text{BaZnO}_5: \text{Yb}^{3+}$ (10%), Er^{3+} (0.3%), Tm^{3+} (1%) and $\text{Y}_2\text{BaZnO}_5: \text{Yb}^{3+}$ (10%), Tm^{3+} (1%) compounds under 463 nm excitation.

It is worth noting that, under selective excitation of Er^{3+} at 405 nm, the main emission bands observed in the visible are centred around 550 nm and 673 nm (Figure 8.8b). No significant emission is observed around 479 nm or 796 nm. Under selective 463 nm excitation of Tm^{3+} , the main emission bands are around 479 nm, 654 nm and 796 nm (Figure 8.8c). No significant emission is observed around 550 nm or 673 nm.



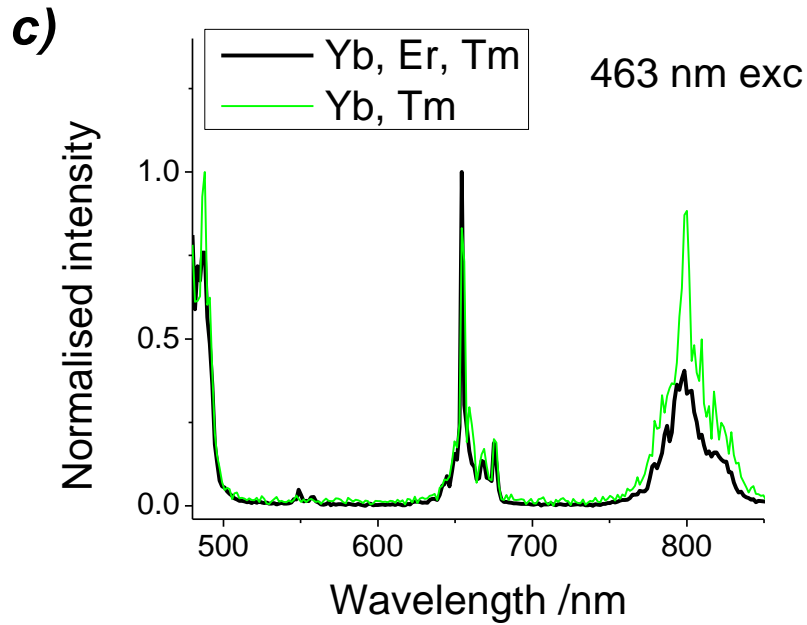


Figure 8.8: Room-temperature emission spectra a) under 977 nm excitation of $\text{Y}_2\text{BaZnO}_5: \text{Yb}^{3+}$ (10%), Er^{3+} (0.3%), Tm^{3+} (1%), $\text{Y}_2\text{BaZnO}_5: \text{Yb}^{3+}$ (10%), Er^{3+} (0.3%) and $\text{Y}_2\text{BaZnO}_5: \text{Yb}^{3+}$ (10%), Tm^{3+} (1%), b) under 405 nm excitation of $\text{Y}_2\text{BaZnO}_5: \text{Yb}^{3+}$ (10%), Er^{3+} (0.3%), Tm^{3+} (1%) and $\text{Y}_2\text{BaZnO}_5: \text{Yb}^{3+}$ (10%), Er^{3+} (0.3%), and c) under 463 nm excitation of $\text{Y}_2\text{BaZnO}_5: \text{Yb}^{3+}$ (10%), Er^{3+} (0.3%), Tm^{3+} (1%) and $\text{Y}_2\text{BaZnO}_5: \text{Yb}^{3+}$ (10%), Tm^{3+} (1%).

8.4. Discussion

Steady-state and dynamic luminescence studies were performed on a variety of white-emitting samples synthesised by host tri-doping ($\text{Y}_2\text{BaZnO}_5: \text{Yb}^{3+}, \text{Er}^{3+}, \text{Tm}^{3+}$) and powder mixing ($\text{Y}_2\text{BaZnO}_5: \text{Yb}^{3+}, \text{Er}^{3+} + \text{Y}_2\text{BaZnO}_5: \text{Yb}^{3+}, \text{Tm}^{3+}$). Under 977 nm excitation ($\sim 90.10^{-3} \text{ W/mm}^2$), relatively good white light upconversion efficiencies of up to $\sim 0.3\%$ were obtained in samples prepared via both methods. The colour coordinates of the samples were measured and shown to fall exactly within the white region of the 1931 CIE diagram. Moreover, some of the coordinates associated with the most efficient white emitting compositions were close to the standard equal energy white light illuminate ($x = 0.33, y = 0.33$). The excitation power densities required for efficient white light production were low, and upon variation of the excitation power, little variation of the colour coordinates was observed.

Under 977 nm excitation, the emission spectra, in the 400-1200 nm range, revealed the presence of 5 main emission bands centred around 479 nm (blue), 550 nm (green), 673 nm (red), 796 nm (near-infrared) and 1022 nm (infrared) (Figure 8.3, Figure 8.4, Figure 8.8a). In view of the results presented in chapter 5 and chapter 7, these emissions can be assigned exclusively to the Tm³⁺ ¹G₄ → ³H₆ (479 nm), Er³⁺ (⁴S_{3/2}, ²H_{11/2}) → ⁴I_{15/2} (550 nm), Er³⁺ ⁴F_{9/2} → ⁴I_{15/2} (673 nm), Tm³⁺ ³H₄ → ³H₆ (796 nm) and Yb³⁺ ²F_{5/2} → ²F_{7/2} (1022 nm) transitions, respectively (Figure 8.9). In some samples, an additional weak blue emission centred around 454 nm was observed, and can be assigned to the Tm³⁺ ¹D₂ → ³F₄ transition (Figure 8.3). Under 977 nm excitation of white emitting samples, there might be an additional weak red emission centred around 654 nm and attributed to the Tm³⁺ ¹G₄ → ³F₄ transition. However, were that to be the case, the 654 nm emission band would be likely to be hidden by the strong and relatively broad Er³⁺ ⁴F_{9/2} → ⁴I_{15/2} emission band (Figure 8.3, Figure 8.4, Figure 8.8a).

Under selective excitation of Er³⁺ (at 405 nm) in samples containing Yb³⁺, Er³⁺ and Tm³⁺ ions, no significant emission of Tm³⁺ was observed (Figure 8.8b). Similarly, no significant emission from Er³⁺ was observed under selective excitation of Tm³⁺ at 463 nm (Figure 8.8c). These results (presented in samples synthesised by host tri-doping but also observed in samples obtained by powder mixing) suggest that there is no significant energy transfer between Er³⁺ and Tm³⁺ in the tri-doped samples. The similarity in the Tm³⁺ excited-state lifetimes measured in Y₂BaZnO₅: Yb³⁺ (10%), Er³⁺ (0.3%), Tm³⁺ (1%) and Y₂BaZnO₅: Yb³⁺ (10%), Tm³⁺ (1%) samples (Table 8.3) corroborates this conclusion.

It is worth noting, however, that Yb³⁺ to Er³⁺ and Yb³⁺ to Tm³⁺ energy transfers do exist under 977 nm excitation of white light emitting samples, as suggested by the shape of the transients associated with the blue, green and red emissions (Figure 8.7). The presence of Yb³⁺ to Tm³⁺ energy transfers is necessary for white light production (and in particular for the production of the blue light component as Tm³⁺ does not absorb the incident 977 nm radiation) (Figure 8.2). Under 977 nm excitation, Tm³⁺ ions are excited exclusively by Yb³⁺ to Tm³⁺ energy transfer (but not by Er³⁺ to Tm³⁺ direct transfer).

The lifetimes associated with the 479 nm (Tm³⁺ ¹G₄ → ³H₆), 796 nm (Tm³⁺ ³H₄ → ³H₆) and 1022 nm (Yb³⁺ ²F_{5/2} → ²F_{7/2}) emissions in Y₂BaZnO₅: Yb³⁺ (10%), Er³⁺ (0.3%), Tm³⁺ (1%) and in Y₂BaZnO₅: Yb³⁺ (10%), Tm³⁺ (1%) were seen to be very similar (Table 8.3). This suggests that the upconversion mechanisms responsible for the population of the Tm³⁺ excited states are governed by Yb³⁺- Tm³⁺ interaction dynamics (rather than by Tm³⁺ intrinsic

lifetimes). Similarly, the lifetimes of the Er^{3+} upconversion emitting states are governed by Yb^{3+} - Er^{3+} interaction dynamics, as suggested by the strong dependence of Er^{3+} ($^4\text{S}_{3/2}$, $^2\text{H}_{11/2}$) and Er^{3+} $^4\text{F}_{9/2}$ lifetimes on the Yb^{3+} $^2\text{F}_{5/2}$ lifetime, in Y_2BaZnO_5 : Yb^{3+} (10%), Er^{3+} (0.3%), Tm^{3+} (1%) and Y_2BaZnO_5 : Yb^{3+} (10%), Er^{3+} (0.3%) (Table 8.3).

The relevant upconversion mechanisms in Y_2BaZnO_5 samples doped with Yb^{3+} , Er^{3+} and Tm^{3+} (white light emitting samples synthesised by host tri-doping or powder mixing) are summarised in Figure 8.9.

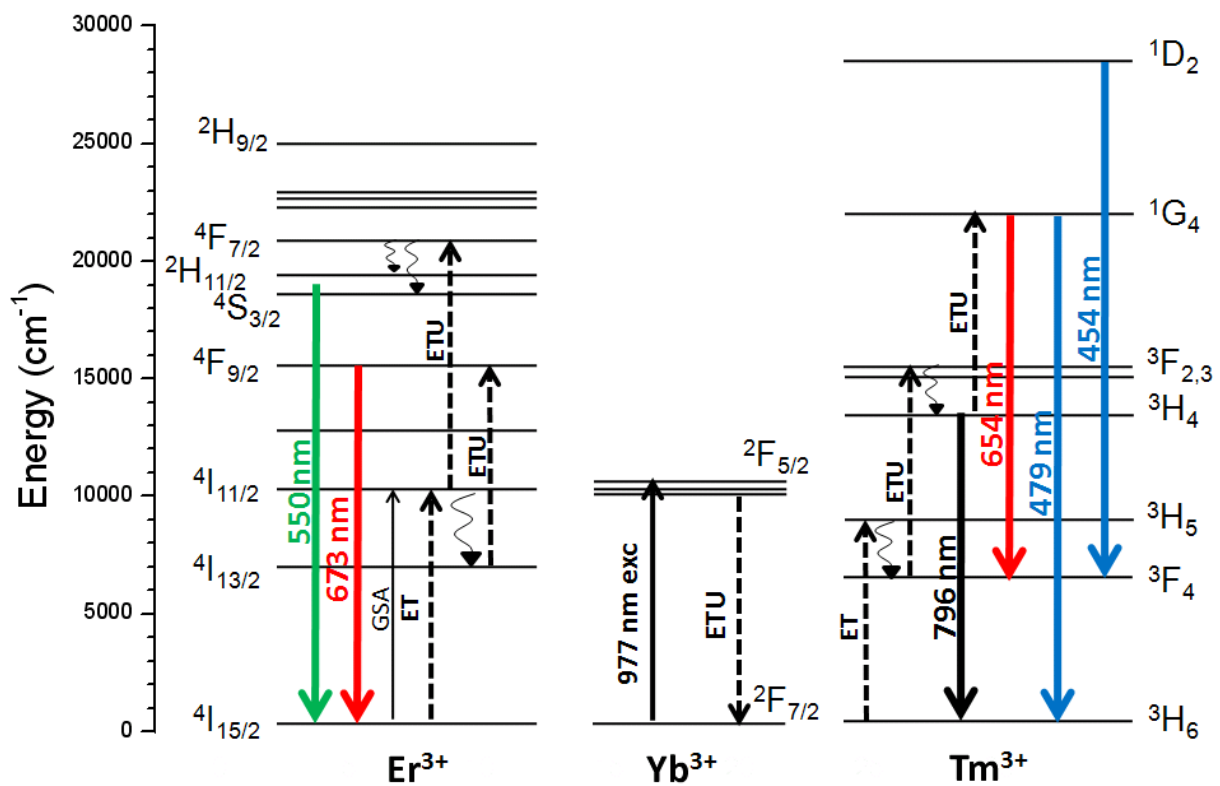


Figure 8.9: Simplified energy diagram of Yb^{3+} , Er^{3+} and Tm^{3+} ions and the dominant upconversion mechanisms in Y_2BaZnO_5 doped with Yb^{3+} , Er^{3+} and Tm^{3+} (synthesised by host tri-doping or powder mixing). Blue, green, red and near-infrared luminescence, as well as energy transfer upconversion (ETU), ground state absorption (GSA) and multiphonon relaxation processes, are represented.

8.5. Conclusions

Near-infrared to white upconversion phosphors were synthesised via 2 methods, namely host tri-doping and powder mixing. The steady-state and dynamic upconversion properties of the produced white emitting samples were investigated. Under 977 nm excitation ($\sim 90.10^{-3}$ W/mm^2), relatively good white light upconversion efficiencies of up to $\sim 0.3\%$ were obtained in the samples prepared via both methods. The literature on white light production by upconversion is still limited, and white light emission efficiencies are not always reported. As far as we are aware, the maximum upconversion efficiencies that have been reported so far are of $\sim 0.2\%$ in a Yb^{3+} , Tm^{3+} , Ho^{3+} tri-doped oxyfluoride system,⁵ and of $\sim 0.1\%$ in a Yb^{3+} , Er^{3+} , Tm^{3+} tri-doped YF_3 .¹ We believe that our samples, with their $\sim 0.3\%$ white light emission efficiency are the most efficient white emitting phosphors reported to date under ~ 977 nm excitation. In addition to their relatively high upconversion efficiencies, they have good colour coordinates (within the white region of the CIE chromaticity diagram, and close to the standard equal energy white light illuminate), relatively low excitation power densities, and small variations of colour coordinates with the excitation power, which makes them very promising candidates for many applications including display backlighting and white LED production. Lifetime measurements, coupled with emission spectra acquired under selective Er^{3+} or Tm^{3+} excitation, provided a model for the main upconversion mechanisms involved in these materials. Under 977 nm excitation, Yb^{3+} to Er^{3+} and Yb^{3+} to Tm^{3+} energy transfers were shown to occur, populating the Er^{3+} and Tm^{3+} upconversion emitting states. No energy transfer was observed, however, between Er^{3+} and Tm^{3+} . This is in agreement with what has been reported by Mahalingam et al. in $\text{Lu}_3\text{Ga}_5\text{O}_{12}:\text{Yb}^{3+},\text{Er}^{3+},\text{Tm}^{3+}$.³ The absence of energy transfers between Er^{3+} and Tm^{3+} makes it easier to tune the emission colour via a control of the dopant concentration ratios.

We believe that white light emission efficiencies can still be significantly improved in Yb^{3+} , Er^{3+} and Tm^{3+} doped Y_2BaZnO_5 , by optimising dopant concentrations. The overall efficiencies are limited however by the relatively inefficient blue emission from the Tm^{3+} component. Further work is required in order to produce a more efficient blue emitting $\text{Y}_2\text{BaZnO}_5:\text{Yb}^{3+},\text{Tm}^{3+}$ phosphor.

References

- ¹ D. Q. Chen, Y. S. Wang, K. L. Zheng, T. L. Guo, Y. L. Yu and P. Huang, *Appl. Phys. Lett.*, 2007, **91**, 251903.
- ² G. Y. Chen, Y. Liu, Y. G. Zhang, G. Somesfalean, Z. G. Zhang, Q. Sun and F. P. Wang, *Appl. Phys. Lett.*, 2007, **91**, 133103.
- ³ V. Mahalingam, F. Mangiarini, F. Vetrone, V. Venkatramu, M. Bettinelli, A. Speghini and J. A. Capobianco, *J. Phys. Chem. C*, 2008, **112**, 17745.
- ⁴ A. S. Gouveia-Neto, L. A. Bueno, R. F. do Nascimento, E. A. da Silva, Jr., E. B. da Costa and V. B. do Nascimento, *Appl. Phys. Lett.*, 2007, **91**, 091114.
- ⁵ D. Chen, Y. Wang, Y. Yu, P. Huang and F. Weng, *J. Solid State Chem.*, 2008, **181**, 2763.
- ⁶ Y. Dwivedi, A. Rai and S. B. Rai, *J. Appl. Phys.*, 2008, **104**, 043509.
- ⁷ R.D. Shannon and C.T. Prewitt, *Acta Crystallogr.*, 1969, **B25**, 925.
- ⁸ CIE (Commission Internationale de l'Eclairage), *Proceedings of 8th Session*, 1931, Cambridge University Press, Cambridge, England, 19.
- ⁹ T. Smith and J. Guild, *Trans. Opt. Soc.*, 1931, **33**, 73.
- ¹⁰ R. Buisson and J. C. Vial, *J. Phys. Lett.*, 1981, **42**, L115.
- ¹¹ E. Nakazawa, in *Phosphor Handbook*, ed. S. Shionoya and W. M. Yen, CRC Press, Boca Raton, 1999, ch. 2, p. 101.
- ¹² G. Dieke, in *Spectra and Energy Levels of Rare Earth Ions in Crystals*, Wiley Interscience Publishers, New York, 1968.

CHAPTER 9: Summary and Conclusions

9.1. Summary

In the previous four chapters, we have seen that green, red, blue and white light can be produced in $\text{RE}_2\text{BaZnO}_5$ oxides ($\text{RE} = \text{Y}, \text{Gd}$) doped with Yb^{3+} and Ln^{3+} (where $\text{Ln}^{3+} = \text{Er}^{3+}, \text{Ho}^{3+}, \text{Tm}^{3+}$), via a room-temperature upconversion process under near-infrared excitation. The upconversion efficiencies were precisely quantified in all the materials as a function of dopant concentrations. The dominant upconversion mechanisms were elucidated via in-depth spectroscopic studies. In the next section, we summarise the results we obtained in $\text{RE}_2\text{BaZnO}_5$ ($\text{RE} = \text{Y}, \text{Gd}$) oxides doped with $\text{Yb}^{3+}, \text{Er}^{3+}$ (Figure 9.1a), $\text{Yb}^{3+}, \text{Ho}^{3+}$ (Figure 9.1b), $\text{Yb}^{3+}, \text{Tm}^{3+}$ (Figure 9.1c) and $\text{Yb}^{3+}, \text{Er}^{3+}, \text{Tm}^{3+}$ (Figure 9.1d).

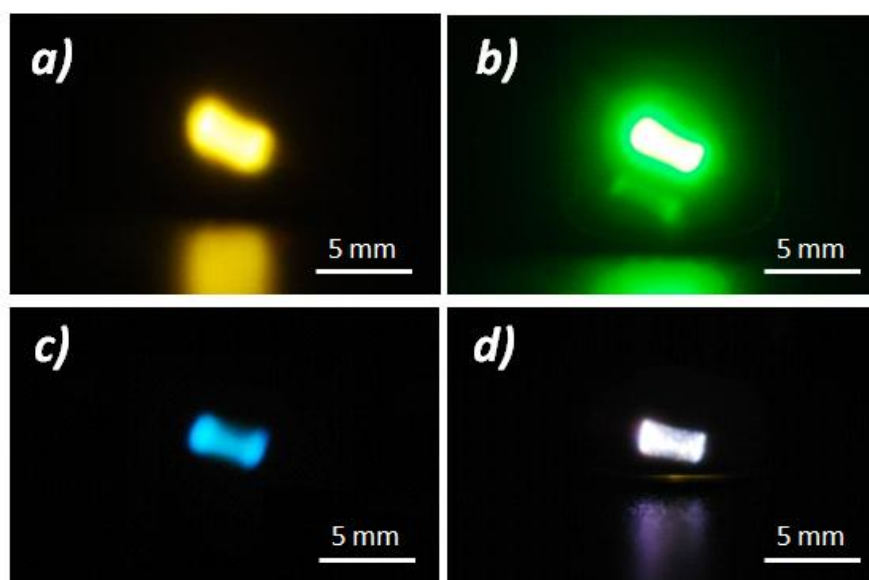


Figure 9.1: Typical emissions of a) $\text{Y}_2\text{BaZnO}_5: \text{Yb}^{3+} (7\%), \text{Er}^{3+} (3\%)$, b) $\text{Y}_2\text{BaZnO}_5: \text{Yb}^{3+} (7\%), \text{Ho}^{3+} (0.5\%)$, c) $\text{Y}_2\text{BaZnO}_5: \text{Yb}^{3+} (6\%), \text{Tm}^{3+} (0.25\%)$ and d) $\text{Y}_2\text{BaZnO}_5: \text{Yb}^{3+} (10\%), \text{Er}^{3+} (0.3\%), \text{Tm}^{3+} (1\%)$ under cw 977 nm excitation. The laser intensity, wavelength and beam waist used for the excitation of the 4 samples are identical. The camera settings used to take the 4 pictures are the same (shutter speed, ISO, aperture, etc).

9.1.1. Upconversion properties of RE₂BaZnO₅: Yb³⁺, Er³⁺ (RE = Y, Gd)

In RE₂BaZnO₅: Yb³⁺, Er³⁺ (RE = Y, Gd), green and red emissions were produced under 977 nm excitation. High upconversion efficiencies of up to 5.2% were measured at room-temperature (chapter 5).¹ We believe that these are the most efficient oxide upconverting phosphors reported to date for infrared to red and green upconversion. The samples were shown to exhibit interesting colour tunability properties when varying the dopant concentrations (in the case of a cw excitation), and also the excitation pulse duration at fixed dopant concentrations (for a pulsed excitation).

Power dependence studies and room-temperature lifetime measurements provided an accurate model for the upconversion mechanisms involved in these materials (Figure 9.2). Under 977 nm excitation, both Yb³⁺ and Er³⁺ were shown to absorb the incident radiation. The green emitting thermalised levels Er³⁺ (⁴S_{3/2}, ²H_{11/2}) were populated mainly by 2 successive Yb³⁺ to Er³⁺ energy transfer steps via the Er³⁺ ⁴I_{11/2} intermediate state, but also by ground-state absorption/excited state absorption (GSA/ESA) by Er³⁺. The red emitting level Er³⁺ ⁴F_{9/2} population occurred mainly by 2 successive Yb³⁺ to Er³⁺ energy transfer steps via the Er³⁺ ⁴I_{13/2} intermediate state, but also by multiphonon relaxation from the higher-lying Er³⁺ (⁴S_{3/2}, ²H_{11/2}) levels. At high Yb³⁺ concentrations, Er³⁺ to Yb³⁺ back-energy transfer mechanisms were shown to depopulate the green emitting levels and to favour high red to green emission intensity ratios.

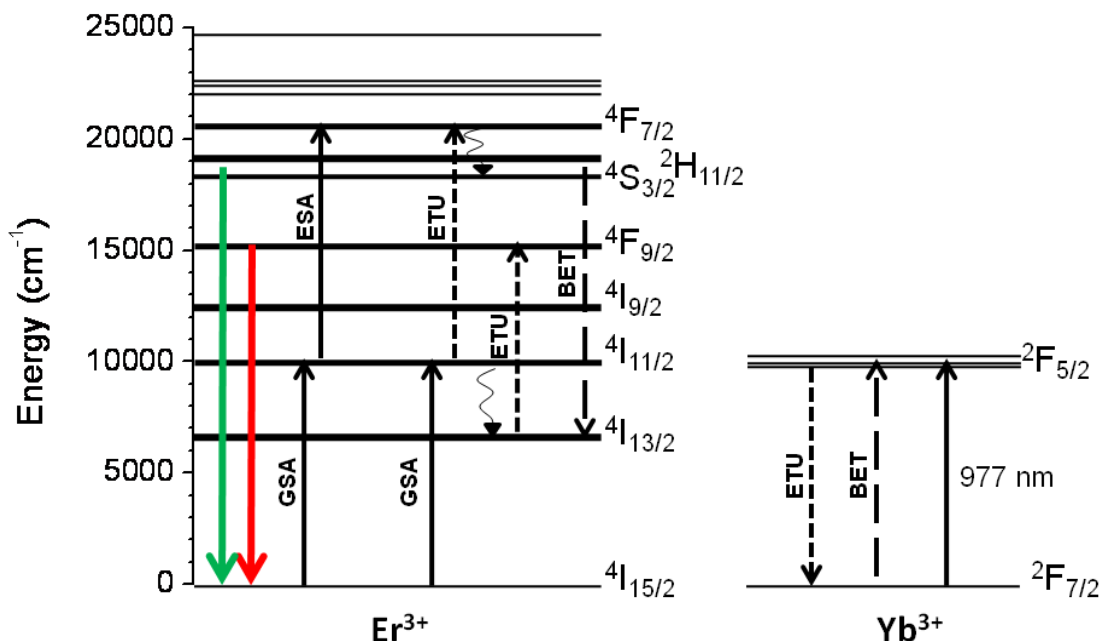


Figure 9.2: Simplified energy level diagram of Er^{3+} and Yb^{3+} ions and the dominant upconversion mechanisms in $\text{RE}_2\text{BaZnO}_5: \text{Yb}^{3+}, \text{Er}^{3+}$ ($\text{RE} = \text{Y}, \text{Gd}$). Radiative processes of ground state absorption (GSA), excited state absorption (ESA) and green and red luminescence, as well as non-radiative energy transfer upconversion (ETU), back energy transfer (BET) and multiphonon relaxation processes are represented.

9.1.2. Upconversion properties of $\text{RE}_2\text{BaZnO}_5: \text{Yb}^{3+}, \text{Ho}^{3+}$ ($\text{RE} = \text{Y}, \text{Gd}$)

A very efficient near-infrared to green upconversion phosphor was reported for the first time in chapter 6.² The upconversion properties of $\text{RE}_2\text{BaZnO}_5: \text{Yb}^{3+}, \text{Ho}^{3+}$ ($\text{RE} = \text{Y}, \text{Gd}$) were investigated as a function of dopant concentrations and their efficiencies quantified at room-temperature. Upconversion efficiencies of up to $\sim 2.6\%$ were measured, which we believe are the highest reported efficiencies for $\text{Yb}^{3+}, \text{Ho}^{3+}$ co-doped phosphors under infrared excitation.

Power dependence studies and temperature-dependent lifetime measurements provided a model for the dominant upconversion mechanism involved in these materials (Figure 9.3). Strong green (545 nm) and near-infrared (760 nm) emissions were shown to arise from the thermalised Ho^{3+} ($^5\text{S}_2, ^5\text{F}_4$) levels populated mainly by two successive Yb^{3+} to Ho^{3+} energy transfer steps under 977 nm excitation. At high Yb^{3+} concentrations, Ho^{3+} to Yb^{3+} back energy transfers were shown to occur, resulting in luminescence quenching. Temperature-

dependent lifetime studies suggested the existence of an interesting change in upconversion dynamics occurring at low temperatures.

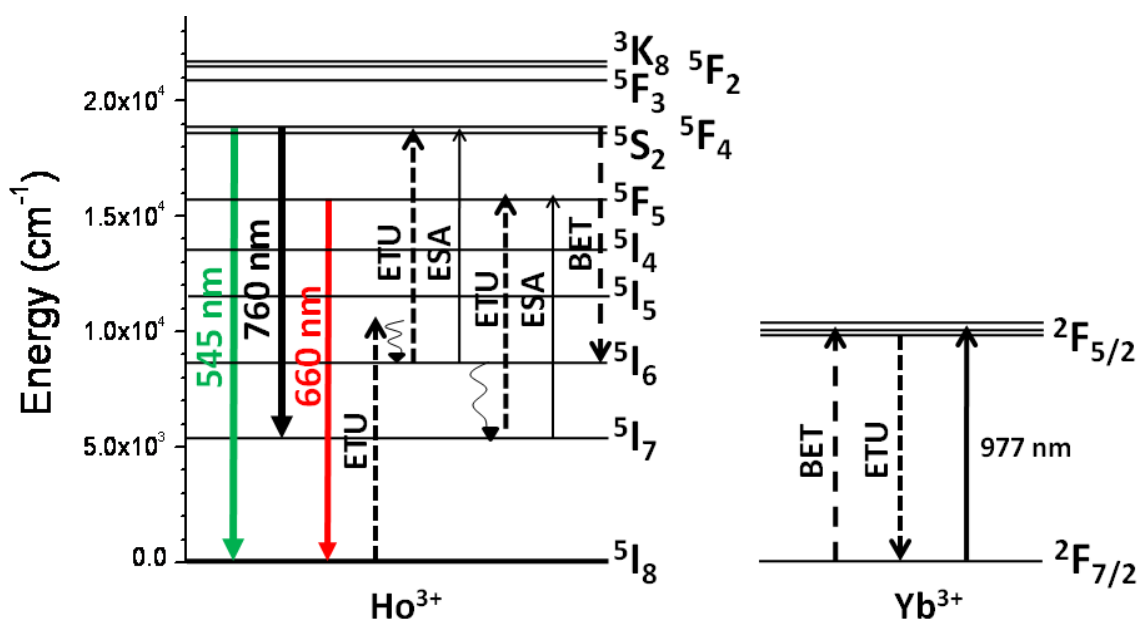


Figure 9.3: Simplified energy level diagram of Ho^{3+} and Yb^{3+} ions and the dominant upconversion mechanisms in $\text{RE}_2\text{BaZnO}_5:\text{Yb}^{3+}, \text{Ho}^{3+}$ ($\text{RE} = \text{Y}, \text{Gd}$). Green, red and near-infrared luminescence, as well as processes of excited state absorption (ESA), energy transfer upconversion (ETU), back energy transfer (BET) and multiphonon relaxation processes, are represented.

9.1.3. Upconversion properties of $\text{Y}_2\text{BaZnO}_5:\text{Yb}^{3+}, \text{Tm}^{3+}$

The upconversion properties of $\text{Y}_2\text{BaZnO}_5:\text{Yb}^{3+}, \text{Tm}^{3+}$ oxide materials have been reported for the first time in chapter 7.³ Under near-infrared excitation (~ 977 nm), the samples emitted mainly in the near-infrared (796 nm), and considerably weaker emissions were observed in the blue (479 nm) and in the red (654 nm). Maximum upconversion efficiencies of $\sim 1.7\%$ (total upconversion efficiency integrated over the 420-870 nm emission range) and 0.09% (blue upconversion efficiency, 420-530 nm emission range) were obtained at room-temperature.

Power dependence studies showed that the blue and red emitting levels were populated via 3-successive Yb^{3+} to Tm^{3+} energy transfer steps, while the near-infrared level population only involved 2 such energy transfers, thus explaining the considerable difference in the blue and

near-infrared emission efficiencies (Figure 9.4). For Tm^{3+} concentrations above $\sim 0.25\%$, cross-relaxation mechanisms were found to occur, depopulating the blue, red and near-infrared emitting levels.

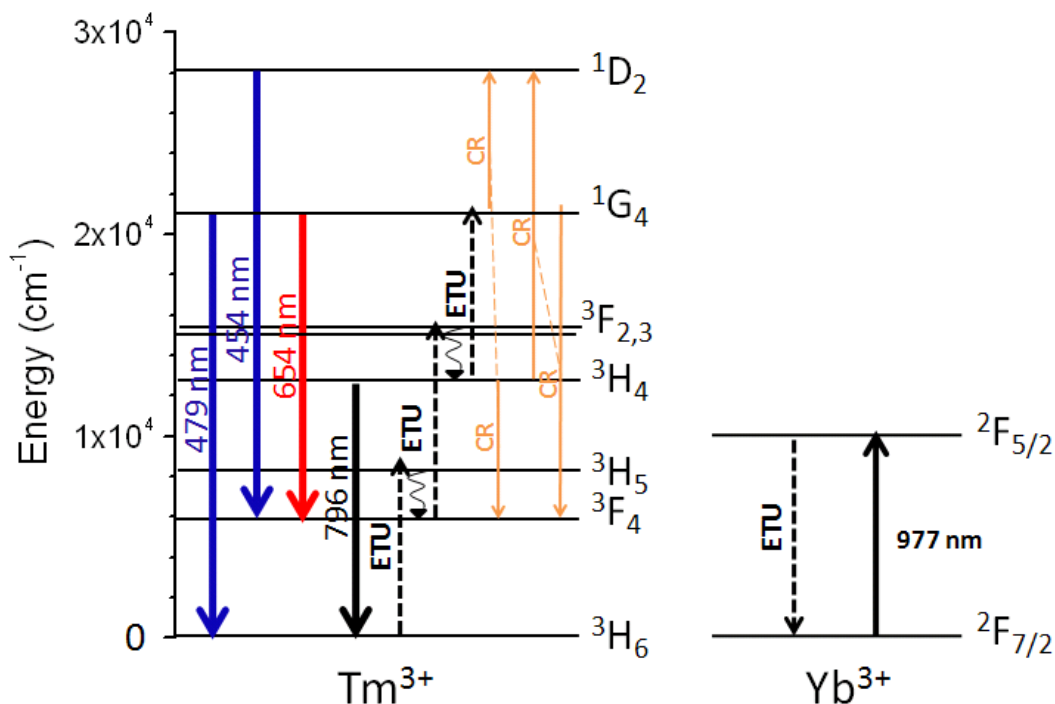


Figure 9.4: Simplified energy diagram of Tm^{3+} and Yb^{3+} ions and the dominant upconversion mechanisms in $\text{Y}_2\text{BaZnO}_5: \text{Yb}^{3+}, \text{Tm}^{3+}$. Blue, red and near-infrared luminescence, as well as (non-resonant) non-radiative energy transfer upconversion (ETU), multiphonon relaxation and cross-relaxation (CR) processes, are represented.

9.1.4. Y_2BaZnO_5 doped with Yb^{3+} , Er^{3+} and Tm^{3+} for white light upconversion emission

Near-infrared to white upconversion properties were reported for the first time in Y_2BaZnO_5 oxides doped with Yb^{3+} , Er^{3+} and Tm^{3+} . The white emitting phosphors were synthesised by 2 methods; host tri-doping and powder mixing (chapter 8). Under 977 nm excitation ($\sim 90 \cdot 10^{-3} \text{ W/mm}^2$), relatively good white light upconversion efficiencies of up to $\sim 0.3\%$ were obtained in the samples prepared via both methods, which we believe are the highest white light emission efficiencies reported to date under $\sim 977 \text{ nm}$ excitation. The white emitting samples presented colour coordinates falling within the white region of the CIE

chromaticity diagram (relatively close to the standard equal energy white light illuminate) at low excitation power densities. The variations of colour coordinates with the excitation power were small, making these systems promising for many applications requiring white light emission.

Lifetime measurements, coupled with emission spectra acquired under selective Er^{3+} or Tm^{3+} excitation, provided a model for the main upconversion mechanisms involved in these materials (Figure 9.5). Under 977 nm excitation, Yb^{3+} to Er^{3+} and Yb^{3+} to Tm^{3+} energy transfers were shown to occur, populating the Er^{3+} and Tm^{3+} upconversion emitting excited states for the blue ($\text{Tm}^{3+} {}^1\text{G}_4$ and $\text{Tm}^{3+} {}^1\text{D}_2$), green ($\text{Er}^{3+} {}^4\text{S}_{3/2}$ and $\text{Er}^{3+} {}^2\text{H}_{11/2}$) and red ($\text{Er}^{3+} {}^4\text{F}_{9/2}$ and $\text{Tm}^{3+} {}^1\text{G}_4$) lights. No energy transfer was observed, however, between Er^{3+} and Tm^{3+} .

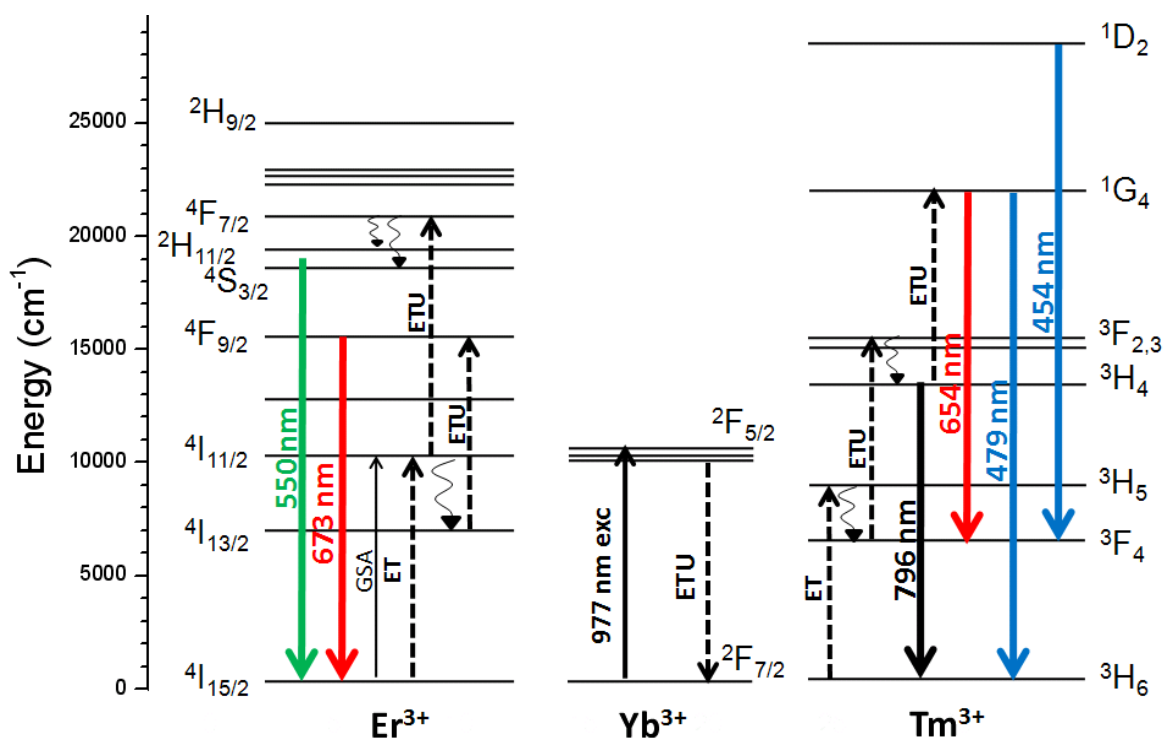


Figure 9.5: Simplified energy diagram of Yb^{3+} , Er^{3+} and Tm^{3+} ions and the dominant upconversion mechanisms in Y_2BaZnO_5 doped with Yb^{3+} , Er^{3+} and Tm^{3+} (syntheses by host tri-doping or powder mixing). Blue, green, red and near-infrared luminescence, as well as energy transfer upconversion (ETU), ground state absorption (GSA) and multiphonon relaxation processes, are represented.

9.2. Conclusions

In this thesis, we presented for the first time results on the upconversion efficiencies of new systems ($\text{Y}_2\text{BaZnO}_5:\text{Yb}^{3+},\text{Er}^{3+}$, $\text{RE}_2\text{BaZnO}_5:\text{Yb}^{3+},\text{Ho}^{3+}$ (RE = Y, Gd), $\text{Y}_2\text{BaZnO}_5:\text{Yb}^{3+},\text{Tm}^{3+}$ and $\text{Y}_2\text{BaZnO}_5:\text{Yb}^{3+},\text{Er}^{3+},\text{Tm}^{3+}$) for efficient red, green, blue and white upconversion efficiencies. Very good upconversion efficiencies were achieved via an optimisation of synthesis conditions and dopant concentrations. Upconversion efficiencies were systematically measured in our systems. For the first time, special care was also given to the understanding of upconversion mechanisms, via in-depth steady-state and time-resolved spectroscopic studies. The transitions associated with the various emission bands could be assigned without any ambiguity. The influence of dopant concentrations and temperature on upconversion mechanisms could be elucidated. Further work is necessary in order to produce an efficient blue emitting phosphor, which will also contribute to an increase in white light emission efficiencies.

9.3. Future work

The use of the above described upconverting materials in solar cells, and the synthesis of nanoparticles will be explored.

References

¹ I. Etchart, A. Huignard, M. Bérard, M. N. Nordin, I. Hernández, R. J. Curry, W. P. Gillin and A. K. Cheetham, *J. Mater. Chem.*, 2010, **20**, 3989.

² I. Etchart, I. Hernández, A. Huignard, M. Bérard, W. P. Gillin, R. J. Curry and A. K. Cheetham, *J. Mater. Chem.*, 2010, DOI: 10.1039/c0jm01652g.

³ *Oxide phosphors for light upconversion; Yb³⁺ and Tm³⁺ co-doped Y₂BaZnO₅*, I. Etchart, I. Hernández, A. Huignard, M. Bérard, M. Laroche, W. P. Gillin, R. J. Curry and A. K. Cheetham, submitted for publication.

APPENDIX A: Rate-Equations in Yb^{3+} , Er^{3+} co-doped materials

In this section, we write the rate equations governing upconversion in $\text{RE}_2\text{BaZnO}_5: \text{Yb}^{3+}, \text{Er}^{3+}$ ($\text{RE} = \text{Y}, \text{Gd}$) (Figure A.1), assuming that dopant concentrations are low, so that cross-relaxation and hopping processes can be neglected.

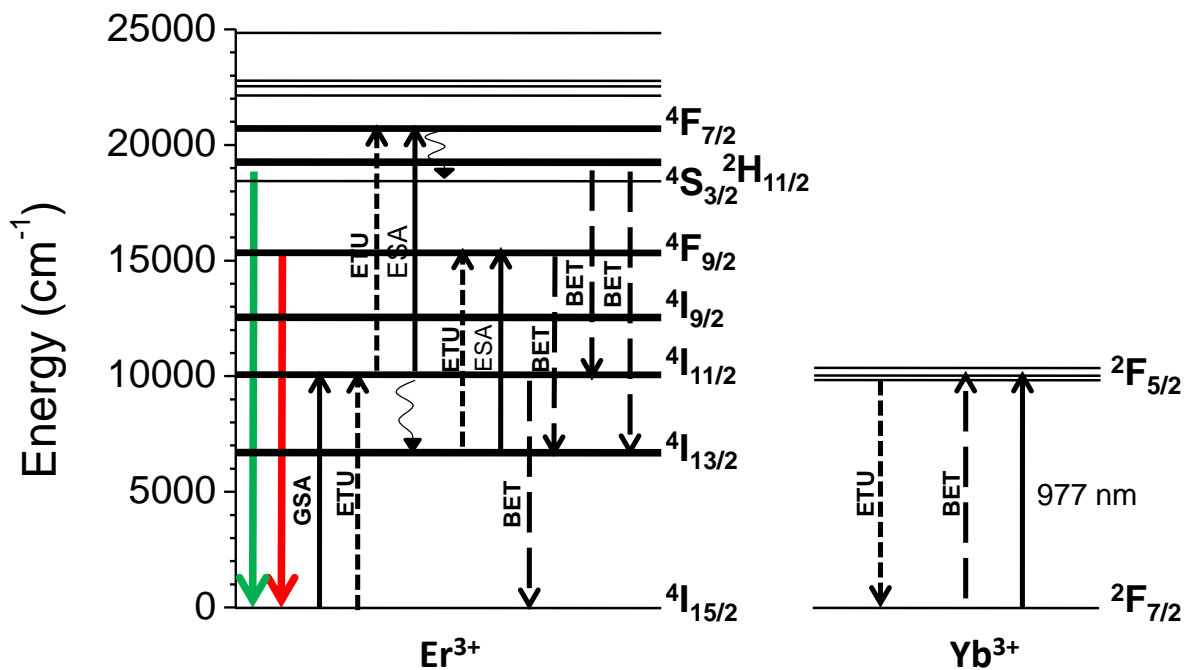


Figure A.1: Simplified energy level diagram of Er^{3+} and Yb^{3+} ions and the dominant upconversion mechanisms in $\text{RE}_2\text{BaZnO}_5: \text{Yb}^{3+}, \text{Er}^{3+}$ ($\text{RE} = \text{Y}, \text{Gd}$). Radiative processes of ground state absorption (GSA), excited state absorption (ESA) and green and red luminescence, as well as non-radiative energy transfer upconversion (ETU), back energy transfer (BET) and multiphonon relaxation processes are represented.

In this section, we denote:

- N_0 the population density of $\text{Er}^{3+} {}^4\text{I}_{15/2}$
- N_1 the population density of $\text{Er}^{3+} {}^4\text{I}_{13/2}$
- N_2 the population density of $\text{Er}^{3+} {}^4\text{I}_{11/2}$
- N_3 the population density of $\text{Er}^{3+} {}^4\text{F}_{9/2}$
- N_4 the population density of $\text{Er}^{3+} ({}^4\text{S}_{3/2}, {}^2\text{H}_{11/2})$
- N_{D0} the population density of $\text{Yb}^{3+} {}^2\text{F}_{7/2}$
- N_D the population density of $\text{Yb}^{3+} {}^2\text{F}_{5/2}$
- τ_i the radiative lifetime of the state $|i\rangle$ of population density N_i
- σ_i the absorption cross-section of state $|i\rangle$ at 977 nm
- W_{ij} the multiphonon rate from state $|i\rangle$ to state $|j\rangle$
- A_{ij} the radiative emission rate from state $|i\rangle$ to state $|j\rangle$
- C_{Di} the rate of the energy transfer (ET) from $\text{Yb}^{3+} {}^2\text{F}_{5/2}$ to Er^{3+} , which results in the population of the state $|i\rangle$ of Er^{3+}
- C_{iD} the rate of the back energy transfer (BET) from the state $|i\rangle$ of Er^{3+} to $\text{Yb}^{3+} {}^2\text{F}_{7/2}$, resulting in the population of $\text{Yb}^{3+} {}^2\text{F}_{5/2}$. We denote C_{4D} and C'_{4D} the rates of the BET processes populating $\text{Er}^{3+} {}^4\text{I}_{11/2}$ and $\text{Er}^{3+} {}^4\text{I}_{13/2}$, respectively.
- ϕ the pump rate

We assume that there is no pump depletion, that the ground state population densities N_{D0} and N_0 are constant, and that the system is continuously pumped into the $\text{Yb}^{3+} {}^2\text{F}_{5/2}$ state. We neglect the population of $\text{Er}^{3+} {}^4\text{I}_{9/2}$, assuming that fast $\text{Er}^{3+} {}^4\text{I}_{9/2} \rightarrow \text{Er}^{3+} {}^4\text{I}_{11/2}$ multiphonon relaxation occurs.

The rate equations can be written as follows:

$$\frac{dN_D}{dt} = \phi \sigma_D N_{D0} + C_{4D} N_4 N_{D0} + C'_{4D} N_4 N_{D0} + C_{2D} N_2 N_{D0} + C_{3D} N_3 N_{D0} - \frac{N_D}{\tau_D} - C_{D2} N_D N_0 - C_{D3} N_D N_1 - C_{D4} N_D N_2 \quad (\text{Eq. 1})$$

$$\frac{dN_1}{dt} = W_{21} N_2 + C_{3D} N_4 N_{D0} + C'_{4D} N_3 N_{D0} - \frac{N_1}{\tau_1} - C_{D3} N_D N_1 - \phi \sigma_1 N_1 \quad (\text{Eq. 2})$$

$$\frac{dN_2}{dt} = C_{D2} N_D N_0 + \phi \sigma_0 N_0 + (A_{32} + W_{32}) N_3 + A_{42} N_4 + C_{4D} N_4 N_{D0} - W_{21} N_2 - C_{D4} N_D N_2 - \frac{N_2}{\tau_2} - \phi \sigma_2 N_2 \quad (\text{Eq. 3})$$

$$\frac{dN_3}{dt} = C_{D3}N_D N_1 + \phi\sigma_1 N_1 + W_{43}N_4 - \frac{N_3}{\tau_3} - C_{3D}N_3 N_{D0} - W_{32}N_3 \quad (\text{Eq. 4})$$

$$\frac{dN_4}{dt} = C_{D4}N_D N_2 + \phi\sigma_2 N_2 - C_{4D}N_4 N_{D0} - C'_{4D}N_4 N_{D0} - \frac{N_4}{\tau_4} - W_{43}N_4 \quad (\text{Eq. 5})$$

In the low power regime, we can simplify the rate equations. In particular, we can neglect the contribution of upconversion terms ($C_{D2}N_D N_0$, $C_{D3}N_D N_1$ and $C_{D4}N_D N_2$) to the depopulation of $\text{Yb}^{3+} {}^2\text{F}_{5/2}$, $\text{Er}^{3+} {}^4\text{I}_{13/2}$ and $\text{Er}^{3+} {}^4\text{I}_{11/2}$, as well as the contribution of back-energy transfer ($C_{4D}N_4 N_{D0}$, $C'_{4D}N_4 N_{D0}$, $C_{3D}N_3 N_{D0}$ and $C_{2D}N_2 N_{D0}$) terms to the population of $\text{Yb}^{3+} {}^2\text{F}_{5/2}$ and $\text{Er}^{3+} {}^4\text{F}_{9/2}$. Excited State Absorption terms ($\phi\sigma_0 N_0$, $\phi\sigma_1 N_1$ and $\phi\sigma_2 N_2$) can also be neglected in the population mechanisms of $\text{Er}^{3+} {}^4\text{I}_{11/2}$, $\text{Er}^{3+} {}^4\text{F}_{9/2}$ and $\text{Er}^{3+} ({}^4\text{S}_{3/2}, {}^2\text{H}_{11/2})$, and in the depopulation mechanism of $\text{Er}^{3+} {}^4\text{I}_{13/2}$ and $\text{Er}^{3+} {}^4\text{I}_{11/2}$. Finally, we can neglect the contribution of multiphonon relaxation and radiative emission from the higher-lying energy levels to the population of $\text{Er}^{3+} {}^4\text{I}_{11/2}$.

In the low power regime, the rate equations become:

$$\frac{dN_D}{dt} = \phi\sigma_D N_{D0} - \frac{N_D}{\tau_D} \quad (\text{Eq. 6})$$

$$\frac{dN_1}{dt} = W_{21}N_2 - \frac{N_1}{\tau_1} \quad (\text{Eq. 7})$$

$$\frac{dN_2}{dt} = C_{D2}N_D N_0 - W_{21}N_2 - \frac{N_2}{\tau_2} \quad (\text{Eq. 8})$$

$$\frac{dN_3}{dt} = C_{D3}N_D N_1 + W_{43}N_4 - \frac{N_3}{\tau_3} - W_{32}N_3 \quad (\text{Eq. 9})$$

$$\frac{dN_4}{dt} = C_{D4}N_D N_2 - C_{4D}N_4 N_{D0} - C'_{4D}N_4 N_{D0} - \frac{N_4}{\tau_4} - W_{43}N_4 \quad (\text{Eq. 10})$$

In the steady-state regime:

$$\frac{dN_D}{dt} = \frac{dN_1}{dt} = \frac{dN_2}{dt} = \frac{dN_3}{dt} = \frac{dN_4}{dt} = 0 \quad (\text{Eq. 11})$$

Therefore, by solving the above simplified equation in the steady-state regime, at low power regime, we get:

$$N_D = \tau_D \phi \sigma_D N_{D0} \quad (\text{Eq. 12})$$

$$N_2 = \frac{C_{D2} N_0}{W_{21} + 1/\tau_2} N_D \quad (\text{Eq. 13})$$

$$N_1 = \tau_1 W_{21} N_2 = \tau_1 W_{21} \frac{C_{D2} N_0}{W_{21} + 1/\tau_2} N_D \quad (\text{Eq. 14})$$

$$N_4 = \frac{C_{D4} N_D N_2}{C_{4D} N_{D0} + C'_{4D} N_{D0} + W_{43} + 1/\tau_4} = \frac{C_{D2} C_{D4} N_0}{(C_{4D} N_{D0} + C'_{4D} N_{D0} + W_{43} + 1/\tau_4)(W_{21} + 1/\tau_2)} N_D^2 \quad (\text{Eq. 15})$$

$$N_3 = \frac{C_{D3} N_D N_1 + W_{43} N_4}{W_{32} + 1/\tau_3} = \frac{1}{(W_{21} + 1/\tau_2)(W_{32} + 1/\tau_3)} \left[C_{D2} C_{D3} N_0 \tau_1 W_{21} + \frac{C_{D2} C_{D4} N_0 W_{43}}{(C_{4D} N_{D0} + C'_{4D} N_{D0} + W_{43} + 1/\tau_4)} \right] N_D^2 \quad (\text{Eq. 16})$$

Since N_{D0} , N_0 , C_{Di} , C_{iD} , W_{ij} , τ_i and σ_D are constants, we obtain:

$$N_D \propto \phi \quad (\text{Eq. 17})$$

$$N_1 \propto \phi \quad (\text{Eq. 18})$$

$$N_2 \propto \phi \quad (\text{Eq. 19})$$

$$N_3 \propto \phi^2 \quad (\text{Eq. 20})$$

$$N_4 \propto \phi^2 \quad (\text{Eq. 21})$$

In the steady-state regime and at low incident powers, the population densities of $\text{Yb}^{3+} \ ^2\text{F}_{5/2}$, $\text{Er}^{3+} \ ^4\text{I}_{11/2}$ and $\text{Er}^{3+} \ ^4\text{I}_{13/2}$ have a linear dependence on the incident pump power, while the population densities of $\text{Er}^{3+} \ ^4\text{F}_{9/2}$ and $\text{Er}^{3+} \ (^4\text{S}_{3/2}, \ ^2\text{H}_{11/2})$ present a quadratic dependence.

**APPENDIX B: Supplementary data on $\text{RE}_2\text{BaZnO}_5: \text{Yb}^{3+}, \text{Ho}^{3+}$
(RE = Y, Gd) materials**

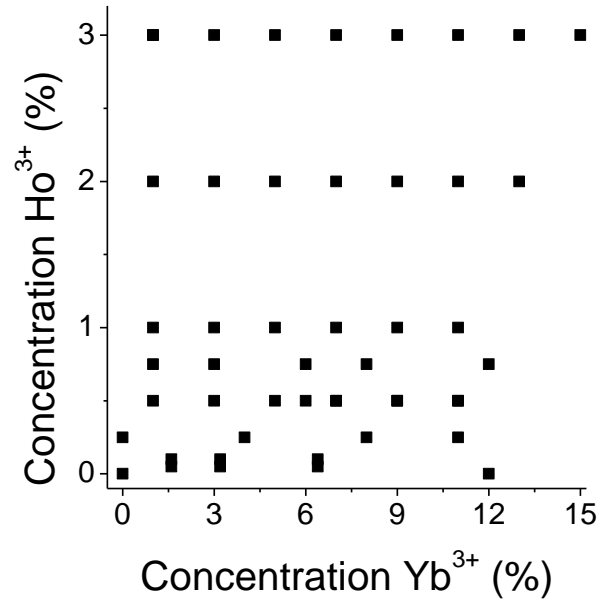


Figure B.1: Yb^{3+} and Ho^{3+} concentrations of the $\text{Y}_2\text{BaZnO}_5: \text{Yb}^{3+}, \text{Ho}^{3+}$ samples for which upconversion efficiencies were measured (see Chapter 6, Figure 6.5).

$\lambda_{\text{excitation}}$	977 nm	977 nm	455 nm	977 nm	455 nm	977 nm	455 nm
$\lambda_{\text{emission}}$	1040 nm	545 nm	545 nm	760 nm	760 nm	1200 nm	1200 nm
T = 80 K	165 μs	208 μs	180 μs	223 μs	172 μs	1730 μs	1630 μs
T = 107 K	178 μs	185 μs	128 μs	183 μs	128 μs	1780 μs	1690 μs
T = 133 K	195 μs	180 μs	102 μs	180 μs	102 μs	1840 μs	1750 μs
T = 185 K	215 μs	219 μs	84 μs	201 μs	72 μs	1800 μs	1730 μs
T = 239 K	275 μs	236 μs	57 μs	224 μs	52 μs	1680 μs	1676 μs
T = 293 K	344 μs	280 μs	46 μs	291 μs	47 μs	1520 μs	1510 μs
T = 348 K	481 μs	298 μs	43 μs	296 μs	43 μs	1240 μs	1280 μs
T = 403 K	522 μs	284 μs	38 μs	287 μs	40 μs	996 μs	1050 μs
T = 458 K	517 μs	247 μs	37 μs	242 μs	37 μs	811 μs	808 μs
T = 513 K	496 μs	219 μs	33 μs	219 μs	33 μs	654 μs	639 μs
T = 573 K	438 μs	214 μs	28 μs	195 μs	29 μs	544 μs	469 μs

Table B.1: Temperature dependence of the lifetimes corresponding to the 1040 nm emission under pulsed 977 nm excitation, and to the 545 nm, 760 nm and 1200 nm emissions under pulsed 977 nm and 455 nm excitations, in $\text{Y}_2\text{BaZnO}_5:\text{Yb}^{3+}$ (7%), Ho^{3+} (0.5%). Percentage errors in the reported values are typically on the order of 5%.

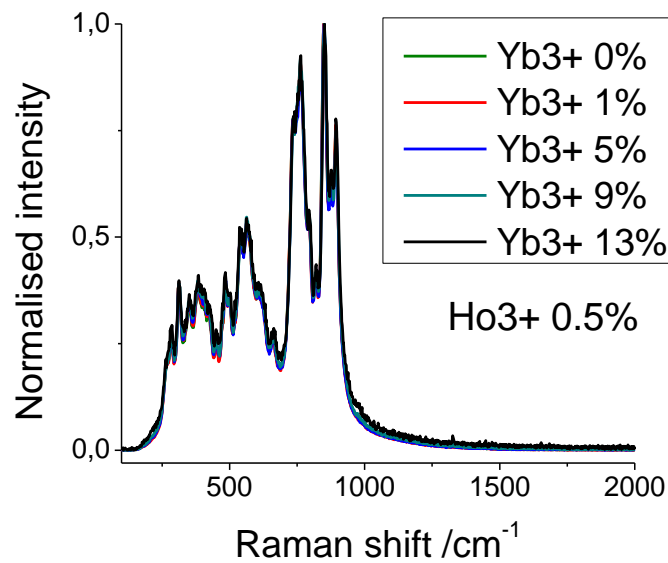


Figure B.2: Raman spectra of $\text{Y}_2\text{BaZnO}_5:\text{Yb}^{3+}$ ($x\%$), Ho^{3+} (0.5%) samples ($x = 0, 1, 5, 9, 13$) under 633 nm excitation at room-temperature.

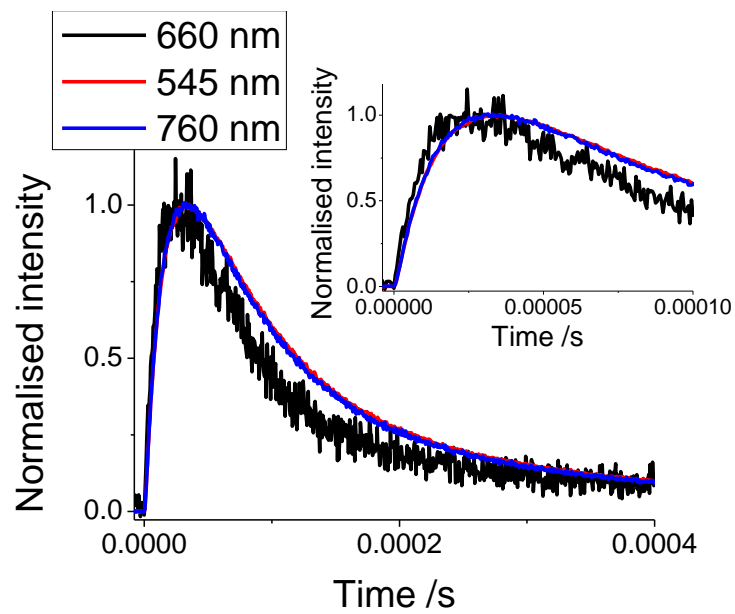


Figure B.3: Normalised transients associated with the emissions at 545 nm, 760 nm and 660 nm of $\text{Y}_2\text{BaZnO}_5:\text{Yb}^{3+}$ (11%), Ho^{3+} (0.5%) under 977 nm excitation at room-temperature. Note that the emission at 660 nm was very weak, hence the poor signal to noise ratio. The inset represents a zoom of the transients at short times.

APPENDIX C: Rate-Equations in Yb^{3+} , Ho^{3+} co-doped materials

In this section, we write the rate equations governing upconversion in $\text{RE}_2\text{BaZnO}_5: \text{Yb}^{3+}, \text{Ho}^{3+}$ ($\text{RE} = \text{Y}, \text{Gd}$), assuming that dopant concentrations are low, so that cross-relaxation and hopping processes can be neglected (Figure C.1).

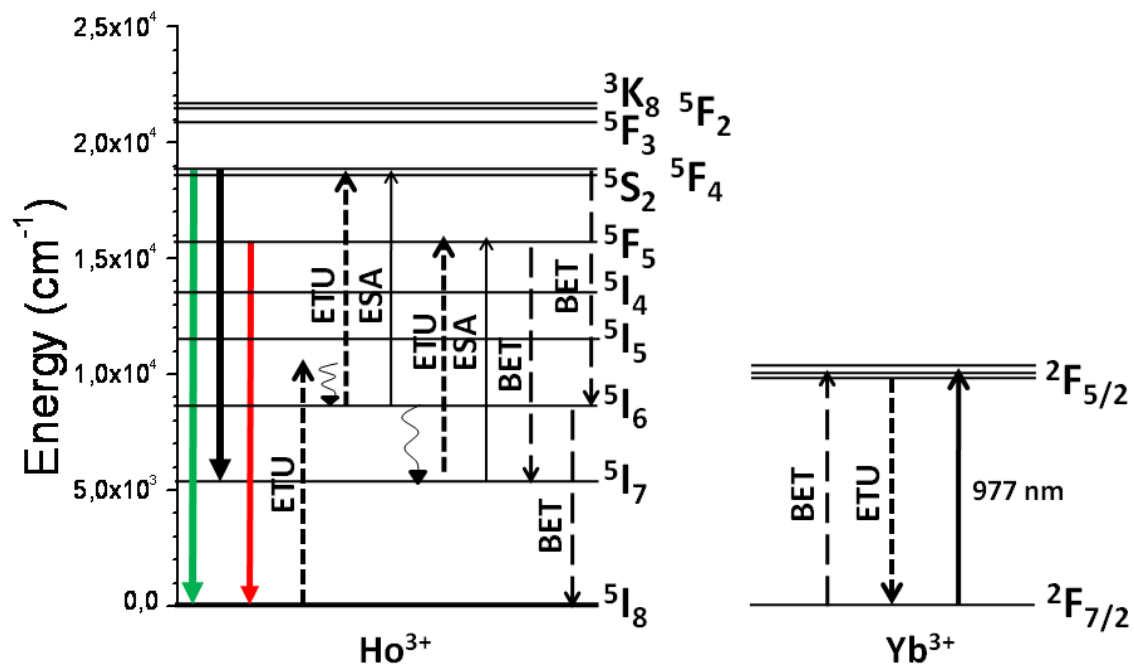


Figure C.1: Simplified energy level diagram of Ho^{3+} and Yb^{3+} ions and the dominant upconversion mechanisms in $\text{RE}_2\text{BaZnO}_5: \text{Yb}^{3+}, \text{Ho}^{3+}$ ($\text{RE} = \text{Y}, \text{Gd}$). Radiative processes of excited state absorption (ESA) and green, red and near-infrared luminescence, as well as non-radiative energy transfer upconversion (ETU), back energy transfer (BET) and multiphonon relaxation processes, are represented.

In this section, we denote:

- N_0 the population density of $\text{Ho}^{3+} \ ^5\text{I}_8$
- N_1 the population density of $\text{Ho}^{3+} \ ^5\text{I}_7$
- N_2 the population density of $\text{Ho}^{3+} \ ^5\text{I}_6$
- N_3 the population density of $\text{Ho}^{3+} \ ^5\text{F}_5$
- N_4 the population density of $\text{Ho}^{3+} \ (^5\text{S}_2, \ ^5\text{F}_4)$
- N_{D0} the population density of $\text{Yb}^{3+} \ ^2\text{F}_{7/2}$
- N_D the population density of $\text{Yb}^{3+} \ ^2\text{F}_{5/2}$
- τ_i the radiative lifetime of the state $|i\rangle$ of population density N_i
- σ_i the absorption cross-section of state $|i\rangle$ at 977 nm
- W_{ij} the multiphonon rate from state $|i\rangle$ to state $|j\rangle$
- A_{ij} the radiative emission rate from state $|i\rangle$ to state $|j\rangle$
- C_{Di} the rate of the energy transfer from $\text{Yb}^{3+} \ ^2\text{F}_{5/2}$ to Ho^{3+} , which result in the population of the state $|i\rangle$ of Ho^{3+}
- C_{iD} the rate of the back energy transfer from state $|i\rangle$ of Ho^{3+} to $\text{Yb}^{3+} \ ^2\text{F}_{7/2}$, resulting in the population of $\text{Yb}^{3+} \ ^2\text{F}_{5/2}$
- ϕ the pump rate

In the following equations, we assume that there is no pump depletion, that the ground state population densities N_{D0} and N_0 are constant, and that the system is continuously pumped into the $\text{Yb}^{3+} \ ^2\text{F}_{5/2}$ state. We neglect the population of $\text{Ho}^{3+} \ ^5\text{I}_5$, assuming that fast $\text{Ho}^{3+} \ ^5\text{I}_5 \rightarrow \text{Ho}^{3+} \ ^5\text{I}_6$ multiphonon relaxation occurs. It is worth noting that Ho^{3+} does not absorb at 977 nm (no ground state absorption by Ho^{3+}).

The rate equations can be written as follows:

$$\frac{dN_D}{dt} = \phi\sigma_D N_{D0} + C_{4D}N_4N_{D0} + C_{2D}N_2N_{D0} + C_{3D}N_3N_{D0} - \frac{N_D}{\tau_D} - C_{D2}N_DN_0 - C_{D3}N_DN_1 - C_{D4}N_DN_2 \quad (\text{Eq. 1})$$

$$\frac{dN_1}{dt} = W_{21}N_2 - \frac{N_1}{\tau_1} - \phi\sigma_1N_1 - C_{D3}N_DN_1 + C_{3D}N_3N_{D0} \quad (\text{Eq. 2})$$

$$\frac{dN_2}{dt} = C_{D2}N_DN_0 + C_{4D}N_4N_{D0} + (W_{32} + A_{32})N_3 + A_{42}N_4 - W_{21}N_2 - C_{D4}N_DN_2 - \phi\sigma_2N_2 - \frac{N_2}{\tau_2} \quad (\text{Eq. 3})$$

$$\frac{dN_3}{dt} = C_{D3}N_D N_1 + \phi\sigma_1 N_1 + W_{43}N_4 - \frac{N_3}{\tau_3} - C_{3D}N_3 N_{D0} - W_{32}N_3 \quad (\text{Eq. 4})$$

$$\frac{dN_4}{dt} = C_{D4}N_D N_2 + \phi\sigma_2 N_2 - C_{4D}N_4 N_{D0} - \frac{N_4}{\tau_4} - W_{43}N_4 \quad (\text{Eq. 5})$$

In the low power regime, we can simplify the rate equations. In particular, we can neglect the contribution of upconversion terms ($C_{D2}N_D N_0$, $C_{D3}N_D N_1$ and $C_{D4}N_D N_2$) to the depopulation of $\text{Yb}^{3+}{}^2\text{F}_{5/2}$ and $\text{Ho}^{3+}{}^5\text{I}_7$, as well as the contribution of back energy transfer ($C_{4D}N_4 N_{D0}$, $C_{3D}N_3 N_{D0}$ and $C_{2D}N_2 N_{D0}$) terms to the population of $\text{Yb}^{3+}{}^2\text{F}_{5/2}$, $\text{Ho}^{3+}{}^5\text{I}_6$ and $\text{Ho}^{3+}{}^5\text{I}_7$. Excited State Absorption terms ($\phi\sigma_1 N_1$ and $\phi\sigma_2 N_2$) can be neglected in the population mechanism of $\text{Ho}^{3+}{}^5\text{F}_5$ and $\text{Ho}^{3+}{}^5\text{S}_2$, ${}^5\text{F}_4$ and in the depopulation mechanism of $\text{Ho}^{3+}{}^5\text{I}_7$ and $\text{Ho}^{3+}{}^5\text{I}_6$. Finally, we can neglect the contribution of multiphonon relaxation and radiative emission from the higher-lying energy levels to the population of $\text{Ho}^{3+}{}^5\text{I}_6$.

In the low power regime, the rate equations become:

$$\frac{dN_D}{dt} = \phi\sigma_D N_{D0} - \frac{N_D}{\tau_D} \quad (\text{Eq. 6})$$

$$\frac{dN_1}{dt} = W_{21}N_2 - \frac{N_1}{\tau_1} \quad (\text{Eq. 7})$$

$$\frac{dN_2}{dt} = C_{D2}N_D N_0 - W_{21}N_2 - \frac{N_2}{\tau_2} \quad (\text{Eq. 8})$$

$$\frac{dN_3}{dt} = C_{D3}N_D N_1 + W_{43}N_4 - \frac{N_3}{\tau_3} - W_{32}N_3 \quad (\text{Eq. 9})$$

$$\frac{dN_4}{dt} = C_{D4}N_D N_2 - C_{4D}N_4 N_{D0} - \frac{N_4}{\tau_4} - W_{43}N_4 \quad (\text{Eq. 10})$$

In the steady-state regime:

$$\frac{dN_D}{dt} = \frac{dN_1}{dt} = \frac{dN_2}{dt} = \frac{dN_3}{dt} = \frac{dN_4}{dt} = 0 \quad (\text{Eq. 11})$$

Therefore, by solving the simplified equations in the steady-state regime and in the low power regime, we get:

$$N_D = \tau_D \phi\sigma_D N_{D0} \quad (\text{Eq. 12})$$

$$N_2 = \frac{C_{D2}N_0}{W_{21}+1/\tau_2} N_D \quad (\text{Eq. 13})$$

$$N_1 = \tau_1 W_{21} N_2 = \frac{C_{D2} N_0 \tau_1 W_{21}}{W_{21} + 1/\tau_2} N_D \quad (\text{Eq. 14})$$

$$N_4 = \frac{C_{D4} N_D N_2}{C_{4D} N_{D0} + W_{43} + 1/\tau_4} = \frac{C_{D2} C_{D4} N_0}{(C_{4D} N_{D0} + W_{43} + 1/\tau_4)(W_{21} + 1/\tau_2)} N_D^2 \quad (\text{Eq. 15})$$

$$N_3 = \frac{C_{D3} N_D N_1 + W_{43} N_4}{W_{32} + 1/\tau_3} = \frac{1}{(W_{21} + 1/\tau_2)(W_{32} + 1/\tau_3)} \left[C_{D2} C_{D3} N_0 \tau_1 W_{21} + \frac{C_{D2} C_{D4} N_0 W_{43}}{(C_{4D} N_{D0} + W_{32} + 1/\tau_4)} \right] N_D^2 \quad (\text{Eq. 16})$$

Finally, in the steady-state regime and at low incident power, since N_{D0} , N_0 , C_{Di} , C_{iD} , W_{ij} , τ_i and σ_D are constants, we obtain:

$$N_D \propto \phi \quad (\text{Eq. 17})$$

$$N_1 \propto \phi \quad (\text{Eq. 18})$$

$$N_2 \propto \phi \quad (\text{Eq. 19})$$

$$N_3 \propto \phi^2 \quad (\text{Eq. 20})$$

$$N_4 \propto \phi^2 \quad (\text{Eq. 21})$$

In the steady-state regime and at low incident powers, the population densities of $\text{Yb}^{3+} \ ^2\text{F}_{5/2}$, $\text{Ho}^{3+} \ ^5\text{I}_6$ and $\text{Ho}^{3+} \ ^5\text{I}_7$ have a linear dependence on the incident pump power, while the population densities of $\text{Ho}^{3+} \ ^5\text{F}_5$ and $\text{Ho}^{3+} \ (^5\text{S}_2, ^5\text{F}_4)$ present a quadratic dependence.

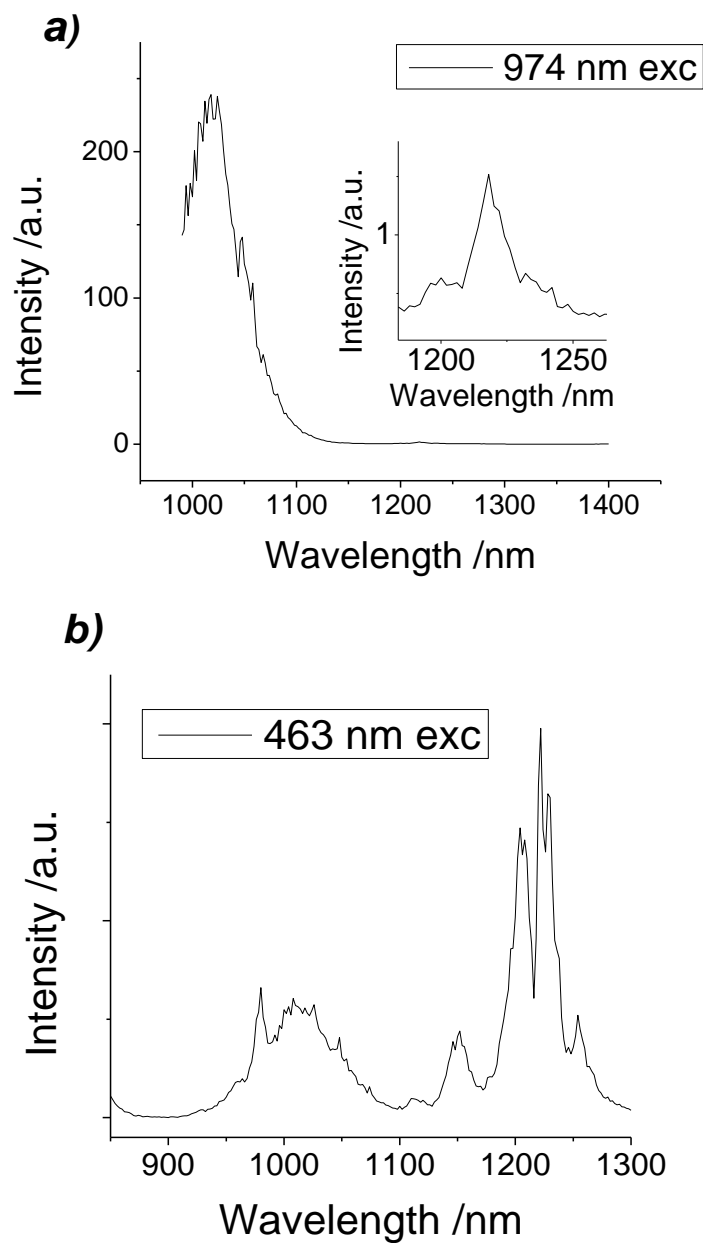
APPENDIX D: Supplementary data on $\text{Y}_2\text{BaZnO}_5: \text{Yb}^{3+}, \text{Tm}^{3+}$ materials

Figure D.1: Typical luminescence emission spectra of $\text{Y}_2\text{BaZnO}_5: \text{Yb}^{3+}$ (6%), Tm^{3+} (0.25%) phosphors at room-temperature under a) 974 nm and b) 463 nm excitations.

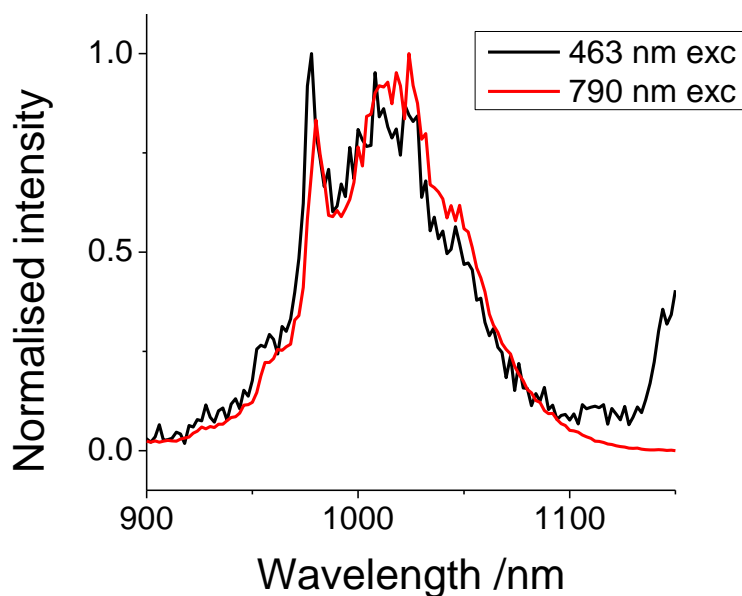


Figure D.2: Typical luminescence spectra of $Y_2BaZnO_5: Yb^{3+} (6\%), Tm^{3+} (0.25\%)$ phosphors at room-temperature under 463 nm and 790 nm excitations.

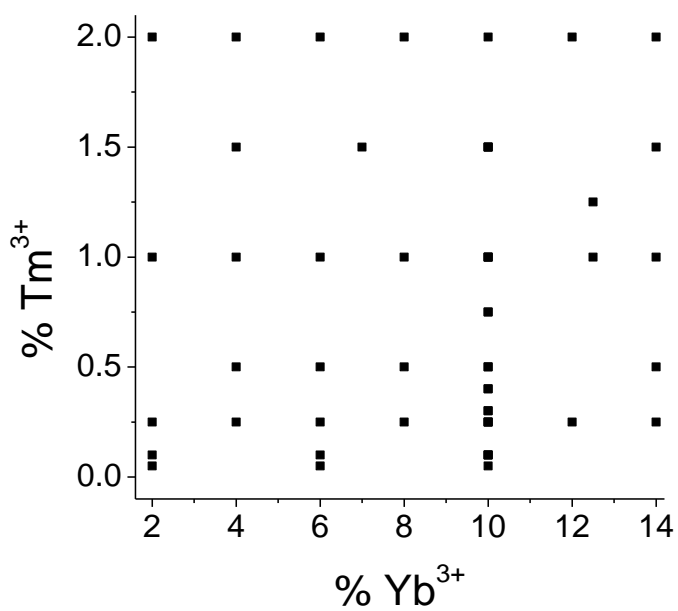


Figure D.3: Yb^{3+} and Tm^{3+} concentrations of the $Y_2BaZnO_5: Yb^{3+}, Tm^{3+}$ samples for which upconversion efficiencies have been measured (see Figure 7.5).

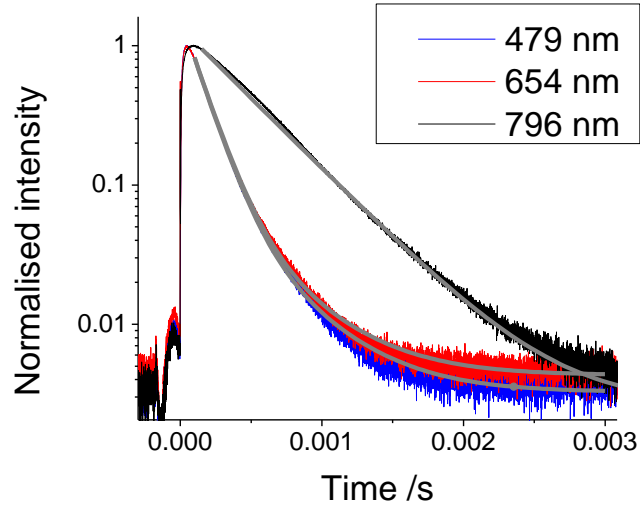


Figure D.4: Typical room-temperature evolution of the blue (479 nm), red (654 nm) and near-infrared (796 nm) emissions under pulsed 974 nm excitation, and data fitting in order to get average lifetimes in $Y_2BaZnO_5: Yb^{3+}$ (6%), Tm^{3+} (0.25%). Note that the small peak observed around $t \sim -45 \mu s$ is due to a triggering artefact.

$\lambda_{excitation}$	974 nm	974 nm	974 nm	974 nm	463 nm	463 nm	463 nm
$\lambda_{emission}$	479 nm	654 nm	796 nm	1022 nm	479 nm	654 nm	796 nm
0% Yb, 0.25% Tm	N.A.	N.A.	N.A.	N.A.	194 μs	193 μs	434 μs
2% Yb, 0.25% Tm	290 μs	279 μs	659 μs	488 μs	191 μs	191 μs	420 μs
6% Yb, 0.25% Tm	176 μs	181 μs	435 μs	303 μs	182 μs	181 μs	352 μs
10% Yb, 0.25% Tm	141 μs	145 μs	319 μs	256 μs	178 μs	175 μs	342 μs
10% Yb, 0.5% Tm	134 μs	135 μs	304 μs	251 μs	157 μs	154 μs	279 μs
10% Yb, 1% Tm	71 μs	75 μs	203 μs	199 μs	129 μs	126 μs	222 μs
10% Yb, 2% Tm	60 μs	73 μs	180 μs	164 μs	101 μs	102 μs	189 μs

Table D.1: Concentration dependence of the lifetimes corresponding to the 479 nm, 654 nm, 796 nm and 1022 nm emissions under pulsed 974 nm and 463 nm excitations of $Y_2BaZnO_5: Yb^{3+}$ ($x\%$), Tm^{3+} ($y\%$) ($x = 0, 2, 6, 10$ and $y = 0.25, 0.5, 1, 2$) materials. Errors in the reported values are typically on the order of 5%.

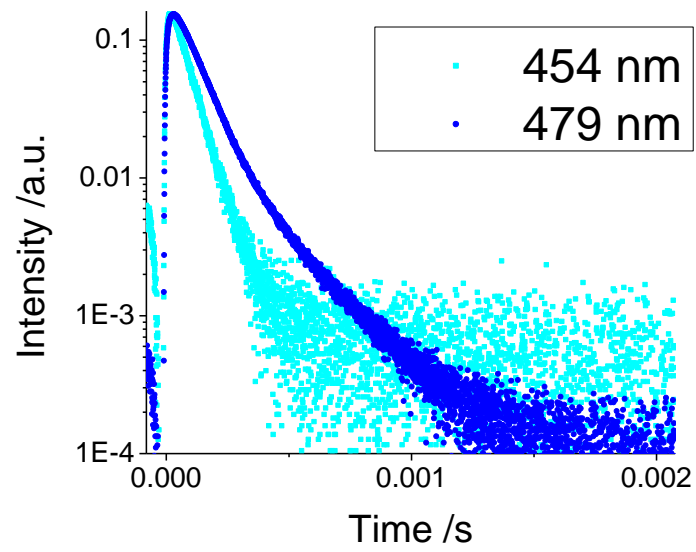


Figure D.5: Typical room-temperature temporal evolution of the 454 nm and 479 nm blue emissions under pulsed 974 nm excitation in $Y_2BaZnO_5: Yb^{3+}$ (6%), Tm^{3+} (0.25%).

APPENDIX E: Rate-Equations in Yb^{3+} , Tm^{3+} co-doped materials

In this section, we write the rate equations governing upconversion in $\text{Y}_2\text{BaZnO}_5: \text{Yb}^{3+}, \text{Tm}^{3+}$ (Figure E.1), assuming that dopant concentrations are low, so that cross-relaxation and hopping processes can be neglected.

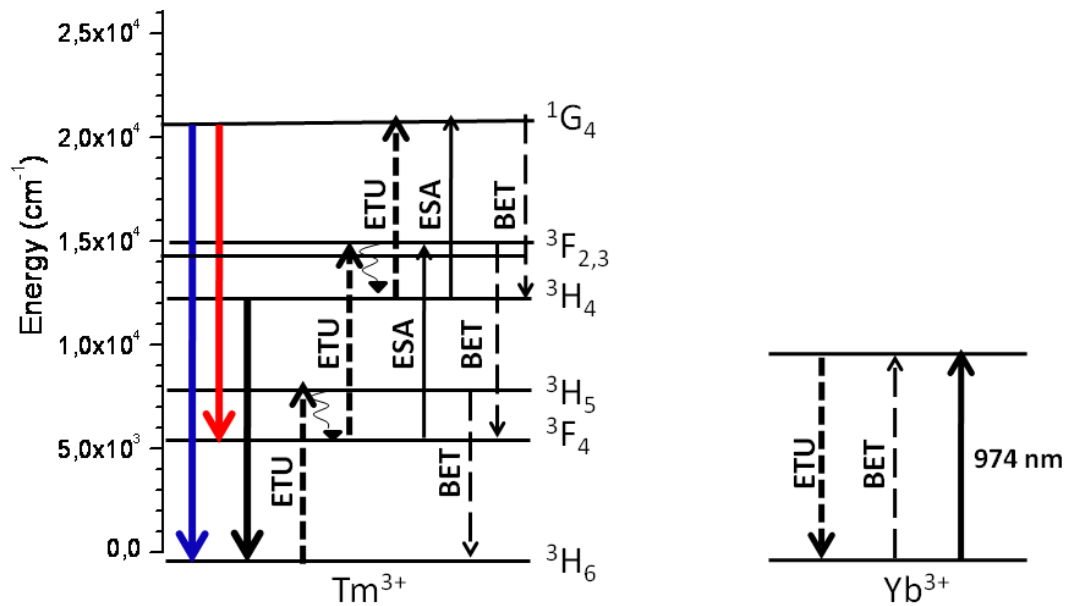


Figure E.1: Simplified energy diagram of Tm^{3+} and Yb^{3+} ions and the dominant upconversion mechanisms in $\text{Y}_2\text{BaZnO}_5: \text{Yb}^{3+}, \text{Tm}^{3+}$. Blue, red and near-infrared luminescence, as well as (non-resonant) non-radiative energy transfer upconversion (ETU), multiphonon relaxation, and cross-relaxation (CR) processes, are represented.

In this section, we denote:

- N_0 the population density of $\text{Tm}^{3+} {}^3\text{H}_6$
- N_1 the population density of $\text{Tm}^{3+} {}^3\text{F}_4$
- N_2 the population density of $\text{Tm}^{3+} {}^3\text{H}_4$
- N_3 the population density of $\text{Tm}^{3+} {}^1\text{G}_4$
- N_{D0} the population density of $\text{Yb}^{3+} {}^2\text{F}_{7/2}$
- N_D the population density of $\text{Yb}^{3+} {}^2\text{F}_{5/2}$
- τ_i the radiative lifetime of the state $|i\rangle$ of population density N_i
- σ_i the absorption cross-section of state $|i\rangle$ at 974 nm
- W_{ij} the multiphonon rate from state $|i\rangle$ to state $|j\rangle$
- A_{ij} the radiative emission rate from state $|i\rangle$ to state $|j\rangle$
- C_{Di} the rate of the energy transfer from $\text{Yb}^{3+} {}^2\text{F}_{5/2}$ to Tm^{3+} , which result in the population of the state $|i\rangle$ of Tm^{3+}
- C_{iD} the rate of the back energy transfer from state $|i\rangle$ of Tm^{3+} to $\text{Yb}^{3+} {}^2\text{F}_{7/2}$, resulting in the population of $\text{Yb}^{3+} {}^2\text{F}_{5/2}$
- ϕ the pump rate

In the following equations, we assume that there is no pump depletion, that the ground state population densities N_{D0} and N_0 are constant, and that the system is continuously pumped into the $\text{Yb}^{3+} {}^2\text{F}_{5/2}$ state. We also assume that the electrons in $\text{Tm}^{3+} {}^3\text{H}_5$ and $\text{Tm}^{3+} {}^3\text{F}_{2,3}$ relax very fast to the $\text{Tm}^{3+} {}^3\text{F}_4$ and $\text{Tm}^{3+} {}^3\text{F}_4$ states, respectively, by multiphonon relaxation. It is worth noting that Tm^{3+} does not absorb at 980 nm (no ground state absorption by Tm^{3+}).

The rate equations can be written as follows:

$$\frac{dN_D}{dt} = \phi\sigma_D N_{D0} + C_{1D}N_1N_{D0} + C_{2D}N_2N_{D0} + C_{3D}N_3N_{D0} - \frac{N_D}{\tau_D} - C_{D1}N_DN_0 - C_{D2}N_DN_1 - C_{D3}N_DN_2 \quad (\text{Eq. 1})$$

$$\frac{dN_1}{dt} = C_{D1}N_DN_0 + C_{2D}N_2N_{D0} + (W_{21} + A_{21})N_2 + A_{31}N_3 - \frac{N_1}{\tau_1} - C_{D2}N_DN_1 - \phi\sigma_1N_1 - W_{10}N_1 - C_{1D}N_1N_{D0} \quad (\text{Eq. 2})$$

$$\frac{dN_2}{dt} = C_{D2}N_DN_1 + (W_{32} + A_{32})N_3 + C_{3D}N_3N_{D0} + \phi\sigma_1N_1 - C_{D3}N_DN_2 - C_{2D}N_2N_{D0} - \frac{N_2}{\tau_2} - W_{21}N_2 - \phi\sigma_2N_2 \quad (\text{Eq. 3})$$

$$\frac{dN_3}{dt} = C_{D2}N_D N_2 + \phi\sigma_2 N_2 - \frac{N_3}{\tau_3} - C_{3D}N_3 N_{D0} - W_{32}N_3 \quad (\text{Eq. 4})$$

In the low power regime, we can simplify the rate equations. In particular, we can neglect the contribution of upconversion terms ($C_{D1}N_D N_0$, $C_{D2}N_D N_1$ and $C_{D3}N_D N_2$) to the depopulation of $\text{Yb}^{3+} \ ^2\text{F}_{5/2}$, $\text{Tm}^{3+} \ ^3\text{F}_4$ and $\text{Tm}^{3+} \ ^3\text{H}_4$, as well as the contribution of back-energy transfer ($C_{3D}N_3 N_{D0}$, $C_{2D}N_2 N_{D0}$ and $C_{1D}N_1 N_{D0}$) terms to the population of $\text{Yb}^{3+} \ ^2\text{F}_{5/2}$, $\text{Tm}^{3+} \ ^3\text{F}_4$ and $\text{Tm}^{3+} \ ^3\text{H}_4$. Excited State Absorption terms ($\phi\sigma_1 N_1$ and $\phi\sigma_2 N_2$) can also be neglected in the population mechanism of $\text{Tm}^{3+} \ ^3\text{H}_4$ and $\text{Tm}^{3+} \ ^1\text{G}_4$ and in the depopulation mechanism of $\text{Tm}^{3+} \ ^3\text{F}_4$ and $\text{Tm}^{3+} \ ^3\text{H}_4$. Finally, we can neglect the contribution of multiphonon relaxation and radiative emissions from the higher-lying energy levels to the population of $\text{Tm}^{3+} \ ^3\text{F}_4$ and $\text{Tm}^{3+} \ ^3\text{H}_4$.

In the low power regime, the rate equations become:

$$\frac{dN_D}{dt} = \phi\sigma_D N_{D0} - \frac{N_D}{\tau_D} \quad (\text{Eq. 5})$$

$$\frac{dN_1}{dt} = C_{D1}N_D N_0 - \frac{N_1}{\tau_1} - W_{10}N_1 \quad (\text{Eq. 6})$$

$$\frac{dN_2}{dt} = C_{D2}N_D N_1 - W_{21}N_2 - \frac{N_2}{\tau_2} \quad (\text{Eq. 7})$$

$$\frac{dN_3}{dt} = C_{D2}N_D N_2 - \frac{N_3}{\tau_3} - C_{3D}N_3 N_{D0} - W_{32}N_3 \quad (\text{Eq. 8})$$

In the steady-state regime:

$$\frac{dN_D}{dt} = \frac{dN_1}{dt} = \frac{dN_2}{dt} = \frac{dN_3}{dt} = \frac{dN_4}{dt} = 0 \quad (\text{Eq. 9})$$

Therefore, by solving the above simplified equations in the steady-state regime and at low incident power, we get:

$$N_D = \tau_D \phi\sigma_D N_{D0} \quad (\text{Eq. 10})$$

$$N_1 = \frac{C_{D1}N_0}{W_{10}+1/\tau_1} N_D \quad (\text{Eq. 11})$$

$$N_2 = \frac{C_{D2}N_1}{W_{21}+1/\tau_2} N_D = \frac{C_{D1}C_{D2}N_0}{(W_{10}+1/\tau_1)(W_{21}+1/\tau_2)} N_D^2 \quad (\text{Eq. 12})$$

$$N_3 = \frac{C_{D2}N_D N_2}{C_{3D}N_{D0} + W_{32}+1/\tau_3} = \frac{C_{D1}C_{D2}^2 N_0}{(W_{10}+1/\tau_1)(W_{21}+1/\tau_2)(C_{3D}N_{D0} + W_{32}+1/\tau_3)} N_D^3 \quad (\text{Eq. 13})$$

Finally, in the steady-state regime and at low incident power, since N_{D0} , N_0 , C_{Di} , C_{iD} , W_{ij} , τ_i and σ_D are constants, we obtain:

$$N_D \propto \phi \quad (\text{Eq. 14})$$

$$N_1 \propto \phi \quad (\text{Eq. 15})$$

$$N_2 \propto \phi^2 \quad (\text{Eq. 16})$$

$$N_3 \propto \phi^3 \quad (\text{Eq. 17})$$

The population densities of $\text{Yb}^{3+} {}^2\text{F}_{5/2}$ and $\text{Tm}^{3+} {}^3\text{F}_4$ have a linear dependence on the incident pump power, while the population densities of $\text{Ho}^{3+} {}^3\text{H}_4$ and $\text{Ho}^{3+} {}^1\text{G}_4$ present quadratic and cubic dependences, respectively.